TESIS DE LA UNIVERSIDAD DE ZARAGOZA

2021 374

Dan Lu

Contagion dynamics in multilevel and structured populations.

Director/es
Dr. D. Yamir Moreno Vega
Dr. D. Dr. Alberto Aleta Casas

ISSN 2254-7606

Prensas de la Universidad
Universidad Zaragoza

ISSN 2254-7606

Universidad Zaragoza
1542

Tesis Doctoral

CONTAGION DYNAMICS IN MULTILEVEL AND STRUCTURED POPULATIONS.

Autor

Dan Lu

Director/es

Dr. D. Yamir Moreno Vega
Dr. D. Dr. Alberto Aleta Casas

UNIVERSIDAD DE ZARAGOZA
Escuela de Doctorado

2021

Universidad de Zaragoza
Departamento de Física Teórica

Contagion Dynamics in Multilevel and Structured Populations

Doctoral Dissertation of:
Dan Lu

Supervisor of the Doctoral Program:
Prof. Yamir Moreno
Dr. Alberto Aleta

October 15, 2021

Abstract

There are abundant contagion processes taking place on networks, such as the spreading of diseases, rumors, information and other nonlinear phenomena in complex human systems. From the perspective of mathematical modelling, contagion processes in networked populations are becoming increasingly sophisticated with various types of nontrivial interactions involved. Models have evolved from the relatively simple compartmental methods to structured frameworks with heterogeneities of populations taken into account. In addition, to portrait the hierarchies and heterogeneities in complex human systems, we also consider the multilayer representative of the populations. In this thesis, we attempt to explore the tip of the iceberg in contagion processes occurring in populations by conceptualizing them with various mathematical models. We aim at understanding the intricacies of contagion dynamics in multilevel and structured populations.

In the first chapter, we focus on recalling the development of the theory to study complex systems. The discovery of nonlinear interactions made the method of reductionism questionable since the overall behavior can not be described by the simple superposition of small scales. Network science is aimed at characterizing the interactions of complex systems' constituents at various scales to understand their macroscopic behavior. At the same time, graph theory provides a mathematical tool that can be used to describe realistic networks. We discuss some of the fundamental quantities and relevant measurements developed to characterize the network structure as well as several typical network models. Moreover, we briefly overview the basic principles of multilayer networks that break the limitation of "one-type" connection in single-layer networks, laying the groundwork for subsequent explorations and generalizations.

Next, the studies of dynamical processes are addressed starting with a brief introduction of some mathematical methods used later on. In the case of the master equation, we emphasize the Markov process framework as well as the mean-field approximation scheme, rather than diving into their complete so-

lutions. Modelling methods and updating rules in numerical simulations are also presented in detail. In this thesis, we focus on the problem of epidemic spreading on networks, an enduring hot topic in the field of spreading and contagion processes. After reviewing the properties and theoretical results of some typical epidemic models with specific assumptions from the mathematical point of view, we explore several important quantities in the field of epidemiology, i.e., the reproduction number and herd immunity. Then, we implement a classical epidemic model on multilayer networks to explore the role of directionality with the generating function approach. We end up Chapter 2 with modelling a kind of social contagion process, namely, the evolution of corruption behaviors, with a compartmental approach. We pay attention to the critical conditions for the emergence of corruption behaviors by developing in detail its mean-field theory and comparing its predictions with simulations. Furthermore, we extend the corruption model to a duplex system where different flows occur in a specific layer to investigate the effect of edge overlap and interlayer degree correlations on the evolution of honesty and corruption activities.

It is clear that the complexity of real-world human systems definitely affects the accuracy of epidemic forecasts and of some specific properties existing in a given system. However, due to the development of data science, massive and informative data sources could conduce to enrich the network topology so that it gets closer to real systems. In the third part of this thesis, we first outline the challenges and opportunities regarding the rise of data science. Then, we try to yield a close real picture of the underlying structure of contact networks from the collected data. Moreover, we illustrate the importance of data-driven network modelling on studying disease transmission on contact networks by incorporating real data. In this case, the variance of contact patterns that stem from population heterogeneities, social behaviors, etc. can be well-portrayed.

Along with this theoretical framework, we consider the age of individuals and social contact patterns to generate a data-driven age-structured multilayer representation of the population to estimate the SARS-CoV-2 herd immunity threshold and evaluate the impact of three vaccination strategies on suppressing the pandemic transmission. Then, to explore the dynamics of healthcare-associated infections (HAIs) that people get while receiving treatment in healthcare settings, we make use of spatio-temporal data collected from three hospitals in Canada to generate networks of interactions among healthcare workers (HCWs). We focus on quantitatively assessing the risks of HAIs spreading in spatial units and occupational groups of HCWs, respectively. We conduct the risk assessment of spatial units by calculating the

disease hitting time and the number of infections produced in each unit. For the HCWs case, the probability of getting infected and effective reproduction number are used as the indicators of HCWs risks.

We round off this thesis by presenting our conclusions and discussing some remaining challenges to be explored in the future.

Resumen

Existen numerosos procesos de contagio sobre redes, como la propagación de epidemias, los rumores, la información u otros fenómenos no lineales propios de los sistemas complejos humanos. Desde la perspectiva de la modelización matemática, los procesos de contagio en poblaciones estructuradas se están volviendo cada vez más sofisticados en lo que respecta al tipo de interacciones no triviales involucradas en ellos. Los modelos han evolucionado desde los simples métodos compartimentales a modelos estructurados en los que se tienen en cuenta las heterogeneidades de la población. Además, para visualizar estas jerarquías y heterogeneidades de los sistemas complejos humanos, también consideramos la representación multicapa de las poblaciones. En esta tesis, intentamos explorar la punta del iceberg en lo que respecta a procesos de contagio sobre poblaciones basándonos en varios modelos matemáticos. Nuestro objetivo es entender la complejidad de las dinámicas de contagio en poblaciones estructuradas y multinivel.

En el primer capítulo, nos centramos en presentar el desarrollo de algunas de las teorías principales que se utilizan para estudiar los sistemas complejos. El descubrimiento de las interacciones no lineales hizo que le método del reduccionismo fuese cuestionado, dado que el comportamiento general no puede describirse como una simple superposición de pequeñas escalas. La ciencia de redes busca caracterizar los sistemas complejos de diversos campos. Al mismo tiempo, la teoría de grafos proporciona las herramientas matemáticas necesarias para describir redes realistas. Discutiremos algunas de las cantidades fundamentales y las métricas más relevantes para la caracterización de la estructura de la red, así como varios ejemplos de modelos de red. Además, repasaremos brevemente los principios básicos de las redes multicapa que rompen la limitación de un solo tipo de conexión existente en las redes monocapa, estableciendo la base para explorar y generalizar estos conceptos.

A continuación, estudiaremos procesos dinámicos comenzando por una breve introducción a los modelos matemáticos que se usarán durante el resto de la tesis. En el caso de la ecuación maestra, resaltaremos el rol de los pro-

cesos de Markov así como la aproximación de campo medio, sin centrarnos en sus soluciones completas. Los métodos de modelización y las reglas de actualización que se utilizan en las simulaciones numéricas también se presentan en detalle. En esta tesis, nos centraremos en el problema de la propagación de epidemias sobre redes, un tema que despierta gran interés en el campo de los procesos de propagación y contagio. Después de revisar las propiedades y los resultados teóricos de algunos de los modelos epidemiológicos típicos, con varias simplificaciones desde el punto de vista matemático, exploraremos varias medidas importantes en el campo de la epidemiología, i.e., el número reproductivo básico y la inmunidad de grupo. Después, implementaremos un modelo clásico de epidemias sobre redes multicapa para explorar el papel que juega la direccionalidad utilizando funciones generatrices. Terminaremos el capítulo 2 modelizando un tipo especial de procesos de contagio social, en particular, utilizaremos un modelo compartimental para estudiar la propagación de la corrupción. Prestaremos atención a las condiciones críticas para que surja este tipo de comportamiento desarrollando la aproximación de campo medio y comparando sus predicciones con simulaciones. Es más, extenderemos el modelo de corrupción a un sistema de dos capas en el que los flujos de contagio pueden ser diferentes en cada capa para investigar el papel que juega el solapamiento de enlaces y las correlaciones de grado entre capas en la evolución de las actividades honestas y corruptas.

Resulta evidente que la complejidad de los sistemas humanos del mundo real afecta la precisión con la que se pueden predecir las epidemias y algunas propiedades específicas de los sistemas. Sin embargo, debido al desarrollo de la ciencia de datos, fuentes de datos masivas y muy informativas pueden utilizarse para enriquecer la topología de la red de forma que se acerque a los sistemas reales. En al tercera parte de esta tesis, comenzaremos describiendo los retos y las oportunidades que han surgido durante el desarrollo de la ciencia de datos. A continuación, intentaremos conseguir una imagen más realista de la estructura interna de las redes de contacto utilizando datos reales. Además, ilustraremos la importancia de utilizar una perspectiva conducida por los datos en lo que respecta a la modelización de redes a la hora de estudiar la propagación de epidemias en redes de contacto. En este caso, la variabilidad de patrones de interacción que surge de la heterogeneidad de la población, sus comportamientos sociales, etc. puede ser capturada correctamente.

Bajo este mismo desarrollo teórico, consideraremos la edad de los individuos y sus patrones de interacción social para generar redes multicapa con estructura de edad para estudiar el problema de la inmunidad de grupo del SARS-CoV-2 y evaluar el impacto que tres estrategias de vacunación pueden

tener a la hora de eliminar la transmisión de la panedmia. Después, para explorar la dinámica de las enfermedades que se propagan en entornos hospitalarios (HAI, por sus siglas en inglés) cuando los pacientes están recibiendo tratamiento en ellos, utilizaremos una colección de datos espacio-temporales recogida en tres hospitales de Canadá para generar las redes de interacción entre los trabajadores hospitalarios (HCWs). Nos centraremos en determinar cuantitativemente el riesgo de que las HAIs se propaguen por las diferentes unidades de un hospital y los varios grupos de HCWs, respectivamente. Calcularemos el riesgo de las unidades espaciales usando el tiempo de llegada de la enfermedad y el número de infecciones producidas en cada unidad. En el caso de los HCWs, la probabilidad de infectarse y el número de reproducción efectivo son usados como indicador del riesgo de HCWs.

Concluiremos la tesis presentando nuestras conclusiones y discutiendo algunos de los restos que quedan por explorar en el futuro.

Contents

List of Figures

List of Tables

Introduction 1

1.1 Complexity in Complex Systems

The universe and everything in it can be regarded as Complex Systems composed of intricately connected segments. Since Newton established the three laws of mechanics, it is generally believed that as long as we can figure out the properties of the components of a system and their interactions between them, then the future behaviors of these systems can be accurately predicted, which makes the primary argument of early methodology *Reductionism* [1, 2] for the analysis of the real-world systems. Thereafter, the famous quotation by Laplace emerged:

> *"An intelligence knowing all the forces acting in nature at a given instant, as well as the momentary positions of all things in the universe, would be able to comprehend in a single formula the motions of the largest bodies as well as of the lightest atoms in the world, provided that its intellect were sufficiently powerful to subject all data to analysis; to it nothing would be uncertain, the future as well as the past would be present to its eyes."*
>
> — Laplace, 1814

which is well-known as *Laplacian determinism*. Accordant with the belief expressed in reductionism, it is possible to give a precise prediction of future states at an arbitrary time according to the fundamental equations of the evolution of a system and the initial states [3].

However, there exists a plethora of systems that are not suited to be discussed with the reductive method. In addition, the great success of reductionism in physics does not mean that it can achieve the same success in different disciplinary fields, such as in social sciences, biological sciences and so on [4]. Admittedly, the interaction of basic elements involves an immense amount of complicated factors which are intricately interlinked. Therefore, not only is it impossible to carry out an analytical discussion of dynamics, but it is also impossible to calculate from scratch with "ideal precise" values without considering approximations. Moreover, as the *"organization"* of the elementary units of such a system will present many *emergent* properties that will not be

exhibited by a considerable number of discrete individuals, it is impossible to make predictions about the rich behavior of the entire system solely based on the characteristics of an independent unit, such as the typical *adaptive system*. Broadly speaking, the above-mentioned circumstances have contributed to the *Complexity* of Complex Systems simultaneously.

In 1984, George Cowan and a group of young scientists in a variety of fields founded the famous *Santa Fe Institute*, committed to exploring the methodology of Complexity and the general laws that govern Complex Systems by means of ideas from multiple fields [5]. Several representative definitions of Complexity are derived from Santa Fe Institute. Holland, the father of genetic algorithms, believes that complexity arises from the adaptive behavior of systems with famous assertion *adaptation builds complexity*. Another scientist, Melanie Mitchell defines complex systems in her book as: *"a system in which large networks of components with no central control and simple rules of operation give rise to complex collective behavior, sophisticated information processing, and adaptation via learning or evolution"*.

Although there is still no unambiguous and formal definition of Complexity or Complex Systems that is widely accepted, there is a largely unified understanding of the property characteristics of complex systems, including nonlinearity, chaos, emergence, self-organization, self-adaptability, and so on. Particularly, nonlinear interactions make it impossible to obtain the overall behavior of a system by a simple superposition of individual behaviors. Moreover, the existence of nonlinear factors makes it impossible to obtain answers to problems at large scales simply by superposition of small scales. The properties that emerge at higher levels cannot be explained directly from those at lower levels. Therefore, the method of reductionism is ill-suited to study complex systems. [6–8].

In a nutshell, complex systems must be explored from a holistic perspective with individual behaviors and their interaction mechanisms taken into account. Broadly speaking, an abundance of complex systems can be modelled as networks which are the essential abstraction of their interaction structures [9–12]. In this sense, exploring the relationship between network structure and function is closely linked to understanding the nature of systems. In a special issue on complex systems published in Science [13], there is an enlightening quote from Barabási who points out that since the underlying structure has a crucial effect on the behavior of the system, there is no way to understand complex systems unless the network structure is explored, which also fuels our passion to explore in depth the topics in next sections.

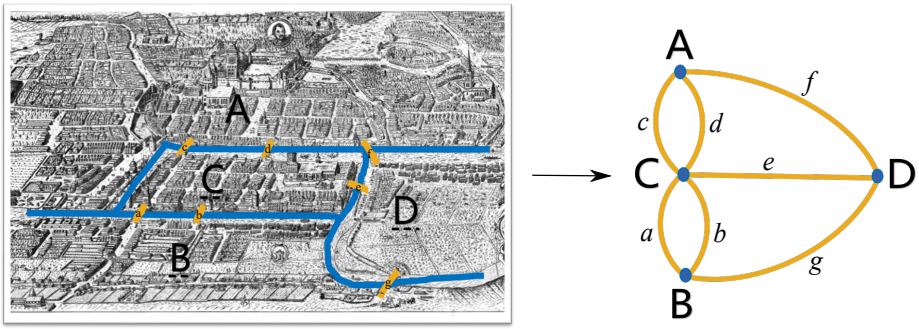

FIGURE 1.1: **Illustration of the problem of the Seven Bridges of Königsberg.** This problem can be easily solved by interpreting it as a graph, in which vertices and edges represent land portions and bridges, respectively.

1.2 A Tentative Discussion on Network Science

There is no denying that *networks* have certainly become the most ubiquitous and powerful tool to characterize Complexity in Complex Systems. Any given system can be rendered as a network composed of a group of components and connections. Therefore, a system can be reduced to an abstract structure, only capturing the basic patterns of interactions which are crucial to comprehend the behavior of systems. Put in the simple terms, a network is a collection of discrete objects joined together, usually described as *nodes* connected by *links* in the jargon of the field [14]. In the subsequent sections, we will present a brief overview of the mathematical foundations of Network science.

1.2.1 The role of graph theory

To conduct complex network research, the knowledge from different fields, such as statistical physics, game theory, probability and mathematical statistics is required. Among them, graph theory is recognized as the mathematical basis of complex network research. In the following, the essential knowledge of graph theory will be introduced.

Currently, it is widely accepted that the first theorem in graph theory is specifically originated from the solution of the Königsberg bridge problem solved by great Swiss mathematician Leonhard Euler [15, 16]. In Fig. 1.1, we present a depiction of Königsberg in the time of Euler, with four regions separated by a river and connected by seven bridges over the river. The mathematical puzzle Euler contemplated is simply expressed as: is it possible to have a path that allows the people to go through all four areas by crossing

each bridge once and only once? Euler published an important article in 1736 and proposed that the bridge crossing problem can be abstractly reduced to the combination of points and lines on the plane. He considered the land portions as four points and the seven bridges as connections between them, as shown in the right side of Fig.1.1. In graph representation, each point is referred to as *vertex*, also called *node*. The connection relation between them is abstracted into an *edge*, or *link*. With this simplified approach, he analytically proved that there is no such path for going through the seven Bridges at a time.

From 1736 to 1950s, the field of graph theory was substantially expanded, but it was limited by the lack of tools for large-scale computation. With the invention of modern computers, the matrix description of graphs attracted a lot of attention. Afterwards, massive problems sprung up about using *graph* to describe the large real networks, e.g. power grids, traffic networks, communication networks and so on. In the decades that followed, a remarkable collection of scientists introduced ideas, methods and analysis tools of statistical physics into graph theory, giving birth to *network science* [17, 18].

1.2.2 Networks representation & statistical characterization

We can encode real-world systems into a mathematical object using graph theory. This way, a network is referred to as $G = (V, E)$ consisting of a set of nodes (vertices) $V(G)$ and links (edges) $E(G)$ in which each edge, e_{ij}, joins a pair of nodes (i, j), with $i, j \in V(G)$.

There are two fundamental mathematical representations of a network, adjacency matrices and adjacency lists. In general, *adjacency matrix*, $\mathcal{A}$, is the most common representation, reflecting the adjacency relations between nodes, in which the topological properties of networks are encoded. The *adjacency matrix* is a square matrix of size $|V| \times |V|$, where each cell $a_{ij} = 1$ if there is an edge between node i and j, i.e., $e_{ij} \in |E|$ and $a_{ij} = 0$ otherwise. The undirected network is the most commonly seen case (see Fig. 1.2A), in which $\mathcal{A}$ is a symmetric matrix. Note that the adjacency table representation of a graph is not unique because for each vertex, the order of linking the other end of edge can be arbitrary which depends on the algorithm used to build the adjacency matrix and the input order of edges. In terms of directed networks, any given pair of nodes (i, j) and (j, i) does not correspond to the same link leading to an asymmetric matrix as shown in Fig. 1.2B.

If we allow the a_{ij} elements to take any real value, we say that it is a *weighted network*. These networks have a broad range of applications. For

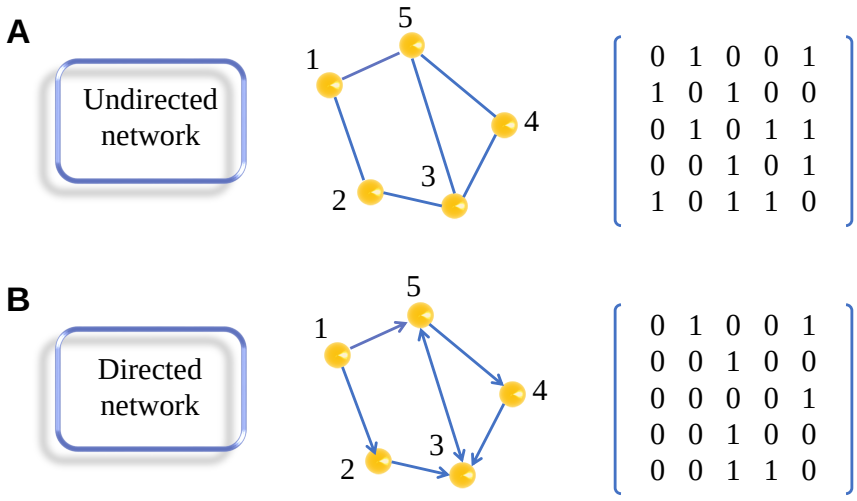

FIGURE 1.2: **Graphical representation of undirected and directed networks with their respective adjacency matrices.** The adjacency matrix for the undirected network is symmetric since the relationship between any two nodes is reciprocal. Instead, the panel below indicates that there is no reciprocal relation among nodes in the case of a directed network.

example, the edges in traffic networks might have weight representing the flow between two stations and the level of intimacy between friends in social networks can be represented by the weight of edges. Similarly, the weighted networks are displayed by an adjacency matrix W where each element w_{ij} specifies the weight between nodes i and j.

When looking at a network, the research task of interest usually can be phrased in terms of its topological properties reflected by its unique connection patterns. Hence, the statistical summaries of network structure can support us in comprehending their topology and, consequently, understanding the mechanisms behind their dynamical processes. There are many fundamental quantities and corresponding measures developed to characterize networks, such as, degree, clustering, path and so on. However, they are far too many to cover all of them in the thesis. Thus, we will introduce the metrics most relevant to our research interests.

1. ***Degree and centrality***

The *degree* of a node is one of the most basic geometric quantities, providing the most important statistical description of connection relations between nodes. Besides, its simplicity makes it analytically tractable. Suppose that

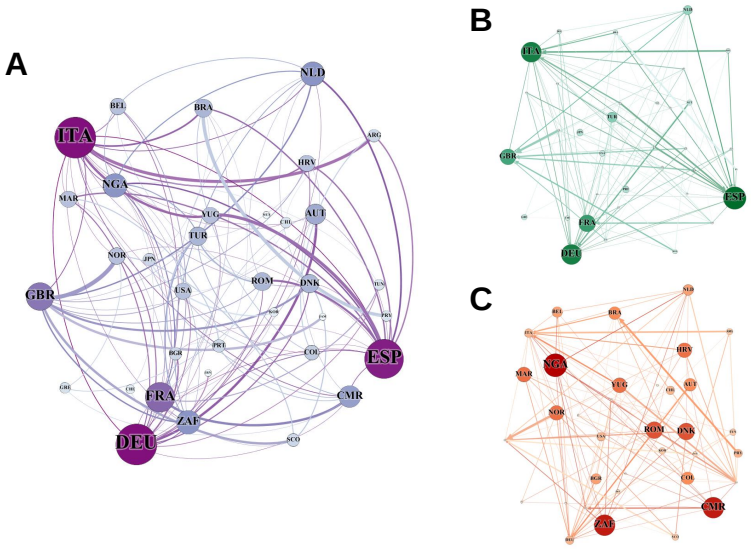

FIGURE 1.3: **Comparison of three different types of degree.** The different types of degree are visualized in a network which consists of 35 countries where 22 soccer teams had contacts, extracted from Pajek datasets (http://vlado.fmf.uni-lj.si/pub/networks/data/sport/football.htm). The network is constructed by counting how many soccer players are exported from country i to country j, forming a valued, asymmetric graph where some countries only import players, while some countries are only exporters. The nodal size is scaled to **A)** the overall degree of the node, **B)** the in-degree of the node and **C)** the out-degree of the node, respectively.

the number of nodes in an undirected network is N, the degree of node i is defined as the number of adjacent edges it has, denoted by k_i. It can be mathematically indicated by the elements of its adjacency matrix as

$$k_i = \sum_j a_{ij}. \tag{1.1}$$

We define m as the total number of links in the network, which is equivalent to $|E|$ and can be measured as the sum of the degrees of all nodes, $\sum_{i=1}^{N} k_i = 2m$. The average degree is conceived to indicate the way in which nodes are connected to each other, given by:

$$\langle k \rangle = \frac{1}{N} \sum_i k_i \tag{1.2}$$

In the case of directed networks, the degree of nodes is generalized as *in-degree* (k_i^{in}) and *out-degree* (k_i^{out}), defined by the number of incoming links

and outgoing links from node i, The formulas are as follows:

$$k_i^{in} = \sum_{j=1}^{N} a_{ij}, \qquad k_i^{out} = \sum_{j=1}^{N} a_{ji}. \tag{1.3}$$

In Fig. 1.3, we show these different types of degree in a small network. The network here is composed of 35 nodes, describing the 22 soccer teams who constitutes a players market within 35 countries. As players in soccer teams often have contacts in other countries where some countries only import players, while some countries are only exporters, the highly asymmetric network is formed. In the graphical representation of the network where the position of nodes is fixed, we can observe different patterns by looking at the size of nodes which is proportional to each type of degree, i.e., A) overall degree k_i, B) in-degree k_{in} and C) out-degree k_{out}. We observe that the apparent importance of each node depends on the type of degree we consider. This provides a stark reminder that the role of different types of degree should be taken into account in the analysis of network dynamics.

Considering weighted networks, each node has not only *degree* but also *strength* according to the variable w_{ij} from the weight matrix W, written as:

$$s_i = \sum_j w_{ij} \tag{1.4}$$

There is a great deal of research associated with the concept of *node degree*, essentially trying to understand its importance in the network. The quantity *centrality* is proposed as an indicator of the influence of nodes in a network. There are many definitions of importance from different perspectives developed by many scholars [10, 19, 20]. Accordingly, many measures of node centrality have appeared successively. The simple and straightforward view of measuring centrality is the degree of a node. The degree occasionally is referred to as *degree centrality* which can be used in some practical applications, especially in the context of social networks where an individual with more connections ("large degree") perceives information more easily and might have more influence. To answer the question whether there is a central node in the entire network, there are other ways for measuring centrality, such as betweenness centrality, closeness centrality, PageRank (see the differences between them in Fig. 1.4) and so on.

2. ***Degree distribution***

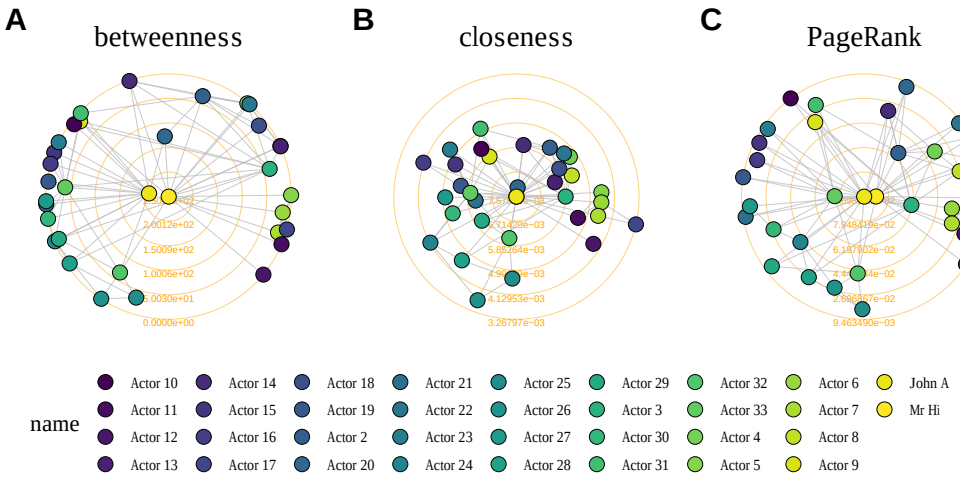

Figure 1.4: **Comparison of three methods for degree centrality calculation.** We calculate the degree centrality in a social network between members of a university karate club, led by president John A. and karate instructor Mr. Hi. The datasets named "karate" is from the datasets in "igraph" package of R language [21]. It shows the differences between three methods, **A)** betweenness centrality, **B)** closeness centrality and **C)** PageRank, respectively.

Another fundamental property, which particularly has a profound effect on characterizing empirical network data, is the frequency degree distribution of nodes. Based on the definition of degree we mentioned in eq. 1.1, we define $P(k)$ as the proportion of nodes whose degree is k. That is, the probability of selecting a node at random in the network with degree k. Obviously, the information of average degree has been embodied in degree distribution, which gives

$$\langle k \rangle = \sum_{k=0}^{\infty} kP(k). \tag{1.5}$$

The concept, *degree distribution*, will recur repeatedly throughout this thesis, considered as a conductive viewpoint in the discussion for the theoretical network models.

It is instructive to visualize how the degree distribution of a network with large-scale structure looks like, which is also a common starting point to analyze network data. In most real-world networks, the frequency distribution of degrees as a function of k turns out showing a long *tail* effect, namely *right-skewed* pattern, which will be explored deeply in the next section.

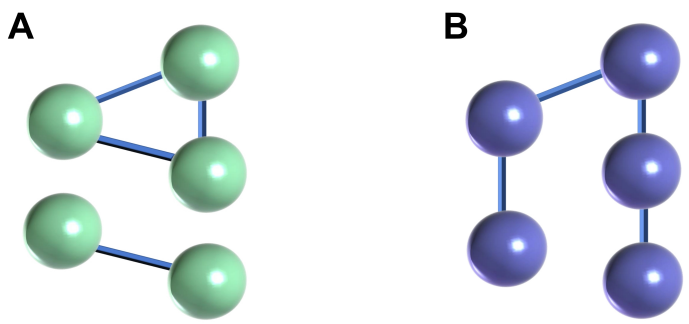

FIGURE 1.5: **Two simple graphs with identical degree distribution. A)** The graph is composed of two subgraphs. **B)** The graph is a connected graph. The difference between the structure of two graphs is particularly visible even though they have the same degree sequence.

Technically, degree distribution in a directed network can also be calculated, just separated into in-degree distribution and out-degree distribution, respectively. The measure of the degree distribution in more sophisticated network, such as multilayer networks we are interested in which will be defined in section 1.3, is realized by using the *joint degree distribution* [1] with degree correlations taken into consideration . It is worth underlining that the knowledge of degree distribution is just a preliminary tool to delve into the structure of the network, but one can not grab the complete topological information through it.

3. ***Degree correlations and mixing patterns***

The average degree of a network is a rough description of the network, and the degree distribution gives us a more specific understanding of the network. However, it can not completely describe the structural characteristics of the network. In some cases, networks may exhibit distinct properties or behaviors even though they have the exact same degree of distribution. To this end, we need to dig a little deeper and investigate another indicator *degree correlation*.

Basically, the degree correlation is depicted by the two-point conditional probability $P(k'|k)$ that any edge emanating from a node with given degree k is connected to a node with degree k', expressed as

[1] See [22] for the original use of terms "joint-degree matrix", "joint-degree sequence" and "joint-degree distribution"

$$P(k'|k) = \frac{\langle k \rangle P(k,k')}{kP(k)}, \tag{1.6}$$

where $P(k,k')$ represents the joint probability of the nodes at both ends of a randomly picked edge in the network whose degree is k and k', respectively [23–25]. The term *joint probability* is introduced due to the common phenomena shown in Fig. 1.5, where the structure of graph A is obviously different from that in graph B even though they have same degree sequence.

As we shall see, it is too complicated to measure the degree correlation directly by the formula with empirical network data. Therefore, a quantity with better practical applicability is defined by the average closest neighbors degree of the nodes with degree k,

$$k_{nn}(k) = \sum_{k'} k' P(k'|k). \tag{1.7}$$

The handy way to get this quantity is to start with calculating the average nearest neighbors degree of a node i, give by

$$k_{nn,i}(k) = \frac{1}{k_i} \sum_{j \in N_i} a_{ij} k_j, \tag{1.8}$$

where N_i is the set of neighbors of node i. Then, the behavior of degree correlation can be characterized by

$$k_{nn}(k) = \frac{1}{N} \sum_{i \in M_k} k_{nn,i}(k), \tag{1.9}$$

where M_k is the number of nodes whose degree is k.

In general, to visualize the pattern of degree correlations, it works well by plotting $k_{nn}(k)$ as a function of node degree k. If the value of slope is positive, it means that on average, the nodes with higher degrees show a strong tendency to link with those with higher degrees, and vice versa. This is called *assortative mixing* [20, 25, 26]. Conversely, *disassortative mixing* can be encountered when the value of slope is negative. It points out a complete reversal of the previous trend, in the sense that nodes with high degrees have a large probability to associate with those with low degrees.

In addition to give us a deeper understanding of the network structure, studying the degree correlation and mixing patterns on the network also has important practical significance, especially employed on the subsequent dynamics studies. Social networks and scientist collaboration networks are all

typical example with assotative mixing patterns [27]. People with great influence preferentially connect to others with similar influence, while many biological networks exhibit the presence of disassortative mixing patterns. It is an important topic in complex network analysis to investigate the causes and effects of the properties yielded by different degree correlations.

1.2.3 Network models

In the last section, we focused on statistical characteristics of static nature in networks. As differences in network topology will lead to different properties, in this section, we will introduce some fundamental models to generate networks showing those specific statistical properties. Moreover, graph models provide a basic structural framework for modelling the complex dynamics of systems. For instance, epidemic models on different networks are employed to describe phenomena of the spread of contagious diseases, the transmission of rumors among population and so on.

1. ***Random graphs and Erdős-Rényi model***

Traditional physics and many other scientific studies have long believed that a variety of complex systems in human life are composed of some basic units. They expect to comprehend the dynamics of systems indirectly by exploring the relationship between them. They assume that basic units are distributed on grid of regular space making the forces between them along the direction of connecting grid points, which is the original description of regular network.

The *regular graph* stated in graph theory refers to a graph in which each node shares the same degree connecting with m nodes adjacent to it. Therefore, the average degree of regular graph is $\langle k \rangle = m$ independent of the network scale and the degree distribution is given by a delta distribution:

$$P(k) = \begin{cases} 1 & \text{if } k = m \\ 0 & \text{if } k \neq m \end{cases} \tag{1.10}$$

As early as 1959, Hungarian mathematicians Paul Erdős and Alféd Rényi proposed a random graph model, commonly known as Erdős-Rényi random graph [28, 29]. In general, there are two ways to generate the ER model. The simplest way is to fix the size of network, N and randomly add M edges initially determined to form the ER graph, denoted as $G(N, p)$ [2]. Therefore,

[2]It was first mentioned and studied by Solomonoff and Rapoport [30] which is currently linked to Erdős-Rényi graph

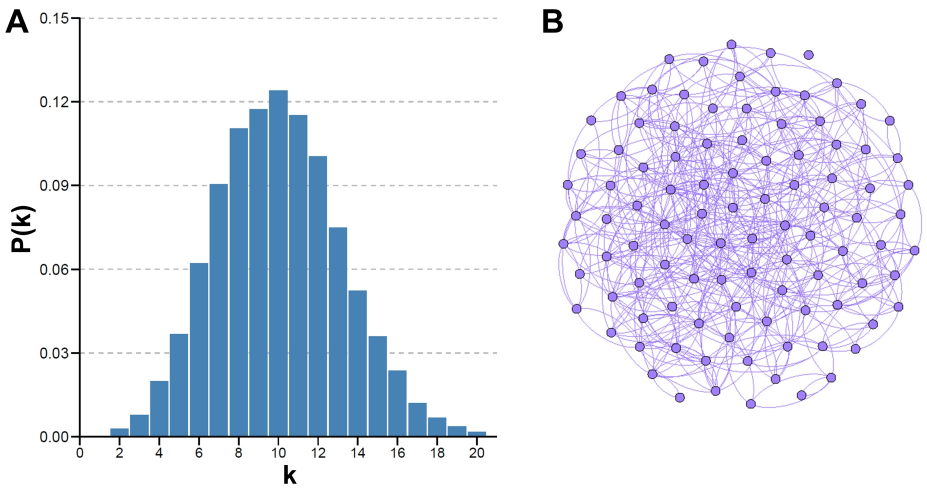

Figure 1.6: **Degree distribution and graphical representation of an Erdős-Rényi graph. A)** The degree distribution of an Erdős-Rényi graph with $N = 10^4$ and average degree $\langle k \rangle = 10$. **B)** The visualization of a small ER graph with $N = 10^2$, $\langle k \rangle = 5$.

the connection probability between two nodes is

$$p = \frac{M}{\binom{N}{2}} \tag{1.11}$$

The maximum possible number of edges is $\binom{N}{2}$. The expected number of graphs will be $\binom{\binom{N}{2}}{M}$. The other equivalent definition is known as the binomial model. Firstly, the total number of nodes in the network is set to N. Then, every pair of nodes is connected with probability p. In this way, the mathematical expectation of the total number of edges is $pN(N-1)/2$. These two definitions are exactly equivalent when the network has reached a sufficient size.

The average degree of ER networks is $p(N-1)$. The degree distribution is strictly proved to be:

$$P(k) = \binom{N-1}{k} p^k (1-p)^{N-1-k} \underset{N\to\infty}{\simeq} e^{-\langle k \rangle} \frac{\langle k \rangle^k}{k!} \tag{1.12}$$

In the case of a large network with constant average degree, the degree distribution can be approximated by a Poisson distribution as seen in Fig. 1.6.

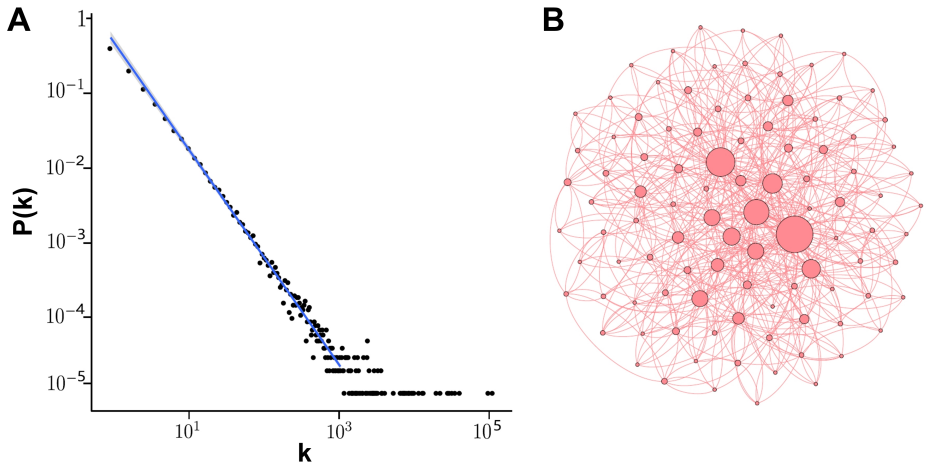

FIGURE 1.7: **Degree distribution and graphical representation of a Barabási-Albert model. A)** The degree distribution of a network produced by the Barabási-Albert model with $N = 10^5$, $m = 3$. The blue line fitting the degree points corresponds to a line with slope 3. **B)** The visualization of a small BA graph with $N = 10^2$, where the size of nodes is proportional to its degree.

Therefore, the ER random graph is also known as Poisson random graph [31, 32].

2. ***Barabási-Albert model***

In 1998, Watts and Strogatz introduced small-world networks whose properties lay between regular and random graphs [33]. This model reflected better the structure of real networks, but there were still areas of doubt about "advanced" features real complex networks have.

It is an indisputable fact that degree distribution is the most notable property. The degree distribution of regular graph and Erdős-Rényi random graph all show some kind of "homogeneity". In 1999, Albert-László Barabási and Réka Albert published a quite influential paper, indicating that the degree distributions in the real complex networks present strong "hetergeneity" [34]. Lots of examples were given in the article that those degree distributions exactly or approximately follow a power-law distribution with the expression $P(k) \propto k^{-\gamma}$. Since for this distribution for certain values of γ, the second moment diverges. Then, networks with this degree distribution are denominated *scale-free* networks [35–37]. Typically, the index of power law is $2 \leq \gamma \leq 3$ [20].

A dynamic network model (also well-known as Barabási–Albert (BA) model) was presented, including two simple assumptions: *growth* and *preference attachment* [34]. The mechanism of generating the model is that they take the initial m_0 vertices to be arbitrarily joined or completely joined. In each step, a new vertex is added based on the original network $G(t-1)$ and m edges starting from that vertex are added simultaneously, forming a new network $G(t)$. Note that the other end of the newly created edge is in proportion to the degree of the existing vertex i, that is the connection probability, $\Pi(i)$, given by

$$\Pi(i) = \frac{k_i}{\sum_j k_j} \tag{1.13}$$

The process of adding new vertex is terminated until the degree distribution of the network satisfies $P(k) \propto k^{-3}$, as shown in Fig. 1.7A. Note that the power exponent γ is independent of the model parameters m_0 and m. Moreover, from the visualization of a small BA model (see Fig. 1.7B), we can clearly observe the typical characteristic of this model that only a few vertices in the graph have extremely large values of degree, called *hubs*, while most vertices have only a very small number of connections.

3. ***Configuration model***

The preferential attachment model or namely BA model characterizes the mechanism of network evolution with a power-law degree distribution as the key focus. The links stay unperturbed in the network as soon as they are established. Such simplifying assumptions make the models feasible for analysis, but fail to capture the complexity of real networks. In order to generate scale-free networks conforming to different exponents (γ), we can use the *configuration model* which was presented by Bender and Canfield [38], and Béla Bollobás [39]. The specific steps to generate a scale-free network are as follows:

(1) Given the size of network N, we generate the N degrees, $k_1, k_2, \cdots, k_N$ with the formula, $k = m/u^{1/(\gamma-1)}$, where m is the minimum degree and u is a random number between 0 and 1 from a uniform distribution.

(2) Generate another degree sequence in the same way. Then connect node i and j which is randomly chosen from two sequences with $p = k_i / \sum_{j=1}^{N} k_j$.

The uncorrelated scale-free network with tunable exponent γ is created until two lists are empty [11, 40]. Note that this algorithm ends up with an even number for the sum of degrees. Additionally, the generation process is likely

to produce multi-edges which occur if there is more than one edge between two vertices or self-loop that is an edge connecting a vertex to itself. However, when the condition $N \to \infty$ is satisfied, it is guaranteed to generate a simple graph with $2 < \gamma \leq 3$ in which there are no loops and multi-edges [20, 41].

4. ***Random regular networks***

Random regular networks (RRN) are a particular case of *k-regular* networks, where each node has the same degree [11, 42]. Therefore, the degree distribution is simply, $P(k_i = k) = 1$. It can be built following the algorithm developed by Steger and Wormald [43], which is actually a natural refinement of the above-mentioned configuration model algorithm. Similarly, we start with N nodes and create N groups with size k in each group. Then, two random nodes i and j which are not in the same set are chosen, i.e., $i \in I$ and $j \in J$ ($I \neq J$). Once they are connected, all the ends of edges belonging to set I and J are not considered in the next step. The edge will be picked following the uniform distribution until we obtain a random regular graph where the maximum degree is always bounded above by k [44]. The simplicity of the model serves the purpose of exploring the dynamical processes on networks without considering lots of cumbersome details.

5. ***Square lattice***

The *lattice graph* or *grid graph* is also known as an Euclidean lattice on account of the fact that the graph is embedded in some Euclidean space $\mathbf{R}^n$. The square lattice is a common type of lattice graph in a two-dimensional Euclidean space [45]. Mathematically, the vertices in the graph correspond to integer coordinate points in the plane with the range of 1. As long as corresponding vertices are located at a distance of 1, an edge is produced to connect the two points.

1.3 Multilayer Networks

So far, real-world complex systems have been mapped into classical graphs or single-layer networks. However, the simple abstraction into single-layer networks ignores the contribution of multiple types of interactions in complex systems. In fact, complex systems composed by the interactions of several networks are commonly found, such as society with different types of social relationship, infrastructure systems including different means of transportation and brain systems containing different functional areas [24, 46–49]. Moreover, the nonlinear interactions and interdependencies between different

subsystems give rise to various forms of correlated structures, exhibiting the temporal-spatial multiscale characteristics [47, 50]. In order to tackle practical problems and break through the limitation of "one-type" connection in single-layer networks, research on complex networks is gradually turning the focus from single-layer networks to multilayer networks, which are nowadays enjoying immense popularity [24, 47].

In this section, we will highlight the definition and basic topological properties of multilayer networks. In the previous methodology, all nodes and edges in a network are considered to be homogeneous, that is, only one type of relationship existing in the network. To embody the diverse properties of nodes and edges more accurately, the interactions with their specific nature in a system can be grouped into a set of different networks connected to each other, forming the structure, namely *multilayer networks*, where each network is called *layer* [47, 51].

There are two cases of multilayer networks generally used to model the real systems. The first one is the *multiplex networks* where each layer contains exactly the same set of nodes. And there may be overlapping links, i.e., two nodes which are linked in one layer may be linked in other layers [24, 52]. The most noteworthy feature of this type of network is that any node can only find its counterpart in the other layer. Social networks could be a representative example of this case where individuals (nodes) can be linked due to their social relationships, like friendship, working relationships and so on [53].

Another specific case is known as *interconnected networks* where each node in a multilayer network belongs to merely one layer. It is impossible to have self-interactions across different layers. The computer-power network is a typical interconnected multilayer network where one layer represents the power transmission between power stations, while another layer represents information exchange between computers. The transmission of power between power plants is controlled by computers, and the communication between computers depends on the plants to provide the necessary power.

Here, we introduce the universal concept of multilayer networks proposed by S. Boccaletti et al [24]. which is a set of networks composed of M single networks, i.e., M layers. And each layer α consists of N_α nodes. There are two ways of mathematical modelling the multiplex networks, *supra-adjacency matrices* and *tensorial representation* [47, 54]. As we are used to encoding the single network by the adjacent matrix, similarly, we will give a brief description of supra-adjacency matrices to represent multilayer networks in the next section.

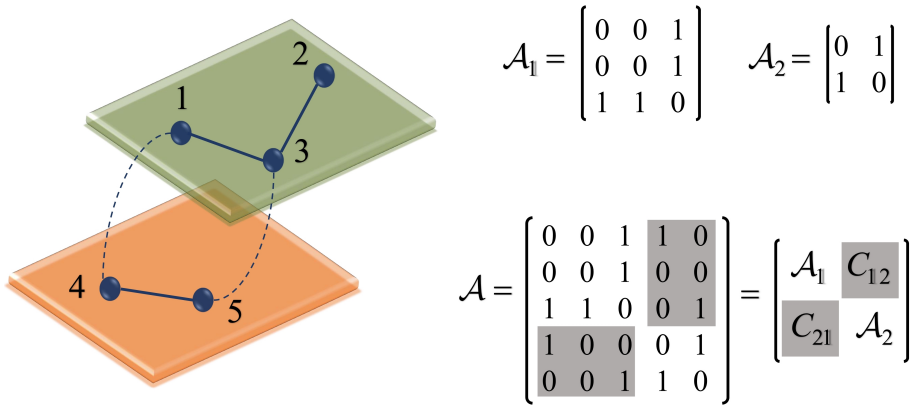

FIGURE 1.8: **Schematic representation of multiplex networks.** The respective adjacency matrix of each layer is shown with $\mathcal{A}_\alpha$, where $\alpha = 1, 2$. The connection between two layers is represented by the adjacency matrices, denoted by $C_{\alpha,\beta}$. Then, the supra-adjacency matrix is formed with intralayer adjacency matrix $\mathcal{A}_\alpha$ and interlayer adjacency matrix $C_{\alpha,\beta}$.

1.3.1 Supra-adjacency matrix representation

In a multilayer network, denoted by $\mathcal{M}$ made up of a set of graphs $\mathcal{G} = \{G_\alpha, \{\alpha = 1, \ldots, M\}\}$, where $G_\alpha = (V_\alpha, E_\alpha)$ in layer α and the nodes in network G_α are represented by the set $V_\alpha = (v_1^\alpha, \ldots, v_{N_\alpha}^\alpha)$, the adjacent matrix $\mathcal{A}_\alpha$ is written:

$$\mathcal{A}_\alpha = \{a_{ij}^\alpha\} \in \mathbb{R}^{N_\alpha \times N_\alpha}, \tag{1.14}$$

where each element in the matrix describing the *intralayer* connection relations is:

$$a_{ij}^\alpha = \begin{cases} 1 & \text{if } (v_i^\alpha, v_j^\alpha) \in E_\alpha \\ 0 & \text{otherwise.} \end{cases} \tag{1.15}$$

Note that node $i, j \in [1, N]$ and $\alpha \in [1, M]$. In addition, there exists a matrix representing coupling relationship, called *interlayer adjacent matrix*, C, where each element is given by:

$$a_{ij}^{\alpha,\beta} = \begin{cases} 1 & \text{if } (v_i^\alpha, v_j^\beta) \in E_{\alpha,\beta} (\alpha \neq \beta) \\ 0 & \text{otherwise.} \end{cases} \tag{1.16}$$

Therefore, the multilayer networks are mapped into a supra-adjacency matrix, defined as:

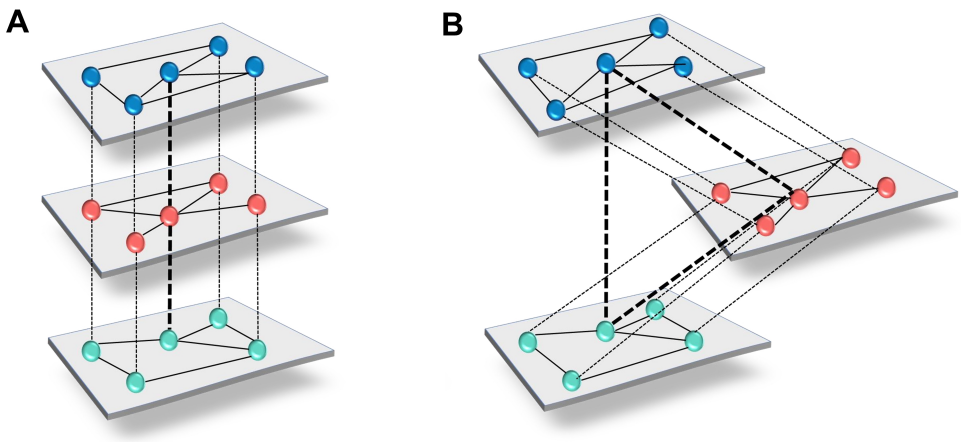

Figure 1.9: **The representation of two specific multilayer networks. A)** The example of three-layer multiplex network. **B)** The example of three-layer interconnected network.

$$\mathcal{A} = \oplus_\alpha \mathcal{A}_\alpha + C. \tag{1.17}$$

We show the schematic representation of a simple multiplex network with two layers in Fig. 1.8. The intralayer adjacent matrix of each layer is presented in the upper panel, represented as $\mathcal{A}_1$ and $\mathcal{A}_2$, respectively. The interlayer adjacent matrices are denoted as C_{12} and C_{21} labeled with shaded area of the supra-adjacency matrix $\mathcal{A}$.

For the two special cases we mentioned, the distinctiveness of the *multiplex networks* is that the node set is fixed, i.e., $V_1 = \cdots = V_M = V$, connected by various types of links where each type is represented by each layer. Here the interlayer links can be re-written as $E_{\alpha,\beta} = \{(v, v), v \in V\}$.

In the case of *interconnected networks* where a set of networks interconnect with each other, it can be projected into a multilayer network with a set of layers $G_1, G_2, \ldots, G_L$. Then, the interactions between any two layer G_α and G_β is denoted by $E_{\alpha,\beta}$. In Fig. 1.9, we show an illustration of the difference between multiplex networks (A) and interconnected networks (B), respectively. It is clear to see the slight differences between these two specific cases of multilayer networks.

After discussing the multilayer formalism mathematically, we come back to a paradigmatic interconnected network to understand its practical applications [48]. As shown in Fig. 1.10, we illustrate a multilayer representation of London railway network. In this case, the network is composed of 369 nodes

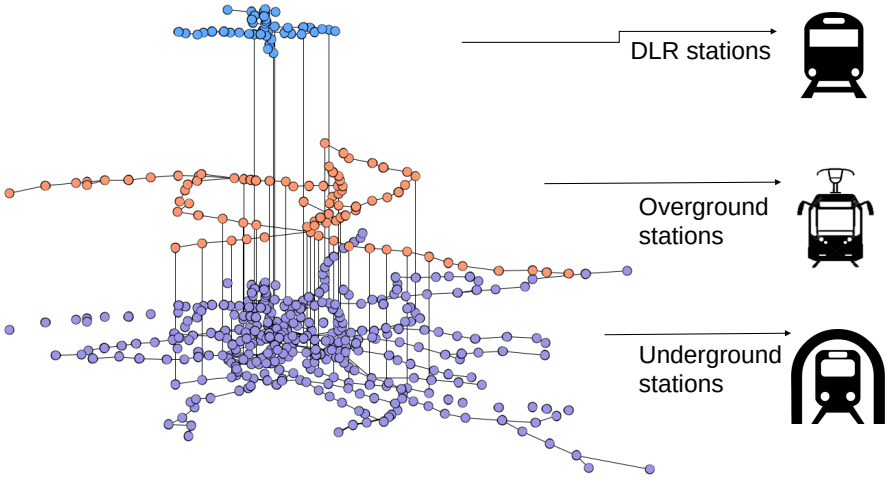

FIGURE 1.10: **A real-world example of multilayer representation.** The London multilayer transportation network consists of 369 nodes (train stations in London) and edges which encode existing routes between stations (https://www.tfl.gov.uk/). The bottom layer represents the networks of stations (purple) corresponding to each underground line. The nodes (orange) in the middle layer represent the overground stations. The top layer corresponds to the network of stations (blue) connected by DLR.

(i.e., train stations) in London and the edges which encode existing routes between stations. Each layer represents the networks of stations corresponding to each underground line, overground line and DLR line, respectively. More specifically, nodes in each distinct layer represent stations of different transportation modes [55]. The interlayer links connecting the stations in different layers make a lot of sense as there exists the possibility of commuting in these means of transportation in London.

1.3.2 Structural metrics

The topological properties of multilayer networks can quantitatively describe the basic characteristics of complex systems, as in single-layer networks. Therefore, it appears necessary to firstly comprehend the properties of topology encoded in multilayer networks before proceeding the in-depth study. In the previous exploration of monolayer networks, some metrics characterizing networks have been introduced. Among all the basic statistical characteristics, there is no way around the fact applying to all networks that the node degree plays a foundational role in exploring the network dynamics. Here, given a

multilayer network, the degree of node $i \in V$ can be extended into a vector:

$$\mathbf{k}_i = (k_i^1, k_i^2, \ldots, k_i^M), \quad i = 1, \ldots, N, \tag{1.18}$$

where $k_i^\alpha = \sum_j a_{ij}^\alpha, \alpha \in [1, M]$, denotes the degree of node i within the layer α. In the case of weighted multilayer networks, the corresponding concept of node strength refers to the sum of the weights of a node in each layer, defined as:

$$\mathbf{s}_i = (s_i^1, s_i^2, \ldots, s_i^M), \quad i = 1, \ldots, N. \tag{1.19}$$

Certainly, compared with single-layer networks, the multilayer networks have more abundant topological properties. In particular, the interactions between layers have attracted considerable attention. In this thesis, two salient aspects in multiplex networks will be especially important: edge overlap and degree correlations. In Ref. [50], the authors proposed the definition of the edge overlap of any pair of nodes (i, j) between layer α and β as:

$$o_{ij}^{\alpha,\beta} = a_{ij}^\alpha + a_{ij}^\beta. \tag{1.20}$$

Therefore, the edge overlap for any edge $i - j$ is written as $o_{ij} = \sum_\alpha a_{ij}^\alpha$, leading to $o_{ij} \in [0, M]$. The matrix $\mathcal{O} = o_{ij}$ is the aggregated overlapping adjacency matrix. In [56], the authors proposed the method for measuring the edge overlap by counting the fraction of edges between layers, obeying:

$$o_s = \frac{\sum_{i,j}^N o_{ij}}{M \sum_{i,j}^N \Theta(o_{ij})}, \tag{1.21}$$

where $\Theta(o_{ij})$ is the Heaviside step function. The $\Theta(o_{ij})$ is taken as 1 when $o_{ij} > 0$. The value of o_s goes from $1/M$ to 1, where the maximum value 1 represents that all layers coincide completely, while o_s is set to $1/M$ when there is no common edge between any two layers. In the specific case of two-layer networks, also namely *duplex* networks, the edge overlap can be obtained based on the above equation by setting $M = 2$. Meanwhile, the overlapping degree of node i can be defined by the edge overlap, given as $o_i = \sum_j o_{ij} = \sum_\alpha k_i^\alpha$.

In addition, the overlap of nodes between layers, denoted by $Q_{\alpha,\beta}$, can be calculated by the proportion of nodes that are common between any two layers α and β:

$$Q_{\alpha,\beta} = \frac{1}{N} \sum_{i=1}^N v_i^\alpha v_i^\beta, \tag{1.22}$$

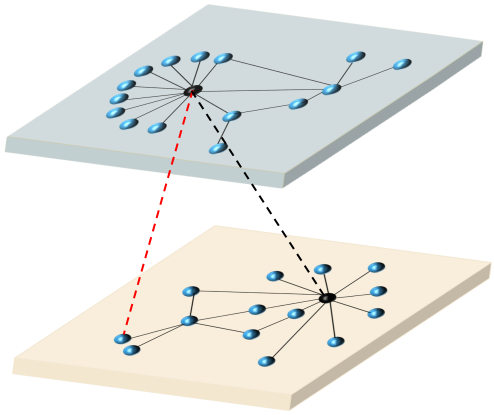

FIGURE 1.11: **Schematic representation of different interlayer degree correlations.** The black dotted line shows the case of assortatively (or positively) correlated duplex networks, where the node with high degree is connected to the similar high-degree node. The red dotted line shows the reverse case, leading to the duplex networks with negative degree correlations.

where v_i^α is an integer with a value of 0 or 1. The value determines whether node i is active in layer α, where 0 represents inactive, while $v_i^\alpha = 1$ if nodes are active.

In real-world multiplex networks, the values of edge overlap appear to be comparatively large [50, 56], which reveals the fact that there exist nontrivial correlations between two layers. The degree correlations that we explored for single-layer networks can also appear in the connected access layers. Fig. 1.11 shows how different interlayer degree correlations may appear. If the hubs in one layer tend to be connected with hubs in another layer, the degree of networks is positively correlated (see black dotted line). Such networks are said to be assortative networks, which are quite common in real life. For instance, in social networks, people have a tendency to be friends with those with similar characteristics, like hobbies, age, jobs, etc, showing the phenomena called *homophily* (see Fig. 1.12). Conversely, if the hubs in one layer have a tendency to connect to the leaves in another layer, we have negative degree correlations (see red dotted line).

To evaluate degree correlations, multiple ways from coarse to fine have been proposed. The relative coarse-grained measure is based on the joint degree distribution between two layers. Given a duplex network with layers α and β, we can compute the average degree of a node on layer α conditional to the degree of the corresponding node on layer β as:

Figure 1.12: **Phenomena of homophily in the social life of ancients.** It shows that there is a tendency that people would like to make friends or socialize with those with similar age or interests.

$$\bar{k}^{\alpha}(k^{\beta}) = \frac{\sum_{k^{\alpha}} k^{\alpha} P(k^{\alpha}, k^{\beta})}{\sum_{k^{\alpha}} P(k^{\alpha}, k^{\beta})}, \tag{1.23}$$

where $P(k^{\alpha}, k^{\beta}) = N(k^{\alpha}, k^{\beta})/N$. The term $N(k^{\alpha}, k^{\beta})$ is the number of nodes whose degrees are k^{α} on layer α and k^{β} on layer β. This function presents the different degree correlations relying on the increase and decrease in k^{β}. Of course, the networks have no degree correlations if the function is independent of k^{β}.

There are some widely known methods for measuring degree correlations, such as Pearson correlation, Kendall rank correlation, Spearman correlation, the Point-Biserial correlation, etc. These methods are called *correlation coefficient* collectively which are not of our following research interest [56]. Hence, we will not go into too much detail here. It is worth to mention that the level of degree correlations can be tuned by replacing the labels of the nodes. By reassigning the new labels, the degree sequences in both layers can be changed according to the increasing or decreasing rank of the degree. For instance, if we have four nodes labelled $1, 2, 3, 4$ with degree $5, 8, 2, 3$, we can re-label them in ascending order of the degree, i.e., $3, 4, 1, 2$. There are two extreme cases called maximally positive correlations when the nodes in two degree sequences

ranked as degree increases are connected, and maximally negative correlated case where the nodes in one degree sequence arranged in ascending order of degree connect to others relabelled as degree decreases.

Dynamical Processes on Networks 2

> *"The whole history of science has been the gradual realization that events do not happen in an arbitrary manner, but that they reflect a certain underlying order, which may or may not be divinely inspired."*
>
> — Stephen Hawking

In the previous chapter, we focused on the topological properties of networks, but one of the key topics in network science is to elucidate the relationship between the structure of the underlying network topology and its function. The humongous amount of research in the last decades has revealed that network function is usually associated with the dynamic behaviors and processes on the network, such as the dissemination of information on the Internet [57, 58], rumor spreading on social networks [59–62], synchronization problems [63–65] and so on.

Complex networks generated by some representative models have replaced random graphs to provide a more accurate description of the structure of complex systems. The ultimate goal of studying complex networks is to understand how the various dynamical processes on the network are affected by the topology of networks [10, 19, 66]. Through the study of the dynamic properties of complex networks, not only we can better understand and explain the various complex dynamic phenomena presented in real networks, but also we can build models that more truly reflect the characteristics of real-world networks.

In this chapter, the first and the most primary question is to figure out what the "dynamics" is and how it is represented on complex networks. Generally, people dive straight into the analysis of the dynamics on various network systems from power grid [67, 68] to neural systems [69, 70], instead of giving an unambiguous definition for dynamics. Here, let us find out "how the wind blows" first and get to the bottom of it.

Dynamics in traditional physics generally is interpreted as finding a universal law about the relationship between interactions of basic elements of systems and their evolution to gain a deep insight into the complexity of the real-world system. From the perspective of network science, *complex networks*

have been widely regarded as a promising and powerful framework to study and characterize complex systems by mapping them into a relational network with nodes and edges [10, 71]. Therefore, dynamics can be interpreted to be the changes of node status or the connection relationship between nodes (i.e., growth or degradation reflected in the network topology) driven by "external stimulus" or triggered by "inside information", leading to obvious or non-obvious "qualitative changes" occurring in the whole network, which can be performed randomly or under some kind of rule constraints [20, 72].

The *state space* and *updating rule* are the key parts to study dynamical systems in the statistical theory [10, 66, 73]. The state space contains all the different kinds of complex paths executed by complex systems under external or internal stimulus. From the mathematical point of view, the state space is associated to a set including finite number of states, denoted as K. In the modelling of systems, it is necessary to define an appropriate state space, forming a mapping relationship with a probability distribution function, which reflects the statistical characteristics of the system [74]. To study the state space, it is enlightening to explore the information hidden in the deterministic processes in which the next execution can be inferred according to the current action, that is so-called *updating rule* [10, 75]. Its mathematical definition is to give the conditional probability of getting some value for x_n giving the previous state x_{n-1} at state $n-1$, statistically characterizing the evolution of systems.

In this chapter, we will first scratch the surface of the methods to analyze the dynamical processes in section 2.1. From the microscopic scale, the *master equation* (ME) approach is used to describe the dynamical phenomena of systems with the disadvantage of being difficult to gain a complete solution. In this thesis, we do not aim to dive into the mathematical representation of ME. Instead, we will focus on the definition and formalism of *Markov process* which is an effective framework used to understand the underlying mechanism of stochastic process for dynamic systems as well as the mean-field approximation method most frequently used to get a solvable form of the ME. In addition, we will present the modelling and simulation methods which will be implemented on resolving the disease dynamics of our interest in this thesis.

With the further development of complex network theory, the problem of epidemics on networks has gradually become an attractive topic in the field of spreading and diffusion processes. The dynamical systems generally can be represented by ordinary differential equations. In brief, the mathematical framework for an arbitrary dynamical system consists of relationship between its states, inputs, and their derivatives, denoted by $\dot{x} = f(x, t)$. In section 2.2,

we will start from the introduction of some typical epidemic models, which portray the probability of each node being in each state at each time from a microscopic point of view to provide a more accurate description of the contagion processes. We will analyze the epidemic threshold and the steady-state condition after the disease outbreak. Additionally, we will explore the properties and theoretical results of typical epidemic models on homogeneous and heterogeneous networks as well as the measurement of reproduction number and herd immunity for the preparation of applications in the next chapter. In section 2.3, we will implement the SIS model on multilayer networks to explore the role of directionality on the dynamics with the generating function approach, following the article

- X. Wang, A. Aleta, **D. Lu**, and Y. Moreno, Directionality reduces the impact of epidemics in multilayer networks, *New Journal of Physics*, 21(9), 093026, 2019.

Most of the existing approaches to microscopic dynamics of the system are based on mean-field theory and its optimization. In section 2.4, we will end up the chapter with the application of compartmental models on exploring the dynamics of a kind of social contagion process, i.e., the evolution of corruption behaviors. We will put the emphasis on deriving the conditions under which corruption activities emerge by developing its mean-field theory in full detail, corresponding to the work

- **D. Lu**, F. Bauza, D. Soriano-Paños, J. Gómez-Gardeñes, and L.M. Floría, Norm violation versus punishment risk in a social model of corruption. Physical Review E, 101(2), 022306, 2020.

Moreover, to get further insights into the mechanism behind driving the dynamics of honesty and corruption behaviors on multiplex networks, we apply the compartmental model on duplex networks where different flows take place separately on a specific layer with two salient structural properties taken into account, i.e., edge overlap and interlayer degree correlations.

2.1 Methods

Here, we give a brief introduction of the methods used in the theoretical analysis of dynamical processes from a microscopic perspective. They enable us to better understand and explain the various dynamics of complex networks in the real world. Then, we can apply the theoretical results of the study on the

dynamic properties of complex networks to specific problems. For example, we can design networks with better characteristics.

In this section, we will systematically explore the theoretical tools used in the study of dynamics, going from stochastic processes to deterministic processes. *Stochastic processes* are handled by probabilistic calculus, which describes the statistical properties of each state and their statistical correlations, ignoring individual properties [76, 77]. In this case, even when given the same set of parameter values and initial conditions, the evolution may lead to an ensemble of different outputs. *Deterministic processes* are governed by dynamic rules described by differential equations, which belong to a fine-grained description with exact relationship between the response and explanatory variables.

In addition, we will discuss modelling methods that are generally proposed to approximately represent a system, satisfying the need to understand complicated evolving dynamical processes taking place on networks. Then, Monte Carlo simulations will be introduced, allowing for the implementation of large-scale computational experiments.

2.1.1 Master equation

We start with the introduction of *master equation* (ME) which is an important method to model stochastic process and plays an essential role in statistical physics. Actually, it is almost universally applicable and has been widely applied to a variety of fields, such as chemistry, biology, finance, etc. [10, 78–83]. Here, we consider particular systems which can be modelled as a probabilistic combination of multiple configurations at any time. The probability that the system occupies in a particular configuration X at a given time t is denoted as $P(X,t)$ which satisfies the normalization condition, $\sum_X P(X,t) = 1$. The transitions from one configuration X to another configuration Y with the rate $W(X,Y)$ represent the dynamical process. The time evolution of the probability distribution can be described in the form of a master equation. Therefore, the master equation composed of a set of time-dependent differential equations for $P(X,t)$ is given by

$$\begin{aligned} \frac{\partial P(X,t)}{\partial t} &= \int [P(Y,t)W(Y,X) - P(X,t)W(X,Y)]\, dY \\ \text{or} \quad \frac{\partial P(X,t)}{\partial t} &= \sum_Y [P(Y,t)W(Y,X) - P(X,t)W(X,Y)]. \end{aligned} \tag{2.1}$$

As we discussed in Chapter 1, complex systems can be modelled as a net-

work by mapping microscopic interactions into an abstract structure. Given a network of size N under a specific configuration at time t, the dynamical description can be denoted by the state variable $X(t)$ for each node i, where $X(t) = (X_1(t), X_2(t), ..., X_N(t))$. In the context of networks, there is a simplified consideration of the transition rate that the switch of node state only depends on the interaction with its neighbors instead of considering all the configurations $X = (X_1, X_2, ..., X_N)$ and $Y = (Y_1, Y_2, ..., Y_N)$. Therefore, the transition rate is rewritten as:

$$W(Y, X) = \prod_{i=1}^{N} w(Y, X_i|X_j), \tag{2.2}$$

where nodes j are the neighbors of node i. It indicates that the dynamical processes on networks are strongly affected by their topology.

1. ***Markov process***

Specifically, we can employ the master equation to describe the *Markov process*, which can be understood as the process without time memory. The master equation in Eq. 2.1 represents the differential form of Markov process. In simple terms, Markov process is a stochastic process that future outcomes can be predicted solely based on the current state and are independent of past states. For example, if we keep casting a dice, past results do not affect future results.

The more accurate mathematical definition of a Markov process [84, 85] is as follows. Assume that there is a stochastic process $\{X(t), t \in T\}$ with state space K, where $X(t)$ is referred to as the state of the process at time t and $K = \{x_1, x_2, \ldots, x_n\}$ $(x \in K)$. At each time t $(t_1 < t_2 < \cdots < t_n)$ for $\forall n \geq 1$, the conditional probability satisfies:

$$P\{X(t_n) = x_n|X(t_1) = x_1, \ldots, X(t_{n-1}) = x_{n-1}\} = P\{X(t_n) = x_n|X(t_{n-1}) = x_{n-1}\}, \tag{2.3}$$

where $\{X(t), t \in T\}$ is said to be a Markov process. The above equation is equivalent to:

$$\mathcal{P}_{n-1|1}(x_1, t_1; x_2, t_2; \ldots; x_{n-1}, t_{n-1}|x_n, t_n) = \mathcal{P}_{1|1}(x_{n-1}, t_{n-1}|x_n, t_n), \tag{2.4}$$

where the left term represents the function of joint conditional probability density, defined as

$$\mathcal{P}_{n-1|1}(x_1,t_1;x_2,t_2;\ldots;x_{n-1},t_{n-1}|x_n,t_n)=\frac{P_n(x_1,t_1;x_2,t_2;\ldots;x_{n-1},t_{n-1};x_n,t_n)}{P_{n-1}(x_1,t_1;x_2,t_2;\ldots;x_{n-1},t_{n-1})}. \tag{2.5}$$

The term $P_n(x_1,t_1;x_2,t_2;\ldots;x_{n-1},t_{n-1};x_n,t_n)$ denotes the joint probability density, that is, the probability of taking x_1 at time t_1, x_2 at time t_2, ..., x_n at time t_n. The right term of Eq. 2.4 is the conditional probability density, given by

$$\mathcal{P}_{1|1}(x_{n-1},t_{n-1}|x_n,t_n)=\frac{P_n(x_{n-1},t_{n-1};x_n,t_n)}{P_{n-1}(x_{n-1},t_{n-1})}. \tag{2.6}$$

According to the interpretation of the terms on both sides of Eq. 2.4, it is obvious to conclude that the joint conditional probability of taking x_n at time t_n is completely determined by the value of x_{n-1} at time t_{n-1}.

The *Poisson Process* and *Wiener process* are two paradigms of continuous-time Markov process [86, 87]. Regarding each transmission process on complex networks, there always exist randomized connections between nodes and edges. This probability property determines that the density of each node state is characterized by random fluctuations which can be analyzed by the continuous-time Markov process.

2. ***Markov chain***

Markov chain is one of the simplest examples of Markov processes which can be deemed to be a transition between discrete random variables occurring at a discrete time [88, 89]. In this sense, it is the discrete-time version of the recurrence relations for Markov process. The accurate definition in a mathematical way is the following: suppose that $\{X_n, n=0,1,2,\ldots\}$ is a stochastic process with the state space $K=\{i_0,i_1,i_2,\ldots\}$ where X_n is the state at time n. If the corresponding random variables $X_0,X_1,X_2,\ldots,X_{n+1}$ for $\forall n \geq$, $\forall i,j$ and all states $i_0,i_1,\ldots,i_{n-1}$ satisfy:

$$P\{X_{n+1}=j|X_n=i_n,X_{n-1}=i_{n-1},\ldots,X_0=i_0\}=P\{X_{n+1}=j|X_n=i_n\}, \tag{2.7}$$

then, $\{X_n, n=0,1,2,\ldots\}$ is said to be a discrete-state and discrete-time Markov process, or *Markov chain* for short.

The probability characteristics of Markov chain can be completely described by the initial distribution and the transition probability [90]. The

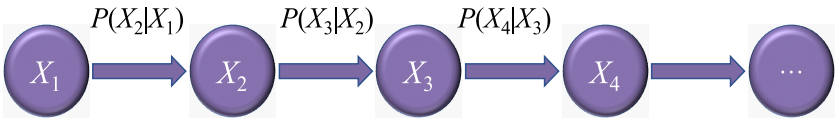

FIGURE 2.1: **A simple representation of Markov chain.** Markov chain is a discrete-state and discrete-time Markov process, denoted as $\{X_n, n = 0, 1, 2, ...\}$. The condition probability shown on the arrows is known as transition probability as the updating rule for Markov chain.

one-step transition probability at time n is defined as the condition probability of being in state j at next step $n+1$ given that a Markov chain is in state i at time n. That is :

$$p_{ij}(n) = P\{X_{n+1} = j | X_n = i\}, \ i, j \in K, \tag{2.8}$$

with the following two properties:

$$p_{ij}(n) \geq 0, \ \forall i, j \in K \quad \text{and} \quad \sum_{j \in K} p_{ij}(n) = 1, \ \forall i \in K. \tag{2.9}$$

Since the elements p_{ij} of transition matrix $\mathbf{P}$ meet above conditions, we can call it a right stochastic matrix [1]. If the Eq. 2.8 goes into the following form:

$$p_{ij} = P\{X_{n+1} = j | X_n = i\}, \ i, j \in K, \tag{2.10}$$

it indicates that the transition probability is independent of time steps, i.e., the transition matrix $\mathbf{P}$ is time-invariant. Then, $\{X_n, n = 0, 1, 2, \dots\}$ is called time-homogeneous Markov chain.

For a Markov chain $\{X_n, n = 0, 1, 2, \dots\}$, if a pair of states i, j belonging to the state space K can communicate with each other, they can be noted as $i \leftrightarrow j$. If any state $i, j \in K$ can communicate with each other, this Markov chain is referred to as *irreducible*. In this case, if there is a distribution of the state space, denoted as $\pi = (\pi_1, \pi_2, ..., \pi_N)$, satisfying $\pi_j = \sum_{i=1}^{N} \pi_i p_{ij}$, π is called the stationary distribution. There exits a theorem that irreducible Markov chains in finite state space must have stationary distributions. Furthermore, if there exists a π so that

$$\pi_i p_{ij} = \pi_j p_{ij}, \tag{2.11}$$

then this Markov chain is reversible with stationary distribution bound to exist. This condition is also known as the *detailed balance condition* [92]. Let

[1] It is also called probability matrix, Markov matrix or substitution matrix in the literature [91].

us recall the master equation in the discrete form (see Eq. 2.1). For stationary processes, we have $\partial_t P(X,t) = 0$, leading to the detailed balance condition [2]

$$P_{eq}(X)W(X,Y) = P_{eq}(Y)W(Y,X), \tag{2.12}$$

where $P_{eq}(X)$ is the probability density function of the system at stationary state. Even if the system is initially in a non-equilibrium state (when the probability density function is time-dependent), the system will gradually enter the equilibrium state after a sufficiently long period of time. This is the theoretical basis for Monte Carlo simulations which will be discussed in section 2.1.3.

3. ***Mean-field approximation***

It must be stressed that the master equation is rarely solvable to obtain the complete solutions unless we have a case with quite simple dynamical rules. Therefore, to obtain the approximate form of the master equation for interpreting the system behaviors, suitable approximation methods have been proposed. Here, we focus on a typical approximation approach, namely *mean-field theory* [93, 94]. The core idea is that the overall effect of the interactions between all fundamental units across all scales plays a dominant role, while the local information about contact conditions of each basic unit is not important and can be neglected. Specifically, in master equation, there is no relevant relationship between micro-state variables, presenting an average interaction for all nodes instead. Hence, instead of precisely deriving the master equation, the general considerations on effective interactions are used to rewrite the equations with the mean-field approximation in which the probability of an arbitrary element i to be in a given state $\sigma_i = x$ is a quantity p_x independent of i.

As a first step in the analysis of a collective phenomenon, a sensible mean-field approximation is a well-known and recommended practice in statistical physics, due to both its simplicity and unbiased character [95]. Often, though not always, it provides a qualitatively correct description of the observed behavior, and, moreover, it reveals basic mechanisms that trigger the collective changes of state for large systems. In the realm of network science, Barabási and Albert as the pioneers came up with a mean-field method mainly used to compute analytically the *connectivity distribution* (i.e., *degree distribution*).

In this thesis, we apply the mean-field theory on solving the differential equations used to describe the dynamical behaviors of contagion processes,

[2] Note that this is a sufficient condition to reach $\partial_t P(X,t) = 0$, not a necessary one. We can get the same result by a more complex cancellation among ME terms.

like epidemic spreading. Since the spread of epidemics is obviously full of the influence from the disparate interaction of each individual, we will make use of this method by just considering the global and average propagation possibility beyond specific details. The specific implementation of the method will be discussed in the forthcoming sections.

2.1.2 Compartmental modelling and agent-based modelling

In this section, we introduce two common framework used for exploring dynamical processes of a system, namely *compartmental modelling* and *agent-based modelling*.

1. ***Compartmental modelling***

Compartmental modelling is to model the system by dividing it into distinct *compartments*. This approach is applied to describe the transition of individuals among different compartments over time with deterministic equations. In terms of large-scale systems, the shortcoming of compartmental modelling appears for solving complicated differential equations.

The compartmental modelling approach is commonly applied to model infectious diseases in mathematical epidemiology. According to the the stage of the disease, the population is separated into various compartments. In this way, a wide class of epidemic models has been developed (see the further discussion in section 2.2.1) [96].

2. ***Agent-based modelling***

In terms of complicated models, it is likely that even the deterministic compartmental modelling can not yield tractable equations as well as neglect the heterogeneity between individuals. Here, we introduce an approach, namely Agent-based modelling (ABM) for exploring the dynamics of large-scale systems. The agent-based modelling is a simulation-based method, convenient to incorporate some rules that are not easy to be mathematically represented, setting it apart from compartmental modelling methods [97].

A basic agent-based modelling must contain three elements, i.e., a certain amount of agents, a complete set of topological relations and action rules, and environment of agents. The fundamental idea of ABM is to assume each individual node, denoted as an *agent* to be in one of all possible states. Each agent is conferred with a kind of behavior rules which is likely to affect other agents or surroundings. The future state of each agent can be influenced by its present state and the present state of its neighbors. The dynamics occur

as a result of microscopic interactions among agents. In addition, we can obtain macroscopic characteristics of the system from average or aggregate quantities. At the microscopic level of agent-based modelling, the specific rule of each agent follows is relatively simple. However, at the macro level, agents can produce the collective behavior that is not usually visualized intuitively [98]. This method can also be used to model transmission processes of infectious diseases [99]. It allows researchers to specifically analyze patterns of population movement and the ways in which people come into contact with each other through social relationships, which are the fundamental pathways of disease transmission.

3. *Comparisons*

The main difference between these two modelling methods is that the compartmental modelling approach usually uses the macroscopic variables, like density, while the ABM method describes systems by taking into account autonomous individuals. To be more specific, the compartmental modelling is an "up-bottom" approach by partitioning the population into compartments relying on some assumptions. However, in the case of ABM approach, complex interactions are modelled in a "bottom-up" way by representing self-organizing individuals that are similar to each other as autonomous agents.

In following sections, the dynamical processes we mainly focus on are contagion processes, especially epidemic transmission. Therefore, in this context, the framework of epidemic models can usually be described in the same manner for these two methods. The compartmental modelling split the population into compartments, each reflecting a typical health state associated with epidemic propagation. The transition rates, capturing dynamical processes, represent the rate by which an average transmission between compartments. However, the ABM approach models the disease transmission by tracking state changes of each individual (*agent*). The transition rates are generally approximated by the rates derived from compartmental models, but are applied at the individual level, i.e., when individuals interact with each other. Although many studies found that they sometimes behave the same and sometimes differently, which depend on formulated assumptions, the conclusion is drawn that two methods usually yield similar results [100–102]. In addition, the advantages of both models can be combined into hybrid models to analyze global effects and local effects as well [103,104]. It is worth to state that neither one of them can be referred as a "gold standard" approach. It is regarded as an advisable modelling approach once it is appropriate for tackling the problem at hand.

2.1.3 Monte Carlo simulations

In this section, we focus on the computational methods used for modelling dynamical processes on networks. Classical statistical methods alone can not describe the dynamics of each individual. As statistical regularities characterizing macroscopic behaviors of systems are obtained by observing aggregate or average quantities, they actually can not be used to describe the dynamics which are expressed by the microscopic interactions among individuals. However, computer simulation methods can largely compensate for deficiencies in the theoretical analysis process. In addition, computer simulations can be more applicable to social systems with complex structures and large scales, and can take into account the influence of actual social factors on the dynamical processes. As a consequence, simulation methods with computers turn out to be an important tool to study complex realities that are not accessible with analytical methods.

1. ***Monte Carlo methods***

The stochasticity of modelling methods we discussed in section 2.1.2 can be introduced with Monte Carlo simulations. Here, we first introduce Monte Carlo methods which are computational methods based on random numbers. Generally, Monte Carlo methods can be roughly divided into two categories. One type is that the problem to be solved is inherently stochastic in nature. This kind of stochastic processes can be directly simulated with the computing power of the computer. The other is that in order to obtain the probability of a certain event occurring, or the expected value of a certain variable, one can count the frequency of the occurrence of required events or the average value of the variable by performing numerous experiments as solutions [105, 106].

Monte Carlo methods facilitate the use of microscopic numerical simulations with computers to study macroscopic properties of large-scale systems. Technically, this kind of methods replicate the system within the computer by mimicking the transition probabilities between events, providing access to the microscopic dynamics of the system [10]. In the following, we will provide the detailed introduction of two methods applied in computer simulations.

2. ***Synchronous and asynchronous updating methods***

Synchronous updating methods and asynchronous updating methods are the two most commonly used computer simulation schemes in the study of dynamics occurring on networks. However, for the same dynamical process, the variability of these two simulation methods in updating the node states

may lead to quantitative and qualitative differences [107,108]. The variability between synchronous and asynchronous updating methods stems from their different perspectives on actual dynamical processes [107]. If we look at dynamical changes from a long time scale, the state changes of all individuals can be considered to be updated synchronously. The synchronous updating simulations can exactly mimic discrete-time processes where the time is discretized into uniform time steps Δt. To put it differently, if we focus on continuous-time changes and only one event is allowed to occur at each instant, the state updates of different nodes are performed asynchronously. It implies that in the limit $\Delta t \to 0$, the discrete-time process is counterpart to the continuous-time Markov process [109]. For many studies on continuous-time Markov process models, one avenue is to use the discrete-time approximation [110–112]. Nonetheless, it is notable that given a finite Δt, discrete-time approach appears significantly different from its continuous-time counterpart [111].

Here, we briefly introduce the mechanistic description of these two methods. The specific application on studying contagion dynamics will be presented in detail in section 2.2.6. The main idea of synchronous updating methods is that each node updates its current state according to the previous state of itself and its neighbors. The state updating processes of all nodes are performed simultaneously in unit time. While, in the implementation of asynchronous updating methods, a node updates its state independently and its neighbor nodes can observe its new state at that moment [113]. Asynchronous update methods are widely used in various dynamics simulations, including voting models, game theory, epidemic propagation, etc. The Gillespie algorithm is a typical representative of asynchronous updating methods, simulating efficient reaction processes in biochemistry, as well as Markov processes and Poisson processes [114,115]. The most important thing in the implementation of the Gillespie algorithm is how to assign to each time step the occurrence process and the time update interval τ. Assume that there are N independent random discrete processes in the system, each with probability of occurrence p_i, $i = 1, 2, ..., N$. For a Poisson process, $\{X(t), t \in T\}$, the probability of a process i to occur between t and $t + \Delta t$ is $p_i(X(t))\Delta t$. The probability of the next process to occur in the time interval $(t + \tau, t + \tau + \Delta t)$ and be process i, is denoted as $P(\tau, i)\Delta t$

$$P(\tau, i)\Delta t = P_0(\tau) \cdot p_i(X(t))\Delta t, \tag{2.13}$$

where $P_0(\tau) = e^{-\tau \sum_{i=1}^{N} p_i(X(t))}$. Therefore, the above equation is rewritten as:

$$P(\tau, i) = p_i(X(t))e^{-\tau \sum_{i=1}^{N} p_i(X(t))}. \tag{2.14}$$

In the Markov process, the probability $P(\tau, i)$ is given by

$$P(\tau, i) = P(\tau|X(t))P(i|\tau, X(t)), \tag{2.15}$$

where $P(\tau|X(t))$ is the updating time distribution conditioned to the state of the system at time t be $X(t)$, given by

$$P(\tau|X(t)) = \sum_{i}^{N} p_i(X(t)) \cdot e^{-\tau \sum_{i=1}^{N} p_i(X(t))}. \tag{2.16}$$

Another term on the right side of Eq. 2.15 is the probability of process i to happen conditioned to the updating time interval be τ and the state of the system at time t be $X(t)$, denoted by

$$P(i|\tau, X(t)) = \frac{p_i(X(t))}{\sum_{i}^{N} p_i(X(t))}. \tag{2.17}$$

The stochastic simulation with Gillespie algorithm is as follows:

(1) Initialize time and system state, $X(t = 0) = X_0$.

(2) Compute the probability of all processes $i = 1, ..., N$ to occur, $p_i(X(t))$. Then get the $p(X(t)) = \sum_{i=1}^{N} p_i(X(t)))$.

(3) Generate random numbers r_1 and r_2 falling within the interval $[0, 1]$. Then, the updating time interval τ is calculated by

$$\tau = \frac{1}{p(X(t))} \log(\frac{1}{r_1}). \tag{2.18}$$

(4) Calculate which process happens by choosing j, down to

$$\sum_{i=1}^{j-1} p_i(X(t)) \leq r_2 p(X(t)) \leq \sum_{i=1}^{j} p_i(X(t)). \tag{2.19}$$

Then, the change of the system caused by the jth reaction is stored in a state-change vector, denoted as $\mathbf{v}_j$.

(5) Update the time $t \leftarrow t + \tau$ and replace the state of the system with $X(t + \tau) \leftarrow X(t) + \mathbf{v}_j$.

(6) Return to the first step and iterate following steps. The procedure is stopped until the condition $t \geq T$ is satisfied.

The Gillespie algorithm is highly applicable and practical which can be used not only for simulating reaction processes, but also for non-equilibrium dynamics [116]. In section 2.2.6, we will present this algorithm applied for simulating the epidemic spreading on networks.

2.2 Epidemics on Networks

> *"As a matter of fact, all epidemiology, concerned as it is with the variation of disease from time to time or from place to place, must be considered mathematically, however many variables as implicated, if it is to be considered scientifically at all."*
>
> — Ronald Ross

Human society has been repeatedly threatened by a variety of serious epidemics, some of which have had a profound impact on the course of human history, such as the plague of Athens in 430 B.C., the Black Death in the 14th century and so on. It was claimed that the plague of Athens which was the first major infectious disease documented in detail not only led to the death of Pericles, ruler of the city state and famous reformer, but also killed nearly half of the population. Another devastating pandemic disaster is the Black Death, a plague that once swept across Europe, killing about one-third of its population and striking a huge blow to Western civilization [117]. There are countless such examples, as the American historian McNeill argues in his book [118], "epidemics predate mankind in history, will coexist with mankind for a long time to come, and will be a fundamental parameter and determinant of human history, just as they have been in the past."

Although the insights into epidemics have progressed relatively slowly, the description and prediction of epidemics has been a long-standing but flourishing topic. The earliest studies of epidemic transmission started in 1760 when Swiss mathematician, Bernoulli, studied the effectiveness of smallpox inoculation [119,120]. By the early 20th century, Hamer and Ross used a quantitative approach to study the spread of measles disease and applied the famous *law of mass action* [3] to explain epidemic behaviors [122]. This work became a historical precedent for using precise mathematical language to study epidemic

[3] It was first used to describe the reaction rate between chemical reactants. It later became one of the main concepts of mathematical epidemiology, which assumes that the net transmission rate of infection (how many people are newly infected per unit time) is proportioned to the multiplication of the density of the susceptible population and the density of the infected population. See [121] for nice explanation.

transmission. In 1927, inspired by previous work, Kermack and Mckendrick first developed the well-known "compartmental model" to obtain a threshold theory for an epidemic to start [4] [123]. In the following decades, almost all relevant studies with compartmental models refer to the *homogeneous mixing* assumption, i.e., individuals are uniformly mixed in space, which is actually not in line with reality [124, 125].

In order to study the dynamics of epidemic transmission, it is necessary to explore in depth how the transmission process of specific infectious diseases takes place. For the mechanism of disease spreading in populations, the pathogen exits from an infected individual at one point in time and space, by direct or indirect contact, and penetrates into a susceptible person at another spatio-temporal point. Then, people who are susceptible will be infected with a certain probability and continue to spread the disease. It has to be said that epidemic spreading is a quite complicate process, depending on the specific scenarios. For example, some diseases enable individuals to acquire immunity after a recovery which means that people who have been infected can not get infected again, like mumps, measles, etc. However, some other diseases can infect people repeatedly, such as tuberculosis, flu, etc. In practice, it is definitely a formidable and large task to consider all biological information in the population [124, 126]. Consequently, mathematical modeling became an important tool for early studies of infectious diseases, with the aim of reflecting their dynamics realistically and devising ways to control or possibly eradicate them. The simplified mathematical models could reveal the main characteristics of infectious diseases by means of assumptions, parameters, variables, and the connections between them. In the beginning, several simple mathematical models were developed to model dynamics of epidemics. It was not until the decade of 1940 that differential equation models began to be taken seriously and a series of great contributions emerged, like those described in the theoretical books by Bailey [127,128], and in the practical ones written by Anderson and May [129, 130]. The analytical results of mathematical models have provided many strong theoretical foundations that contribute to effectively predicting disease outbreaks or controlling the spread of diseases, such as chicken pox, tuberculosis, smallpox, measles and so on [131–134].

With the discovery of small world networks and scale-free networks at the end of the 20th century [33, 34], a new era in the study of epidemic transmission was ushered in [82]. The mathematical epidemiologists have

[4] It says that the introduction of a small number of infected individuals into a population full of susceptible individuals does not trigger an epidemic outbreak unless the initial number of susceptible individuals in the population is above a certain threshold.

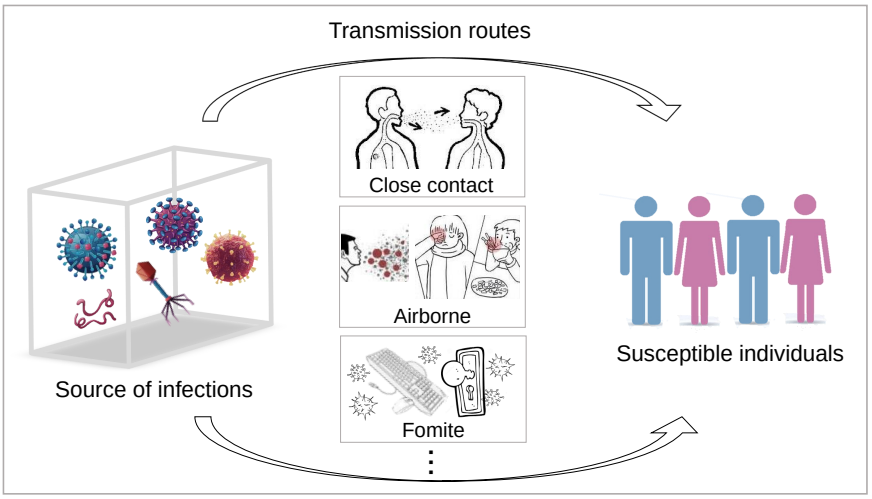

Figure 2.2: **Transmission process of epidemics.** The epidemic process is mainly dominated by three elements, i.e., infection source, transmission routes and susceptible population.

shifted their attention to network modelling of disease transmission, driven by the maturation of complex network theory [20, 32]. The human systems can be abstracted into networked populations using the framework of complex networks. The interactions between individuals that underlie the disease transmission show some complex network characteristics as we discussed in section 1.2 [135, 136]. The theoretical framework of complex networks not only captures the essential characteristics of real human systems by considering their heterogeneities, but also has good mathematical properties, i.e., it can perform rigorous mathematical calculations. Using ideas from statistical physics and other disciplines, researchers have proposed many different theoretical approaches, such as mean-field theory, point-pair approximation, message-passing approach, etc., to study the behaviors of epidemic transmission on complex networks [137–141], and have achieved many insightful results [10, 142, 143], which can even provide some important rationales for policy formulation in public health institutions.

The spread of infectious diseases is mainly determined by infection source, transmission routes and susceptible population (see Fig. 2.2), which are controlled by their biological characteristics, contact behaviors and environmental factors. Consequently, those aspects find their manifestation on an impressive array of epidemic models. The compartmental models have become

increasingly sophisticated over time by incorporating more details, like various contact patterns between individuals and different structures of underlying networks. From this perspective, studies of epidemic spreading on complex networks can be broadly classified into the following two categories: (1) contact-based network models that emphasize the influence of the structure of interactions between individuals on epidemic transmission [137, 144–147]. (2) metapopulation models [148–152]. Some representative work in this context incorporates transportation networks (e.g., global airline networks) to study the spread of epidemics at the population level, yielding impressive results in the study of global epidemic transmission [153–155], especially in the exploration of COVID-19 we are suffering from [156–159].

From the above discussion, it is known that the spread of epidemics in real systems can be observed at different scales, and the corresponding network structure needs to be considered at the respective scale. Studies have revealed that the network structure has a great influence on the dynamics of epidemic transmission [137,144,160]. On the other hand, the spread of epidemics can in turn affect the network structure. For example, during an epidemic outbreak, healthy individuals who are conscious of precautions may actively dissociate from infected individuals [161–163]. It is evident that there is an interaction between network structure and the dynamics of epidemic transmission. Therefore, in this section, in addition to introducing several of the most common compartmental models in epidemiology, we will explore some theoretical analysis methods that facilitate accurately understanding and describing the dynamics of disease transmission on complex networks from a multilevel perspective. As we stated in section 1.2.3, complex networks can be categorised into homogeneous networks and heterogeneous networks in terms of degree distribution. In the case of homogeneous networks, the dynamics can be given by means of mean-field theory or mixing uniformly, while for the heterogeneous ones, the impact of degree distribution must be taken into account. Hence, we will look in more detail at contagion dynamics to better understand these models applied on different types of networks.

2.2.1 Introducing basic epidemic models

The next point to be covered has to start with the work from Kermack and McKendrick who put forward the first compartmental model when they studied the Black Death in London in 1927, that is the well-known *SIR model* [164]. In 1932, they proposed another famous model, called *SIS model* [165]. On this basis, the more elaborate models have been developed by more and more re-

searchers, which mainly adopt the deterministic modeling method composed of differential equations [10, 82, 166].

The assumptions in compartmental modelling (see section 2.1.2) are specified in the field of disease transmission that the population is separated into several "compartments" for a certain type of disease, and each compartment corresponds to the specific state of individuals in relation with the disease [164]. For example, the compartment "infectious" represents a group that has been infected and is contagious. Meanwhile, it assumes that individuals in each compartment are identical. Then, differential equations are used to define the dynamic evolution processes of the number of individuals in each group. As we shall see, the number of variants in the class of compartmental models is far beyond what can be covered in this space. Therefore, we will only introduce the compartmental models that will play an important role in this thesis.

1. ***SIS model***

Let us firstly consider a paradigmatic model, known as the *susceptible-infected-susceptible model* or *SIS model* [128]. The population is divided into two groups: one that is free from the disease but can be infected, *Susceptible* (S), and one that is infected and can transmit disease to others, *Infected* (I). In SIS model, people who are infected can transmit the diseases to susceptible neighbors with probability β. The infected can be cured with probability μ and become susceptible again without conferring immunity [137, 167–169]. The effective infection rate is denoted by $\lambda = \beta/\mu$. The infection mechanism of SIS model illustrated in Fig. 2.3A can be expressed in the following form:

$$\begin{aligned} S(i) + I(j) &\xrightarrow{\beta} I(i) + I(j) \\ I(i) &\xrightarrow{\mu} S(i) \end{aligned} \tag{2.20}$$

To represent the number of susceptible and infected individuals may change over time, we consider the precise number of individuals in any of the two states at time t, denoted as $S(t)$ and $I(t)$, respectively. Here, we consider the model which assumes that vital dynamics (birth and death) are not taken into account. Thus, the total population remains a constant at any time, i.e., $S(t) + I(t) = N$. The model assumes that each individual in the population makes contact with others randomly and uniformly, i.e., *homogeneous mixing* assumption [11, 124]. The infectivity rate is defined as β/N. Therefore, the whole number of susceptible individuals infected by infected persons per unit time is $\beta/NS(t)I(t)$. The equations describing the systems are written:

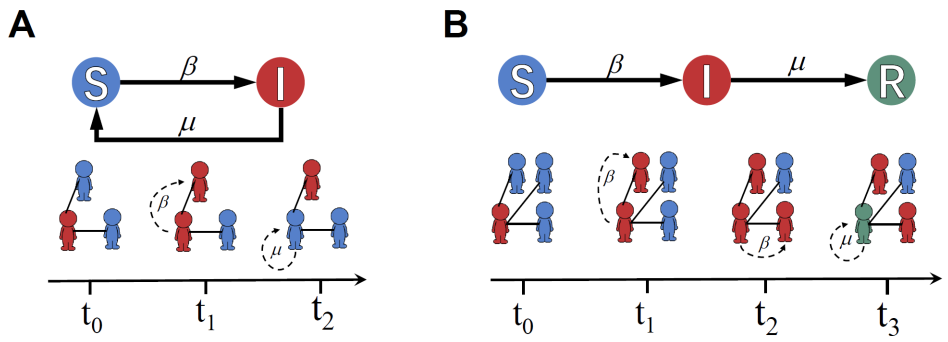

FIGURE 2.3: **Illustration of transmission process with two typical epidemic models. A)** Flow chart for the SIS model. **B)** Flow chart for the SIR model.

$$\begin{cases} \dfrac{\mathrm{d}S(t)}{\mathrm{d}t} = -\dfrac{\beta}{N}S(t)I(t) + \mu I(t) \\ \dfrac{\mathrm{d}I(t)}{\mathrm{d}t} = \dfrac{\beta}{N}S(t)I(t) - \mu I(t) \end{cases} \tag{2.21}$$

In most literature associated to the introduction and application of epidemic models, there is another version for the above set of equations which is presented in terms of the fraction of individuals in two states, given by

$$s(t) = \frac{S(t)}{N}, \qquad i(t) = \frac{I(t)}{N}, \tag{2.22}$$

Then, Eqs.(2.21) can be written:

$$\begin{cases} \dfrac{\mathrm{d}s(t)}{\mathrm{d}t} = -\beta s(t)i(t) + \mu i(t) \\ \dfrac{\mathrm{d}i(t)}{\mathrm{d}t} = \beta s(t)i(t) - \mu i(t) \end{cases} \tag{2.23}$$

where the normalization constrain $s(t) + i(t) = 1$ is always valid. Then, we obtain the most common model used in the analysis of epidemics on networks known as *frequency dependent* approach [170]. There is another approach referred as *density dependent* where the infectivity rate is defined as β, yielding a set of equations slightly different from Eqs.(2.23). The expression for the infected individuals as a function of time is

$$\frac{\mathrm{d}i(t)}{\mathrm{d}t} = \beta N s(t)i(t) - \mu i(t). \tag{2.24}$$

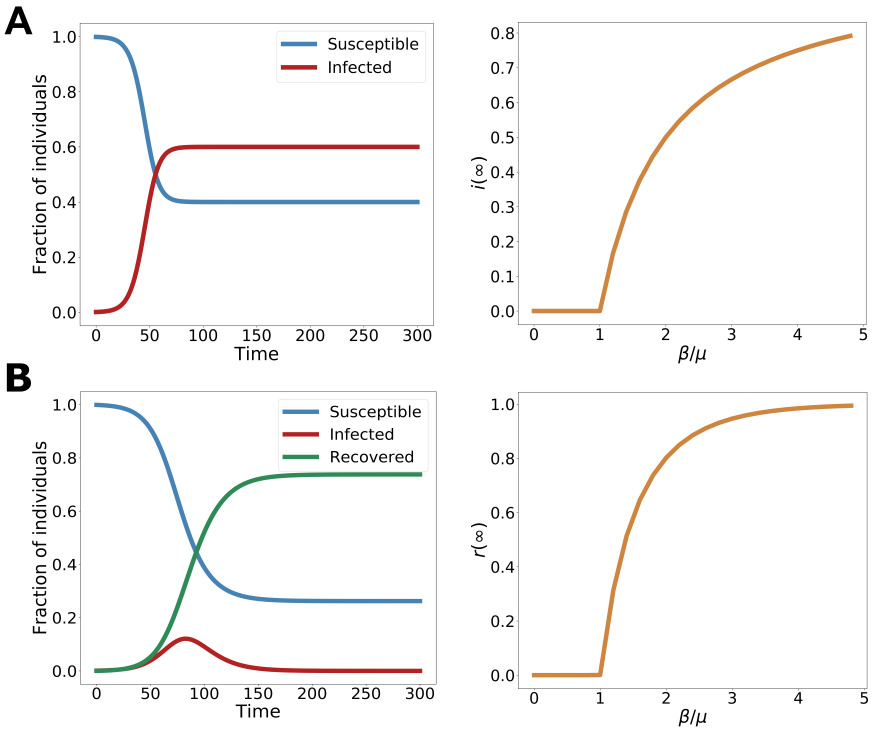

Figure 2.4: **Comparison results of the two models. A)** Time evolution of the SIS model based on the equations (2.23) with $\beta = 0.25$ and $\mu = 0.1$ and the steady fraction of infected individuals a function of β/μ. **B)** The fractions of individuals in SIR model obtained from the equations (2.26) as a function of time. The fraction of recovered individuals in equilibrium conditions as a function of β/μ.

The dynamics of the disease in later approach rely on the population size N, leading to the faster propagation at larger N. It should be noted that these two approaches are valid. Moreover, an in-depth discussion and their specific applications which largely depend on the disease under consideration can be referred in the literature [170].

In the epidemiology jargon, the quantity measured straightforwardly from the differential equations is the steady fraction of infected individuals in the sufficiently long time limit, called *endemic disease state* [5] in epidemiology [172]. The stable solution is $i(\infty) = 1 - \mu/\beta$ by calculating $\mathrm{d}i(t)/\mathrm{d}t = 0$, assuming $i(t) \neq 0$. It can be seen from the solution that the dynamics of

[5] In epidemiological jargon, it is interpreted as when an infection persists at baseline levels in a geographic area without external input, the infection is said to be endemic in the population, a term originally derived from the Greek *έν* (*en*) "in or within" and *δῆμος* (*demos*) "people". See [171] for more details.

epidemic is governed by the value β/μ:

$$\begin{aligned} \beta/\mu \leq 1 &\Rightarrow \lim_{t\to\infty} i(t) = 0, \\ \beta/\mu > 1 &\Rightarrow \lim_{t\to\infty} i(t) = 1 - \mu/\beta. \end{aligned} \tag{2.25}$$

Thus, the critical value β/μ determining whether there always exists a finite fraction of infected individuals is known as *epidemic threshold*. When $\beta > \mu$, an example showing how the epidemic spreads out is numerically visualized in the left panel of Fig. 2.4A. The right panel of Fig. 2.4A, where we show the final fraction of infected individuals as a function of the ratio β/μ, renders the critical role of $\beta/\mu = 1$ clearly observed.

2. ***SIR model***

In this model, some infected individuals may obtain immunity to the disease or may die. Thus, those people can neither be infected nor infect others, falling into a new third state, the *removed state* (R). We refer to this model as *susceptible-infected-removed model* or *SIR model*, which was firstly presented in a paper written by Reed and Frost in 1920 [96].

The SIR model developed by Kermack and McKendrick in 1927 is one of the most common used epidemic model, proposed for the number of people infected with a contagious disease in a closed population over time. It is assumed that the total population with constant size N is divided into three compartments [6]. As shown in Fig. 2.3B, Susceptible individuals (S) become infected by contacting with infected neighbors at a transmission rate β. Infected (I) is said to be those individuals who can spread the disease. Recovered individuals (R) who leave the infected group with the recovery rate μ will be removed from the disease and possess the permanent immunity. Therefore, they no longer have any effect on the corresponding dynamic behaviors. The SIR model is suitable for describing diseases in which the infected individuals can acquire lifelong immunity after cure, such as chickenpox, mumps, etc. [173–176].

Based on the above assumptions, the SIR model proposed by Kermack and McKendrick [177] uses coupled differential equations for $S(t)$, $I(t)$ and $R(t)$ to describe the system with frequency dependent approach presented as:

[6] It is called *class* in its original reference [164]

$$\begin{cases} \dfrac{\mathrm{d}S(t)}{\mathrm{d}t} = -\dfrac{\beta}{N} S(t)I(t) \\ \dfrac{\mathrm{d}I(t)}{\mathrm{d}t} = \dfrac{\beta}{N} S(t)I(t) - \mu I(t) \\ \dfrac{\mathrm{d}R(t)}{\mathrm{d}t} = \mu I(t) \end{cases} \tag{2.26}$$

where the three variables satisfy the condition, $S(t) + I(t) + R(t) = N$. If we define the fraction of individuals in three states as we did in SIS model, we obtain the expression for the time evolution of infected individuals

$$\frac{\mathrm{d}i(t)}{\mathrm{d}t} = \beta s(t)i(t) - \mu i(t), \tag{2.27}$$

As shown in Fig. 2.4B, the fraction of susceptible individuals has a monotonically decreasing trend, while the fraction of population who are recovered increases monotonically. The proportion of infections goes up at first and then decreases as they recover to zero when the time $t \to \infty$ due to lack of enough susceptible individuals.

Here, the asymptotic value of the fraction of recovered individuals, r, carries a major implication in practical terms. It represents the number of individuals who ever got infected, i.e., the total size of an outbreak. Therefore, the final infection density can be measured with quantity $r(T)$, where T is the time at which the infection process is over, i.e., $i(T) = 0$. The value of $r(T)$ can be obtained by setting $\mathrm{d}r(t)/\mathrm{d}t = 0$, giving:

$$r(T) = 1 - s(0)\mathrm{e}^{-\beta/\mu(r(T)-r(0))} = 1 - s(T), \tag{2.28}$$

which illustrates that there are still some susceptible individuals remaining unless $s(0) = 0$. If we assume that the population is almost fully susceptible in the beginning with extremely small proportion of infected individuals, denoted as ϵ, the initial condition for the fraction of three compartments satisfies

$$(s(0), i(0), r(0)) = (1 - \epsilon, \epsilon, \epsilon). \tag{2.29}$$

Then, at this point, we can obtain

$$\left.\frac{\mathrm{d}i(t)}{\mathrm{d}t}\right|_{t=0} \approx \beta - \mu. \tag{2.30}$$

It demonstrates that there exits the epidemic threshold β/μ. There is no epidemic at all if $\beta/\mu \leq 1$, while infected individuals continue to reproduce,

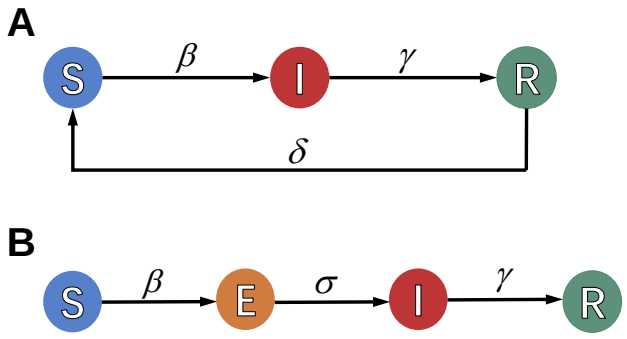

FIGURE 2.5: **Illustration of transmission process with two epidemic models. A)** Flow chart for the SIRS model. **B)** Flow chart for the SEIR model.

giving rise to disease outbreaks, which can be clearly seen in the right panel of Fig. 2.4B.

3. *SIRS model and SEIR model*

Here, we introduce two variants of epidemic model which will be useful later. The first is the *SIRS model* with *reinfection phenomena* taken into account [144,178]. In this model, the removed individuals can not permanently disappear from the system. Instead, after some duration of time, they will lose immunity and become susceptible at a rate, δ (see Fig. 2.5A), that can be used to explain seasonal virus transmission [179–181]. One can well perceive that the parameter δ provides transformation from SIR model with $\delta \to 0$ to SIS model when δ tends to infinity.

Generally, the actual situation is more complicated where susceptible people will experience an incubation period in which they have already been infected without onset of symptoms. Therefore, the *exposed state* (E) is introduced on the basis of SIR model, known as *SEIR model* [10, 182]. Once the infection has progressed to a point after a period of time, the exposed individuals will become infected with the rate ε (see Fig. 2.5B). This model, albeit simplistic, can already capture many properties of the current COVID-19 pandemic, attracting a lot of popularity [157, 183, 184].

There are far more than the epidemic models we mentioned above. However, discussing more variants is beyond the scope of this thesis. These mathematical compartmental models under the homogeneous-mixing assumption simplify the complex process and transmission factors of epidemic transmis-

sion and only focus on the description of general macroscopic law in epidemic spreading. Although these homogeneous-mixing compartmental models have been proved to be successful in disease prediction [166], they can not directly reflect diverse contact patterns between individuals. Gradually, mathematical epidemiologists turned to use a network perspective to consider interactions in a population. In this case, as we discussed in section 1.2.2, complex networks are generalized into homogeneous and heterogeneous networks according to the degree distribution [20]. In next sections, we will investigate how the classical epidemic models (SIS model and SIR model) behave on these two types of structured networks.

2.2.2 Epidemic models on homogeneous networks

In homogeneous networks, the degree of each node is approximately equal to the average degree, i.e., $k \approx \langle k \rangle$. The incidence per capita for susceptible individuals depends on the average number of infected neighbors, denoted ki. In numerical simulations from the microscopic point of view, each infected individual spreads the epidemic to a connected susceptible node with a per-individual rate $\beta \mathrm{d}t$ during an infinitesimal time interval $\mathrm{d}t$. Then a susceptible node in the network will get infected with the probability $1-(1-\beta \mathrm{d}t)^{ki}$, approximated as βki if $\beta \mathrm{d}t \ll 1$ [10]. By employing the mean-field approximation which considers an average effect to approximate the effect of all the other individuals, the average density of individuals being infected as a function of time for SIS model can be described as:

$$\frac{\mathrm{d}i(t)}{\mathrm{d}t} = -\mu i(t) + \beta \langle k \rangle i(t)[1-i(t)], \tag{2.31}$$

where higher order terms are neglected. In the long time limit, the system finds a stable state by setting $\mathrm{d}i(t)/\mathrm{d}t = 0$ to give:

$$\rho[-\mu + \beta \langle k \rangle (1-\rho)] = 0, \tag{2.32}$$

where ρ is the endemic state of the infected fraction $\rho = i(t \to \infty)$. The epidemic threshold is given by the solution, $\lambda_c = \langle k \rangle^{-1}$. In addition,

$$\begin{aligned} &\rho = 0, \quad \text{if } \lambda < \lambda_c \\ &\rho \sim \lambda - \lambda_c, \quad \text{if } \lambda \geq \lambda_c \end{aligned} \tag{2.33}$$

In the case of the SIR model mapped to homogeneous networks, the density of three types of individuals reads as:

$$\begin{cases} \dfrac{\mathrm{d}s(t)}{\mathrm{d}t} = -\beta\langle k\rangle i(t)s(t) \\ \dfrac{\mathrm{d}i(t)}{\mathrm{d}t} = \beta\langle k\rangle i(t)s(t) - \mu i(t) \\ \dfrac{\mathrm{d}r(t)}{\mathrm{d}t} = \mu i(t)\ , \end{cases} \tag{2.34}$$

where the three variables satisfy the condition, $s(t) + i(t) + r(t) = 1$. Then, the equations are solved to get the solution:

$$s(t) = s(0)\mathrm{e}^{-\beta\langle k\rangle r(t)/\mu}, \tag{2.35}$$

where $s(0)$ is the initial fraction of susceptible individuals at $t = 0$.

As discussed in section 2.2.1, the final infection density can be measured in terms of the final fraction of recovered individuals r_∞ which represents the total number of infections during the entire course of the epidemic. If we incorporate Eq.(2.35) into the normalization condition, we can obtain the description of r_∞, giving:

$$r_\infty = 1 - \mathrm{e}^{-\beta\langle k\rangle r_\infty/\mu}. \tag{2.36}$$

So as to obtain a nonzero solution, it meets the following condition,

$$\frac{\mathrm{d}}{\mathrm{d}r_\infty}\left(1 - \mathrm{e}^{-\beta\langle k\rangle r_\infty/\mu}\right)\Big|_{r_\infty=0} \geq 1. \tag{2.37}$$

The condition corresponds to the critical limit $\beta/\langle k\rangle\mu \geq 1$. From the equation, we can see that the size of epidemics depends on the infection and recovery rate, β and μ and the epidemic dies out under the condition of $\beta\langle k\rangle/\mu \leq 1$.

2.2.3 Epidemic models on heterogeneous networks

To characterize the influence of heterogeneous topology of networks induced by the different connectivity between nodes on epidemic spreading, we consider the *degree-based mean-field* theory (or *heterogeneous mean-field* (HMF) theory) in which the nodes of networks can be classified into different groups according to their degree [137, 167, 168, 185]. Here, we denote by $\rho_k(t)$ the density of infected individuals in the groups of degree k at time t, similarly $s_k(t)$ for susceptible nodes in SIS model. These two variables are connected by means of the normalization condition, i.e., $\rho_k(t) + s_k(t) = 1$. In the case of uncorrelated networks, let $P(k)$ represent the general degree distribution.

Then, global quantities are represented by the average over various connectivity groups, e.g., $s(t) = \sum_k P(k)s_k(t)$. At the mean-field level, the dynamic evolution of ρ_k satisfies the following differential equation:

$$\frac{\mathrm{d}\rho_k(t)}{\mathrm{d}t} = -\mu\rho_k(t) + \beta k[1-\rho_k(t)]\sum_{k'} P(k'|k)\rho_{k'}(t). \tag{2.38}$$

The first item on the right of equation describes the decrease of the infected population due to recovery rates. The second one is proportional to the density of the susceptible population $1-\rho_k(t)$ at time t, the transmission rate β, the number of neighbours k and the probability of any neighbour being infected. The latter $P(k'|k)\rho_{k'}(t)$ is the probability of being in contact with a node of degree k' which is infected. The item $\sum_{k'} P(k'|k)\rho_{k'}(t)$ can be denoted by $\Theta_k(t)$, transforming the equation into:

$$\frac{\mathrm{d}\rho_k(t)}{\mathrm{d}t} = -\mu\rho_k(t) + \beta k[1-\rho_k(t)]\Theta_k(t). \tag{2.39}$$

In the stationary state, the density of infected individuals ρ_k is only a function of $\beta k/\mu$ ($\lambda = \beta/\mu$). Then, the probability that an edge leads to an infected node becomes the implicit function of λ, denoted by $\Theta_k(\lambda)$ [137,185]. The solution in the steady state of Eq.2.39 is obtained by setting $\mathrm{d}\rho_k(t)/\mathrm{d}t = 0$:

$$\rho_k = \frac{\beta k\Theta_k(\lambda)}{\mu + \beta k\Theta_k(\lambda)}. \tag{2.40}$$

For uncorrelated networks, the probability $P(k'|k)$ is equal to $k'P(k')/\langle k\rangle$. This relation simply states that the probability that a node with k' links can be reached by one randomly selected link of its k' links is proportional to $k'P(k')$. Therefore, Θ can be written as:

$$\Theta = \sum_{k'} P(k'|k)\rho_{k'}(t) = \sum_k \frac{kP(k)}{\sum_s sP(s)} \cdot \frac{\beta k\Theta}{\mu + \beta k\Theta}, \tag{2.41}$$

where $\langle k\rangle = \sum_s sP(s)$ denotes the average degree in the network. Here, we can estimate the order parameter ρ using the relation $\rho = \sum_k P(k)\rho_k$. In order to have the nontrivial solution with the condition $0 < \Theta \leq 1$, it is equivalent to fulfill the condition

$$\frac{\mathrm{d}}{\mathrm{d}\Theta}\left(\frac{1}{\langle k\rangle}\sum_k kP(k)\frac{\beta k\Theta}{\mu+\beta k\Theta}\right)\bigg|_{\Theta=0} \geq 1. \tag{2.42}$$

Then, the epidemic threshold on SIS model can be obtained by solving the Eq.2.41:

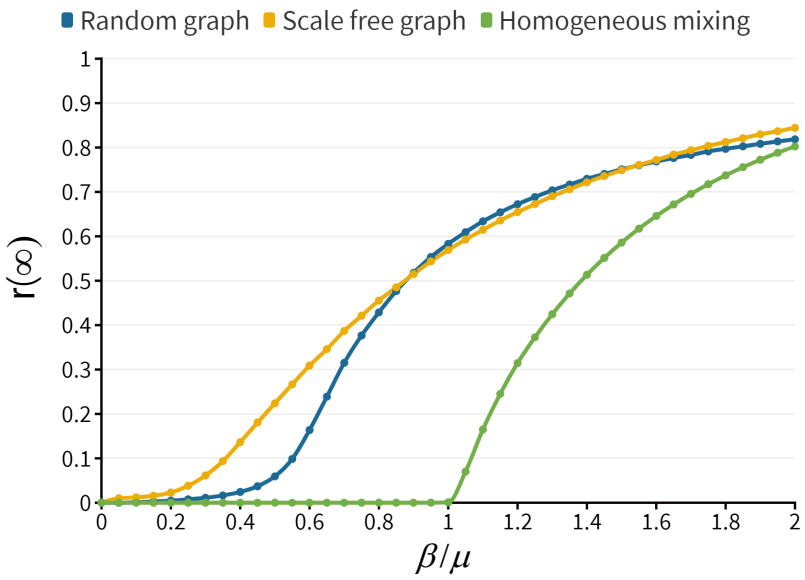

FIGURE 2.6: **Comparison of the epidemic threshold with different topologies.** The total fraction of recovered individuals in equilibrium conditions as a function of β/μ with SIR model is calculated on different types of graph. In the case of random graph with $N = 10^4$ and $\langle k \rangle = 3$, the epidemic threshold $\beta_c/\mu = 1/3$. While, the critical value is approximate to 0.1 when the SIR model is applied on a scale free graph with $N = 10^4$ where $\langle k \rangle \approx 3$ and $\langle k^2 \rangle \approx 29$. In the homogeneous mixing condition as described in the last section, the epidemic threshold is 1.

$$\left(\frac{\beta}{\mu}\right)_c = \lambda_c = \frac{\langle k \rangle}{\langle k^2 \rangle}. \tag{2.43}$$

For large enough scale-free networks ($N \to \infty$) with degree distribution following $P(k) \sim k^{-\gamma}$ and $\gamma \leq 3$, it leads to $\langle k^2 \rangle = \infty$ and $\lambda_c = 0$ correspondingly [141]. It has a practical meaning that the epidemics always exist no matter how small the infection probability is on scale-free networks. This result explains why virus or opinions can spread so fast on Internet and social networks.

Regarding the SIR model, we define $s_k(t)$, $i_k(t)$ and $r_k(t)$ to be the density of individuals with degree k that are susceptible, infected or recovered, respectively at time t, together with the normalization condition: $s_k(t) + i_k(t) + r_k(t) = 1$. Applying the analytical method as for the SIS model, we obtain the following dynamic evolution equations:

$$\begin{cases} \dfrac{\mathrm{d}s_k(t)}{\mathrm{d}t} = -\beta k s_k(t)\Theta(t) \\ \dfrac{\mathrm{d}i_k(t)}{\mathrm{d}t} = \beta k s_k(t)\Theta(t) - \mu i_k(t) \\ \dfrac{\mathrm{d}r_k(t)}{\mathrm{d}t} = \mu i_k(t)\ . \end{cases} \tag{2.44}$$

The above equations can be solved under the initial conditions $r_k(0) = 0$, $i_k(0) = i_0$ and $s_k(0) = 1 - i_0$. In the limit of $i_0 \to 0$, we let $i_k(0) \approx 0$ and $s_k(0) \approx 1$. Under this approximation, the equation can be directly integrated:

$$s_k(t) = \mathrm{e}^{-\beta k \phi(t)/\mu}, \tag{2.45}$$

where $\phi(t)$ is the auxiliary function:

$$\phi(t) = \int_0^t \Theta(t')\,\mathrm{d}t' = \frac{1}{\langle k\rangle}\sum_k (k-1)P(k)r_k(t). \tag{2.46}$$

Note that the expression of the probability Θ is different from that we stated in the SIS model. In the SIR model, the infected node with k links catches the disease through one of them which can not spread the disease anymore [137]. It means that the probability Θ only needs to consider $k-1$ links, while the mechanism of the state transition in SIS model allows the disease to spread back along the same link.

Then, we can get the derivative of $\phi(t)$ versus time by substituting the obtained expression of Eq. (2.45) into it:

$$\frac{\mathrm{d}\phi(t)}{\mathrm{d}t} = 1 - \phi(t) - \frac{1}{\langle k\rangle}\sum_k (k-1)P(k)\mathrm{e}^{-\beta k\phi(t)/\mu}. \tag{2.47}$$

The total fraction of recovered individuals r_∞ which measures the overall size of the outbreak of the disease is a function of $\phi_\infty = \lim_{t\to\infty}\phi(t)$. Taking $r_k(\infty) = 1 - s_k(\infty)$, we get:

$$r_\infty = \sum_k P(k)(1 - \mathrm{e}^{-\beta k\phi_\infty/\mu}). \tag{2.48}$$

The self-consistent equation of ϕ_∞ can be solved since $i_k(\infty) = 0$ and $\lim_{t\to\infty}\frac{\mathrm{d}\phi(t)}{\mathrm{d}t} = 0$:

$$\phi_\infty = 1 - \frac{1}{\langle k\rangle}\sum_k (k-1)P(k)\mathrm{e}^{-\beta k\phi_\infty/\mu}. \tag{2.49}$$

To get a non-zero solution, the following criteria must be satisfied:

$$\frac{1}{\langle k\rangle}\sum_{k}(k-1)P(k)(\beta k/\mu)=\frac{\beta}{\mu}\cdot\frac{\langle k^2\rangle-\langle k\rangle}{\langle k\rangle}>1. \tag{2.50}$$

Finally, the epidemic threshold in SIR model is given by:

$$\lambda_c=\frac{\langle k\rangle}{\langle k^2\rangle-\langle k\rangle}. \tag{2.51}$$

Let us proceed a limited extrapolation of the epidemic threshold by considering the networks with correlated structure that are widely present in real systems [186, 187]. We go back to the original form of factor Θ in the SIS model, giving:

$$\Theta_k(t)=\sum_{k'}P(k'|k)\rho_{k'}(t). \tag{2.52}$$

The epidemic threshold can be extracted by analyzing the stability of the solutions in the stationary state. As the evolution of the infection density can be linearized, we get:

$$\frac{\mathrm{d}\rho_k(t)}{\mathrm{d}t}\simeq\sum_{k'}L_{kk'}\rho_{k'}(t), \tag{2.53}$$

where $L_{kk'}$ is the elements belonging to the Jacobian matrix $\mathbf{L}$. The term $L_{kk'}$ is given by

$$L_{kk'}=-\mu\delta_{kk'}+\beta kP(k'|k)=-\mu\delta_{kk'}+\beta C_{kk'}, \tag{2.54}$$

where another matrix, namely *connectivity matrix* $\boldsymbol{C}$ is introduced, composed of the elements $C_{kk'}=kP(k'|k)$. Given the largest eigenvalue of $\mathbf{C}$, Λ_{max}, the condition causing the instability of the solution $\rho_k=0$ is

$$\frac{\beta}{\mu}>\frac{1}{\Lambda_{max}}. \tag{2.55}$$

Analogously, in the SIR model, under the situation that one less edge, i.e., only $k-1$ free links is considered, the form of $\Theta_k(t)$ is written as

$$\Theta_k(t)=\sum_{k'}\frac{k'-1}{k'}P(k'|k)\rho_{k'}(t). \tag{2.56}$$

Performing a linear stability analysis like in the SIS model, we obtain an identical relation for the destabilization of the solution $\rho_k=0$:

$$-\mu + \beta\tilde{\Lambda}_{max} > 0, \tag{2.57}$$

where $\tilde{\Lambda}_{max}$ is the largest eigenvalue of the connectivity matrix $\tilde{\mathbf{C}} = \{\tilde{C}_{kk'}\}$. And the elements $\tilde{C}_{kk'}$ are denoted by

$$\tilde{C}_{kk'} = k\frac{k'-1}{k'}P(k'|k). \tag{2.58}$$

Then, we can get the epidemic threshold for SIR model, i.e., $\lambda_c = 1/\tilde{\Lambda}_{max}$ [188]. In the case of scale-free networks, it has been numerically validated that as N tends to infinity, the epidemic threshold still vanishes in the thermodynamic limit, independent of the existence of the positive correlation [174]. The value of the critical point mainly depends on the definition of the matrix $\tilde{\mathbf{C}}$. For example, the expression of $\tilde{C}_{kk'}$ is simplified to $kk' - 1P(k')/\langle k\rangle$ for uncorrelated networks, yielding a unique largest eigenvalue $\tilde{\Lambda}_{max} = \langle k^2\rangle/\langle k\rangle - 1$ [10]. Thus, the epidemic threshold corresponds to the previous results as Eq.2.51 says.

The heterogeneous mean field (HMF) method is generally applicable to networks with infinite topological dimensions [54, 189]. However, this method does not completely describe the structure of the contact network, instead of roughly describing it in terms of degree distribution. In addition, the kinetic correlation between the nodes is neglected. These simplifications allow this method to describe the propagation dynamics on annealed networks more accurately, in which edges are continuously reconnected at a much faster rate than that of the epidemics with the degree distribution preserved. However, they are not applicable to quenched networks in which the degree of each node is fixed. For the first drawback, an improved approach is based on *individual mean-field* theory (or *quenched mean-field* theory) [190, 191]. The core idea of the quenched mean-field (QMF) approach is to represent the network structure completely in terms of the connections of each node, denoted by $\mathcal{A}_{ij}$ and describe the time evolution with a set of N equations taken into consideration. The equations are given as:

$$\frac{\mathrm{d}\rho_i(t)}{\mathrm{d}t} = -\mu\rho_i(t) + \beta[1-\rho_i(t)]\sum_{j=1}^{N}\mathcal{A}_{ij}\rho_j(t). \tag{2.59}$$

Similarly, we can obtain the epidemic threshold $\lambda_c = 1/\Theta$, where Θ is the maximum eigenvalue of the adjacency matrix [7]. It can be seen that for a

[7] Here we only briefly describe the method and the results. The specific derivation process can be found in the literature [54]

scale-free network without degree correlation, when $\gamma \leq 2.5$, the epidemic threshold is $\lambda_c \simeq \langle k \rangle / \langle k^2 \rangle$ consistent with that obtained with HMF approach. Moreover, when $\gamma > 2.5$, we get is $\lambda_c \simeq 1/\sqrt{k_{max}}$, which also tends to 0 in the thermodynamic limit. This conclusion is obviously different from the theoretical results of HMF. Although QMF yields results more accurately than HMF, it still ignores the dynamical correlation between the node states in the network. In other words, it neglects the fact that the probability of a susceptible node being infected will increase due to the presence of its infected neighbors [191]. Then, a more accurate method to portray the dynamical correlation between node states is proposed, known as the point-pair approximation method [192, 193]. However, we will not enter into details since these more advances and techniques will not be necessary for the rest of this thesis. A more comprehensive description of these theoretical analysis methods based on contact-network models is available in the literature [54, 141].

2.2.4 The basic reproduction number

In previous sections, we have explored the theoretical results of some typical epidemic models implemented on networks with different topologies. In reality, as a new infectious disease is identified, it is an important theoretical basis for disease prevention and control to clarify the ability of pathogen transmission among people. Here, we will introduce an epidemiological concept, R_0, first proposed as a threshold quantity by Ross in the study of malaria control [194]. Since then it has become a core idea in mathematical epidemiology. It was not until 1957 that this quantity was officially named as *basic reproduction number* [195] with the explicit definition that the expected number of additional people (or *new infections*) an infected individual passes the disease to infect during an entire infection cycle. Note that, this definition is based on the assumption that the population is full of susceptible individuals. After decades of silence, the real popularity of this concept was driven by the book of Anderson and May [196], and the exploration of its computational methods flourished under the influence of Diekmann et al. [197].

There is a famous and well-known *threshold criterion* for this quantity that the disease can spread out if $R_0 > 1$ whereas it can not if $R_0 < 1$. Therefore, $R_0 = 1$ can be regarded as an indicator of stability between disease-free equilibrium and endemic equilibrium, drawing a line between the growing and shrinking behaviors [198]. It is used to describe the same concept mentioned earlier, i.e., *epidemic threshold*, where separate the scenarios where the epidemic dies out or spreads over the population. The larger the value of R_0

is, the more contagious a disease is, leading to greater difficulty to control it. Before considering the measurement of R_0, it is worth noting the three main factors that determine its value:

(i) **Infectious period**

The so-called infectious period refers to the time span of a patient from infection to recovery, or from infection to death. Obviously, the longer the infection cycle of the disease, the more opportunities for patients to contact healthy people, and the higher the R_0. In this way, although those infectious diseases that can quickly cause death are fierce, they are not the most infectious. The most typical is the pneumonic plague, because the host dies too quickly, which prevents the yersinia pestis from spreading to other hosts [166].

(ii) **Transmission route**

Different diseases have different transmission routes, resulting in very different efficiency of disease transmission. For example, SARS-CoV-2 can be transmitted by droplets, and, as a consequence, the phenomenon of person-to-person transmission is very common [199]. Yet, AIDS can only be transmitted through blood, mother-to-child, and similar pathways, rendering it non-transmissible to healthy people in most cases [200].

(iii) **Contact frequency**

In different countries and regions, the population density varies greatly. Obviously, in first-tier cities with concentrated populations, person-to-person contacts are more frequent and diseases are more likely to spread, while in sparsely populated areas, where human contact is limited, the spread of diseases will be hindered to some extent.

1. ***Measuring*** R_0

Although accurately measuring the basic reproduction number R_0 is not a simple task, the above influencing factors allow us to orient to its measurement. According to its definition [201, 202], the described factors expressed in the evaluation of R_0 mathematically correspond to the duration of the infectious period, the probability of infection resulting from a contact between an infected and susceptible individual, and the contact rate. Here, we will introduce some derivation methods.

The definition proposed by Diekmann et al. in 1990 [197], which is probably the most general one, is given by:

$$R_0(\eta) = \int_\Omega S(\xi) \int_0^\infty A(\tau, \xi, \eta) \mathrm{d}\tau \mathrm{d}\xi. \tag{2.60}$$

This expression can be interpreted by taking out each quantity. The familiar term $S(\xi)$ is the density function of susceptible where individuals are characterized by the variable ξ. The expected infectivity of an individual that was infected τ units of time ago, in infectious state η, towards to a susceptible ξ is denoted by $A(\tau, \xi, \eta)$. Hence, the expected number of infections in a complete period of infectiousness, R_0, generated by an individual infected τ steps ago in state η depends on the amount of individuals in susceptible state where size is denoted by Ω in the expression and the infectivity of individuals.

Let us simply discuss its application in the SIR model to calculate the value of R_0. Referring to the Eq.(2.26), the quantity $A(\tau, \xi, \eta)$ is simplified to $\beta e^{-\mu\tau}$. Hence, the formula for R_0 is rewritten as:

$$R_0 = S(0) \int_0^\infty \beta e^{-\mu\tau} d\tau, \tag{2.61}$$

where $S(0)$ is the initial amount of susceptible individuals in the population, usually considered as N at the beginning of infection. As a result,

$$R_0 = N\frac{\beta}{\mu}, \tag{2.62}$$

where the equation is $R_0 = \beta/\mu$ in the application of frequency dependent approach, exactly consistent with the result obtained from the linear analysis of SIR model.

In addition, another method based on the local stability of disease free equilibrium, x_0, is proposed by Diekmann et al. [197] and advanced by van den Driessche and Watmough [203] to derive R_0, namely the *next generation matrix* approach. Here, the model is composed of n compartments with m infected compartments ($m < n$). Let $x = (x_1, x_2, ..., x_n)$, where $x_i > 0$ ($i = 1, 2, ..., n$), represent the number or proportion of individuals in each compartment. For the sake of calculation, x is divided into two parts, the first m items $(x_i, ..., x_m)$ denote the number of infected individuals in the corresponding infected compartments, and the remaining $(x_{m+1}, ..., x_n)$ represent the non-infected group of individuals. The division of infected and non-infected individuals should be based on biological significance of epidemiology, rather than simply by mathematical equations. The model is expressed as:

$$\frac{\mathrm{d}x_i}{\mathrm{d}t} = \mathcal{F}_i(x) - \mathcal{V}_i(x), \tag{2.63}$$

where $\mathcal{F}_i(x)$ is the rate of newly infected individuals in the i^{th} compartments and $\mathcal{V}_i(x) = \mathcal{V}_i^-(x) - \mathcal{V}_i^+(x)$ represents the transfer rate for individuals out of the compartment (with minus sign) or from other sources in the compartment (with plus sign) respectively. At the disease-free equilibrium point x_0, we define:

$$F = \left[\frac{\partial \mathcal{F}_i}{\partial x_j}(x_0)\right], \quad V = \left[\frac{\partial \mathcal{V}_i}{\partial x_j}(x_0)\right], \tag{2.64}$$

where $1 \leq i, j \leq m$ and they are $m \times m$ matrices. The matrix FV^{-1} is so-called next generation matrix. Then, the basic reproduction number R_0 is equal to the spectral radius of the this matrix, $\rho(FV^{-1})$, that is, the maximum of the eigenvalue modulus of FV^{-1}, which has been applied in a variety of disease studies, such as tuberculosis, malaria and so on [198, 204, 205].

For a completely susceptible population with a tiny number of infected individuals, when $R_0 > 1$, i.e., the number of infected individuals who can be infected during the average infection period is greater than 1, the number of infected individuals gradually increases. Let us recall the analysis of SIS model on heterogeneous networks in section 2.2.3. The necessary and sufficient condition for the autonomous equation Θ to have the only positive solution on $(0, 1)$ is when $\Theta = 0$, obtaining

$$R_0 = \frac{\beta\langle k^2\rangle}{\mu\langle k\rangle}, \tag{2.65}$$

Similarly, the results for R_0 can be derived in the SIR model, given by

$$R_0 = \frac{\beta(\langle k^2\rangle - \langle k\rangle)}{\mu\langle k\rangle}. \tag{2.66}$$

For epidemic models on networks, R_0 is also related to the transmission parameters (e.g., transmission rate β, recovery rate μ) other than the relevance to the network topology. It is worth pointing out that the existing calculation methods are not accurate for many real applications. Moreover, due to the diversity of disease transmission modes and network topology, we have no way to fully derive the exact R_0 for every disease, that is, it is model-dependent. In section 3.3, we will describe its specific calculation with real data.

2. ***The effective reproduction number***

R_0 measures the capability of an epidemic to spread in natural conditions. However, people are bound to step in to contain the spread of the disease. Some individuals are probably granted life-long immunity due to prior infection or vaccinated to get immunity. Therefore, the average number of secondary cases per infectious case will be lower than R_0. This introduces another important quantity with more extensive practical application, the effective reproduction number, generally mentioned as $R(t)$, also called R_e, R_t or R_{eff} in some literature [206–209]. The effective reproduction number is defined as the average number of new infections caused by an infectious individual in a population where some people are protected against the disease. It indicates the ability of an epidemic to spread when there is some immunity or some intervention measures are in place. The most straightforward way to estimate $R(t)$ mathematically with simple homogeneous models is based on the basic reproduction number and the fraction of susceptible individuals, $s(t)$ [210], leading to:

$$R(t) = R_0 s(t). \tag{2.67}$$

According to the definition of R_0 in Eq.2.62, the mean infectious period, $1/\mu$, can also be denoted as D and the transmission rate in some cases is a time-varying quantity as $\beta(t)$ [209, 211, 212]. Therefore the Eq.2.67 can be given as:

$$R(t) = \beta(t) s(t) D, \tag{2.68}$$

which is named *instantaneous reproductive number* in the case of homogeneous populations. It reveals that the sooner the number of susceptible falls due to death or gained immunity, the smaller $R(t)$ will be. The expression also implicates that the value of effective reproduction number is affected by the number of susceptible individuals with whom infected people contact. Another way proposed by Cori et al. [209, 211] to measure the effective reproduction number depends on the number of new infections occurring at time t and the current generation interval $g(s)$ [8], as

$$R(t) = \frac{I(t)}{\sum_{s=1}^{t} I(t-s) g(s)}, \tag{2.69}$$

where the denominator of the equation describes the total infectivity of the infected at time t, that is the cumulative sum of the number of infections incident in the past s days and the infectiousness $g(s)$ on day s. The point

[8] The quantity is also referred to as *generation time* in some literature [201, 213]

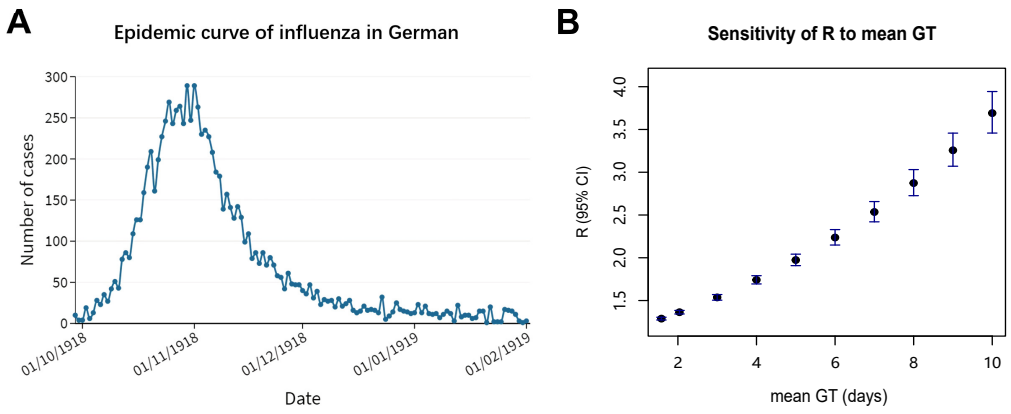

Figure 2.7: **Estimation of the reproduction number R with empirical data. A)** The temporal distribution of cases for the pandemic influenza in Germany from 1918–19 (see ref [217]). **B)** The calculated values of R with 95% confidence interval as a function of different mean values in generation time distribution.

of interest here is that the the generation interval $g(\cdot)$ is a probability density function, allowing any type of distribution, such as gamma distribution, negative binomial distribution and Weibull distribution [156, 211, 214].

There is another algorithm to be presented compatible with both kinds of reproduction numbers, R_0 and $R(t)$. For the sake of simplicity, we refer to them as R, given by:

$$R = 1 + rT_c, \tag{2.70}$$

where r is the exponential growth rate, T_c indicates mean duration of generation interval, $g(t)$, defined as the interval between the onset of an infected individual and the infection time of the next person he or she infects [196,215]. See the direct source of this expression [216], followed by:

$$R = \frac{1}{M(-r)}, \tag{2.71}$$

where $M(\cdot)$ is termed as *moment generating function* of the distribution of $g(t)$ in the context of statistics [218]. The relation between $M(\cdot)$ and $g(t)$, where t represents the number of days since being infected, can be expressed as:

$$M(-r) = \int_{t=0}^{\infty} e^{-rt} g(t) \mathrm{d}t. \tag{2.72}$$

If the functional form of $g(t)$ are assumed ahead, then it can immediately be reduced to a simpler form. For example, assuming that the generation interval $g(t)$ follows an exponential distribution:

$$g(t) = ge^{-gt}. \tag{2.73}$$

Taking it into Eq.2.72 and Eq.2.71, we obtain $R = 1 + r/g$, where $T_c = 1/g$ corresponds to Eq.2.71 [219]. The linear relationship between the growth rate r and the reproduction number R exclusively represents the shape of the generation interval distribution, and in turn, the shape of the generation interval distribution is responsible for the appropriate relationship between them.

Furthermore, if we consider the existence of a latent period T_L in the case of SEIR epidemic model, then we assume that the two components of $g(t)$, T_L and T_I, each obeys an exponential distribution with mean g_1 and g_2, where $g_2 = g - g_1$ The generation interval then becomes a "superposition" of two exponential distributions, the expression of R [213, 216] is obtained as:

$$R = (1 + r/g_1)(1 + r/g_2). \tag{2.74}$$

It is also possible, of course, to assume a normally distributed generation interval [220] or gamma-distributed generation interval [221]. In addition to assuming a strictly mathematical distribution, the approximate distribution of generation interval can be attained by fitting a set of real observations. Then, we can get the mean generation interval g and mean duration of incubation period g_1 from the empirical distribution.

To sum up, according to the application of this approach, there are several crucial points needed: 1) At the beginning, it is assumed that the number of newly infected people increases exponentially every day. 2) The growth rate r of the number of newly infected persons must be calculated. 3) There must be an assumption about the distribution of generation interval. Certainly, the parameters must be able to be obtained after assuming the corresponding distribution. Here, we put this method into practice based on the extracted data [217] that contains the daily number of pandemic influenza deaths in Prussia, Germany for five months from 1918–1919. The epidemic curve is shown in Fig. 2.7A. Then, we estimate the value of R with exponential growth rate. To explore the impact of generation time on the estimation of R, multiple mean values of the distribution of generation time are given with fixed value of standard deviation ($sd = 1$) for the sake of simplicity (see Fig. 2.7B).

Moreover, the distribution of generation time can be obtained from the observed duration in empirical studies. Therefore, the reproduction number R is given by:

$$R = \frac{r}{\sum_{i=1}^{n} y_i(e^{-ra_{i-1}} - e^{-ra_i})/(a_i - a_{i-1})}, \tag{2.75}$$

where y_i is bounds of the relative frequencies and a_i represents the category bounds in the histogram of generation time. The specific application of this method combined with real data will be presented in section 3.3.4.

2.2.5 Vaccination and herd immunity

Providing the guidance on the prevention of disease transmission is one of the purposes in the study of diffusion processes on complex networks. Therefore, an important direction in the study of transmission dynamics on complex networks is the search for effective and appropriate vaccination strategies. The most typical immunization strategies include random immunization which immunizes a portion of nodes selected completely at random in the network [222], targeted immunization which selectively immunizes a class of nodes based on a certain criterion [223], and acquaintance immunization which immunizes the neighbors of randomly selected nodes [224].

After a long period of exploration, both in the mathematical [10] and biological [166] context, the random immunization has been proved to be an overly expensive and largely inapplicable immunization strategy, since for scale-free networks with infinite size, immunization of all nodes in a network is called for to eliminate the virus. The targeted immunization strategy initially received much attention, implemented by immunizing highly-connected nodes in the network, increasing the network resilience to epidemics. The drawback is that it relies on the global structural knowledge of the network, or at least a better understanding of the degree of each node to identify key nodes with large degrees for immunization, which is difficult to achieve in many cases, such as for the complicated and constantly evolving human society. To avoid the problem, the acquaintance immunization strategy was proposed by Cohen et al. [222] in which only local knowledge (i.e., directly connected neighbour nodes) of randomly selected nodes is sufficient to achieve relatively cost-effective immunization [223, 225, 226]. In recent years, many immunization strategies similar to those discussed or further improved have been continuously put forward and have exhibited favorable effect [227, 228].

The practical implication of the implementation of those immunization strategies is that once a part of the population is immunized or vaccinated, it

means that they will be disconnected from the interpersonal network with other people, leaving the transmission route of disease cut off. Although widespread vaccination offers many benefits, such as reduced prevalence of pathogens, a significant decline in the number of cases, and a possible extension of the epidemic cycle [229,230], the costs and benefits arising from vaccine coverage need to be weighed against each other, raising a thought-provoking question that whether it is possible to contain an outbreak or eliminate infectious disease by vaccinating only a small fraction of susceptible individuals. The term *herd immunity* can provide the answer, which seems to have been co-created by George Potter, Adolph Eichhorn, and W. J. MacNeal in 1911 [231] to fight against the epidemics of "contagious abortion" in the livestock with the idea that more cows could be protected by immunizing a certain number of cow to achieve herd immunity instead of killing the sick [232]. In the early days, this term was primarily applied in response to epidemics in animal herds [233]. It was not until 1924 that Dudley applied "herd immunity" to human for the first time to enable the transition from animal to human. Subsequently, as more effective vaccines were developed and vaccine coverage increased, the buzz around the language of "herd immunity" increased [234]. Currently, a new disease induced by the SARS-CoV-2 coronavirus spread around the world with dramatic disastrous effects. To thwart its continued prevalence, the development of Covid-19 vaccine was highly anticipated, while herd immunity is brought to the forefront as the focus of discussion [232, 235–237].

During the development of herd immunity, different interpretations have emerged and it has been widely addressed in a variety of fields [229, 233, 234, 238]. Currently, in the context of epidemiology, herd immunity plays a significant role in protecting unvaccinated individuals from the spread of a contagious disease since there is a sufficient proportion of people who have been immune through infection and recovery or through vaccination. Recall the previous question, what share of population has to be immune to prevent an epidemic. Let us answer it with the theorem established by Smith [239] and Dietz [240] that if individual immunization occurs randomly within a randomly mixed population, so that each individual is exposed to additional R_0 individuals on average, then the fraction of population who has to be immunized must be greater than $1-1/R_0$ to control or eradicate the epidemic. Much of the early theoretical work on herd immunity has since been grounded in this assumption as a consequence that the herd immunity threshold (HIT) [9], is mathematically defined by

[9] According to the definition of the herd immunity threshold, some literature also use the critical coverage level of vaccination, denoted by V_c or ρ_c, to express the same meaning [241–243].

$$\text{HIT} = 1 - \frac{1}{R_0} \quad \text{or} \quad \frac{R_0 - 1}{R_0}. \tag{2.76}$$

Considering the different effectiveness of vaccines, the vaccine coverage required to achieve the same protection also may be different. Therefore, the quantity E is proposed to measure the vaccine effectiveness, leading to a realistic expression for the level of vaccine coverage as $(1 - 1/R_0)/E$ [242]. It is particularly to be noted that the reproduction number R_0 in the formula highly depends on the contact patterns of population in response to different types of pathogens. Hence, in the construction of contact network to simulate the epidemic transmission, the previous randomly-mixed assumption is no longer valid, since the mixing behaviors in heterogeneous population must be described by various parameters that characterize how human groups interact with each other. The interactions within high-risk groups could lead to an increase in R_0, the average number of secondary infections arising from an infected, subsequently increasing the herd immunity threshold.

Once the herd immunity threshold is achieved, the intensity and duration of immunity play an important role on its efficiency. For example, in the case of measles and smallpox, people receive lifelong immunity after vaccination enabling herd immunity to be practiced smoothly. However, the level of protective antibodies produced by the pertussis vaccine decays over time, causing individuals to regain susceptibility and therefore increasing the incidence in adolescents or adults, which considerably affects the efficacy of herd immunity [235, 244]. For the ongoing SARS-CoV-2 pandemic, since we still do not have a complete picture of its pathological characteristics and transmission dynamics, it remains unclear whether the Covid-19 vaccine can offer protection against infection [235]. In reality, there are many other factors that can affect the success of herd immunity, such as the efficacy of vaccines, the efficiency of vaccine roll-out, people's willingness to be vaccinated, etc. In addition, people's behavior may change after vaccination, and frequent communication will increase the risk of infection leading to weakened protection [242, 245]. Although there are many difficulties to conquer in order to attain herd immunity, it is still a rewarding path for human society to continue to explore, especially for the biggest challenge we are facing, COVID-19. We will rely on empirical data in the next chapter to do our part in exploring the estimate of SARS-CoV-2 herd immunity.

2.2.6 Numerical simulations of epidemic spreading

In modern studies of epidemic transmission, most scholars use a combination of theoretical analysis and computer simulation to reveal its mechanisms. It is noteworthy that theoretical methods to analyze epidemic spreading usually involve some assumptions. For example, the heterogeneous mean-field theory we discussed in section 2.2.3 assumes that there is no difference between nodes with the same degree and states of neighbor nodes are independent of each other [137]. In the face of complicated epidemic transmission processes, these basic assumptions might lead to some differences between theoretical predictions and actual propagation processes, greatly hindering the wide application of theoretical methods. Fortunately, numerical simulations with computers allow for more accurate modelling of epidemic spreading processes. In this section, considering the SIS epidemic model as an example (see section 2.2.1), we describe in detail the specific implementation steps of discrete-time simulations and continuous-time simulations which are performed with synchronous and asynchronous updating methods as we discussed in section 2.1.3.

1. ***Discrete-time simulations***

In the case of performing discrete-time numerical simulations on SIS dynamics, we apply the commonly used scheme, synchronous updating method, also propagation with SIS model, a fraction of nodes ρ_0 are selected randomly or according to some strategy initially as infected, and the rest of nodes are in susceptible state. We denote the state of node i at time t as $X_i(t)$ where $X_i(t) = 1$ represents that node i is infected and 0 otherwise. Then, at each time step, the spreading process where nodes change their states with synchronous updating methods proceeds as follows:

(1) We first copy the state of every node, $X_i(t+1) = X_i(t)$. Each infected node at time t, denoted as $X_i(t) = 1$, is recovered with the probability μ, resulting in $X_i(t+1) = 0$.

(2) We iterate through all infected nodes. Each infected node tries to infect all its susceptible neighbors j with probability β in the reactive process (RP) [148, 246], while in the case of contact process (CP), a stochastic contagion is expanded from an infected node to one neighbor per unit time [116, 247]. If the infection succeeds, then $X_j(t+1) = 1$.

(3) The system time is updated to $t' = t+1$. Then, we repeat steps from (1) to (3) until $t = t_{max}$ or there are no infected nodes in the system.

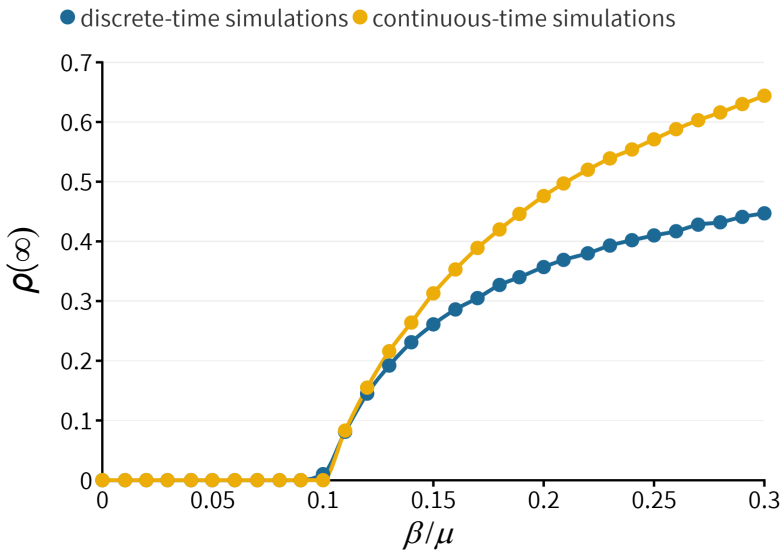

Figure 2.8: **Fraction of infected individuals as a function of the spreading state.** We perform discrete-time simulations and continuous-time simulations for the SIS dynamics on a Erdős-Rényi network with $\langle k \rangle = 10$ and $N = 10^4$. The spreading rate is $\lambda = \beta/\mu$ where recovering rate $\mu = 1$.

Note that this algorithm allows reinfections to occur since the changes of node state are not achieved in the same time window and the spreading process happens after the recovery process.

2. ***Continuous-time simulations***

We still consider the classical SIS scenario to specify the Gillespie algorithm in which the state is switched with asynchronous updating methods. As the focus of our research in this thesis is mainly on the multilayer networks, we here adapt the method to the case of multilayer networks. Due to the existence of interlayer links and intralayer links, we assume two spreading probabilities: the interlayer spreading probability γ, and the intralayer spreading probability β [248]. The recovery process occurs with the probability μ. We assume that the number of infected nodes is N_i and the number of active intralayer and interlayer edges emanating from them are N_k and N_m respectively. Then, at each moment, the SIS spreading process is modelled according to the following steps:

(1) One randomly selected infected node recovers and becomes susceptible with the probability $\frac{\mu N_i}{\mu N_i + \beta N_k + \gamma N_m}$.

(2) One infected node, selected with a probability proportional to its intralayer degree, passes the disease to an edge chosen in a uniformly random way with the probability $\frac{\beta N_k}{\mu N_i+\beta N_k+\gamma N_m}$.

(3) One infected node, chosen with a probability proportional to its interlayer degree, spreads the disease to an edge chosen uniformly at random with the probability $\frac{\gamma N_m}{\mu N_i+\beta N_k+\gamma N_m}$.

(4) The time of each process in the system is updated to $t' = t + \tau$, where $\tau = \frac{1}{\mu N_i+\beta N_k+\gamma N_m}$. We repeat the all above steps until the time t reaches to t_{max} or the system does not have any infected node.

Note that, both synchronous and asynchronous updating methods on the SIS dynamics involve the time parameter t_{max} which directly affects final transmission results. The reason is that there exits an epidemic threshold λ_c we discussed in section 2.2.1. When $\lambda \leq \lambda_c$, the number of infected nodes decays rapidly at an exponential rate with time. On the contrary, there will always be nodes in the infected state in the system. In a finite system, close to the critical point, there are usually high fluctuations that lead the system into the absorbing state. In this case, infected nodes will be presented in the system for a long time [249]. If t_{max} we set is too small, the system remains in the relaxation state. However, if it is set too large, the system is more likely to get into an absorbing state, resulting in only a few simulation processes being active [250].

To analyze the impact of these two simulations on the SIS dynamics, we perform simulations with synchronous and asynchronous updating methods, respectively. The results are obtained on a ER network with $\langle k \rangle = 10$ and $N = 10^4$. In the case of discrete-time simulations, all infected state nodes try to infect all their susceptible neighbors before they may recover. However, two events in continuous simulations, i.e., the infection process along active edges and the recovery process, occur randomly with a certain probability. Therefore, the increase in the number of infected nodes produces more active edges, leading to a greater probability for the occurrence of infection events. Then, as the spreading rate increases, the difference of the fraction of infected individuals obtained in the stationary state continues to increase (see Fig. 2.8).

3. ***Quasi-stationary algorithm***

In the numerical simulations, the average fraction of infected nodes in the steady state is counted only for those simulation processes that survive, i.e., the system does not fall into the absorbing state. As time is incremented,

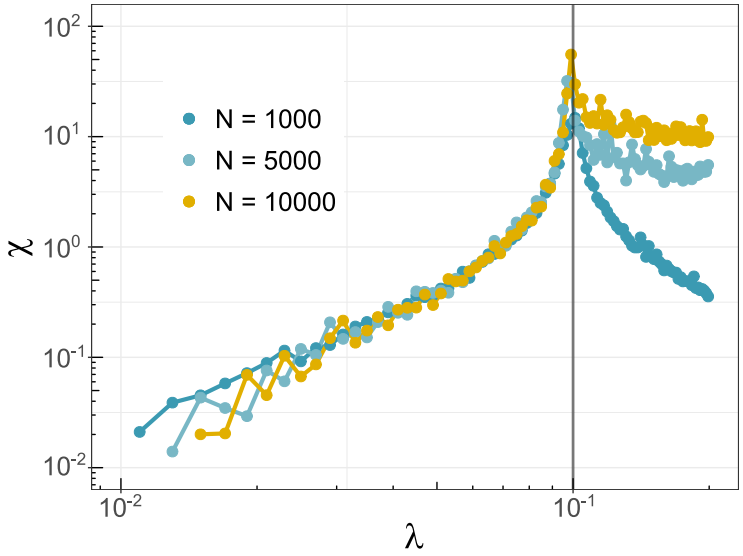

Figure 2.9: **Susceptibility as a function of spreading rate λ.** We apply the quasi-stationary algorithm for the SIS dynamics on a Erdős-Rényi network with $\langle k \rangle = 10$ and $N = 1000, 5000, 10000$. The spreading rate is $\lambda = \beta/\mu$ where recovering rate $\mu = 1$.

the probability that the system is active becomes smaller, implying that more simulations need to be implemented. In particular, near the critical point, the probability of the system being active is even smaller. The question about how to prevent the system with SIS model from getting trapped into the absorbing state and obtain more accurate steady-state values with only a small number of experimental simulations is well addressed by the *quasi-stationary* algorithm [251, 252].

The main mechanism behind the approach is to keep the system in the active state by using the previously visited state to replace the current state. It is worth to note that updating the node state can be done either using synchronous updating methods or asynchronous updating methods. In the implementation, it is necessary to use a list Q to keep M active configurations which is constantly updated. Given a certain time when a process tries to visit an absorbing state, an active configuration previously visited is randomly selected from the list Q and is replaced by the present one with the probability $p_r \Delta t$. The probability that the system is not driven into the absorbing state is given:

$$P(t) = \sum_n p_n(t) \qquad n \geq 1, \tag{2.77}$$

where $P(t)$ is called survival probability [253] and $p_n(t)$ is the probability that there are n infected nodes in the system at time t. Then, the quasi-stationary distribution (QS), is defined:

$$p_n(t) = P(t)\bar{p}_n, \tag{2.78}$$

where $\bar{p}_n$ is independent of time. And we have $\bar{p}_0 \equiv 0$ and the normalization condition $\sum_{n\geq 1} \bar{p}_n = 1$. From a computational point of view, after the relaxation time t_r, we obtain the QS probability $\bar{p}_n$ that there are n infected nodes in the system during an average time t_a. Further, the infection density is derived as:

$$\rho_s = \frac{1}{N} \sum_{n\geq 1} n\bar{p}_n. \tag{2.79}$$

The epidemic threshold can be determined by the susceptibility [252]:

$$\chi = N \frac{\langle \rho_s^2 \rangle - \langle \rho_s \rangle^2}{\langle \rho_s \rangle}. \tag{2.80}$$

Here, we apply the quasi-stationary algorithm to calculate the susceptibility χ as a function of λ on the Erdős-Rényi network with different network sizes. Given the average degree of ER networks is $\langle k \rangle = 10$, the epidemic threshold is expected to get $\lambda_c = 0.1$ with mean-field theory. In Fig. 2.9, as we change the network size, the peak of susceptibility corresponds to the same point on the x-axis, i.e., $\lambda_p(N) = \lambda_c = 0.1$ and scales with N. This practical application of the QS algorithm presents its usefulness in getting the epidemic threshold on the SIS dynamics.

2.3 The effect of directionality on epidemic threshold

Directionality reduces the impact of epidemics in multilayer networks [254].

X. Wang, A. Aleta, **D. Lu**, and Y. Moreno

In this section, we will explore the dynamical processes on multilayer networks, especially the processes of disease transmission. In Chapter 1, we introduced the framework of multilayer networks. In practice, there are considerable examples of two or more dynamics that are interdependent. The introduction of multilayer networks could help to unveil the mechanism behind these multiple paradigms of dynamic interactions [47, 51, 54].

Generally speaking, there are two ways to study the dynamic process on multilayer networks. One is that the multiple interaction mechanism operates at different layers of networks with different dynamics in each layer, such as modelling the interaction between public opinion and disease in social contact networks. The other is that various interaction patterns may be presented in different layers while the same dynamics are in all layers [24, 255]. For example, rumors can spread on multiple social media such as Facebook, Twitter, and Instagram, forming a multilayer network. On the one hand, the rumor propagation process on these social media sites modelled as different network structures has a similar dynamic mechanism. On the other hand, rumors can also be transmitted by word of mouth among real people offline. By this time, it is necessary to model it with a transmission mechanism different from that online. Therefore, diverse network patterns at each layer of multilayer networks effectively depict common phenomena.

Here, we will focus on investigating the same dynamic behaviors under different network structures in detail regarding our work. In most studies, the underlying networks are usually considered undirected while studying diseases spreading processes [54, 82]. However, *directionality* not only can not be ignored, but also is a very important property in a lot of scenarios, such as meerkats in which transmission varies between groomers and groomees [256] and the transmission of HIV between humans, with male-to-female transmission being 2.3 times greater than female-to-male transmission [257]. When dealing with the problems of diseases spreading among different species, we need to consider the fact that disease transmission is more likely to happen from an infected host to the other through an appropriate entry point with an unchangeable direction. For example, the bubonic plague can be endemic in rodent populations and spread to humans and other animals under certain conditions. If it evolves to the pneumonic form, it may then spread from human to human [258]. Analogously, Andes virus usually spreads within rodent populations, but it can be transmitted to humans and then spread via person-to-person contacts [259]. In addition, it is not just the nature of diseases that can cause non-symmetrical transmission. Human behavior by itself can also introduce asymmetric patterns of disease spreading [260]. For instance, vaccination might induce asymmetric interactions among vaccinated and unvaccinated individuals [261]. There are also diseases with long latent periods that induce complicated dynamics between individuals who develop further the disease and those who do not, such as the interaction between individuals in the primary infection phase of Tuberculosis and those in the active state [262, 263]. For those cases, multilayer networks might be able to

help disentangling dynamics that would be otherwise hidden.

2.3.1 The generating function approach

In this work, we focus on investigating how the epidemic threshold is influenced by the directionality of both interlayer and intralayer links. In addition to numerical simulations, we will analytically derive the epidemic thresholds. To this end, we will introduce an approach based on the application of *generating functions*. The description of the generating function formalism in the context of epidemic spreading was introduced by Callaway and Newman [19, 264, 265], which can be adapted specially for the analysis of directed networks.

Here, we consider a general directed network where contacts between individuals are distinguished in undirected and directed links [255, 266]. Hence, the crucial point in this methodology is the joint probability p_{jlm} that a random node has j incoming edges, l outgoing edges, and m undirected edges (or called in-degree j, out-degree l and inter-degree m, respectively). Then, the generating function G for the degree distribution of a node is defined to be:

$$G(x, y, z) = \sum_{j=0}^{\infty} \sum_{l=0}^{\infty} \sum_{m=0}^{\infty} p_{jlm} x^j y^l z^m. \tag{2.81}$$

For normalized p_{jlm}, the function has the property:

$$G(1, 1, 1) = \sum_{j,l,m} p_{jlm} = 1. \tag{2.82}$$

Here, the average in-degree for directed intralinks in multilayer networks is $\langle k_d \rangle$. Note that $G^{(r,s,v)}$ represents differentiation of G according to the three parameters r, s, v times. This gives:

$$\langle k_d \rangle = \frac{\partial G(1, 1, 1)}{\partial x} = G^{(1,0,0)}(1, 1, 1). \tag{2.83}$$

Likewise, the out-degree of a node is necessarily same with $\langle k_d \rangle$ since every incoming edge is also the outgoing edge at some nodes. Then, we can get $\langle k_d \rangle = G^{(1,0,0)}(1, 1, 1) = G^{(0,1,0)}(1, 1, 1)$. Whereas, the average degree for the undirected edges is:

$$\langle k_u \rangle = \frac{\partial G(1, 1, 1)}{\partial z} = G^{(0,0,1)}(1, 1, 1). \tag{2.84}$$

The *excess degree* distribution is another quantity related to the nodal degree distribution which indicates the degree distribution of nodes arrived at

by following a randomly selected link. Therefore, the probability to arrive at a node by following a directed edge in the direction of a randomly chosen link is $jp_{jlm}/\sum_{jlm} jp_{jlm}$. So, we can get the corresponding generating function:

$$H_d(x,y,z) = \frac{\sum_{jlm} jp_{jlm}x^{j-1}y^l z^m}{\sum_{jlm} jp_{jlm}} = \frac{G^{(1,0,0)}(x,y,z)}{\langle k_d \rangle}. \tag{2.85}$$

Then, the generating function obtained by following a directed link in the reverse direction is written as:

$$H_r(x,y,z) = \frac{\sum_{jlm} lp_{jlm}x^j y^{l-1} z^m}{\sum_{jlm} lp_{jlm}} = \frac{G^{(0,1,0)}(x,y,z)}{\langle k_d \rangle}. \tag{2.86}$$

Lastly, the excess degree distribution at a node arrived at by following an undirected link is:

$$H_u(x,y,z) = \frac{\sum_{jlm} mp_{jlm}x^j y^l z^{m-1}}{\sum_{jlm} mp_{jlm}} = \frac{G^{(0,0,1)}(x,y,z)}{\langle k_u \rangle}. \tag{2.87}$$

Next, we take into account the probability of an edge being "infected" by a disease which means that a node i being susceptible gets infected with the disease transmitted by node j along that edge, denoted by T. The probability that exactly m of the k edges of a vertex are occupied is given by the binomial distribution, i.e., $\binom{k}{m} T^m (1-T)^{k-m}$. Hence, in terms of the edge being directed and undirected, the average probability is represented by T_d and T_u, respectively. Then, we consider the generating function for the distribution of the number of infected links of a randomly selected node which is modified in the following form:

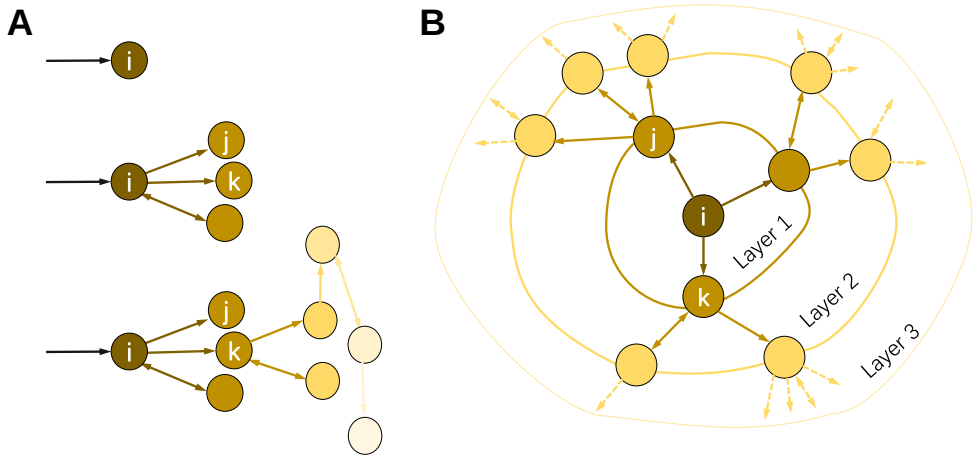

FIGURE 2.10: **The schematic of generating function method. A)** The generating function for the excess degree, denoted by $H(x)$, gives the degree distribution of the node reached by following a randomly selected link. **B)** The generating function for the degree of the node is G(x). Therefore, for an outbreak starting from a random node i, the generating function of the degree distribution on the first layer can be calculated by $G(H(x))$. Then, on the second layer, the generating function can be obtained by $G(H(H(x)))$.

$$
\begin{aligned}
G(x,y,z;T_d,T_u) &= \sum_{a,b,c}\left[\sum_{j=a}^{\infty}\sum_{l=b}^{\infty}\sum_{m=c}^{\infty} p_{jlm}\binom{j}{a}T_d^a\left(1-T_d\right)^{j-a}\binom{l}{b}T_d^b\left(1-T_d\right)^{l-b}\right. \\
&\qquad \left.\binom{m}{c}T_u^c(1-T_u)^{m-c}\right]x^a y^b z^c \\
&= \sum_{jlm} p_{jlm}\left[\sum_{a=0}^{j}\binom{j}{a}\left(T_d x\right)^a\left(1-T_d\right)^{j-a}\sum_{b=0}^{l}\binom{l}{b}\left(T_d y\right)^b\left(1-T_d\right)^{l-b}\right. \\
&\qquad \left.\sum_{c=0}^{m}\binom{m}{c}\left(T_u z\right)^c\left(1-T_u\right)^{m-c}\right] \\
&= \sum_{jlm} p_{jlm}\left(1-T_d+T_d x\right)^j\left(1-T_d+T_d y\right)^l\left(1-T_u+T_u z\right)^m \\
&= G(1-T_d+T_d x, 1-T_d+T_d y, 1-T_u+T_u z).
\end{aligned}
\tag{2.88}
$$

We similarly derive the generating function for the number of infected links

emanating from a node arrived at by following a randomly chosen links so that we get

$$\begin{aligned} H_d(x,y,z;T_d,T_u) &= H_d(1-T_d+T_dx, 1-T_d+T_dy, 1-T_u+T_uz) \\ H_r(x,y,z;T_d,T_u) &= H_r(1-T_d+T_dx, 1-T_d+T_dy, 1-T_u+T_uz) \\ H_u(x,y,z;T_d,T_u) &= H_u(1-T_d+T_dx, 1-T_d+T_dy, 1-T_u+T_uz) \end{aligned} \tag{2.89}$$

The quantity that we are interested in is the outbreak size, that is, the number of nodes infected in an outbreak that started from a randomly chosen node. Firstly, the probability of the size s of an outbreak beginning at a single infected node is denoted as P_s. Then, we define $g(w;T_d,T_u)$ as the generating function for the size distribution, written as:

$$g(w;T_d,T_u) = \sum_s P_s(T_d,T_u)w^s. \tag{2.90}$$

We need to evaluate the probability that an outbreak starting with an infection event along a randomly chosen edge will be size s'. Furthermore, given the size of an outbreak s', we define the generating function $h_d(w;T_d,T_u)$ for this probability distribution to solve Eq. 2.90:

$$h_d(w;T_d,T_u) = \sum_{s'} P_{s'}(T_d,T_u)w^{s'}. \tag{2.91}$$

The left panel in Fig. 2.10 illustrates that the generating functions for the size of an outbreak starting with a randomly chosen directed edge satisfying a condition of the form:

$$h_d(w;T_d,T_u) = wH_d(1, h_d(w;T_d,T_u); h_u(w;T_d,T_u); T_d, T_u). \tag{2.92}$$

We also can get the expression for undirected case:

$$h_u(w;T_d,T_u) = wH_u(1, h_d(w;T_d,T_u); h_u(w;T_d,T_u); T_d, T_u). \tag{2.93}$$

Given the above-defined expression Eq. 2.89, the distribution of the size of an outbreak, s', can be obtained combined with the two equations we just mentioned. If the infection starts from a randomly selected node (shown in Fig. 2.10), the generating function of the size distribution is given by:

$$g(w;T_d,T_u) = wG(1, h_d(w;T_d,T_u); h_u(w;T_d,T_u); T_d, T_u). \tag{2.94}$$

Finally, the average size of an outbreak beginning from a randomly chosen node is

$$\langle s \rangle = \sum_s s P_s(T_d, T_u) = g'(1; T_d, T_u). \tag{2.95}$$

Note that the prime shown in the equation represents differentiation concerning w. Here, setting $w = 1$, we get the following expressions after implementing the derivatives:

$$g'(1; T_d, T_u) = 1 + G^{(0,1,0)} h'_d + G^{(0,0,1)} h'_u, \tag{2.96}$$

$$h'_d(1; T_d, T_u) = 1 + H_d^{(0,1,0)} h'_d + H_d^{(0,0,1)} h'_u, \tag{2.97}$$

$$h'_u(1; T_d, T_u) = 1 + H_u^{(0,1,0)} h'_d + H_u^{(0,0,1)} h'_u, \tag{2.98}$$

where the arguments of all generating functions are $(1, 1, 1; T_d, T_u)$ and the fact $h_d(1; T_d, T_u) = h_u(1; T_d, T_u) = 1$ is applied. Eqs. 2.97 and 2.98 can be rewritten as:

$$\begin{aligned} h'_d(1; T_d, T_u) &= \frac{1 - H_u^{(0,0,1)} + H_d^{(0,0,1)}}{(1 - H_d^{(0,1,0)})(1 - H_u^{(0,0,1)}) - H_d^{(0,0,1)} H_u^{(0,1,0)}}, \\ h'_u(1; T_d, T_u) &= \frac{1 - H_d^{(0,1,0)} + H_u^{(0,1,0)}}{(1 - H_d^{(0,1,0)})(1 - H_u^{(0,0,1)}) - H_d^{(0,0,1)} H_u^{(0,1,0)}}. \end{aligned} \tag{2.99}$$

Then, we insert these expressions into Eq. 2.96, obtaining the average size of outbreak:

$$\langle s \rangle = 1 + \frac{G^{(0,1,0)}(1 - H_u^{(0,0,1)} + H_d^{(0,0,1)}) + G^{(0,0,1)}(1 - H_d^{(0,1,0)} + H_u^{(0,1,0)})}{(1 - H_d^{(0,1,0)})(1 - H_u^{(0,0,1)}) - H_d^{(0,0,1)} H_u^{(0,1,0)}}. \tag{2.100}$$

For the sake of simplicity, we assume that the probability is the same about the the direction of edges along which the disease transmits, that is, $T_d = T_u = T$. In this case, $G^{(0,1,0)}(1, 1, 1; T_d, T_u)$ is replaced by the form $G^{(0,1,0)}(1, 1, 1; T)$. Meanwhile, we make use of the conditions:

$$G^{(0,1,0)}(1, 1, 1; T) = T G^{(0,1,0)}(1, 1, 1) \quad \text{and} \quad H_d^{(0,1,0)}(1, 1, 1; T) = T H_d^{(0,1,0)}(1, 1, 1), \tag{2.101}$$

Consequently, the size of the outbreak is written as:

$$\langle s \rangle = 1 + \frac{TG^{(0,1,0)}(1 - T(H_u^{(0,0,1)} + H_d^{(0,0,1)})) + TG^{(0,0,1)}(1 - T(H_d^{(0,1,0)} + H_u^{(0,1,0)}))}{(1 - TH_d^{(0,1,0)})(1 - TH_u^{(0,0,1)}) - T^2 H_d^{(0,0,1)} H_u^{(0,1,0)}}. \tag{2.102}$$

where the arguments in the expression are set to $(1, 1, 1)$.

As the expression diverges when denominator of the above equation is equal to zero, which characterizes a phase transition from small size of outbreaks with tree-like structure to the occurrence of large-scale outbreaks, we end up with:

$$(1 - TH_d^{(0,1,0)})(1 - TH_u^{(0,0,1)}) - T^2 H_d^{(0,0,1)} H_u^{(0,1,0)} = 0. \tag{2.103}$$

Next, the only step to get the epidemic threshold is to substitute the proper values of H_d and H_u. Then, the epidemic threshold can be expressed as the derived critical value, T_c. In what follows, the formalism of generating functions will be adapted slightly according to network configurations and employed to derive the analytical epidemic threshold.

2.3.2 The model considering directionality

Here, we will introduce the model for the disease transmission in multilayer networks with directionality taken into account. Let us firstly take a step back into the basic components constructing multilayer networks. Among those, the interlayer links connecting nodes within each layer and the interlayer links representing the connection relationship of nodes between layers are the main subjects undertaking the proposed research problem. Particularly, we will choose the multiplex networks composed of two layers as the study model where a node can only be connected to its counterpart in the other layer. Moreover, we will analyze several combinations of directionality: (i) Directed layer - Undirected interlinks - Directed layer (DUD); (ii) Directed layer - Directed interlinks - Directed layer (DDD); and (iii) Undirected layer - Directed interlinks - Undirected layer (UDU). For the sake of comparison, we also include the standard scenario, namely, (iv) Undirected layer - Undirected interlinks - Undirected layer (UUU) [254]. To define the degree distribution in the layers, we use Poisson and power-law distributions, which are the typical representatives of homogeneous and heterogeneous distributions, corresponding respectively to Erdős–Rényi (ER) and Scale-Free (SF) network models.

Here, we also need to define how many links point from one layer to another layer, either in the opposite direction for the configurations (UDU and DDD)

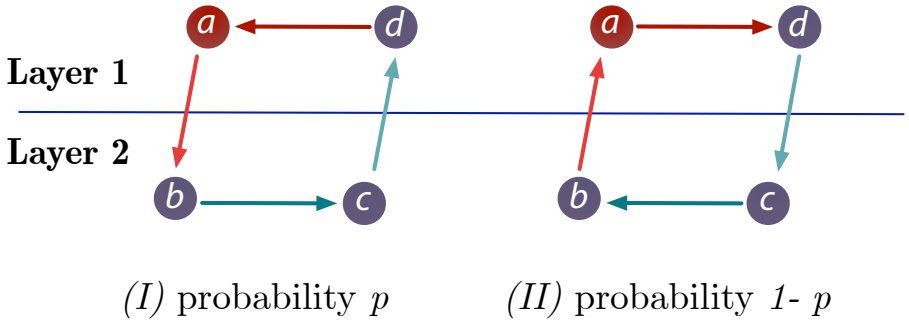

FIGURE 2.11: **Diagram for two types of closed loops.** In the case of DDD and UDU, two types of closed loops coexist, type I with probability p and type II with probability $1-p$. Starting from a randomly chosen infected node a in layer 1, the disease in type I spreads to the opposite layer 2 via the directed interlink $a \to b$ from layer 1 to layer 2 (with probability p) and loops back to the started node a via the directed path $b \to c \to d \to a$. The spreading diagram in type II is the reverse of the diagram in type I, but with probability $1-p$ for a randomly chosen node to have an interlink directed from layer 2 to layer 1

in which the interlinks are directed. Indeed, if all interlinks have the same direction, the epidemic threshold would be trivially the one of the source layer and thus the multiplex structure would play no role. For this reason, for each directed link connecting layers u and v, we set the directionality to be $u \to v$ with probability p and $u \leftarrow v$ with probability $(1-p)$, shown in Fig. 2.11 with a simple schematic. Consequently, in networks with directed interlinks the epidemic threshold will be given as a function of this probability p.

2.3.3 Numerical results

To study the evolution of the epidemic threshold as a function of the directionality and the coupling strength between layers, we implement a susceptible-infected-susceptible (SIS) model on these networks. In our model, we use same parameters for characterizing the intralayer and interlayer spreading processes, β and γ, as we denoted in section 2.2.6. Hence, an infected node transmits the disease with probability β to those susceptible neighbors of the same layer and with probability γ to those located in other layers. The recovery rate is denoted as μ for all the nodes. As previously stated in section 2.2.2, the epidemic threshold is defined as β/μ in the single layer network. Here, in this work, it is possible to find a critical value of β_c by exploring its value as a function of γ. For simplicity, we set the recovery rate is to $\mu = 1$ in the simulations. Thus, we define the epidemic threshold in this project as a function of β and γ.

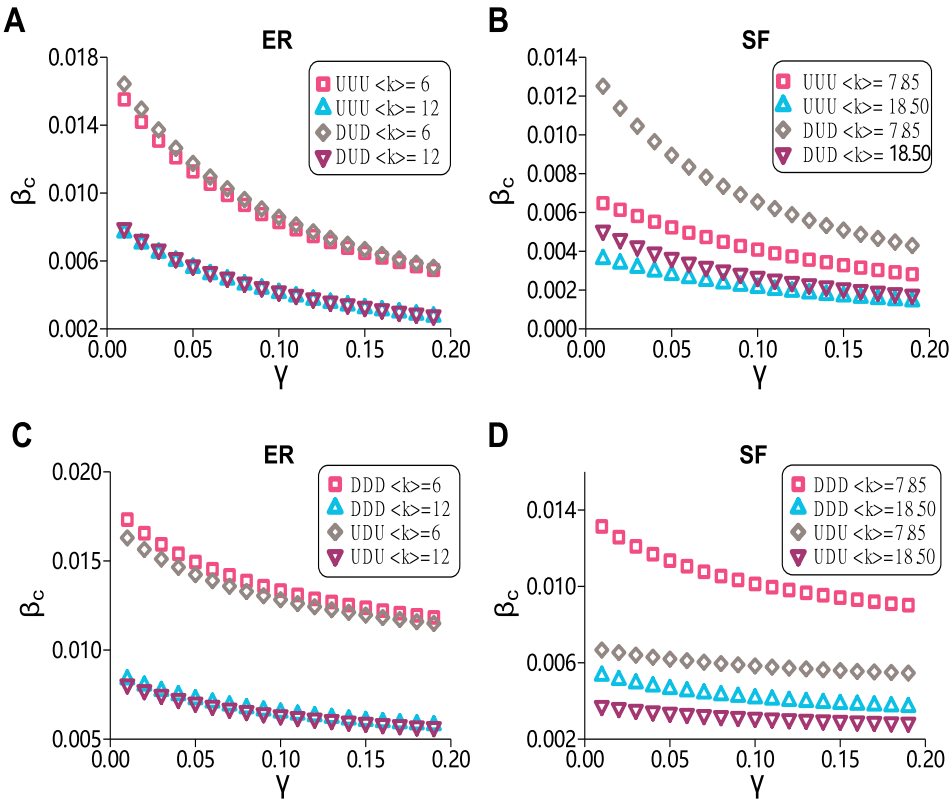

Figure 2.12: **Evolution of epidemic threshold for the four configurations.** Epidemic threshold for the spread of a disease within layers, β_c, as a function of the probability of interlayer contagion, γ. Panels **(A)** and **(B)** show results for the UUU and DUD configurations with ER **(A)** and SF **(B)** degree distributions in the layers. Panels **(C)** and **(D)** exhibit results for the DDD and UDU configurations built up using the p-model with ER **(C)** and SF **(D)** degree distributions in the layers, where $p = 0.5$. In all cases, $\mu = 0.1$, the number of nodes is $N = 2 \times 10^4$ and for each directionality configuration, there are two sets of networks: in the ER case one with $\langle k \rangle = 6$ in both layers and another one with $\langle k \rangle = 12$ in both layers; in the SF case one with $k_{min} = 4$ and $\alpha = 2.7$ (average degree $\langle k \rangle = 7.85$) and another one with $k_{min} = 10$ and $\alpha = 2.8$ (average degree $\langle k \rangle = 18.50$).

Here, we conduct numerical simulations with asynchronous updating methods, that is, continuous-time simulations (see section 2.2.6). All the nodes in the system are initially susceptible. The spreading starts when one node is set to the infectious state. Then, at each time step, each infected node spreads the disease through each of its links with probability β if the link is contained in a layer and with probability γ if the link connects nodes in different layers. Besides, each infected node recovers with probability μ at each time step. The simulation runs until a stationary state for the number of infected individuals

is reached.

To determine the epidemic threshold, we fix the value of γ and run the simulation over multiple values of β, repeating 10^3 times the simulation for each of those values. The recovery probability in the simulations is set to $\mu = 1$. The minimum value of β at which, on average, the number of infected individuals in the steady state is greater than one determines the value of the epidemic threshold, β_c/μ obtained with the quasi-stationary algorithm (see section 2.2.6). This procedure is then repeated for several values of γ to obtain the dependency of β_c with the spreading across layers. Lastly, this dependency is evaluated for 10^2 realizations of each network considered in the study and the curves of β_c/γ are averaged.

We first present results of numerical simulations of a stochastic SIS model on ER and SF networks with different average degrees. In Fig. 2.12, we show the evolution of the epidemic threshold, β_c, as a function of γ for the four configurations. We can see that for networks with $\langle k \rangle = 6$, the epidemic threshold is very similar in both UUU and DUD configurations. This effect is again seen for denser networks, $\langle k \rangle = 12$, implying that it is the directionality of the interlinks, and not the one of the links contained within layers, the main driver of the epidemic in these networks. On the other hand, in Fig. 2.12(B), we can see that this behavior is not replicated for SF networks. Certainly, there is a large difference between the curves of the UUU and DUD configurations, implying that the directionality of intralinks is much more important in this type of networks. In agreement with these observations, when the interlinks are those that are directed, we found the same difference between ER and SF networks observed in Fig. 2.12(C) and (D). Besides, the evolution of the epidemic threshold as a function of γ is again quantitatively similar for the configurations (UDU and DDD). So far, in all the cases considered, the epidemic threshold is always lower for those configurations with undirected links within the layers, compared to those in which those links are directed, given the same interlink directionality.

2.3.4 Theoretical results

In order to obtain theoretical insights into the mechanisms driving the spreading process on directed multiplex networks, we analytically derive the epidemic threshold for all the configurations considered in this work. To this end, we extend the generating function formalism, which has been used previously for directed monolayer networks in section 2.3.1 to multiplex networks. Within the generating function formalism, we assume a node has an in-degree j, out-

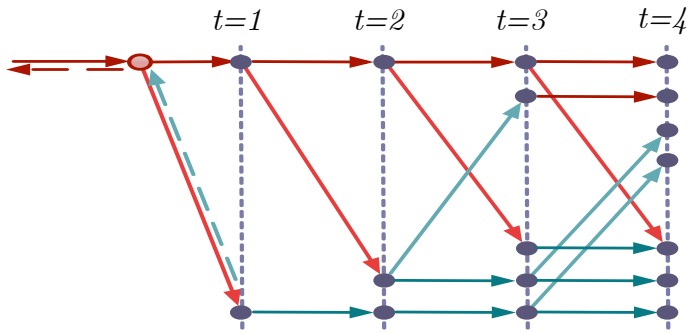

Figure 2.13: **The future transmission diagram on multilayer networks.** The transmission starts from a single infected node reached by following the direction of a randomly chosen link. Solid lines represent the disease transmission on directed links and dashed lines depict the bidirectional disease transmission on undirected links.

degree l and inter-degree m with probability p_{jlm}, being the first two related to the links contained in each layer and the latter to links connecting nodes in different layers. The generating function for the degree distribution of a node is denoted by $G(x, y, z)$ same with what we discussed before. Note that the combinations of directionality to be considered lead to different forms. In the case of UXU (UUU and UDU), we regard j as an indicator for the number of undirected links. The generating function is changed to $G(x, z)$ instead of $G(x, y, z)$ for the DXD case, where z represents the interlayer links.

The quantity needed for the derivation of the epidemic threshold is excess degree whose distribution of the generating function is same as we described in section 2.3.1. To obtain the epidemic threshold, as well as the size of an outbreak, we need to compute the fraction of the occupied links in the network. Here, the difference appears when we consider the occupied link which refers to a link along which the disease was transmitted. Since there are different parameters (β and γ) indicating the intralayer and interlayer spreading probability, respectively, we regard the probability of a link within layers being infected as T and the probability of a link across layers being infected as T_{uv}. Therefore, the generating function for the distribution of the number of infected links of a randomly selected node is given by:

$$G(x, y, z; T, T_{uv}) = G(1 + Tx - T, 1 + Ty - T, 1 + T_{uv}z - T_{uv}). \quad (2.104)$$

In the SIS epidemic model, we assume both the spreading process and the recovering process are independent Poisson processes with rate β and μ, respectively. The time, denoted as τ_i, that an infected node i remains infected

is a random variable, whose distribution follows an exponential distribution with rate μ. The probability 1 - T_{ij} that the disease will not transmit from an infected node i to a susceptible node j is $e^{-\beta\tau_i}$. As τ_i is a random variable, the probability T_{ij} of disease transmission is also a random variable. When assuming a homogeneous recovering rate for each node, the average of disease transmission probability between infected and susceptible individuals is the average over the distribution of infectious time, which follows:

$$T = 1 - \int_0^\infty e^{-\beta\tau}\mu e^{-\mu\tau}d\tau, \tag{2.105}$$

from which we obtain

$$T = 1 - \frac{\mu}{\beta + \mu}. \tag{2.106}$$

Analogously, the average transmission probability of individuals between different layers reads, given that the spreading rate between layers is γ,

$$T_{uv} = 1 - \frac{\mu}{\gamma + \mu}. \tag{2.107}$$

To get the generating function for the distribution of the size of an outbreak, we first show the transmission diagram in the Fig. 2.13. It shows the future transmission diagram starting from a single infected node reached by following a randomly chosen link within layers. Solid lines represent the disease transmission on directed links and dashed lines depict the bidirectional disease transmission on undirected links. The possible ways of future transmission are: the disease spreads along an intra-link in the same layer, it spreads along an inter-link to the opposite layer, it spreads along two intra-links, it spreads along one intra-link and one inter-link. To account for all the transmission possibilities, we construct the corresponding recursive relation of generating functions for the size distribution of outbreaks by following four types of links shown in Fig. 2.14. Hence, we use h_1, h_{12}, h_2, h_{21} to denote recursive relations if link is in layer 1, link is pointing from layer 1 to layer 2, link is in layer 2 and link is going from layer 2 to layer 1, respectively. The generating functions satisfy recursive relations:

$$\begin{aligned}
&h_1(w;T,T_{uv}) = wH_1(1, h_1(w;T,T_{uv}), h_12(w;T,T_{uv});T,T_{uv}),\\
&h_12(w;T,T_{uv}) = wH_12(1, h_2(w;T,T_{uv}), h_21(w;T,T_{uv});T,T_{uv}),\\
&h_2(w;T,T_uv) = wH_2(1, h_2(w;T,T_{uv}), h_21(w;T,T_{uv});T,T_{uv}),\\
&h_21(w;T,T_{uv}) = wH_21(1, h_1(w;T,T_{uv}), h_12(w;T,T_{uv});T,T_{uv}).
\end{aligned} \tag{2.108}$$

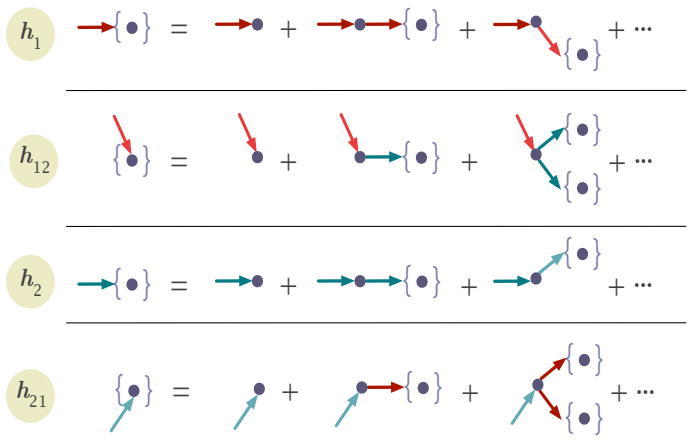

Figure 2.14: **Scheme of the generating functions.** The recursive relation of generating functions for the size distribution of outbreaks by following four types of links which are (i) intralink in layer 1, (ii) interlink pointing from layer 1 to layer 2, (iii) intralink in layer 2 and (iv) interlink pointing from layer 2 to layer 1.

Similarly, generating function for the distribution of the size of an outbreak along a randomly chosen node in layer 1 follows:

$$g(w;T,T_{uv}) = wG(1,h_1(w;T,T_{uv}),h_1 2(w;T,T_{uv});T,T_{uv}). \tag{2.109}$$

Then, we calculate the average size of an outbreak starting from a randomly chosen node:

$$\langle s\rangle = \sum_{s=1}^{N} sP_s(T) = \left.\frac{\mathrm{d}g(w;T,T_{uv})}{\mathrm{d}w}\right|_{w=1}. \tag{2.110}$$

After performing the derivative with respect to w on both sides of Eqs. 2.109 and 2.108, we get the expression for the average size $\langle s\rangle$ of an outbreak in terms of the generating functions. Likewise, the expression goes to infinity when the denominator equals zero. Therefore, the critical equation that determines epidemic threshold reads

$$\begin{aligned} 0 = &\left[\left(1-H_1^{(0,1,0)}\right)H - H_1^{(0,0,1)}H_{12}^{(0,0,1)}H_{21}^{(0,1,0)}\right] \\ &\times\left[\left(1-H_2^{(0,1,0)}\right)H - H_2^{(0,0,1)}H_{21}^{(0,0,1)}H_{12}^{(0,1,0)}\right] \\ &- H_1^{(0,0,1)}H_2^{(0,0,1)}H_{12}^{(0,1,0)}H_{21}^{(0,1,0)} \end{aligned} \tag{2.111}$$

The expression applies to all the configurations (UXU and DXD). Under each configuration, we only need to obtain the derivatives of the generating

function H_1, H_{12}, H_2, H_{21} to derive the epidemic threshold. For example, considering the directed multilayer network with DUD configuration composed of two ER networks. If both the in-degree and out-degree follow a Poisson distribution with the same average degree $\langle k\rangle$, the generating function for the excess degree H_d follows:

$$H_d\left(x,y,z\right)=\frac{\sum_{j=0}^{\infty}\sum_{l=0}^{\infty}\frac{\langle k\rangle^j e^{-\langle k\rangle}}{j!}\frac{\langle k\rangle^l e^{-\langle k\rangle}}{l!}jx^{j-1}y^l z}{\langle k\rangle}, \tag{2.112}$$

from which we obtain the partial derivative with respect to y evaluated at the point $x=y=z=1$ as:

$$H_d^{(0,1,0)}(1,1,1)=\langle k\rangle,\quad H_u^{(0,1,0)}(1,1,1)=\langle k\rangle. \tag{2.113}$$

The generating function H_1 for layer 1 is substituted by H_d which reads

$$H_1^{(0,1,0)}=H_d^{(0,1,0)}(1,1,1;T,T_{uv})=TH_d^{(0,1,0)}(1,1,1). \tag{2.114}$$

Similarly, the generating functions H_2 in layer 2 following:

$$H_1^{(0,1,0)}=H_2^{(0,1,0)}=T\langle k\rangle, \tag{2.115}$$

As two layers of graphs are connected by undirected or bidirected interlinks, the disease thus can be transmitted with probability T_{uv} from layer 1 to layer 2 and, meanwhile, with probability T_{uv} to be transmitted from layer 2 to layer 1. The bidirectionality for disease transmission of undirected interlinks is reflected by the generating functions:

$$\begin{aligned}H_{12}^{(0,1,0)}&=H_u^{(0,1,0)}(1,1,1;T,T_{uv})=T\langle k\rangle,\\ H_{12}^{(0,0,1)}&=T_{uv}+H_u^{(0,1,0)}(1,1,1;T,T_{uv})=T_{uv}.\end{aligned} \tag{2.116}$$

Then, we get all the derivatives of the generating functions H_1, H_2, H_{12} and H_{21} needed for deriving the epidemic threshold:

$$\begin{aligned}H_1^{(0,1,0)}&=H_2^{(0,1,0)}=T\langle k\rangle,\\ H_{12}^{(0,1,0)}&=H_{21}^{(0,1,0)}=T\langle k\rangle,\\ H_1^{(0,0,1)}&=H_2^{(0,0,1)}=T_{uv},\\ H_{12}^{(0,0,1)}&=H_{21}^{(0,0,1)}=T_{uv}.\end{aligned} \tag{2.117}$$

Substituting these generating functions into the Eq. 2.111, which characterizes the critical point of phase transition, we derive the epidemic threshold for DUD configuration as:

$$T_c = \frac{1 - T_{uv}}{\langle k \rangle}. \tag{ER-DUD}$$

Analogously, we can get the epidemic threshold for other configurations:

$$T_c = \frac{1 - T_{uv}}{\langle k \rangle + 1 - T_{uv}}, \tag{ER-UUU}$$

$$T_c = \frac{2}{\langle k \rangle \left(2 + m + \sqrt{m(m+8)}\right)}, \tag{ER-DDD}$$

where $m = p(1-p)T_{uv}^2$.

$$T_c = \frac{2\left(1 + \langle k \rangle\right) + m' - \sqrt{m'\left(4 + 8\langle k \rangle + m'\right)}}{2\left(\left(1 + \langle k \rangle\right)^2 - m'\langle k \rangle\right)}, \tag{ER-UDU}$$

where $m' = \langle k \rangle p(1-p)T_{uv}^2$.

We further present the generalization to directed multilayer networks consisting of scale-free networks with power-law degree distributions. For a power-law degree distribution with an exponential cutoff, the degree distribution is written as

$$\Pr[D = k] = Ck^{-\alpha}e^{-k/\kappa}, \tag{2.118}$$

where $C = [\sum_{k_{\min}}^{k_{\max}} k^{-\alpha}e^{-k/\kappa}]^{-1}$ is a normalization constant to ensure condition $\sum_{k_{\min}}^{k_{\max}} \Pr[D = k] = 1$. The constant $k_{\min}$ is the minimum degree and $k_{\max}$ denotes the maximum degree and κ is a constant determining the cutoff.

Assume both the in- and out- degree in each layer are independently and identically power-law distributed. The generating function for the degree distribution of a node with in-degree i, out-degree j and inter-degree m reads

$$G(x, y, z) = \sum_{j=0}^{\infty}\sum_{k=0}^{\infty}\sum_{m=0}^{\infty} \frac{j^{-\alpha}e^{-j/\kappa}k^{-\alpha}e^{-k/\kappa}p_m}{\sum_{j_{\min}}^{j_{\max}} j^{-\alpha}e^{-j/\kappa}\sum_{k_{\min}}^{k_{\max}} k^{-\alpha}e^{-k/\kappa}} x^j y^k z^m, \tag{2.119}$$

with $p_m = 1$ to have an undirected interlink.

Then, the distributions of excess degree by following a randomly chosen link within a layer is accordingly modified by the power-law degree distribution. With the same method, we can obtain derivatives of the set of generating functions (H_1, H_2, H_{12} and H_{21}) under different configurations. In the case of

DUD with directed interlinks, the in-degree and out-degree are distinguishable and $H_1^{(0,1,0)}(1,1,1) = H_2^{(0,1,0)}(1,1,1) = T\langle k\rangle$. As the interconnection topology between different layers remains unchanged, the generating functions regarding interconnections are the same with generating functions of XUX in ER networks (see Eq. 2.117). Therefore, the epidemic threshold for DUD configurations with scale-free layers remains unchanged with the ER case, which reads

$$T_c = \frac{1 - T_{uv}}{\langle k\rangle}, . \tag{SF-DUD}$$

For the multiplex networks of UUU, The difference emerges in deriving the generating function H_1 for the excess degree of a node reached by following a randomly chosen intra-link is modified as

$$H_1(1, y, z) = \sum_{l=0}^{\infty}\sum_{m=0}^{\infty} \frac{l p_{jlm} y^{l-1} z^m}{\langle k\rangle}, \tag{2.120}$$

from which

$$H_1^{(0,1,0)}(1,1,1) = \sum_{l=0}^{\infty}\sum_{m=0}^{\infty} \frac{l(l-1)p_{jlm}}{\langle k\rangle} = \frac{\langle k^2\rangle - \langle k\rangle}{\langle k\rangle}, \tag{2.121}$$

instead of $H_1^{(0,1,0)}(1,1,1) = \langle k\rangle$ for the case of ER networks with Poisson degree distribution. Therefore, we obtain:

$$H_1^{(0,1,0)}(1,1,1;T,T_{uv}) = T + T\frac{\langle k^2\rangle - \langle k\rangle}{\langle k\rangle}, \tag{2.122}$$

where the term T represents the backward spreading along the undirected intralink that we came along and the term $T((\langle k^2\rangle - \langle k\rangle)/\langle k\rangle)$ represents the spreading along the excess neighbors of the node that we reached. Thus, the epidemic threshold is

$$T_c = \frac{\langle k\rangle\,(1 - T_{uv})}{\langle k^2\rangle\,(1 - T_{uv}) + \langle k\rangle^2 T_{uv}}, \tag{SF-UUU}$$

On the other hand, using the p-model, the epidemic threshold for DDD and UDU with scale-free layers as:

$$T_c = \frac{2}{\langle k\rangle\left(2 + m + \sqrt{m(m+8)}\right)}, \tag{SF-DDD}$$

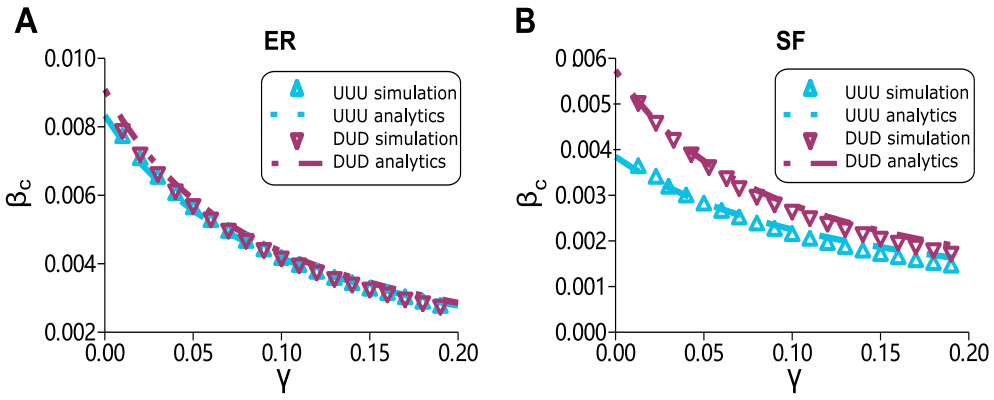

Figure 2.15: **Comparisons between simulations and analytical results for UUU and DUD configurations.** The epidemic threshold β_c as a function of γ. It shows the results for UUU and DUD configurations with **A)** ER degree distribution ($\langle k\rangle = 12$) and **B)** SF degree distribution ($k_{min} = 10$, $\alpha = 2.8$ (average degree $\langle k\rangle = 18.50$)) in both layers. In all cases, $\mu = 0.1$, the number of nodes is $N = 2 \times 10^4$ and for each directionality configuration.

$$T_c = \frac{2\langle k^2\rangle\langle k\rangle + \langle k\rangle^2\left(\langle k\rangle m - \sqrt{m(4\langle k^2\rangle + \langle k\rangle^2(4+m))}\right)}{2(\langle k^2\rangle^2 - \langle k\rangle^4 m)}, \qquad \text{(SF-UDU)}$$

where $m = p(1-p)T_{uv}^2$.

Relying on these analytically derived thresholds, we first compare them with numerical simulations for two configurations (UUU and DUD) as shown in Fig. 2.15, showing favorable analytical predictions. We also explore the evolution of β_c as a function of γ for the whole range of possible values of the latter parameter (see Fig. 2.16). In this case, we can see that the value of the epidemic threshold of the DUD configuration in SF networks tends to the value of the UUU case for large values of the spreading probability across layers, mimicking the behavior of ER networks. Besides, we reach the state in which both networks exhibit the same properties when $\gamma \to 1$. Hence, in general, we can conclude that the directionality (or lack of) of the interlinks is the main driver of the epidemic spreading process. The exception is the limit of small spreading from layer to layer, as in this scenario, the directionality of interlinks makes SF networks much more resilient, see the dashed–dotted line in Fig. 2.16(B).

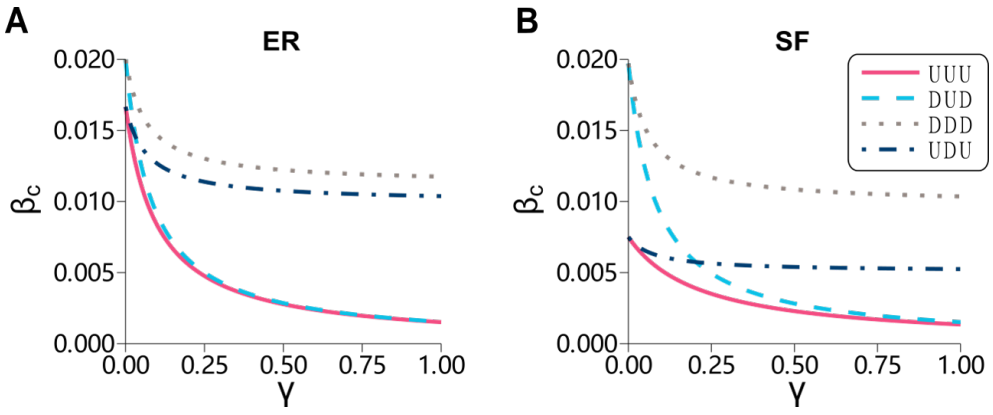

FIGURE 2.16: **Comparison of the analytically derived epidemic thresholds for four configurations.** For each network configuration UXU or DXD (X = U or D), we perform simulations on the networks with different degree distributions. **A)** ER networks with $\langle k \rangle = 6$ and $p = 0.5$. **B)** SF networks with $k_{min} = 3$, $\alpha = 2.6$, resulting in the theoretical average degree $\langle k \rangle = 6.1$ and $p = 0.5$.

2.3.5 Discussion

Our results show that the presence of directed links results in larger epidemic thresholds with respect to the case of undirected networks, and that the system is more resilient when the interlayer links are directed. Therefore, our conclusions are in line with previous works [267, 268] in that directionality is a key topological feature that should not be disregarded as it can lead to new phenomenology and sizable dynamical effects.

In addition, it is important to note that these results are not only relevant for the situations we just described. These results are not restricted only to epidemic modeling, as these kind of diffusion processes can be applied to a broad range of systems. For example, the generating function approach has been proposed as a tool to identify influential spreaders in social networks [269]. One particularly interesting and open challenge is to quantify the effects that the interplay between different social networks could have on spreading dynamics. The theoretical framework developed here is particularly suitable to study this and similar challenges related to the spreading of information in social networks. On the one hand, social relations are, by default, directed. For instance, in social platform, a user is not necessarily followed by her followings. On the other hand, disease-like models have been widely used to study information dissemination, or in other words, simple social contagion [112, 270].

Then, we have analyzed the dependence of the epidemic threshold with

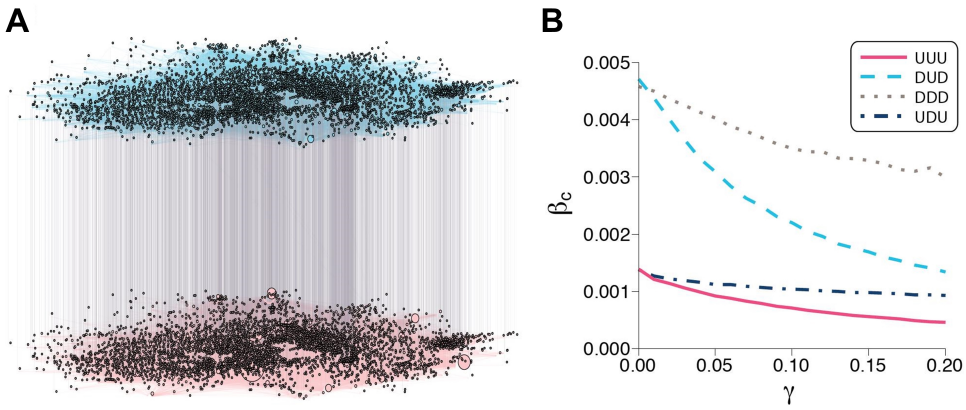

Figure 2.17: **Epidemic threshold measured in a multiplex social network.** The multiplex network is composed by users of two different social platforms: FriendFeed and Twitter. **A)** The original network has directed intralinks and undirected interlinks, thus it corresponds to the DUD configuration. **B)** The four configurations studied in this paper are considered to explore the effects of directionality. For those configurations with directed interlinks we used the p-model to generate them, setting $p = 0.5$.

the inter-spreading rate in a real social network composed by two layers, see Fig. 2.17(A). The first layer of the multilayer systems is made up by the directed set of interactions in a subset of users of the now defunct FriendFeed platform, whereas the second layer is defined by the directed set of interactions of those same users in Twitter. Even though this multiplex network originally corresponds to a DUD configuration, we have also explored the other configurations, i.e., DDD, UDU and UUU. Note that in contrast with the synthetic networks studied in the previous section, in this network the layers have different average degrees. In particular, the FriendFeed layer has 4768 nodes and 29501 directed links, resulting in an average out-degree of 6.19, and the Twitter layer is composed by 4768 nodes and 40168 directed links, with an average out-degree of 8.42. Nevertheless, their degree distributions are both heavy tailed, although the maximum degree in the FriendFeed network is much larger than in the Twitter network [271]. The results, Fig. 2.17(B), confirm those findings for synthetic networks. In particular, for the range of γ under consideration, the configurations with some directionality are always more resilient against the disease. These results imply that information travels much more easily in undirected systems than in directed systems. To sum up, directionality has a positive impact on the system's resistance to disease propagation and that the way in which interdependent social networks are coupled could determine their ability to spread information. Furthermore, our results could be applied

to a plethora of systems and show that more emphasis should be put in studying the role of directionality in diffusion processes that take place on top of them.

2.4 Another Application of Compartmental Models

Norm violation versus punishment risk in a social model of corruption [272].

D. Lu, F. Bauza, D. Soriano-Paños, J. Gómez-Gardeñes, and L.M. Floría

There are a variety of applications for compartmental models besides epidemic modelling. Certainly, compartmental models are not only applied on analyzing the dynamics of disease spreading but also used to model social behaviors and information dissemination with more details taken into consideration.

In this work, we adopt the compartmental model to tackle the analysis of the *corruption behaviors*, a ubiquitous kind of social-norm-violating behaviors. The existence of social norms whose violation is socially agreed to deserve some punishment is perhaps one of the most widespread features across the history of human cultures and societies, to the point that its absence seems a most unexpected observation [273–276]. Not surprisingly, the conceptual frame of social norm (and its enforcement) is transversal across socio-economical disciplines, ranging from experimental (e.g., human behavior, experimental economy) to deeply theoretical (e.g., norms ancestry, their evolution and relation to modern social and political institutions) research [277–282].

Corruption, explicitly realized as bribery practices in public administration, has received academic attention in social and economical mathematical modeling research [282–289], a field of much recent interest for interdisciplinary physicists [290]. Most of literature is framed in either classical or evolutionary game theory, a modeling frame for tackling the analysis of corrupt behaviors which is clearly prevalent in modern theoretical economics, where, in brief, behaviors are formally represented by game's strategies, each earning a payoff, and economic behavior that optimizes benefit [291]. In the simplest game-theoretical settings, the *honest vs corrupt* behavioral dilemma is somewhat identified with the *cooperator vs defector* strategic dilemma. Nonetheless, the generalization to $n \geq 3$ strategies is needed if punishment (the hallmark of norm violation) to defectors has to be introduced in a stronger way than a mere fine to wrongdoers, such as a penalty in their benefit.

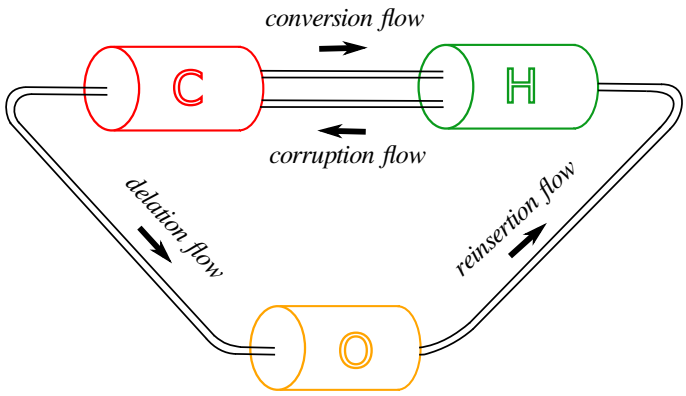

Figure 2.18: **Chart flow representation of the model.** Four flows between population compartments are possible. The flow $O \to H$ (reinsertion) occurs at a constant rate r. The flow $C \to H$ (conversion) is fueled by the perception of the delation risk that we simply quantify by $\langle o \rangle$. However, only pairwise social contacts $C \to H$ determine the other two flows, say, corruption flow at an infection rate f_{α}^{HC} and delation flow at a delation rate f_{β}^{CO}.

With this simple compartmental model [10, 292], the population is divided into three possible states, say, H (honest),C (corrupt), and O (out of society) with flows among them. In this setting, corrupt behavior is not assumed to be a greedy strategy in a population game dynamics but a simpler general formal entity, an infectious state, that nevertheless allows a game-theoretical perspective. This can be seen from the consideration that what makes a behavior spread socially to the point of becoming endemic is the likelihood it is copied, transmitted, imitated, or diffused following any game dynamics perspective [293, 294] that might be found more appropriated, e.g. adaptive, best response, evolutionary, etc.

These three "compartments" contains the corresponding fractions, say, $\langle h \rangle$, $\langle c \rangle$, and $\langle o \rangle$, in the population. In this work, we attempt to capture some essential ingredients such as the contagion of corrupt behaviors to honest agents, the delation of corrupt individuals by honest ones, and the warning to wrongdoers (fear like that triggers the conversion of corrupt people into honesty).

Let us start with formulating the sensible hypothesis on the population flows among compartments to complete the definition of the compartmental flow model. That means to postulate the microscopic dynamics. Our modeling assumptions are summarized in the next items, where general structured (in terms of social contacts) populations are being considered:

(*i*) Our first assumption is that corruption is a socially infective event: Honest individuals become corrupt *only* by infection from their corrupt neighbors, at an infection rate f_α^{HC}, that is a function of their local microstates. This assumption for the *corruption* flow, $H \to C$ formalizes the corrupt behavior as an infective state, a certainly simpler and less elaborate concept than that of a game strategy, without excluding its consideration, because it is the (social) infectious power of a strategy that allows its diffusion. It is this aspect of corrupt behavior that this assumption tries to capture in its simplest form.

(*ii*) We also assume that the flow $C \to O$ is *exclusively* the result of the delation of corrupt individuals by their honest neighbors, at a delation rate f_β^{CO}, also a function of their local microstates. Note that this flow is not the consequence of, e.g., administrative inspection or police investigation; Only interaction with honest agents is the source of this $C \to O$ flow that we call *delation* (or *punishment*) flow. Also note that from the honest agents perspective, delation is not optional. This avoid the need of introducing subtypes of agent states.

(*iii*) Our third assumption is that, at a given constant rate r, the O individuals are reinserted into social population as H individuals. The flow $O \to H$ is called *reinsertion* flow.

(*iv*) Finally, we consider a fourth flow, the *conversion* flow $C \to H$, which simply incorporates the warning-to-wrongdoers effect of social punishment. The rate at which this flow takes place is controlled by the social perception of risk to be delated, which we simply quantify as the fraction, $\langle o \rangle$, of population in the O compartment.

It is worth emphasizing that corruption and delation flows are the only ones that have their origin in the pairwise interactions among individuals of the socially active population. Both the reinsertion and conversion flows do not: individuals in the O state are socially inactive (i.e., noninteracting), and we only use its fraction (in the fourth assumption above, when implementing the warning-to-wrongdoers effect of social punishment) as the only available information for the estimation of the level of risk that corrupt people perceive. In other words, an O agent does not influence the eventual conversion of its corrupt neighbors more than it does on other far away corrupt agents. However, it is a sort of (temporary) hole in the network of contacts among agents. In Fig. 2.18 for a chart flow graphical representation of the model, where our assumptions for the flow between any two compartments are illustrated.

To seek for generality, we assume that the interactions (corruption and delation) among socially active agents define transition probabilities for the corresponding compartmental flows through some functions f_α (for corruption of a honest agent) and f_β (for the delation of a corrupt one), whose argument is the configuration of agent states in the local neighborhood of the focal agent i, say $\{\sigma_j(i)\}$, where σ_j $(j = 1, \ldots, k(i))$ denotes the state (H, C, or O) of the neighbor j of i, and $k(i)$ is the degree, i.e., the number of neighbors, of the focal agent i.

Due to our assumption on the corruption flow that it originates exclusively from interaction among individuals in different (H, C) states, the function $f_\alpha^{HC}(i, \{\sigma_j\})$, which gives the transition probability $H \to C$, has to satisfy:

$$f_\alpha^{HC}(i, \{\sigma_j\}) = 0 \;\text{ if }\; \sigma_j \neq C \;\text{ for all }\; j = 1, \ldots k(i)\,. \tag{2.123}$$

A similar consideration on the delation flow $C \to O$ leads to

$$f_\beta^{CO}(i, \{\sigma_j\}) = 0 \;\text{ if }\; \sigma_j \neq H \;\text{ for all }\; j = 1, \ldots k(i)\,. \tag{2.124}$$

In addition, for the sake of simplicity, we will use f_α and f_β for the notation of infection rate and delation rate instead of those with superscripts HC and CO later. A simple scheme for Monte Carlo discrete-time simulations of the dynamics (see section 2.1.3) is the following: At each time step (t), we choose uniformly at random an agent i. Then, we have the following:

(*i*) If $\sigma_i(t) = H$, then $\sigma_i(t+1) = C$ with probability f_α, a (yet unspecified) function of the local configuration around i. The agent remains honest with probability $1 - f_\alpha$.

(*ii*) If $\sigma_i(t) = C$, then $\sigma_i(t+1) = H$ (warning to wrongdoers effect) with probability $\langle o \rangle$, the fraction of population in O state. Then if not converted (probability $1 - \langle o \rangle$), the corrupt agents will be delated to O state with transition probability f_β, a (yet unspecified) function of the local configuration around i. Thus, agent i is still corrupt at $t + 1$ with probability $(1 - \langle o \rangle)(1 - f_\beta)$.

Note that an equally acceptable scheme would try first delation, then conversion, which produces different transition probabilities for $C \to H$ and $C \to O$. We will comment on this later on.

(*iii*) If $\sigma_i(t) = O$, then $\sigma_i(t+1) = H$ with conditional probability r, remaining out with probability $1 - r$.

One can associate to this dynamics on agents' state configurations, a non linear Markov process in the following way [110, 111]. Assign to each agent i, and at time t, a real vector $\vec{\rho}(i;t)$ whose components are the probabilities (at time t) that the agent is in each of the possible states, namely $\rho_h(i;t)$, $\rho_c(i;t)$, $\rho_o(i,t)$. The transition probabilities (i)-(iii) introduced above define a non-linear Markov process for the time evolution of these probabilities $\vec{\rho}(i;t+1) = \mathbf{Q}\ \vec{\rho}(i;t)$, where

$$\begin{bmatrix} 1-f_\alpha & \langle\rho_o\rangle & r \\ f_\alpha & (1-f_\beta)(1-\langle\rho_o\rangle) & 0 \\ 0 & f_\beta(1-\langle\rho_o\rangle) & 1-r \end{bmatrix}$$

is the matrix representation of $\mathbf{Q}$, and $\langle\rho_o\rangle$ is the fraction of population in O state, i.e.

$$\langle\rho_o\rangle = N^{-1}\sum_i \rho_o(i)\ . \tag{2.125}$$

Note our choice of relative order of trial, conversion *before* eventual delation, in the second column of the matrix $\mathbf{Q}$ above written. The alternative choice would correspond to $\mathbf{Q}_{hc} = (1-f_\beta)\langle\rho_o\rangle$ (instead of $\langle\rho_o\rangle$) and $\mathbf{Q}_{oc} = f_\beta$ (instead of $f_\beta(1-\langle\rho_o\rangle)$), the rest of elements being unchanged.

To complete the model formal setting, one has to specify the functions f_α and f_β, for the conditional probabilities of corruption and delation, respectively. They define the specific social interactions postulated, and also incorporate the information on the social network, that we assume it is encoded in the *neighborhood* matrix, whose i-th row tells us who the $k(i)$ neighbors of the agent i are. The following choice mimics the familiar implementation of infective interactions in Monte-Carlo simulations on compartmental epidemic models as SIS, SIR, etc.:

$$f_\alpha(i,\{\sigma_j\}) = 1 - \prod_{j=1}^{k(i)}(1-\alpha\delta_{\sigma_j,C})\ , \tag{2.126}$$

$$f_\beta(i,\{\sigma_j\}) = 1 - \prod_{j=1}^{k(i)}(1-\beta\delta_{\sigma_j,H})\ , \tag{2.127}$$

where $\delta_{x,y}$ is the Kronecker's delta. The rationale for (2.126) is that a honest focal agent contacts all its corrupt neighbors, and in each one of these contacts, the probability of infection is α. Similarly, for (2.127) a corrupt focal

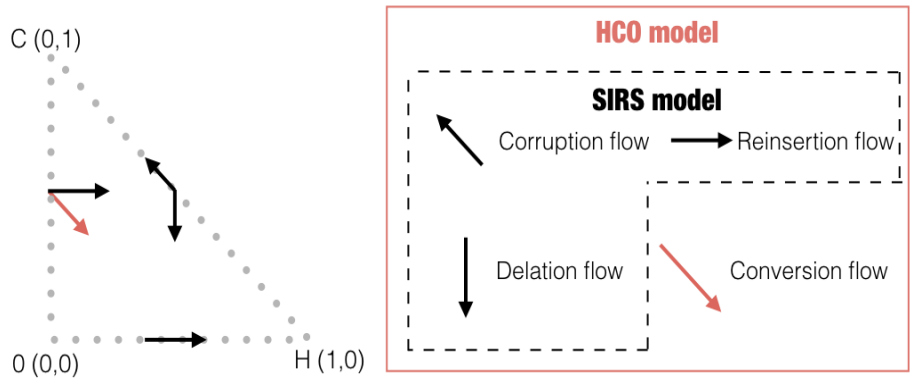

Figure 2.19: **Schematic visualization of the simplex $\mathcal{S}_2$ and flows directions.** The directions of the contributions in the simplex $\mathcal{S}_2$ (left panel) for each of the four compartmental flows to the (flow vector) $\vec{F}$ field is shown in right panel. The arrows on the face boundaries of the simplex visualize that there is no flow outwards, and thus the simplex is an invariant set, as required by consistency. If one excludes the conversion flow, the model (HCO) becomes a (non-standard) version of the epidemic SIRS model.

agent contacts all its honest neighbors, and in each contact is delated with probability β.

For the associated Markov process of an honest agent i, the transition probability, f_α is related to the current probability of its neighbours $j \in [1, k(i)]$ who are in the corrupt state, i.e., $\rho_c(j)$. Similarly, the other transition probability f_β is transformed according to the previous definition. Therefore, Eqs. 2.126 and 2.127 translate into

$$f_\alpha(i, \{\vec{\rho}(j)\}) = 1 - \prod_{j=1}^{k(i)} (1 - \alpha \rho_c(j)) \ , \tag{2.128}$$

$$f_\beta(i, \{\vec{\rho}(j)\}) = 1 - \prod_{j=1}^{k(i)} (1 - \beta \rho_h(j)) \ . \tag{2.129}$$

Although in the computations shown below we have used these specific forms for f_α and f_β, other alternative forms, based on some different corruption and delation schemes are, no doubt, of potential interest. The microscopic mechanisms of "becoming corrupt" should inform the appropriate functional form of f_α, as much as those of "delating corrupts" must inform that of f_β.

For the choice made in equations (2.126,2.127), or (2.128,2.129), and if the conversion flow channel is suppressed (see Fig. 2.19 and section 2.4.2 be-

low), the model admits to be interpreted (by the identifications $S \equiv H$, $I \equiv C$, $R \equiv O$) as a kind of SIRS model where the recovery rate is mediated by the interaction of the susceptible neighbors with the infected agent, as if the recovery from infection would crucially depend on the assistance from healthy neighbors [295].

2.4.1 Analysis under mean-field approximation

In the language of population dynamics, well-mixed population approximation is the usual term employed for revealing the basic mechanism of the corruption dynamics. In the corruption model, homogeneity of both field (agent state; H, C or O), and structure of contacts (environment) is the essential assumption of a mean-field (MF) approximation.

1. ***Mean-field dynamics***

If every agent behaves as the average of all ("average" agent), i.e.: $\vec{\rho}(i) = \langle\vec{\rho}\rangle$ (for all i) for the associated Markov process, and the neighborhood of size $k(i) = k$ is "indifferent" regarding i, so that it can be selected at random among the population at each time step (well-mixed population assumption), one arrives to the following mean field discrete time evolution equations for the probabilities ρ_h, ρ_c, ρ_o (or alternatively, for the compartmental fractions ($\langle h\rangle$, $\langle c\rangle$, and $\langle o\rangle$)):

$$\vec{\rho}(t+1) = \begin{pmatrix} 1-f_\alpha & \rho_o & r \\ f_\alpha & (1-f_\beta)(1-\rho_o) & 0 \\ 0 & f_\beta(1-\rho_o) & 1-r \end{pmatrix} \vec{\rho}(t) \ ,$$

where suitable changes (see paragraph just below equation (2.125)) in the second column of the matrix have to be made for a different order of "trial for flow" out from the C compartment.

Due to the normalization constraint, $\rho_h + \rho_c + \rho_o = 1$, the mean field discrete time dynamics is a non linear two-dimensional map of the simplex $\mathcal{S}_2$ (i.e., $0 \leq \rho_h, \rho_c \leq 1$, $\rho_h + \rho_c \leq 1$) onto itself. This simplex is visualized on the left panel of Fig. 2.19, as the triangle defined by the vertices ($H \equiv (1,0), C \equiv (0,1), O \equiv (0,0)$), in the (ρ_h, ρ_c) plane (say, $\rho_h = 1$, $\rho_c = 1$, $\rho_o = 1$, respectively).

The associated two-dimensional flow (continuous time dynamics) is defined by the velocity (2d vector) field on the simplex $\vec{F}(\vec{\rho})$,

$$\vec{F}(\vec{\rho}) = \dot{\vec{\rho}}$$

whose components are:

$$F_h(\vec{\rho}) = -(f_\alpha + r + \rho_c)\rho_h + (r + \rho_c)(1 - \rho_c)$$
$$F_c(\vec{\rho}) = (f_\alpha + (1 - f_\beta)\rho_c)\rho_h + ((1 - f_\beta)\rho_c - 1)\rho_c \quad (2.130)$$

In the right panel of Fig. 2.19, we indicate the direction of the contribution to the total flow vector field on the plane (ρ_h, ρ_c) of each of the four compartmental flows. The preliminary step of the analysis is to check that the simplex is an invariant set of initial conditions, as obviously required by consistency. Indeed, see left panel of Fig. 2.19, one easily realizes that

(i) On the hypothenuse of the simplex, where $\rho_h + \rho_c = 1$, both the reinsertion and the conversion flow are null ($\rho_o = 0$); the corruption flow is co-linear to this boundary, and the delation flow points vertically inwards.

(ii) On the vertical (ρ_c)-axis, where $\rho_h = 0$, both the delation and the corruption flows are null; both the non-zero remaining flows point inwards.

(iii) On the horizontal axis, where there are no corrupt people, only reinsertion flow is non-zero, which is co-linear to this boundary, and points towards the full honesty corner of the simplex, with the proviso that $r > 0$, the generic case.

From now on in this section we will consider the generic case ($r > 0$) where reinsertion flow does not vanish. Also, we restrict the analysis to one-dimensional functions $f_\alpha(\rho_c)$ and $f_\beta(\rho_h)$. This simplifying restriction amounts to saying that, e.g. the probability that a honest agent becomes corrupt at time t only depends on the agent contacts with corrupt agents, and its contact with others have no influence on its corruption.

It is important to realize that a direct consequence of the model assumptions, namely that infection and delation flows originate *exclusively from* agent interactions, is that the functions f_α and f_β have to be such that $f_\alpha(\rho_c = 0) = 0$ (i.e., no corruption flow without corrupt agents) and $f_\beta(\rho_h = 0) = 0$ (no delation flow without delators). Indeed this has been implicitly used in the previous simple vector field analysis, when we considered in item (ii) above that delation flow was null when $\rho_h = 0$, and in item (iii) that corruption flow vanished at $\rho_c = 0$.

Now we look for possible existence of boundary fixed points. From the previous analysis, they can only be located at corners. While $\rho_o = 1$ (i.e. $(\rho_h = 0, \rho_c = 0)$, the origin), is a fixed point only in the limit $r \to 0$, when reinsertion

flow vanishes, the two other corners of the simplex, say *full honesty* ($\rho_h = 1$), and *total corruption* ($\rho_c = 1$), are always fixed points of this dynamics (i.e.: zeroes of the field $\vec{F}(\vec{\rho})$), irrespective of the parameter values. These are the only fixed points on the simplex boundary.

Let us now analyze, in the linear regime of perturbations, the stability of these corner fixed points, by looking at the "restoring forces (flows)" induced by perturbations.

$\rho_h = 1$: The full honesty corner H, provided $r > 0$, is clearly stable against a small increase, $\delta\rho_o$, in the population fraction of O compartment, for it just induces a (stabilizing) reinsertion flow. However, a small perturbation $\delta\rho_c$ generates an infection flow $f_\alpha(\delta\rho_c) \simeq f'_\alpha(0)\delta\rho_c$, which unless overcome by the (also induced by perturbation) delation flow $f_\beta(1)\delta\rho_c$, would render unstable the full honesty state. In other words, the full honesty state is a *local attractor* of (nearby) trajectories provided the following stability condition holds:

$$f'_\alpha(0) < f_\beta(1) \; . \tag{2.131}$$

Note that the rate r of reinsertion has no influence on this stability condition. Only the balance among corruption and delation flows determines the instability of the full honesty state, because inactivity ($\delta\rho_o$) fluctuations induce restoring flow, and have no linear effects on the instability driving this *corruption* transition.

$\rho_c = 1$: Regarding the full corruption corner, also for $r > 0$, a small perturbation of component $\delta\rho_h$ generates a restoring corruption flow $f_\alpha(1)\delta\rho_h$, which, to keep this fixed point stable, has to overcompensate the sum of the (destabilizing) delation flow $f_\beta(\delta\rho_h) \simeq f'_\beta(0)\delta\rho_h$, and conversion flow $\delta\rho_o \times 1 \simeq f_\beta(\delta\rho_h)/r$, generated by perturbation. Thus, the linear stability condition for the total corruption is

$$\left(1 + \frac{1}{r}\right) f'_\beta(0) < f_\alpha(1) \; . \tag{2.132}$$

Note that now, the balance corruption/delation is interfered by the influence of ρ_o, which helps small honest fluctuations to further develop. We see that the stability condition of the full corruption state depends on the rate r of reinsertion, via the conversion flow induced by linear perturbation, and then this *honesty* transition is not exclusively driven

by agent-agent interactions, but also by the (self-consistent, global field) value of the fraction of agents in O state.

Here, we use a linear approximation to the competing flows that a generic small fluctuation induces, i.e., by analyzing the linear response to generic fluctuations. In general systems of differential equations this physically appealing approach is rarely doable in such a simple way. A more formal, and easier to generalize, method of analysis of a fixed point is provided by the spectral analysis (eigenvalues and its associated eigen-subspaces) of the Jacobian matrix of the flow at this invariant point. This matrix is the linearized flow in the tangent space of the fixed point. We will use it here to show that both transitions, corruption and honesty, are unaffected if the relative order or priority of channels (delation and conversion) flowing out from the C compartment is reversed.

In the channels' priority scheme used before, the trial for conversion is prior to delation, where from the velocity field, $\vec{F}(\vec{\rho}) = \dot{\vec{\rho}}$, is given by equations (2.130), while if conversion is conditional on evading delation, the corresponding equations of motion are slightly different:

$$\begin{aligned} \dot{\rho}_h = &- (f_\alpha + r + (1 - f_\beta)\rho_c)\rho_h \\ &+ (r + (1 - f_\beta)\rho_c)(1 - \rho_c) \\ \dot{\rho}_c = &(f_\alpha + (1 - f_\beta)\rho_c)\rho_h + ((1 - f_\beta)\rho_c - 1)\rho_c \end{aligned} \tag{2.133}$$

The Jacobian matrix, at a point (ρ_h, ρ_c) in phase space is defined as

$$J(\rho_h, \rho_c) = \begin{pmatrix} \frac{\partial \dot{\rho}_h(\rho_h,\rho_c)}{\partial \rho_h} & \frac{\partial \dot{\rho}_h(\rho_h,\rho_c)}{\partial \rho_c} \\ \frac{\partial \dot{\rho}_c(\rho_h,\rho_c)}{\partial \rho_h} & \frac{\partial \dot{\rho}_c(\rho_h,\rho_c)}{\partial \rho_c} \end{pmatrix} . \tag{2.134}$$

Though at an arbitrary point of the simplex the Jacobian matrices of the flows (2.130) and (2.133) are generally different, a direct calculation shows that at the full honesty corner, ($\rho_h = 1$, $\rho_c = 0$), both are equal:

$$J_H = \begin{pmatrix} -r & -r - f'_\alpha(0) \\ 0 & f'_\alpha(0) - f_\beta(1) \end{pmatrix} .$$

Being this matrix triangular, the eigenvalues are just the diagonal elements, $\lambda_1^H = -r$, and $\lambda_2^H = f'_\alpha(0) - f_\beta(1)$. The H corner is stable whenever both eigenvalues are negative, thus requiring the inequality $f'_\alpha(0) < f_\beta(1)$, as we already know.

At the full corruption corner, the Jacobian matrices of the flows (2.130) and (2.133) are also equal:

$$J_C = \begin{pmatrix} -r-1-f_\alpha(1) & -r-1 \\ f_\alpha + 1 - f'_\beta & 1 \end{pmatrix}.$$

The eigenvalues of J_C are the roots of the characteristic polynomial $\lambda^2 - \lambda T + D$, where $T = \mathrm{Tr}(J_C)$, and $D = \mathrm{Det}(J_C)$ are respectively the trace and the determinant of the Jacobian matrix, explicitly given by

$$T = -r - f_\alpha(1) < 0\ , \quad D = r f_\alpha(1) - (r+1) f'_\beta(0)\ . \tag{2.135}$$

Thus, the stability of the fully corrupt state requires that $D > 0$, that is

$$\left(1 + \frac{1}{r}\right) f'_\beta(0) < f_\alpha(1)\ .$$

We should note that the irrelevance of the priority of channels out from C regarding the onset of stability of both, H and C, corners, by no means imply that in the parameter region where the attractor is an interior point of the simplex, this mixed population state is unaffected by the chosen priority; our numerical investigations clearly show that the surfaces of asymptotic equilibrium, $\vec{\rho}(\alpha, \beta, r)$ are (in general, slightly) different for different choices.

In the final stage of our search for absorbing states of the dynamics, we pay attention to the $\vec{F}$ field nulclines, i.e. the loci where each of its components vanishes, $F_h(\vec{\rho}) = 0$ and $F_c(\vec{\rho}) = 0$, given explicitly by equations (2.130). An interior fixed point will exist whenever these loci intersect in the interior of the simplex.

$F_h = 0$: The equation of the F_h nulcline is

$$-(f_\alpha + r + \rho_c)\rho_h + (r + \rho_c)(1 - \rho_c) = 0\ . \tag{2.136}$$

Note, in the first place, that this locus is independent of f_β, because the delation flow leaves ρ_h unchanged; next, one quickly convinces oneself that it contains both C and H corners. Finally, one realizes that, provided f_α is independent of ρ_h, equation (2.136) defines, inside the simplex, a unique function $\rho_c(\rho_h)$ whose graph joins those corners.

$F_c = 0$: The F_c nulcline satisfies the following equation

$$(f_\alpha + (1 - f_\beta)\rho_c)\rho_h + ((1 - f_\beta)\rho_c - 1)\rho_c = 0\ . \tag{2.137}$$

One easily realizes that the horizontal axis, $\rho_c = 0$ belongs to this set. This is one of the (curve, in general) branches that are solutions of this nonlinear implicit equation. The rest of them must solve for the equation obtained by dividing (2.137) by ρ_c:

$$(f_\alpha/\rho_c + (1 - f_\beta))\rho_h + ((1 - f_\beta)\rho_c - 1) = 0 \; . \tag{2.138}$$

It is also straightforward to check that the C corner always belongs to some of these branches. Another simple general result is the following. There is always one of these branches that crosses the horizontal axis. The argument is simple if one assumes that f_α is an analytic function of ρ_c at 0^+. By keeping second order terms in the power expansion of $f_\alpha(\rho_c) \simeq f'_\alpha(0)\rho_c + (1/2)f''_\alpha(0)\rho_c^2$, one obtains the following (nonlinear) approximation to the solution of (2.137) close to the horizontal axis:

$$\rho_c = \frac{1 - (f'_\alpha(0) + 1 - f_\beta)\rho_h}{1 - f_\beta + (1/2)f''_\alpha(0)\rho_h} \; , \tag{2.139}$$

which intersects $\rho_c = 0$ at the abscissa value $\rho_h = \rho_h^*$, the solution of the nonlinear equation

$$(f'_\alpha(0) + 1 - f_\beta(\rho_h^*))\rho_h^* = 1 \; . \tag{2.140}$$

Whether the curve branch of the F_c nulcline that intersects the horizontal axis at ρ_h^* is the same one that passes through the C corner, or it is a different branch, both are possible situations (conditional to the specific functions f_α and f_β). In fact, we will show numerical examples of both situations below, for a single one-parametric functional form of them (equations (2.143,2.144) below).

The stability of the states of full honesty and full corruption is closely tied to the nulclines' geometrical configuration around them. Indeed, using (2.131) we easily conclude that the stability condition of the full honesty corner is equivalently expressed as "ρ_h^* is not in the simplex", where ρ_h^* is the intersection of the curve branch of the F_c nulcline with the horizontal axis, defined by (2.140) above.

$$H \text{ corner is unstable } \equiv \; \rho_h^* < 1 \; , \tag{2.141}$$

that is to say, the difference in relative position of F_h and F_c nulclines (from the fixed point perspective) determines the stability of the full honesty state.

In a similar, though geometrically very different, way one can see that if the slope of the curve branch of the F_c nulcline at the C corner is lower than

the slope of the F_h nulcline, i.e.

$$1 + f_\alpha(1) - f'_\beta(0) > 1 + \frac{f_\alpha(1)}{1+r}\,, \tag{2.142}$$

then the C corner is stable, see equation (2.132), and viceversa. Again, the change of the relative position of nulclines at C marks the instability of the full corruption state.

In the next subsection we show numerical and analytical results for the phase portraits and phase diagrams, for the particular choice, inspired by epidemic analogy, that we made above for the flows originated from social interactions $C-H$ (2.126,2.127,2.128,2.129); the expressions for the conditional probabilities f_α and f_β in the mean field approximation are:

$$f_\alpha(k,\vec{\rho}) = 1 - (1-\alpha\rho_c)^k, \tag{2.143}$$

$$f_\beta(k,\vec{\rho}) = 1 - (1-\beta\rho_h)^k\,. \tag{2.144}$$

It should be kept in mind the "epidemic", or "contact interaction", character of this choice for both transition probabilities, corruption and delation. On one hand, the knowledge from closely related epidemic models can be capitalized on here, while on the other, the results that we analyze could plausibly be of use in some epidemiology contexts of potential interest, wherever recovery needs assistance from susceptible neighbors.

2. ***Mean field phase portraits and diagrams***

For the particular *contact interaction* functions (2.143,2.144), the instability of the full honesty state, from equation (2.131), occurs at the value of the (infection) corruption rate α_c:

$$\alpha_c(\beta) = \frac{1-(1-\beta)^k}{k}, \tag{2.145}$$

for all values of the reinsertion rate r (i.e., it is independent of this parameter value). This value of the infectivity power of corruption is the benchmark for the appearance of observable corruption, under the mean field, well-mixed population, assumptions. Also, from equation (2.132), the instability of the state of full corruption occurs at a value β_c of the delation rate given by

$$\beta_c(\alpha) = \left(\frac{r}{1+r}\right)\frac{1-(1-\alpha)^k}{k}. \tag{2.146}$$

From (2.145) and (2.146), it is easily seen that the stability regions, in the (α,β) parameter plane, of corner fixed points (H and C) do not overlap,

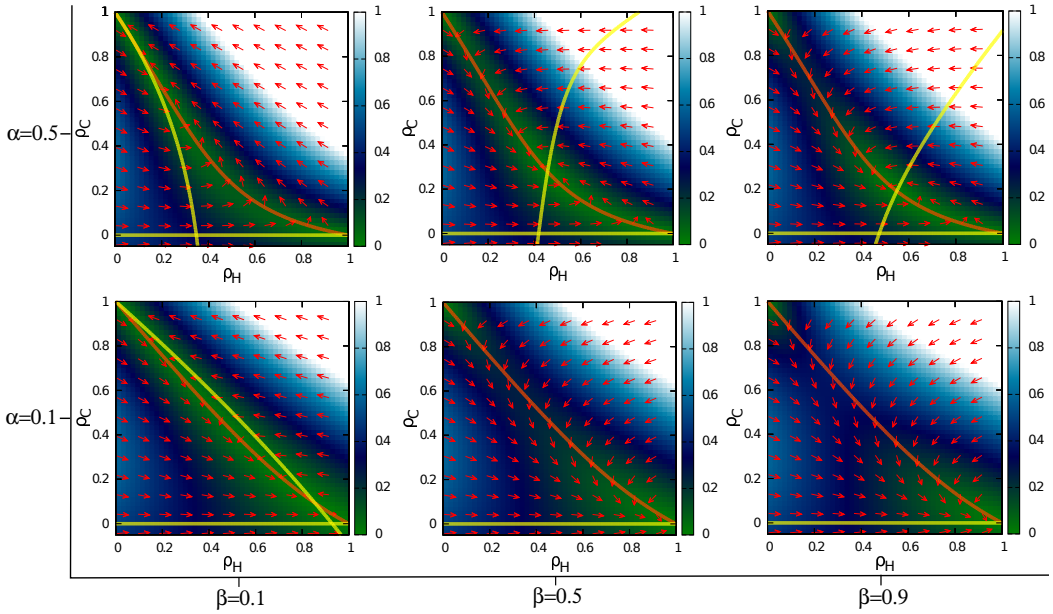

FIGURE 2.20: **The nullclines $F_h = 0$ (red line) and $F_c = 0$ (yellow line) with $r = 0.5$.** The infection rate is given as $\alpha = 0.1, 0.5$. The delation rate is set as $\beta = 0.1, 0.5, 0.9$. In each of plane, color level used to represent the numerical value of the flow.

meaning that there is neither bi-stability region in the phase diagram of the model, nor hysteresis behavior. In other words, no discontinuous change full C - full H can occur by tuning a model parameter, for our choices (2.143) and (2.144) of f_α and f_β. In the region of the parameter plane (α, β) where both fixed points are unstable, an interior (stable) fixed point $\vec{\rho}(r, \alpha, \beta)$ is the unique global attractor of phase space flow. By no means this conclusion is forcefully valid for more general choices of the corruption, f_α, and delation, f_β, transition probability functions, for multiple interior nulclines crossing cannot be discarded in general cases.

In Fig. 2.20, we show the phase portraits for a reinsertion rate $r = 0.5$, and values of $\alpha = 0.1, 0.5$, and $\beta = 0.1, 0.5, 0.9$. Arrows indicate the local direction of the $\vec{F}$ field, the flow, while its modulus is color encoded. The F_h nulclines are plotted in red color; one sees that they are independent of β, and that they deviate away from the simplex hypothenuse for increasing values of α.

The branches of the F_c nulclines are plotted as yellow lines. Note that the horizontal axis is always one of them. When no other branch is visible (as for $\alpha = 0.1$ and $\beta = 0.5, 0.9$), meaning that $\rho_h^* > 1$, the full honesty state H is stable, and it is the global attractor. For the other cases shown in Fig.

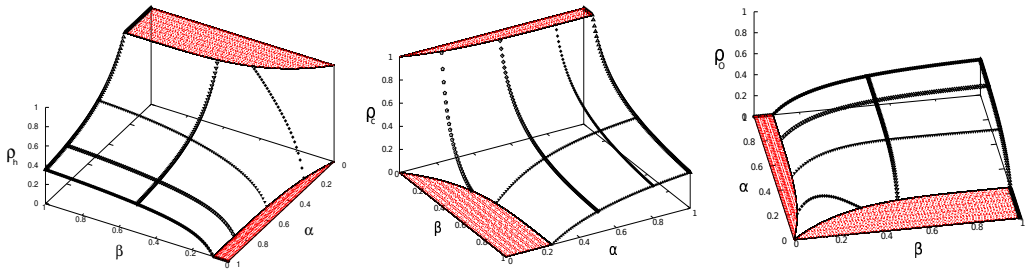

FIGURE 2.21: **Visualizations of the equilibrium surfaces.** We plot surfaces $\rho_m(\alpha, \beta, r = 0.5)$, $m = h, c, o$, on the (α, β) parameter plane with a constant value of the reinsertion rate $r = 0.5$. The sections of these surfaces at cutting planes corresponding to values of $\alpha = 0.2, 0.5, 0.8, 1$ and $\beta = 0.5, 1.$, are also plotted to help a three-dimensional mental image. The stability regions of full C and full H states are red colored.

2.20, the trajectories evolve asymptotically to the interior fixed point where the F_h nulcline and a curve branch of the F_c nulcline intersect. While for $\beta = 0.1$ and $\alpha = 0.1, 0.5$ the yellow curve passes through the full corruption corner, for $\alpha = 0.5$ and $\beta = 0.5, 0.9$ it does not. In these cases, there is a different curve branch of the F_c nulcline, passing through the C corner, from outside the simplex. The transition between these two qualitatively different phase portraits of the entire plane (ρ_h, ρ_c) occurs when the two yellow curve branches "anti-cross" far outside the simplex; this is a bifurcation on the whole plane phase portrait which has no qualitative effects (no local influence) on the interior of the simplex.

In the three panels of Fig. 2.21 we try to summarize the effect of parametric variation of α and β (in the mean field dynamics) on the mixed population absorbing state, through perspective visualizations of the compartmental fractions at the equilibrium (attractor) for a fixed arbitrary value of $r = 0.5$, i.e., of the surfaces $\vec{\rho}(\alpha, \beta, r = 0.5)$ of the asymptotic equilibrium. The regions colored in red in the three panels of this figure correspond to the respective regions of stability of the full honesty ($\alpha \leq \alpha_c(\beta)$) and full corruption ($\beta \leq \beta_c(\alpha)$) absorbing states, where the transition lines are given by (2.145) and (2.146). We hope that the simple inspection of this figure is more informative than lengthy and wordy explanations of the general trends of the model behavior.

2.4.2 Comparison with a SIRS-type model

Here, leaving aside the fourth of model assumptions we proposed before, we will take out from the model the conversion flow (warning to wrongdoers

effect). The number of flow channels is thus reduced from four to three (contagion, delation and reinsertion), and thus the "flow chart" between the three compartments is now that of a SIRS model, with the identifications $S \equiv H$, $I \equiv C$, and $R \equiv O$.

While in the standard SIRS model the rate of recovery ($I \to R$) is a constant, in this variant of the SIRS model the recovery of an infected individual is only possible through contact interaction with its susceptible neighbors. A plausible epidemic situation leading to it, may be e.g., one in which the recovery from disease requires, *sine qua non*, imperatively the assistance (care) from relatives [295]. Though the consideration made above may certainly add some interest in the following results by themselves in plausible epidemic contexts, our main purpose in this subsection is to make a precise assessment on the warning to wrongdoers effect in the HCO model, by revealing the aspects on which its presence makes a difference, and how much this difference amounts to.

The mean field analysis goes along the same lines as explained previously, and one arrives to the following 2d flow on the simplex:

$$\begin{aligned} F_h(\vec{\rho}) &= -(f_\alpha + r)\rho_h + r(1-\rho_c) \\ F_c(\vec{\rho}) &= f_\alpha \rho_h - f_\beta \rho_c \end{aligned} \tag{2.147}$$

Both $\rho_h = 1$ and $\rho_c = 1$ corners are fixed points, whose linear stability analysis we now summarize. The stability condition for the full honesty corner is the same as it was in the presence of "warning to wrongdoer" (conversion flow):

$$f'_\alpha(0) < f_\beta(1). \tag{2.148}$$

This is an expected result, because we already saw previously that the conversion flow has no influence on this transition, which is only determined by the competition of corruption and delation flows generated by linear perturbations.

On the other hand, now the stability condition of the total corruption state no longer depends on the reinsertion rate r:

$$f'_\beta(0) < f_\alpha(1). \tag{2.149}$$

The stability of both homogeneous population states is unaffected by the value of the reinsertion ($R \to S$) rate in this SIRS model. In other words, the rate r of reinsertion is an irrelevant parameter regarding both, corruption and honesty, transitions.

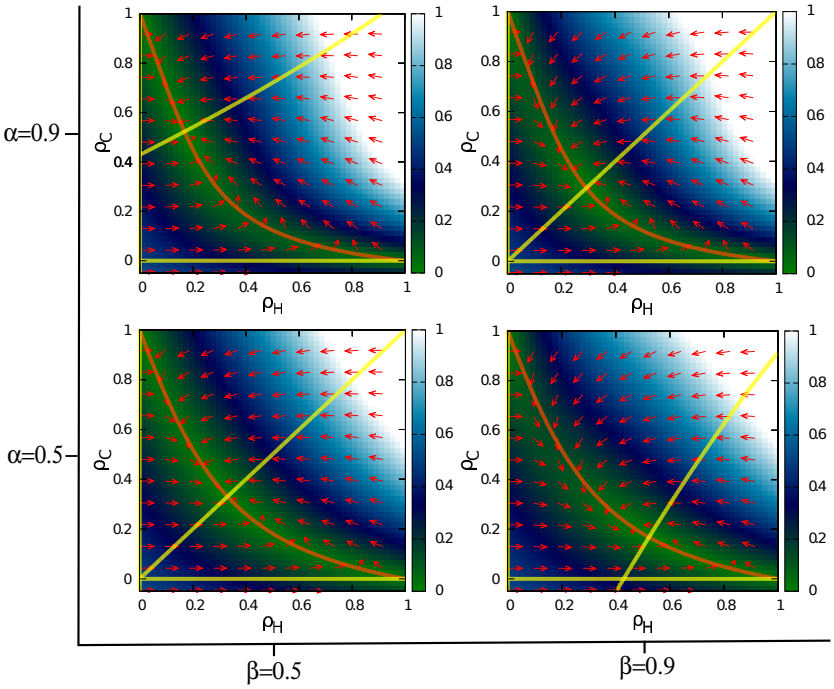

FIGURE 2.22: **The nullclines $F_h = 0$ (red line) and $F_c = 0$ (yellow line) with $r = 0.5$ in the SIRS model.** The infection rate is given as $\alpha = 0.5, 0.9$, while the delation rate is $\beta = 0.5, 0.9$.

We first pay attention to the nulclines (see Fig. 2.22 for examples). The F_h nulcline connects the corners C and H, is independent of f_β. Indeed, it is qualitatively very similar to that of the HCO model. On the contrary, the F_c nulcline (whose relevant branches are plotted as yellow lines in Fig. 2.22) shows important differences. The equation of this nulcline is

$$f_\beta \rho_c = f_\alpha \rho_h \,. \tag{2.150}$$

Two branches of this nulcline are easily obtained, namely $\rho_c = 0$ (horizontal axis) and $\rho_h = 0$ (vertical axis). Note that the latter is incompatible with the warning to wrongdoers (or conversion) flow, and thus it is absent in the HCO model. The rest of branches of this nulcline must solve for the equation

$$\frac{f_\beta}{\rho_h} = \frac{f_\alpha}{\rho_c} \,. \tag{2.151}$$

For the infective type of f_α and f_β functions in Eqs. (2.143) and (2.144), this equation has a useful symmetry: It is invariant under the simultaneous

interchange $\alpha \leftrightarrow \beta$ and $\rho_c \leftrightarrow \rho_h$. This symmetry of the F_c nulcline is illustrated in Fig. 2.22. A simple consequence of this symmetry is that if $\alpha = \beta$, then the F_c nulcline is $\rho_c = \rho_h$, the main diagonal. Furthermore, $\rho_h \leq \rho_c$ if and only if $\beta \leq \alpha$. We will later on discuss some other features of the model that are associated to this symmetry.

After (2.149) and (2.148), the transition lines, $\beta_c(\alpha)$ and $\alpha_c(\beta)$

$$\alpha_c(\beta) = \frac{1-(1-\beta)^k}{k} \tag{2.152}$$

$$\beta_c(\alpha) = \frac{1-(1-\alpha)^k}{k} \tag{2.153}$$

are mirror symmetric around the line $\alpha = \beta$ in the (α, β) plane, and as we already remarked, they do not change with the value of r. However, when the attractor is an interior point of the simplex, and thus the flow through the three channels is, at equilibrium, the same:

$$f_\beta \rho_c = r\rho_o = f_\alpha \rho_h \ , \tag{2.154}$$

the reinsertion flow rate r regulates the $S - I$ $(H - C)$ balance. In particular:

- For $r = 1$, meaning that the recovery time is just one time step (the shortest possible time scale), we are as closer as the model can be to the limit of zero (instantaneous) recovery time.

  In the strict instantaneous recovery limit the $R \equiv O$ state ceases to exist, it just disappears; the feasible region is in this limit case reduced to the hypothenuse ($\rho_o = 0$) of the simplex, and the model becomes a variant of the (kinetic two-states) SIS model, with $I \to S$ rate mediated by S. For our choice of the functions f_α and f_β there is now a strict symmetry of the dynamics (equations of motion) under simultaneous interchange of parameters $\alpha \leftrightarrow \beta$ and labels $h \leftrightarrow c$. Note that though the existence of R (O) state breaks this symmetry, the broken symmetry is still manifest in the F_c nullcline symmetry discussed above. However, even when recovery takes just one step of time, the instantaneous fraction ρ_o of inactive individuals does not affect infected (do not delate corrupt) neighbors, and the balance infection-recovery is biased towards infection.

- For $1 > r > 0$, the larger the characteristic stay time, $1/r$, at the O state the easier the infective state can spread.

- For $r = 0$ the model becomes a variant of the SIR model.

We conclude that the reinsertion rate r, though being irrelevant regarding the onset of instabilities that operate at both, *corruption* and *honesty*, transitions, is a determinant factor regarding the stationary values of the compartmental fractions of the SIRS model when the dynamic equilibrium is a mixed population macro-state. Finally, we pay now a closer attention to the symmetry that a unique choice of the functional form for the corruption and delation transition probabilities, f_α and f_β, induces on this version of the SIRS model: if one assumes that both transition probabilities are given by a unique function $g(x,z)$ in the sense that $f_\alpha(\rho_c) = g(\alpha,\rho_c)$ and $f_\beta(\rho_h) = g(\beta,\rho_h)$, a general simple argument concludes that in the mixed population stationary state regime of this model, the fractions (ρ_h,ρ_c) of corrupt and honest people are such that

$$\rho_c(\alpha,\beta) = \rho_h(\beta,\alpha) \;\text{ and }\; \rho_h(\alpha,\beta) = \rho_c(\beta,\alpha)\ , \tag{2.155}$$

in other words, the *equation of stationary state* $\vec{\rho}(\alpha,\beta)$ is symmetric under the simultaneous interchange $\alpha \leftrightarrow \beta$ and $\rho_c \leftrightarrow \rho_h$. This might be at a first sight unexpected, because the equations of motion, and then the phase portraits (see Fig. 2.22), are by no means invariant. In the extent that there is no fundamental reason why delation and corruption transition probabilities should be described by the same function, this is an accidental (non-fundamental) symmetry. As already stated, both models, HCO and SIRS, exhibit the same *corruption* transition lines:

$$\alpha_c^{HCO}(\beta) = \alpha_c^{SIRS}(\beta)\ , \tag{2.156}$$

for all values of β, because the conversion flow has no influence on the onset of corruptive fluctuations. On the contrary, honest instabilities in the full C state are enhanced by the warning to wrongdoers, thus shrinking the full C stability region, see (2.146) and (2.153), in the HCO model:

$$\beta_c^{HCO}(\alpha) < \beta_c^{SIRS}(\alpha)\ , \tag{2.157}$$

for all values of $\alpha > 0$.

As expected, removing the conversion flow closes an input channel of the H compartment, and favors higher levels of corruption, thus leading to a decrease of the fraction of honest agents in the SIRS model with respect to the HCO model.

For a comparison of both models in their mixed population equilibria regimes, we show in Fig. 2.23 the mean field predictions for the fraction of corrupt agents ρ_c. The upper panels on this figure show the graphs of $\rho_c(\alpha)$ at

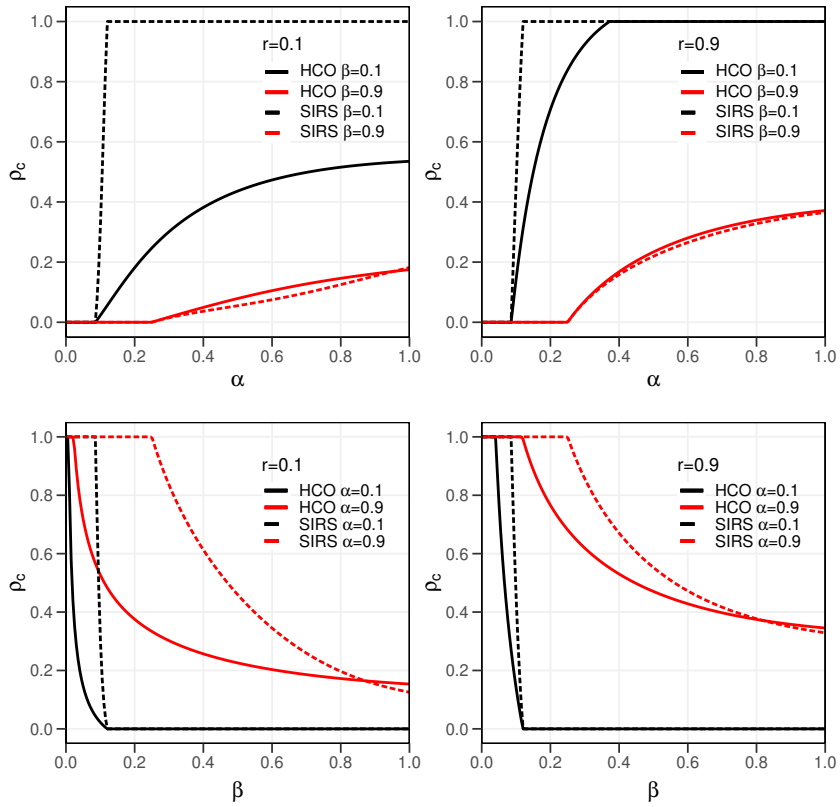

Figure 2.23: **Fraction of C agents as a function of α and β.** Top: Fraction of corrupt agents as a function of the corruption rate $\rho_c(\alpha)$ fixing the delation rate to $\beta = 0.1$ and $\beta = 0.9$. Bottom: $\rho_c(\beta)$ for $\alpha = 0.1$ and $\alpha = 0.9$. The mean field predictions for SIRS model are represented with dashed lines whereas solid lines correspond to the HCO model. The reinsertion rate is fixed to $r = 0.1$ (Left panels) and $r = 0.9$ (Right panels).

several fixed values of β $(0.1, 0.9)$ and r $(0.1, 0.9)$. Beyond the transition point α_c, one could intuitively expect that the fraction of corrupt agents is always higher for the SIRS model due to the lack of the conversion flow forcing corrupt agents to recover honesty. This holds for low β values since the evolution of corruption is clearly much more boosted in the SIRS model and, as a result, the system undergoes the second transition towards a full corrupt society much before than for the HCO model. Interestingly, for very high values of the delation flow β, this phenomenon is reversed as clearly seen on the curves for $\beta = 0.9$ (upper panels), where $\rho_c^{HCO}(\alpha) > \rho_c^{SIRS}(\alpha)$. To heuristically explain this surprising result, we must realize that, for β values very close to 1 (and in the absence of conversion flow), corrupt agents are very likely to be delated

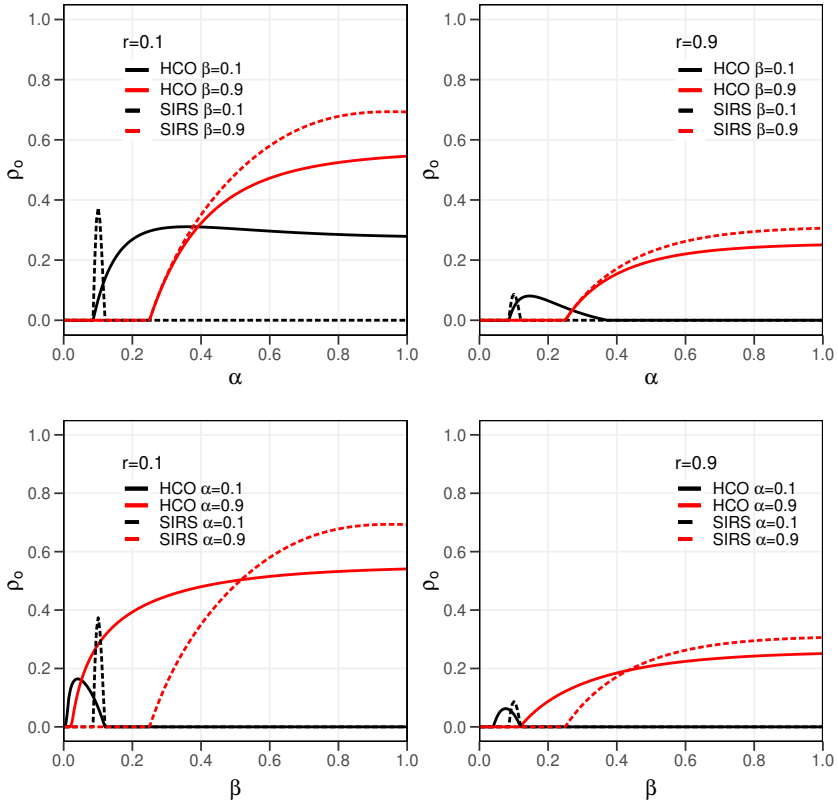

FIGURE 2.24: **Fraction of O agents as a function of α and β.** Top: Fraction of agents in Ostracism as a function of the corruption rate $\rho_o(\alpha)$ fixing the delation rate to $\beta = 0.1$ and $\beta = 0.9$. Bottom: $\rho_o(\beta)$ for $\alpha = 0.1$ and $\alpha = 0.9$. The mean field predictions for SIRS model are represented with dashed lines whereas solid lines correspond to the HCO model. The reinsertion rate is fixed to $r = 0.1$ (Left panels) and $r = 0.9$ (Right panels).

and go to ostracism; this is a dynamically inactive state, and thus immune to infection, thus preventing the diffusion of corruption for a typical reinsertion time r^{-1}. In this sense, the existence of the warning to wrongdoers in the HCO model partially prevents the emergence of ostracism, thus facilitating the unfolding of corruption. Obviously, this effect is reinforced as r decreases, for it makes the staying time in the inactive state longer.

The lower panels on Fig. 2.23 show the graphs of $\rho_c(\beta)$ at several fixed values of $\alpha(0.1, 0.9)$ and $r(0.1, 0.9)$. One sees there how the *honesty* transition occurs at lower delation values for the HCO model, and the detrimental effect on corruption of the warning to wrongdoers, provided the delation rate β is not very large. Finally, the *undesired* effect of the warning to wrongdoers is

observed for values of β close to maximum, when corruption better spreads for the HCO model.

In Fig. 2.24 we show, for both models, the mean field predictions for the fraction of agents out of active population, i.e. in the O compartment. The upper panels in this figure show the graphs of $\rho_o(\alpha)$ at several fixed values of β $(0.1, 0.9)$ and r $(0.1, 0.9)$. We see that close above the *corruption* transition, $\alpha \gtrsim \alpha_c(\beta)$, ostracism increases faster for the SIRS model than for the HCO model, because in the latter converted corrupt agents can no longer be delated. This trend is obviously overcompensated, at very low values of β, before the SIRS transition to the full C state is reached for $\alpha < 1$, because ρ_o should then decrease to zero for the SIRS model, while the HCO model still remains in a mixed population equilibrium. The graphs of $\rho_o(\beta)$ represented on the lower panels of Fig. 2.24 illustrate further this change of trend in the ρ_o evolution between transitions, for $\alpha = 0.1$. On the other hand, the comparison between left (corresponding to $r = 0.1$) and right ($r = 0.9$) panels of this figure shows the important effect of increasing the reinsertion rate on the ρ_o fraction at equilibrium.

2.4.3 Validation of theoretical results

The theoretical analysis of the mean field equations for both HCO and modified SIRS dynamics has shed light into the interesting phenomena arising from mechanisms which drive the presence of corrupt agents in the society. Some of these phenomena are the existence of two critical transitions or the crucial role that social interactions like delation or the warning to wrongdoers play in the evolution of corruption. Here we aim at validating these theoretical results by performing extensive Monte Carlo simulations on networked populations. At this point, for the sake of simplicity, we consider homogeneous networks (random regular networks or lattices) as the backbone for corruption and delation processes. To carry out the simulations, we start with a 10% of corrupt agents and we let the system evolve, following the microscopical rules defined in Sec. 2.4.1, until the stationary state is reached. In this sense, to reduce stochastic fluctuations, we compute the equation of (stationary) state $\vec{\rho}(\alpha, \beta, r)$ by averaging them over 400 realizations.

Let us first analyze the evolution of the fraction of honest agents as a function of both delation and corruption probabilities. For this purpose, we fix the reinsertion flow to $r = 0.5$ and we represent the curves $\rho_h(\alpha)$ for several β values and its counterpart. Regarding the topologies for the contact networks, we make use of a RRN of $N = 10^4$ agents and $\langle k \rangle = 4$ and a square lattice of

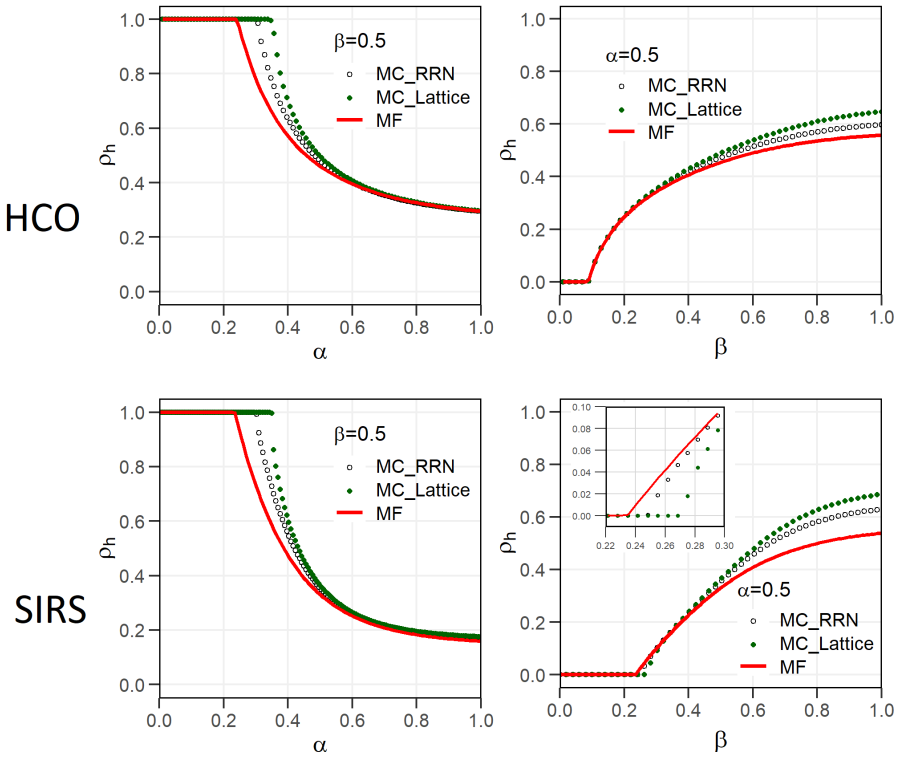

FIGURE 2.25: **Fraction of H agents as a function of α and β with HCO and SIRS model.** We calculate ρ_h, as a function of α and β, for Mean-field approximation (red solid lines) and Monte Carlo simulations. Parameter r is fixed to 0.5 for all graphs. Simulations are performed on random regular networks with $\langle k \rangle = 4$ (black empty points) and lattice networks (green filled points), whose size is $N = 10^4$. Top panels correspond to HCO model and bottom ones to SIRS model.

$N = 10^4$ vertices with periodic boundary conditions. Fig. 2.25 contains the comparison between theoretical predictions obtained via mean field equations and the results yielded by simulations for both lattices and RRN. There we confirm that the mean field theory developed above correctly predicts the existence of the two aforementioned transitions: the first one related to the destabilization of a honest population at $\alpha_c(\beta)$ and the second one associated with the irruption of honest agents in a totally corrupted society at $\beta_c(\alpha)$.

Although we are able to reproduce most of the phase diagrams, some relevant differences appear between theory and simulation, especially in the region of the parameters space close to the full honesty corner. In particular, it becomes evident that the value α_c is underestimated by our formalism. These discrepancies are mainly rooted on two facts: the so-called "echo chamber"

effect [138, 141] and the influence of structural correlations [296–298]. On the one hand, the "echo chamber" effect is caused by the reinforcement of agents corruption from neighboring agents who have been previously corrupted by them. On the other hand, the formalism here presented is constructed by neglecting the possible dynamical correlations existing in the contact network. However, the existence of strongly correlated agents can be of great importance for the evolution of the system, especially close to the transition points. In particular, it has been shown recently that the presence of high-order structures like cycles or motifs tends to make the network more resilient to diffusion processes [298]. In our case, this is reflected in Fig. 2.25 where it becomes clear that spatially structured topologies (lattices) display a larger value of α_c than uncorrelated ones (RRN).

Interestingly, these structural correlations do not have any impact at the full corrupt corner, since mean field equations accurately capture the value of β_c for both topologies. To explain this, we must realize that, apart from the delation processes caused by local interactions with honest agents, corrupt agents are also influenced by the warning to wrongdoers. This way, our hint is that having access to information about the global state of the network hinders the role of local interactions, thus giving rise to the same threshold for both topologies.

To confirm this statement, we now remove this effect and perform Monte Carlo simulations using the rules of the modified SIRS model. As observed in Fig. 2.25 , the local nature of delation processes regains its relevance, leading to a splitting of the thresholds $\beta_c(\alpha)$ (see inset). This separation is much smaller than for the former $\alpha_c(\beta)$ splitting, given that the transition from a full corrupt population to the honesty is not affected by any "echo chamber" effect.

In section 2.4.1, we have motivated the use of a simple compartmental population-flow model consisting of three states (compartments) and four flow channels connecting them, as a highly stylized model for the social dynamics of corruption, a punishable, and infectious, norm-violating behavior. The model may also be viewed as an epidemic model, and thus one can capitalize on recent advances in contagion dynamics in complex social nets. However, two major differences respect to usual epidemic models are at work. First, recovery from infectious state (delation) requires the interaction with susceptible people in the local neighborhood, which might, however, be a plausible situation in epidemics. Second, the conversion flow, implementing the warning to wrongdoers effect of punishment, has no obvious counterpart in epidemic contexts.

The mean-field analysis reveals a phase diagram (in the three-dimensional space of model parameters) with three generic absorbing states: (i) full honesty, (ii) full corruption, and (iii) a mixed state with nonzero flow through all the channels. There is no coexistence of stable absorbing states (no multistability). The transition from full honesty to the mixed state is continuous, with a linear increase of the fraction of corrupt population, and is not influenced by the warning to wrongdoers. The transition from full corruption to the mixed state is also continuous, and the fraction of honest people increases linearly, as well; however, the warning to wrongdoers (*wtw*) plays a very important role regarding the onset of honest instabilities. On the one hand, *wtw* reduces the stability region of the full corrupt state. On the other hand, because the rate of conversion flow is assumed to be the fraction of punished population (not a local quantity), the mean-field prediction for the locus (a surface in the parameter space) of this transition becomes exact for random and nonrandom regular (homogeneous) networks. Both features are in contrast with the irrelevance of the *wtw* regarding the transition from full honesty to a mixed state and the (network dependent) shift of the locus of this transition that we observe in homogeneous graphs due to the presence of dynamical correlations induced by the existence of higher-order motifs in the structure of the network.

2.4.4 Further results on multilayer networks

In the previous sections, social contagion dynamics of the HCO model have been analyzed with simulations conducted on several simple networks which are applied to the single layer. However, in view of recent studies on the spread of social contagions, the complexity of network configurations and the existence of multiple relations between agents should be taken into account [299, 300]. Here, we will focus on exploring the dynamics of honesty and corruption activities on multiplex networks, where nodes connected by interlayer links represent the same entity [47].

Fruitful results have been achieved in modelling multiplex networks and exploring their structural properties [11, 24]. As we described in section 1.3.2, degree-degree correlations as well as the edge overlap between layers are two of the main topological properties of multilayer networks. The effects on stability of collective and dynamical behaviours on multiplex networks have been found to be linked to both characteristics [301]. Those findings give us an insight to explore their impacts on the dynamics of honesty and corruption behaviors.

Therefore, we extend the HCO model to a two-layer interdependent network where different flows only occur on a specific layer. As shown in Fig. 2.26, we

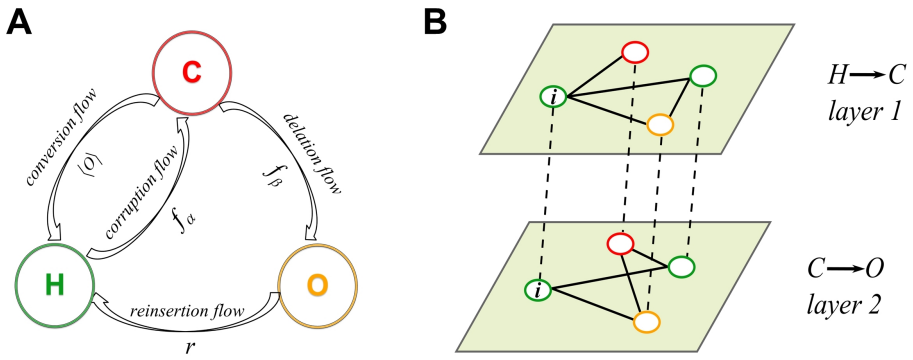

Figure 2.26: **The schematic of the HCO model applied on a duplex system. (A)** The graphical representation of the HCO model. The four flows among three agents are shown by the direction of the arrows. **(B)** The schematic of a duplex system. The agents on the layer 1 are connected to themselves on the layer 2 by the dotted edges. The agents with different colors in each layer represent the possible states they could be, i.e., H, C and O, at a given time. The corruption flow, $H \to C$, only takes place in the layer 1, while the delation flow, $C \to O$, only occurs in the layer 2. The reinsertion and conversion process can be performed on the whole duplex system.

represent the schematic of the HCO model applied on a duplex network. The system is made up of two undirected networks with N agents respectively on layer 1 and 2, where the corresponding nodes in two layers are transformed simultaneously. We assume that the corruption flow only takes place on the first layer, which means the honest agents are "infected" only by the corrupt neighbours, i.e., $H \to C$ on layer 1. The corrupt agents are particularly delated by their honest neighbours of the network on layer 2, where delation flow ($C \to O$) occurs. The reinsertion flow and the conversion flow take place on both two layers.

Hence, the corresponding transition probability of node i, where the state of its neighbour j is denoted as $\sigma_j(i)$, is defined based on the interactions among agents in different H or C states. The functions $f_\alpha(i, \{\sigma_j\})$ and $f_\beta(i, \{\sigma_j\})$ supporting the implementation of corruption and delation flow have to satisfy:

$$f_\alpha^{HC}(i, \{\sigma_j\}) = 0 \text{ if } \sigma_j \neq C \text{ for all } j \text{ where } \mathcal{A}_{ij}^1 = 1 \tag{2.158}$$

$$f_\beta^{CO}(i, \{\sigma_j\}) = 0 \text{ if } \sigma_j \neq H \text{ for all } j \text{ where } \mathcal{A}_{ij}^2 = 1. \tag{2.159}$$

For the stochastic Monte Carlo simulations, we assume that the scheme is implemented in the following way. The state of agent i at each time step t is denoted as $\sigma_i(t)$:

(*i*) If $\sigma_i(t) = H$, then $\sigma_i(t+1) = C$ due to the corrupt neighbours of the network on layer 1 with the transition probability f_α^{HC}. And the state of agent keeps unchanged with the probability $1 - f_\alpha^{HC}$.

(*ii*) If $\sigma_i(t) = C$, then $\sigma_i(t+1) = H$ with the probability $\langle o \rangle$, quantified by the fraction of O individuals at this time step. If not turned into H state with the probability $1 - \langle o \rangle$, the corrupt agent will be delated by the honest neighbours in the network on layer 2 with the transition probability f_β^{CO}. The corrupt agent remains its state with probability $(1 - \langle o \rangle)(1 - f_\beta^{CO})$.

(*iii*) If $\sigma_i(t) = O$, then $\sigma_i(t+1) = H$ with the probability r. The agent i holds its state with probability $1 - r$.

In Monte Carlo simulations, transition probabilities f_α^{HC} and f_β^{CO} (f_α and f_β for short) in Eqs. 2.126 and 2.127 are rewritten correspondingly:

$$f_\alpha(i, \{\sigma_j\}) = 1 - \prod_{j=1}^{N} (1 - \alpha \mathcal{A}_{ij}^1 \delta_{\sigma_j, C}) \ , \tag{2.160}$$

$$f_\beta(i, \{\sigma_j\}) = 1 - \prod_{j=1}^{N} (1 - \beta \mathcal{A}_{ij}^2 \delta_{\sigma_j, H}) \ , \tag{2.161}$$

where, $\mathcal{A}_{ij}^1$ and $\mathcal{A}_{ij}^2$ are the adjacency matrix of the network in layer 1 and layer 2, respectively.

It is worth to mention that in single-layer network (monoplex), the probability density function (*p.d.f* for short) of node degree is denoted as $P(k)$, while in duplex networks, the degree of nodes is a vector. Therefore, the *p.d.f* is written as $P(\vec{k})$ ($\vec{k} = (k_1, k_2)$). The specific form for the *p.d.f* in each layer is as follows:

$$P_1(k) = \sum_{k_2} P(k, k_2) \ , \tag{2.162}$$

$$P_2(k) = \sum_{k_1} P(k, k_1) \ . \tag{2.163}$$

In this work, we aim at understanding the impact of edge overlap and interlayer degree correlations on the evolution of honesty and corruption activities on multiplex networks. To this end, we consider the role of edge overlap plays on the uncorrelated and correlated duplex networks, respectively. Furthermore, we explore the effect of various values of edge overlap caused by the correlated coupling on social dynamics.

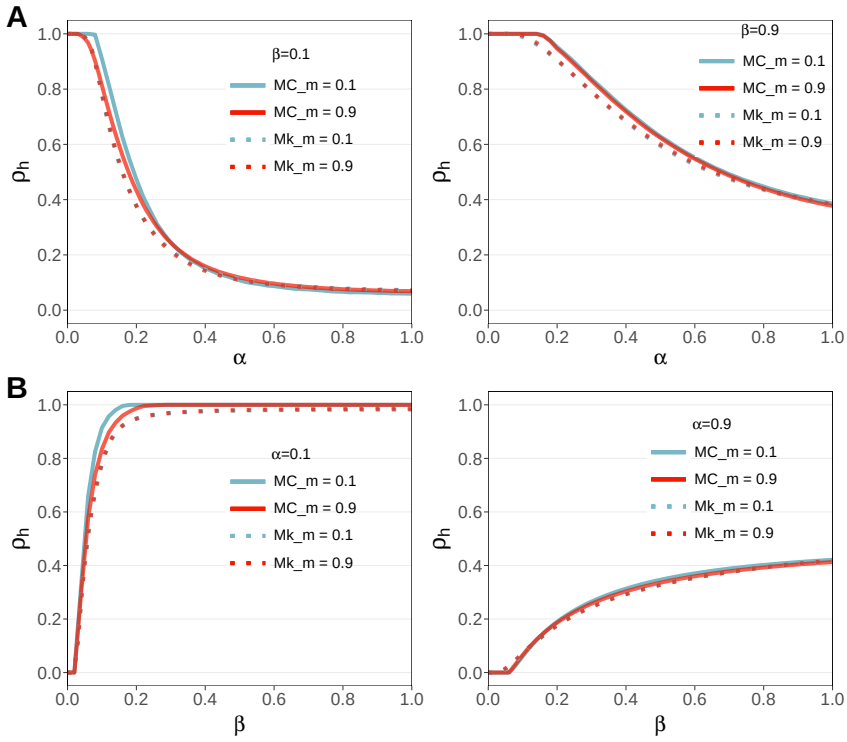

Figure 2.27: **Phase diagrams for H individuals on scale-free duplex networks.** The fraction of H individuals in the stationary state as a function of **A)** corruption rate α and **B)** delation rate β. The value of r is set to 0.5. The results obtained based on Markovian process (dotted line) are compared with Monte-Carlo simulations with $m = 0.1$ and $m = 0.9$, performed on a duplex network composed of scale-free networks with $\gamma = 3$, $k_{min} = 2$ ($\langle k \rangle \approx 3.5$), $N = 10^4$ for each layer. The numerical results have been averaged over 300 realizations.

1. *Scale-free duplex networks*

To build the uncorrelated duplex networks with desired values of edge overlap, m, we first generate a network with an arbitrary $\langle k \rangle$ for layer 1. Then, we copy the network to layer 2 and rewire the edges with the probability $p = 1 - m$ [50]. We first perform discrete-time simulations (see section 2.2.6) on scale-free duplex networks with $\gamma = 3, k = 2$ ($\langle k \rangle \approx 3.5$). The results for the fraction of honest individuals as a function of α and β are shown in Fig. 2.27. We find that the individual-based Markovian approach yields the same results with different values of m. This is due to the fact that the $P(\vec{k})$ remains the same as edge overlap changes. In addition, the predictions

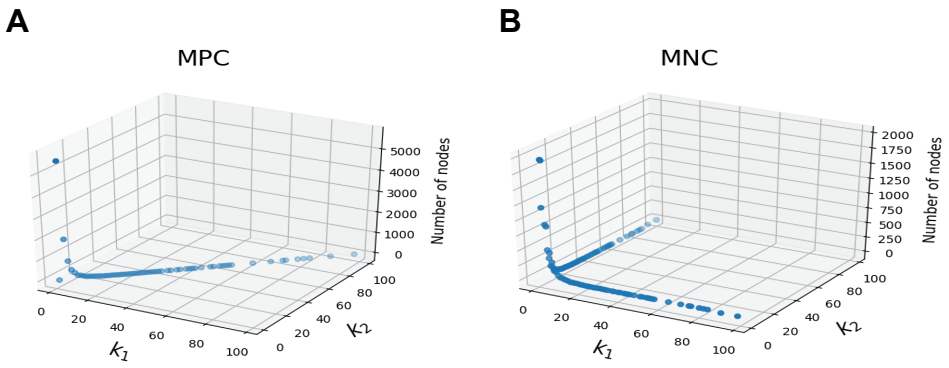

FIGURE 2.28: **Joint degree distribution for the *MPC* case and the *MNC* case.** The joint degree distribution on a duplex system made of scale-free networks with $\gamma = 3$, $k_{min} = 2$ for **(A)** the *MPC* case and **(B)** the *MNC* case are visualized graphically in three dimensions.

associated to the Markov process are basically consistent with numerical simulations. However, in the case of small values of α and β, there exist slight differences in simulation results between different m close to the total honest state ($\rho_h = 1$). It can be explained that the connection between nodes C and H is quite important when approaching the full H state. Therefore, the small m induced by rewiring many links greatly increases the probability of disconnecting links $C - H$, delaying the transition of H individuals at the full honesty corner when α and β are relatively small. Conversely, large transition rates hinder those discrepancies, yielding same phase diagrams.

Taking into account of different patterns of degree-degree correlations between layers, we generate three representative correlated structures, maximally positive correlations (*MPC*), maximally negative correlations (*MNC*) and structure in between, namely *MIX*. In this case, we apply the approach (see section 1.3.2) that allows to tune the level of interlayer degree correlations. The detailed steps to generate a duplex system with an arbitrary joint degree distribution are described as follows:

(1) Construct a scale-free network with desired parameters for layer 1. Copy this network to layer 2.

(2) Sort the node list of the above-built network on layer 2 in the degree's descending order. Select two sets of nodes with a specific number (n_p) from the degree-ordered node list for permutation.

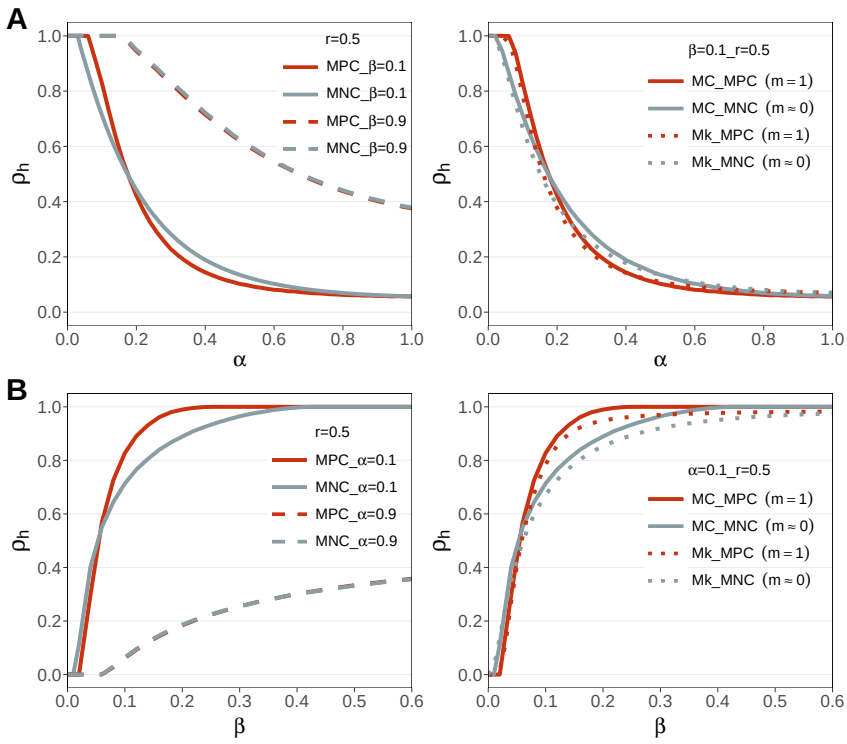

Figure 2.29: **Phase diagrams for the *MPC* case and the *MNC* case.** The fraction of population in H state, ρ_h, obtained in the steady state, as a function of **(A)** α and **(B)** β. Monte-Carlo simulations are performed on duplex networks with two extreme cases, *MPC* and *MNC*, composed of scale-free networks with $\gamma = 3$, $k_{min} = 2$ ($\langle k \rangle \approx 3.5$). The numerical results are compared with those obtained from the associated Markov process.

(3) Permute the selected nodes. The metric, edge overlap m, is measured as the number of repeated edges in both layers.

Through permuting different number of nodes, we can generate underlying structures with three patterns of interlayer degree correlations mentioned above. When the nodes in two degree sequences ranked as degree increases are connected with $n_p = 0$, the two layers in the duplex system have maximally positive interlayer degree correlations with the joint degree distribution shown in Fig. 2.28A. Note that the above exploration on the effect of edge overlap is conducted on the basis of the *MPC* case. In the maximally negative case (also called maximally disassortative, *MNC*), the system is constructed by permuting half of the nodes, $n_p = N/2$, back and forth from the degree-ordered node list. The three dimensional joint degree distribution of *MNC* case (see

Fig. 2.28B) visualizes its structural features that the hubs in one layer are connected to the leaves in the other layer. Obviously, maximally positive and maximally negative interlayer degree correlations are two extreme cases, resulting in $m = 1$ and $m \approx 0$ respectively.

Here, we first investigate the relevance of these two cases on the honesty dynamics. As shown in Fig. 2.29, we plot the curves $\rho_h(\alpha, r)$ and $\rho_h(\beta, r)$ obtained on scale-free duplex networks with $\gamma = 3$, $k_{min} = 2$. In the left panel of Fig. 2.29, given a fixed reinsertion rate $r = 0.5$, the large corruption rate α and delation rate β overshadow the influence of these two structural correlations, producing the consistent results. However, there occurs an obvious intersection as α increases with a relatively small value of $\beta = 0.1$. As shown in Fig. 2.29A, when the value of α is small in the beginning, the *MNC* case favors the instability of full honesty state as a result of a smaller α_c than that in the *MPC* case. This is because the permutation process performed to generate the *MNC* structure likely induces the hub node to be in the state C, accelerating the transition of neighbouring H nodes. However, as the corruption rate α increases, the system with *MNC* undergoes the transition $H \to C$ more slowly compared with the *MPC* case. It happens largely due to the increase of the fraction of O individuals, some of which are delated by C hubs, driving the reinsertion and conversion processes. Similarly, in the case of $\alpha = 0.1$, the curve $\rho_h(\beta, r)$ shows that the total corrupt population is less resilient in the duplex networks with *MNC* than that with *MPC* and the transition from all-corrupt to all-honest with *MNC* are achieved more slowly, resulting in a cross-point. In addition, the results obtained from the associated Markov process are basically identical with the numerical simulations (see the right panel of Fig. 2.29).

To explore the effect of the reinsertion rate, r, on honesty dynamics, we first compare the time evolution of honesty with fixed $\alpha = 0.1$ and $\beta = 0.1$ as shown in Fig. 2.30A. Provided a constant value of r, we intuitively observe the differences of honesty evolution between different m caused by edge rewiring (left panel) and nodes permutation (right panel). The presence of correlated structure, as m decreases especially in the extreme case of *MNC*, facilitates the decrease of ρ_h in contrast to the behavior in uncorrelated networks. Under the same network configuration, as we discussed in monolayer network (see Fig. 2.23 in the section 2.4.2), the conversion flow as a warning to wrongdoers in the HCO model triggers the unfolding of corruption. As r increases, the effect is boosted, leading to a smaller ρ_h in the system. In particular, with fixed $\beta = 0.1$, we observe that the structure with maximally negative interlayer degree correlations under the condition $r = 0.9$ speeds up the decline of the

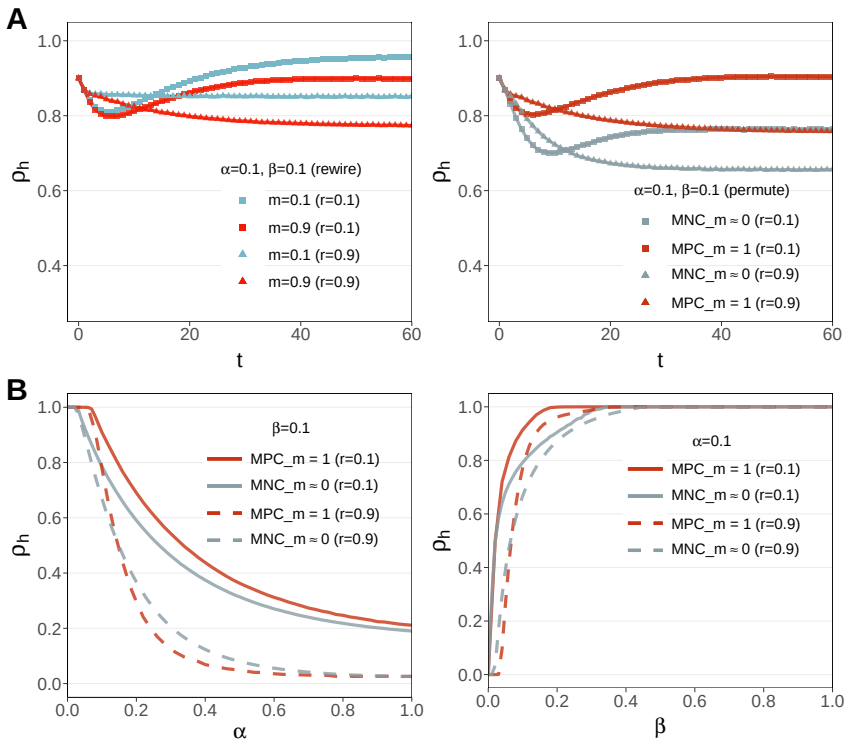

Figure 2.30: **Effect of the reinsertion rate under different network structures. (A)** The time evolution of H individuals given $\alpha = 0.1$, $\beta = 0.1$ performed on the uncorrelated and correlated structure. **(B)** The fraction of population in H state, ρ_h, obtained in the steady state, as a function of α (left) and β (right). Monte-Carlo simulations are implemented on duplex networks with *MPC* and *MNC* cases made of scale-free networks with $\gamma = 3$, $k_{min} = 2$ ($\langle k \rangle \approx 3.5$). The reinsertion rate r is given by $r = 0.1$ (dashed line) and $r = 0.9$ (solid line), respectively.

fraction of honest individuals in steady state compared with the *MPC* case as α increases.

For the interlayer degree correlations between two extremes, denoted as *MIX*, we randomly and specifically select the number of nodes $n_p = 500$ for the permutation to reassign the labels of nodes. In the case of the *MIX randomly*, the duplex network is constructed by randomly selecting two unrepeated lists with 500 nodes to permute, yielding $m \approx 0.8$. As expected in Fig. 2.31, the results obtained from the duplex networks with *MIX randomly* are nearly close to those with *MPC* as a result that the random selection is more difficult to make hubs involved to permute. If we select the nodes $n_p = 500$ specifically back and forth from the degree-ordered node list to generate the *MIX specifi-*

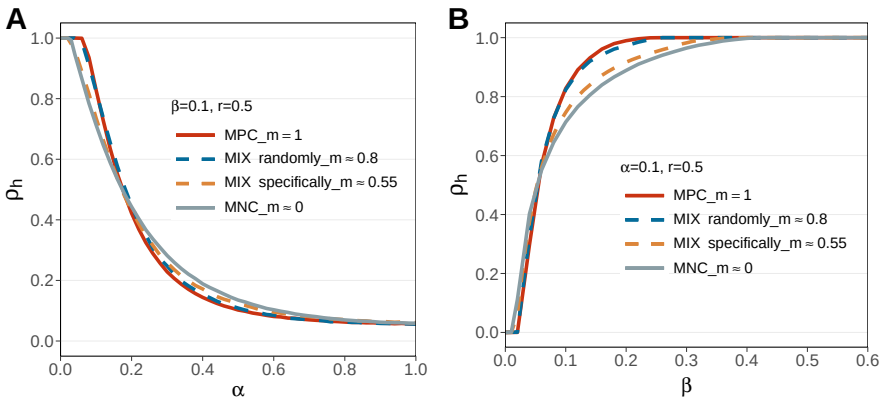

FIGURE 2.31: **Comparisons of three representative correlation patterns (*MPC*, *MNC*, *MIX*).** The total fraction of honest individuals in stationary state as a function of α (A) and β (B) is obtained on the scale-free duplex networks with $\gamma = 3$, $k_{min} = 2$ ($\langle k \rangle \approx 3.5$). The size of network for each layer is $N = 10^4$.

cally case, which produces the edge overlap $m \approx 0.55$, the results get closer to those with *MNC*. The curves of $\rho_h(\alpha, \beta = 0.1)$ and $\rho_h(\beta, \alpha = 0.1)$ present the expected results that the dynamics on the correlated structure, *MIX*, between two extremes also take place at a level between them.

To figure out the influence of the interplay between interlayer degree correlations and edge overlap on the dynamics of HCO model, we tune the value of edge overlap for the *MNC* and *MIX specifically* cases by rewiring links in one layer. In this way, the joint degree distribution keeps unchanged. We begin with the *MNC* case where $m \approx 0$ in the beginning. Generally, the reachable maximum value of edge overlap are determined by the degree sequences of the network in each layer. According to this criterion, we rewire the links in one layer to increase m until no further increase is achievable. Here, we choose a value of $m \approx 0.4$ which approximates the maximum to compare with the case without rewiring links. In Fig. 2.32A, small discrepancies appear at the full honesty state when α and β are small. The large m through edge rewiring favors the unfolding of corruption, lowering the fraction of honest individuals in the duplex system. The same procedure goes for the *MIX specifically* case to get a $m \approx 0.65$ close to the maximum and a representative small value of $m \approx 0.1$ with results presented in Fig. 2.32B. Those results are basically in line with the scenarios observed in the case of *MPC* shown in Fig. 2.27. It illustrates that different values of edge overlap due to links rewire under the conditions of existing degree correlated coupling has a little influence on

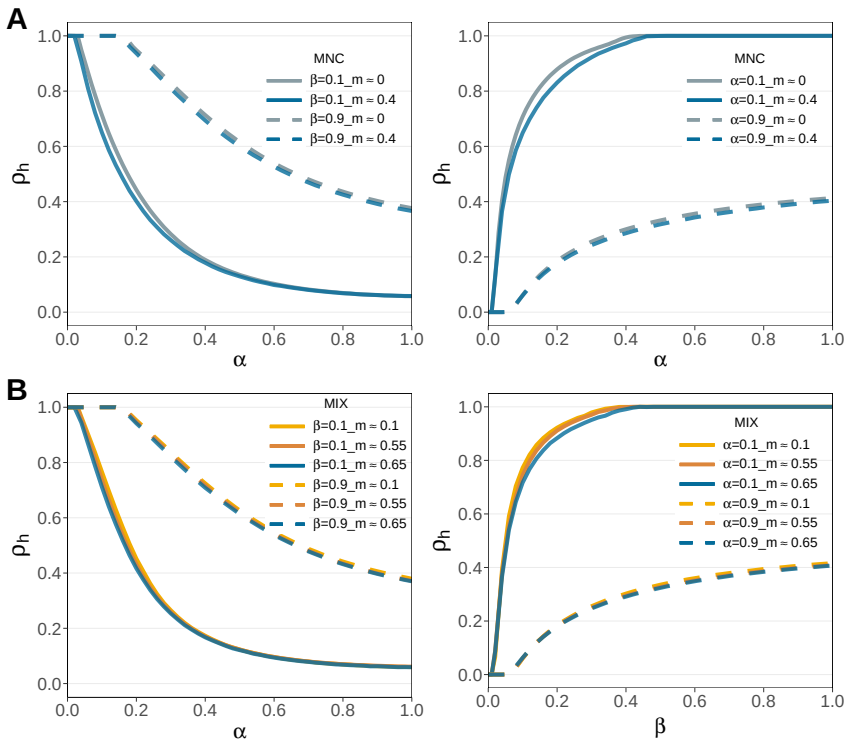

Figure 2.32: **Effect of edge overlap on scale-free duplex networks.** The fraction of population in H state in equilibrium conditions, ρ_h, as a function of α and β with a fixed $r = 0.5$ is performed on scale-free duplex networks with $\gamma = 3$, $k_{min} = 2$ ($\langle k \rangle \approx 3.5$), $N = 10^4$ for each layer. We get various values of m by rewiring links on the basis of **(A)** the *MNC* case and **(B)** the *MIX specifically* case.

the evolution of honesty and corruption behaviors beyond at the full honest corner.

2. *Scale-free and RRN duplex networks*

Here, we construct the duplex system composed of scale-free networks on one layer and random regular networks on another layer to explore the effect of edge overlap and interlayer degree correlations. The duplex networks with tunable edge overlap, m, are specifically generated in the following way:

(1) Construct a scale-free network with given parameters on one layer and copy it to another layer. The approximate average degree, $\langle k \rangle$, can be calculated by the number of edges divided by the total number of nodes.

(2) Randomly choose two nodes (i and j), where $k_i \leq \langle k \rangle - 1$ and $k_j \geq \langle k \rangle + 1$.

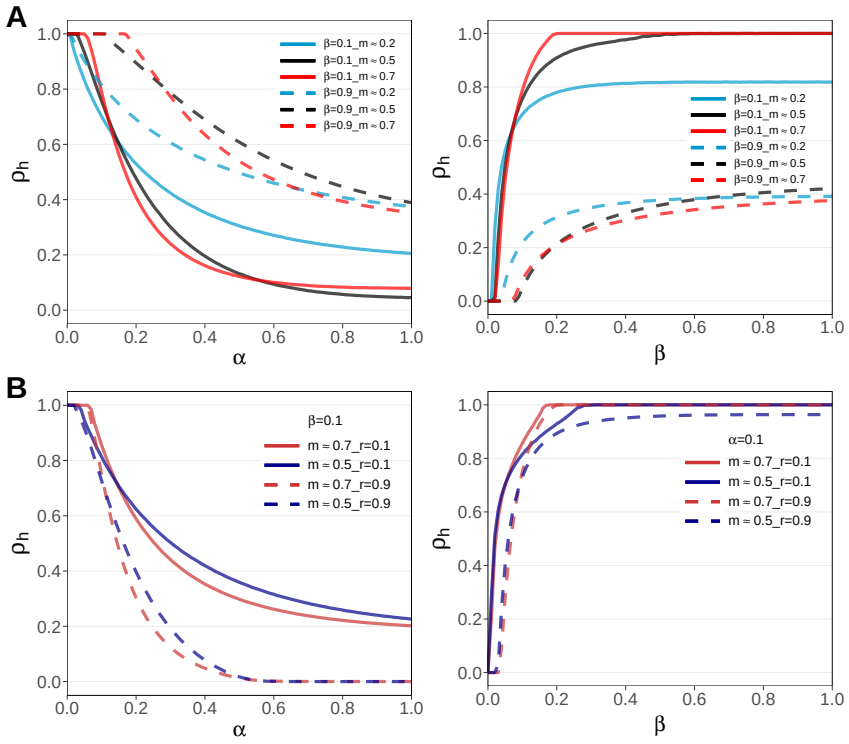

FIGURE 2.33: **Phase diagrams for H individuals on scale-free and RRN duplex networks.** We perform numerical simulations to get $\rho_h(\alpha)$, $\rho_h(\beta)$ **(A)** with a fixed $r = 0.5$ and **(B)** with different r, obtained in the stationary state. The curves with different values of edge overlap, $m \approx 0.2, 0.5, 0.7$, are obtained on duplex networks composed of scale-free network in one layer with $\gamma = 2.2$, $k_{min} = 2$ ($\langle k \rangle \approx 8.7$), $\gamma = 2.8$, $k_{min} = 2$ ($\langle k \rangle \approx 4$), and $\gamma = 3.5$, $k_{min} = 3$ ($\langle k \rangle \approx 4.5$), respectively and the random regular network in another layer with the approximate $\langle k \rangle$ correspondingly.

Exchange their neighbours until degrees of all nodes are approximately equal to $\langle k \rangle$.

It is worth mentioning that, there exit differences between the value of m computed from the generated duplex network and the one set initially. To get the desired duplex network where the calculated edge overlap is nearest to the target value, we set a termination criterion that in our simulations, we iteratively create the network until m falls within 0.5% of the pre-determined value.

Firstly, to characterize the influence of interlayer degree correlations present in this kind of system on the honesty and corruption dynamics, we built the

duplex networks composed of scale-free networks in layer 1 given $\gamma = 2.2$, $k_{min} = 2$ ($\langle k \rangle \approx 8.7$), $\gamma = 2.8$, $k_{min} = 2$ ($\langle k \rangle \approx 4$), and $\gamma = 3.5$, $k_{min} = 3$ ($\langle k \rangle \approx 4.5$), respectively and random regular networks in layer 2 with approximate $\langle k \rangle$ correspondingly. In this way, we generate the correlated duplex networks with different values of edge overlap $m \approx 0.2, 0.5, 0.7$ respectively. Then, we implement simulations with a fixed $r = 0.5$ as shown in Fig. 2.33A. The curves $\rho_h(\alpha)$ show that the larger m leads to a larger corruption threshold, α_c, and makes the fraction of honest individuals in population decline more quickly as α increases. The results in the curves $\rho_h(\beta, \alpha = 0.1)$ state that the larger m is beneficial to the presence of the full honesty state which is basically consistent with those (see Fig. 2.31) got on scale-free duplex networks. However, the differences from those on scale-free duplex networks appear in the case of $\rho_h(\alpha, \beta = 0.9)$ and $\rho_h(\beta, \alpha = 0.9)$. The small m facilitates the instability of the full honest and full corruption state. The reason is most likely caused by the fact that the smallest m corresponds to the system with a large average degree.

Meanwhile, there are differences arising when investigating the effect of reinsertion rate on the phase diagram of H individuals in Fig. 2.33B. As r decreases, the large m still makes honesty stay in the inactive state longer, but the transition occurs at a faster rate compared with those on scale-free duplex networks. We also consider the impact of edge overlap on scale-free and RRN duplex networks with $m \approx 0.5, 0.7$. Similarly, we obtain different values of m by rewiring links. The comparisons are shown in Fig. 2.34. The scenarios remain in the similarity for the *MNC* case and the *MIX specifically* case in Fig. 2.32 that the decrease in the value of edge overlap under the circumstances of $\alpha = 0.1$ and $\beta = 0.1$ makes the extension of stability region of full honesty though not obviously noticeable.

3. *Conclusions*

In summary, to exclusively assess the role played by edge overlap, we first perform Monte Carlo simulations on uncorrelated duplex networks with different m got through rewiring links. In particular, the results obtained from Markov chain equations which capture the structural heterogeneity show that the analytical results are independent of the value of edge overlap since rewiring links remain the joint degree distribution $P(\vec{k})$ unchanged. However, It can be seen from the numerical results between different m that there occur small discrepancies at the full honest corner in the case of small α and β. This is because more links to rewire lead to a reduction in connections $C - H$, allowing a late onset of instability.

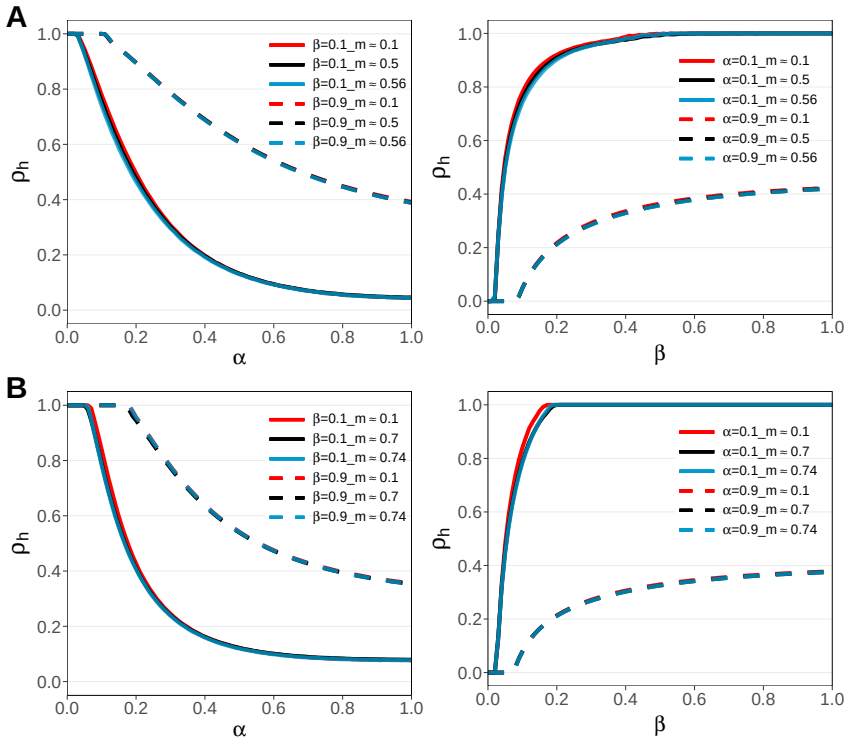

FIGURE 2.34: **Effect of edge overlap on scale-free and RRN duplex networks.** Numerical simulations are performed to obtain $\rho_h(\alpha)$, $\rho_h(\beta)$ with a fixed $r = 0.5$. The various values of m are produced by rewiring links on the correlated scale-free and RRN duplex networks with initial **(A)** $m \approx 0.5$ and **(B)** $m \approx 0.7$, respectively. The size of duplex networks is $N = 10^4$ at each layer.

Then, we investigate the impact of interlayer degree correlations on the dynamics of honesty and corruption behaviors by generating three kinds of correlated duplex networks, *MPC*, *MNC* and *MIX*. The curves $\rho_h(\beta, r)$ and $\rho_h(\alpha, r)$ got on the scale-free duplex networks show that the evolution of honesty is not subject to the edge overlap and interlayer degree correlations in the case of large α and β. However, the outcomes got on maximally positive correlated (*MPC*, $m = 1$) duplex networks display a larger value of α_c and β_c with faster transition as well than that with *MNC* ($m \approx 0$) when α or β is set to a smaller value. Then, an intersection appears in both phase diagrams. In addition, the dynamical behaviors of *MIX* lies between two extremes. Similarly, numerical simulations on a duplex system composed of scale-free network on layer 1 and random regular network on layer 2 show that various values of m caused by different correlated coupling make a difference on honesty dynam-

ics. The larger m is beneficial to the presence of the stability region of the full honesty state. However, in the case of large transition rates, the effect of degree correlations on the dynamics remains the same as that with small α and β which is distinct from the behaviors in scale-free duplex networks.

Moreover, we rewire the links on the basis of previously built duplex correlated networks to explore the effect of edge overlap. The results with smaller m given $\alpha = 0.1$ and $\beta = 0.1$ indicate a role of edge overlap in promoting the larger area of full H state though not clearly visible. In a nutshell, under the same network structure, either correlated or uncorrelated, various values of edge overlap caused by rewiring links have nearly negligible impact on the evolution of honesty and corruption activities. However, the different edge overlap due to interlayer degree correlations makes a great difference on their dynamics.

Data-driven Social Networks 3

From the history of network science, the "six degrees of separation" small-world experiment conducted by Stanley Milgram is one of the earliest empirical studies of network science [302, 303]. On top of it, as we have discussed in chapter 1, both the small-world model and the scale-free model were proposed by researchers who have found certain patterns from many empirical networks in the late twentieth century, representing the rise of network science in real sense. Along with richer available data, the scientific interest has shifted from the application of concepts developed based on graph theory to the investigation of the dynamical evolution of network topology, structural representation, pattern recognition, etc [9]. It is thus clear that the most primitive driving force behind the development of complex networks is the acquisition of the new data as Barabási's view [304] states:

> *"Fuelled by cheap sensors and high-throughput technologies, the data explosion that we witness today, from social media to cell biology, is offering unparalleled opportunities to document the inner workings of many complex systems."*
>
> — Albert-László Barabási

Coincidentally, the term *data science* had also started to appear in the 1970s when the random graph theory was developed. To be precise, in 1974, Turing award winner, Peter Naur explicitly put forward the notion *data science* in the preface of his book with a clear definition that "data science is a science based on the processing of data" [305]. However, the real rise of data science has been driven by the boom of big data which presents important development opportunities and challenges to network science, and in the meanwhile, data science centered on data processing requires the relevant theories of network science as support [306]. Nowadays, online social networks, brain science and traffic network analysis are some of the key areas of big data research in which data science and network science can be immensely useful. Taking the research of online social networks as an example, the theory in network science could automatically regard each user as a node and the interaction between users as a connected edge for dynamic analysis.

Thanks to advances in high technology, it has become effortless and inexpensive to collect massive amounts of multi-relational data [307]. Nevertheless, for many complex systems, it has not been possible to obtain a complete data of network structure through effective methods [9, 308]. Particularly, as the data on web are generated randomly and dynamically, they have many characteristics different from natural science data, such as multi-source heterogeneity, interactivity, time-sensitivity and high noise, etc. In addition, much of data are duplicated and with low value density, increasing the difficulties in generating an appropriate data-based mathematical model of complex systems [309]. To this end, in the face of the enormous volume of data, in addition to mining the relational data that can serve to construct the basic structure of the network, how to make good use of additional information sources to enrich the topology of the network according to specific research demands is something that requires in-depth consideration.

In chapter 2, we simply explored the influence of network structure on dynamics of transmission behaviors, especially on epidemic spreading processes. However, the analysis was mainly performed with classical epidemic models on top of synthetic networks in which the population is assumed to be homogeneous or heterogeneous, ignoring the demographic information, such as age, occupation, location, etc. Furthermore, facing a complex social network with billions of nodes and tens of billions of edges, the dynamical changes are reflected in different scales of scenarios such as macro networks, mesoscopic groups, micro user behavior, and dynamic propagation of information on the network. Therefore, leveraging the data science, collecting data, processing and extracting the desired information is now the driving force behind the development of complex networks. In addition, the traditional dynamic models are difficult to describe the dynamics of such complex social network systems, fueling the development of theoretical framework for data-driven networks.

In this chapter, we first investigate how the development of data science affects the study of complex networks, triggering the data-driven network modelling in section 3.1. In section 3.2, we then put the emphasis on the infection transmission on contact networks modelled with the real data. In particular, the theoretical framework of age-specific contact networks will be introduced with the data extracted from the POLYMOD study with heterogeneity of mixing patterns and demographic information taken into consideration.

Along with the framework, we are capable to technically generate realistic contact networks with age-dependent mixing patterns by incorporating the data. In section 3.3, we will present a data-driven framework to estimate the herd immunity threshold and evaluate different immunization strategies

against SARS-CoV-2 by making use of the collected data for several countries. To accurately describe the evolution of the incidence of COVID-19, two determinants, namely age and contact patterns will be encoded in building the multilayer network which represents the social interactions in the population. Based on this framework combining with a SARS-CoV-2 stochastic transmission model, we will conduct an extensive discussion of different vaccine prioritization from various aspects. Accordingly, the section corresponds to the following work

- **D. Lu**, A. Aleta, M. Ajelli, R. Pastor-Satorras, M. E. Halloran, A. Vespignani, and Y. Moreno, Data-driven estimate of SARS-CoV-2 herd immunity threshold in populations with individual contact pattern variations, *medRxiv*, 2021.

Then, we will focus on the applications of data-driven model about solving a realistic problem. In section 3.4, we will explore in depth the dynamics of healthcare-associated infections (HAIs) on the constructed networks and quantitatively assess the risk of spatial units and individuals with the spatio-temporal data collected in three hospitals in Canada. The section will mainly based on the article

- **D. Lu**, A. Aleta, Y. Moreno, Assessing the risk of spatial spreading of diseases in hospitals, *In preparation*, 2021.

3.1 From Big Data to Good Networks

With the rapid development of information technology, there are increasing amounts of data that are more readily available than previously possible. Simultaneously, scientific research has also entered the era of big data [304,310]. In addition, as the scale and type of data we are able to collect continues to grow, it is becoming increasingly imperative in complex network research to discover the desired nodes relationship from the vast amount of data, to find the patterns and "extra" features hidden in the data, and to use them rationally to build a close-to-reality networks [307]. Meanwhile, it is accompanied by the emergence of some tough questions. For example, how to efficiently extract information from large amounts of data sources. To what extent can an analysis be based on incomplete network structure data be generalized to the entire network?

Another major challenge in this regard is the sampling problem. In 2005, the paper published by May et al. [311], proved that the sub-networks sampled

from any strictly power-law distribution network are not strictly power-law. Most of the data we actually use are the results of sampling. Yet, there are many sampled networks with power-law distribution. The questions then, are: what is the distribution form of the original network remains unclear? how can we predict the properties of the original network from the sampling network?

To briefly summarize, there are two issues involved to address the way from big data to good networks. One is "from big data to good data" in which the focus is preprocessing the data, such as denoising and cleaning, mainly solved by the knowledge of *data science* [312]. The other is "from good data to good networks" where even with high-quality network data, it is still necessary to process the data appropriately to generate a suitable network for the specific research questions.

3.1.1 The rise of data science

The term *data science* seems to have been introduced by Naur [305]. Afterwards, the research of data science underwent a long period of silence until Cleveland in Bell labs published paper to advocate *data science* as an important research direction [313]. Thereafter, it gradually plays an important role in addressing the problems pertaining to complex network analysis, such as community structure mining, link prediction in giant social networks [314,315].

In the field of complex network research, the development of network theory is driven by a wealth of empirical observations. For example, the discovery of *small-world effect* and *scale-free nature* are preceded by data recording. Those network concepts firmly have practical implications in reality. Afterwards, a great deal of theoretical findings are motivated by data collection. In particular, the study of epidemic propagation processes are fuelled by detailed observations and analysis of real data [156, 157, 316].

In the course of the study, the advantages of data science are primarily demonstrated in two aspects. Firstly, the abundant data resources enrich the topology of networks and strengthen the expressiveness of the network structure, rendering more characteristics. An example are given by multilayer networks where different layers can be used to model different relations in the domain of social networks [317] (see the discussion in section 1.3). On the other hand, the rise of data science has prompted the improvement in dynamical models. The classical epidemic models are no longer sufficient to describe the transmission process of some novel infectious diseases, say the current hottest research on the COVID-19 pandemic [221,318], as their specific characteristics make it possible to classify population not only in a few compartments. The

rise of data science enables the availability of multiple data to help extract the transition probabilities between states, making the model more approximate to the practical situation and thus yielding more accurate dynamic analysis results.

3.1.2 Data-driven network modelling

In the early stage of statistical science and epidemiology, researchers could only make mathematical assumptions about the distribution of a small amount of data and then build some hypothetical mathematical models. They derived some properties of the results obtained from these models through manual calculations as the derivation of the properties of epidemic models in section 2.2.1, denoted by *model-driven* method. Obviously, the complexity of social dynamics is far from being fully elucidated by those simplified models. Therefore, the data-driven method was developed benefited from the proliferation of data, advances in technology that contribute to rich data collection, and the boom of data science that allows data to be further processed. The data-driven network modelling approach aims to take advantage of representative data to make the network structure continuously approach the real situation.

To understand human social dynamics, it is essential to construct a reliable contact network. For this purpose, more and more real-world data reflecting interactions between individuals are leveraged to augment the robustness of network models. Additionally, with the increasing access to sufficiently detailed data, in-depth studies on contact dynamics have been carried out on networks from theory to practical application [319, 320]. For example, for the online social networking services, the same user may have multiple social accounts, such as Facebook, Google, Twitter, etc. The interconnected networks involving people behavioral patterns built with the rich data on different platforms can be employed to study social contagion processes, like rumor spreading. Moreover, in the early days, research in network science focused on the single network, but in fact most networks do not remain isolated, instead experiencing interdependent, cooperative or competitive relationships with other networks [51]. Things like the failure of one network in infrastructure networks may trigger the successive failures of other networks [146, 321]. For cases like the above, it is time for the data-driven modelling method to come into play.

It is called data-driven approach because it takes advantage of available data rather than a predefined model. In terms of large-scale transmission processes, it is employed by the use of a small amount or real-time updated data to

construct network models which can closely conform to the specific situation as much as possible. This process includes data processing and some statistical calculation methods, such as least squares method and Markov chain Monte Carlo (MCMC) methods [322,323], so that unknown parameters of the model are determined. For example, in the study of SARS-CoV-2 pandemic, the data associated with spatially distributed population density, geographic contact patterns, human mobility, etc., give rise to forming metapopulation network models which offer a more realistic interpretation of its spatio-temporal spread pattern [157, 159]. Furthermore, we can use the data-driven approach to study multimedia content, user behavior and their local popularity patterns, and propose corresponding deployment based on propagation prediction, risk evaluation based on user behaviors, etc.

3.2 Infection Transmission on Data-driven Contact Networks

In the modern society with advanced information and technology, people are constantly interacting and communicating with each other through face-to-face contact or the Internet and other means. Such frequent population movements are accompanied by the spread of various human behaviors, ideas and diseases, inadvertently facilitating the transmission of new infectious diseases [158, 324]. For example, in 2009, influenza A virus subtype H4N1 was detected in Mexico, and in just three months, the disease swept the world as humans moved around. More recently, COVID-19 did it in one or two months. In addition, the proximity of interpersonal social behaviors contributes to the spread of respiratory infectious diseases like influenza and tuberculosis [157, 325].

In the previous section, we have explored some advantages of data-driven approach in the context of social networks. We herein focus on exploiting it in the domain of epidemiology. Human behaviors have become a salient aspect to be considered in the study of modeling and simulation of infection transmission [326–328]. However, classical epidemic models and the assumption of homogeneity exhibit many deficiencies in describing the spread of infectious diseases in real society [329]. First, most of epidemic models do not fully consider the heterogeneity of individual attributes, and also fail to describe the heterogeneous contact patterns among individuals, as individual behaviors vary by time, occasion and contact frequency [330]. Second, the majority of contagion models do not capture the adaptive changes in individual behaviors during an epidemic outbreak, which needs to be addressed by modifying the model parameters. Therefore, in addition to the availability of more di-

verse data to support the improvement of disease transmission models, the construction of the underlying networks needs to take into account the social contact patterns of populations.

Although infection transmission can vary differently depending on various pathogens, it is also conditioned by the structure of contact networks [331]. The structure of the contact network may also vary considerably across diseases in the same population, depending mainly on the route of transmission of the infectious disease. For highly infectious diseases, which are transmitted mainly by droplets, fomites, etc., the contact network for such diseases forms a large number of edges. In contrast, for closely contact-transmitted diseases or sexually transmitted diseases, the contact network is more sparse. The complicated social network structure of a population largely determines the likelihood of transmission of an infectious disease from one individual to another [112, 332, 333]. In other words, the transmissibility of an infectious disease is determined by the network of contacts in the population. In a contact network, each individual is represented as a node, and the contacts among individuals that may lead to infection transmission are denoted as links, demonstrating the decisive impact of constructing realistic population contact networks in understanding the transmission dynamics of infectious diseases.

The main difficulty in studying data-driven disease transmission processes lies in obtaining the structure of the underlying contact network for the population under study. For diseases with small transmission rates caused by specific modes of transmission or casual contact, such as HIV and other sexually transmitted diseases, specific contact patterns between individuals can be described more precisely by tracing transmission pathways, so that contact networks may be reconstructed [334, 335]. Alternatively, when the population size is rather small, detailed contact information between individuals can be collected for network construction. Once the population size is relatively large, one possibility is to select representative data and build a synthetic contact network based on the characteristics of theoretical or numerical studies [336]. Another one is to structure the population with the contact data aggregated according to the specific attributes or role of individuals, such as age, occupation, etc. [332, 337].

In addition, the shift of contact patterns in a population have an extremely large impact on the spread of infectious disease over the pathways changes [338]. So far, there have been many empirical explorations of contact patterns, involving various types of contacts [339, 340]. The contact patterns generally depend on the life context or attributes to which people belong, especially exhibiting age-specific or other setting-specific features related to

the susceptibility and infectivity which are reflected by the effective contact rate [341, 342]. In the following, we will discuss the construction of contact networks and the characterization of contact patterns according to a collected high-resolution contact data. Recalling back to section 1.2, one of the important characteristics of network structure is assortative mixing of nodes attributes. Here, we will focus on capturing the role of age-specific mixing patterns on the infection transmission by considering the likelihood of contacts between different age groups.

3.2.1 Data collection

To perform the study of infection transmission on data-driven contact networks, we first need to obtain the data that reflects complex human interactions in order to build a reliable contact network. Moreover, the study on contact dynamics in contagious diseases, especially respiratory infections, requires massive detailed data of human proximity. In this case, gathering more and more accurate and high-resolution data plays a key role in in-depth understanding the dynamics of contagion spreading.

Currently, there have been various methods to collect detailed information on individual contact events (e.g., duration, location) and proximity interactions between individuals, mainly by surveys and wireless sensors [343, 344]. Until now, the description of contact patterns have mostly relied on the data gathered by conducting surveys [332, 345, 346]. This data collection mechanism enable to distinguish various types of contacts (e.g. physical contacts included), and collect human contacts in different settings, such as home, school, etc. In addition, the survey answers from different age groups can provide valuable information, facilitating access to mixing patterns. Another informative source of data can be provided by the recently developed wireless technology. It has made it much more accessible to obtain relatively larger scale and spatio-temporal contact data by mobile devices or other state-of-the-art wearable sensors, such as WiFi, GPS, RFID sensors, Bluetooth, etc [347–349]. For example, the wearable wireless devices are useful to monitor and record close-range contacts that potentially transmit infectious diseases. The portable smartphones are possible to detect high fidelity information on the location and frequency of contacts between individuals.

There is no one-fit-all way to gather highly satisfactory data due to their exclusive drawbacks. For the answers from surveys, their accuracy might be affected by the design of questions and the biases from respondents [345]. Although the resolution and scale of the data gathered by wireless devices

are increased, there are still deficiencies in some cases. For instance, the data collected by Bluetooth scanners is relatively coarse resolution for close-contact transmitted disease [336]. The detection mechanisms through WiFi suffer from restricted communication protocols. Some limitations of wearable sensors lie in the restricted duration of usage, high cost and exclusion of the information on the events conducive to infection transmission [349]. Therefore, further campaigns of high-resolution data collection are always essential to devise models of disease spread in contact networks.

3.2.2 Characteristics of contact networks

The dynamics of infectious diseases are sensitive to the contact patterns which are known to be highly heterogeneous. The variance of contact patterns stems from social behavior, geographical features, population heterogeneity, etc. The contact patterns underlying the disease transmission between hosts govern the structure of the contact network [350, 351]. In a contact network, nodes represent the synthetic individuals labelled by their demographics, such as age, gender, geographical location, etc., and links is representative of contacts between individuals, labelled by the conditional probability of contagion transmission [335, 352]. In the case of airborne infections or sexually transmitted diseases, differential contact patterns within each age group are closely related to the final size of epidemics. Therefore, the exploration of age-specific or other setting-specific mixing patterns can assist in our interpretation of human behavior while also contributing to the design of epidemic models [353].

The contact patterns are generally embedded into contact matrices to describe the heterogeneity of contact behaviors which have a direct effect on the transmission process of infections. Mathematically, the contact matrix is generally denoted by $C_{a,b}$, characterizing the average number of contacts between groups a and b given the specific setting [166, 354, 355]. Technically, the mixing patterns can be presented in the form of a matrix proposed by Anderson and May, termed "Who-Acquires-Infection-From-Who" (WAIFW) matrix [196, 229]. Each element in the WAIFW matrix characterizes the infection transmission rate between different groups, namely $\beta(a, b)$ (i.e., the rate at which an individual in group a conducts an effective contact capable of yielding infection transmission with a person of group b). In the case of a simple system with two groups, the matrix is denoted by

$$C_{a,b} = \begin{pmatrix} \beta_{aa} & \beta_{ab} \\ \beta_{ba} & \beta_{bb} \end{pmatrix}. \tag{3.1}$$

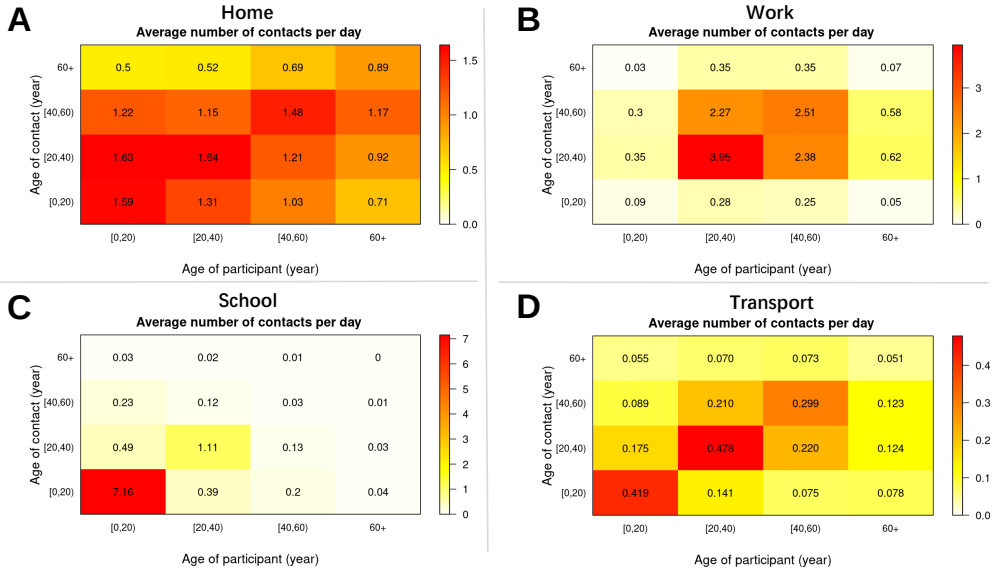

Figure 3.1: **Contact matrices of the Poland population in different locations.** The contact matrices extracted from the POLYMOD study [332] show the average number of contacts for different locations, i.e., **A)** home, **B)** work, **C)** school and **D)** transport. The diversity of contact patterns is dependent of the reality of each location.

Generally, it is necessary to assume a specific mixing pattern. The development of methodology for the estimation has evolved according to the change of transmission assumptions. For example, in the case of the well-known homogeneous mixing assumption, the transmission rate in WAIFW matrix is assumed to be the same independent of group characteristics [356,357]. There exist some deficiencies that hinder its further use in this methodology, such as the need of pre-judgement on the underlying structure and extra information needed. Another approach to estimate $\beta(a, b)$, called *contact surface model* fitted from large serological survey data, was proposed especially for the common infections transmitted by direct contact and airborne droplets [358]. However, these two methods under *ad hoc* scenarios restrict the portrayal of contact heterogeneity [349].

In addition, elements in contact matrix are specified parametrically based on the empirical data about contacts, such as the number of contacts, contact duration, etc. [359]. Over the last decade, inferring contact patterns from census data or other sources of data has gradually developed as an important direction for characterizing the infection transmission [219, 360, 361]. Along with that, the hypothesis, namely *social pattern hypothesis*, was proposed to

state the proportional relationship between transmission rates and contact rates, i.e., $\beta_{ab} \propto c_{ab}$, by applying self-reported social contact data [362]. It has become a fundamental idea of combining the social contact data with epidemic models. There is a landmark project, namely POLYMOD study, that provides an informative dataset involving social mixing contacts. The participants from eight European countries reported their socio-demographic information, such as age, sex, education level, etc. Meanwhile, the contact information during the specific time period between volunteers is recorded using contact diaries [332]. Numerous studies were conducted by making use of the POLYMOD contact data [361,363,364]. In Fig. 3.1, we show an example of comparisons between contact matrices in different locations which are based on the Poland data from the POLYMOD study. The mixing matrices describing contact rates between different age groups exhibit varying contact patterns under different settings that are compatible with the reality.

Under ideal circumstances, we should measure everything to the maximum extent appropriate to gather the most complete and detailed information, and to capture the most valuable part of the data that is indicative of infection transmission. Nowadays, there are more granular contact data available that provides the information on the relevant context for the occurrence of contacts [332,365]. However, in practice, it is impossible to build an ideal contact network that precisely characterizes the spreading processes, albeit with enormous advances in the ability to measure all aspects of contacts in terms of technology and mathematical theory. As a result, we have to exploit the data available to make a certain degree of plausible hypothesis and simplifications in line with our expectations [344]. In the following section, we will mainly discuss the theoretical framework for the age-dependent contacts further.

3.2.3 Age-dependent mixing patterns in contact networks

In a heterogeneous mixing population, it is plausible to observe the phenomenon that infected individuals in some age groups transmit diseases to more susceptible agents than average. Age is a significant source of demographic heterogeneity. For example, in the case of measles transmission, contact rates are perceived to be the highest among children [357]. In many respiratory infectious diseases, such as influenza, pertussis, especially the ongoing COVID-19 pandemic, age differences in transmissibility and susceptibility to infections make a great difference on the transmission process [221,363]. Therefore, it is crucial to explore the formation of contact network considering the age-dependent heterogeneity of population in order to understand

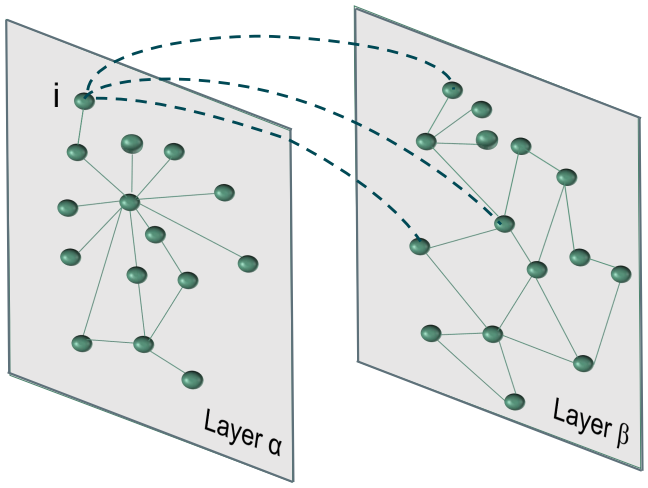

Figure 3.2: **A simplified framework of the age-specific contacts.** In the contact network, each layer denotes the contacts of each individual in a specified age group which means that the age of people in this layer falls within the age bracket. The node i has the degree in layer α is $k^{\alpha}_{i,\alpha} = 1$, while $k^{\beta}_{i,\alpha} = 3$ in layer β.

transmission dynamics of some specific infections diseases.

To accurately describe the process of infection transmission and effectively predict outbreaks on an age-structured network, the measurement of age-specific transmission parameters is a critical issue to be addressed. The method to model the age-specific contact patterns has evolved from being encoded in the form of WAIFW matrix, which is originally developed for characterizing the infection heterogeneity between different age groups, to being presented with social contact data, as in the POLYMOD study [332, 366].

Let us formally describe the construction of an age-dependent contact network with Poland data from the POLYMOD project. We firstly extract the contact distribution and demographic structure (i.e., age) from the dataset. Generally, the system with age-dependent mixing patterns is represented by a multilayer network, shown in Fig. 3.2. Each age group $[a_{min}, a_{max})$ is encoded in one layer l which means that the age of individuals in layer l is set in this bracket. The degree of node i in layer α with total number of nodes N_α is denoted as $k^{\alpha}_{i,\alpha}$, while the layer-to-layer degree of i, representing the contacts of i with nodes in layer β, is quantified by $k^{\beta}_{i,\alpha}$. The element in the adjacency matrix of age-structured multilayer networks is $\mathcal{A}_{ij}$ which represents the number of links between node i in layer α and j in layer β, given by

$$\mathcal{A}_{ij} = k_{i,\alpha} p_{\alpha(i),\beta(j)} \frac{k_{j,\beta}}{\sum_{l\in\beta(j)} k_l}, \tag{3.2}$$

where $p_{\alpha(i),\beta(j)}$ is the probability to connect node i in age group α and node j in age group β. It is time for the age-contact matrix to play a role in obtaining this value, which reads:

$$p_{\alpha,\beta} = \frac{M_{\alpha,\beta}}{\sum_\beta M_{\alpha,\beta}}, \tag{3.3}$$

The element $M_{\alpha,\beta}$ in contact matrix represents the average number of contacts between age group α and β, which is the scale typically reported when contact patterns are measured in an empirical way [332, 367–369]. There exists the reciprocity condition:

$$M_{\alpha,\beta} N_\alpha = M_{\beta,\alpha} N_\beta. \tag{3.4}$$

Note that $M_{\alpha,\beta}$ is the relatively common form of describing the contact matrix, which is called *intensive scale* [260]. There are another two magnitude usually used which are namely *extensive scale* and *density scale*, denoted by $C_{\alpha,\beta}$ and $F_{\alpha,\beta}$, respectively. The extensive scale represents the total number of contacts between two age groups with relation to matrix $M_{\alpha,\beta}$, i.e.,

$$C_{\alpha,\beta} = M_{\alpha,\beta} N_\alpha, \tag{3.5}$$

which is a symmetry matrix [370]. The density scale is also related to the commonly used matrix $M_{\alpha,\beta}$, written as:

$$F_{\alpha,\beta} = \frac{M_{\alpha,\beta}}{N_\beta} = \frac{C_{\alpha,\beta}}{N_\alpha N_\beta}. \tag{3.6}$$

Similarly, the matrix is symmetric. Although these two scales are to be constructed more readily due to their non-reciprocal property, they are characterized by the fact that they cannot remain unchanged as the total number of people increases. Therefore, we mainly use $M_{\alpha,\beta}$ as the representation of contact matrix to keep the shape of demographic structure in the following section to model the real disease transmission.

To illustrate the procedure for generating a synthetic age contact network, we take the Poland population from the POLYMOD study as a sample [332]. As previously mentioned, the first step is to perform the preparation of the data that contains the degree distribution of the number of contacts, the demographic information and the contact matrix (see Fig. 3.3(A), (B) and (C)).

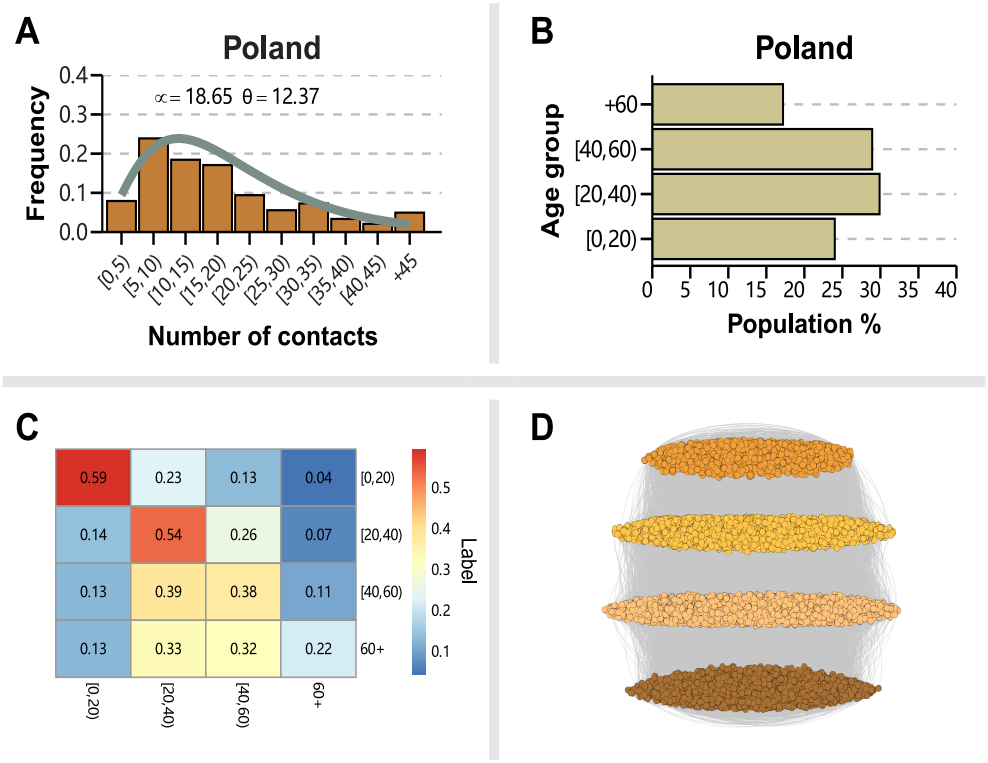

Figure 3.3: **The construction of synthetic age contact network for the Poland population. A)** The distribution of number of contacts. **B)** The proportion of the population within each age-group. **C)** The heatmap of contact matrix. **D)** The visualization of age-specific network where each layer represents each age group.

For ease of calculation and presentation, we classify the population into four age groups simply with 20 y.o. as a dividing line. In Fig. 3.3(A), the empirical contact distribution based on the reported data from the study is discrete and right-censored. Here, the negative binomial distribution, that is the most typical methods for the analysis of survey data [371], is used to fit the degree distribution with mean value μ and size θ. In the process of generating age contact networks, the number of nodes needs to be determined with specific age assigned. In our case, we set the number is $N = 10^4$ with age sampled in proportion to the demographic structure in Fig. 3.3(B). Then, the degree of node in each age group is assigned by sampling from the negative binomial distribution. The required parameters in the distribution are the average number of contacts taken from the age-mixing matrix (see the heatmap in Fig. 3.3(C)) and the dispersion (i.e., size) from the previous fit. Eventually, we construct the synthetic contact network by connecting the nodes in differ-

ent layers with mixing patterns exhibited in Fig. 3.3(D). In the next section, we will employ this framework to estimate the herd immunity threshold of ongoing SARS-CoV-2 pandemic.

3.3 Data-driven Estimate of SARS-CoV-2 Herd Immunity Threshold

Data-driven estimate of SARS-CoV-2 herd immunity threshold in populations with individual contact pattern variations [372].

D. Lu, A. Aleta, M. Ajelli, R. Pastor-Satorras, M. E. Halloran, A. Vespignani, and Y. Moreno

The SARS-CoV-2 pandemic has resulted in the implementation of non-pharmaceutical interventions (NPIs) of different intensity with the aim of reducing the burden of the disease on the healthcare system and minimize deaths among the population. Preventive measures and severe restrictions alike strive for a reduction of social mixing and contacts among individuals [373–379], which help diminish transmission of the virus and ensure the proper functioning of health-care systems. Thus far, only a few countries have used NPIs to pursue a suppression policy with long and strict lockdowns until community transmission is locally eliminated followed by control at borders [373]. The development of several efficacious vaccines against SARS-CoV-2 [380, 381] and the start of vaccination campaigns open a new chapter in the fight against COVID-19. At the center of the discussion about vaccine is the herd immunity threshold, i.e., when the epidemic starts to decline after a critical fraction of individuals in the host population is immune [382, 383].

Herd immunity is the level of immunity in a population of hosts, in contrast to an individual host. Herd immunity can be high if much of the population is immune to infection, or low if a lower proportion of the population is immune. The higher the herd immunity, the harder it is for a pathogen to find susceptible hosts and to maintain chains of infection, and the epidemic slows. When a certain level of population immunity, known as the herd immunity threshold, is reached, the epidemic starts to decline, at least locally. The herd immunity threshold can be achieved either because hosts become immune once recovered from infection or via vaccination of susceptible hosts. These two alternatives for the suppression of SARS-CoV-2 have been at the center of policy and public debates [383], along with the discussion concerning the calculation of the herd immunity threshold in realistic populations and trans-

mission settings [382, 384, 385]. Furthermore, vaccine production constraints, lack of definitive information on effectiveness properties of the vaccines, and logistic issues in rolling out vaccination campaigns have raised the question of what vaccination strategies should be implemented to avoid social disruption and avert the largest possible number of deaths regardless of herd immunity threshold considerations.

In this work, we focus on two important determinants for the evolution of the incidence of COVID-19 that are encoded in the structure of the population, namely, age and contact patterns. These two components shape individuals' social mixing, hence, how chains of transmissions emerge and grow. To this end, we will use modeling framework present in section 3.2.3 for generating contact network with age-dependent mixing patterns. The contact network with the social interactions of populations will be represented in the form a multilayer network, in which layers correspond to different age groups and connectivity patterns are encoded in both intra- and inter-layer connections [51, 316]. The age-mixing matrices of 34 countries are obtained from the Ref. [361] thanks to the advances in data science. Then, we will use a SARS-CoV-2 stochastic transmission model [221] which is a SEIR-type epidemic model (see section 2.2.1) to estimate the infection-induced immunity threshold. In addition, we will have in-depth discussions of different vaccine prioritization strategies in the context of averted deaths and with respect to the overall disease infections.

3.3.1 Data description

To estimate herd immunity threshold and vaccination coverage in populations with realistic individual contact pattern variations, we collected age and behavioral mixing patterns for several countries from all continents except Antarctica that are structurally different in at least one of the two ingredients i.e., age and contact patterns. The age mixing matrix of each region and country was obtained from [361]. The 85 age-groups originally considered in Ref. [361] were aggregated into 18 groups, going from age 0 to 84 in groups of 5 and a last group for 84 years old or older. For the degree distribution, we rely on the survey on contact patterns that was carried out in Italy for the POLYMOD project [332]. In such survey, the distribution of contacts per age-group can be described using a negative binomial distribution, see Fig. 3.4. For this reason, we choose a negative binomial distribution for the number of contacts per individual in each layer. As previously mentioned, the average of the distribution is fixed in each layer by the value of the age mixing matrix.

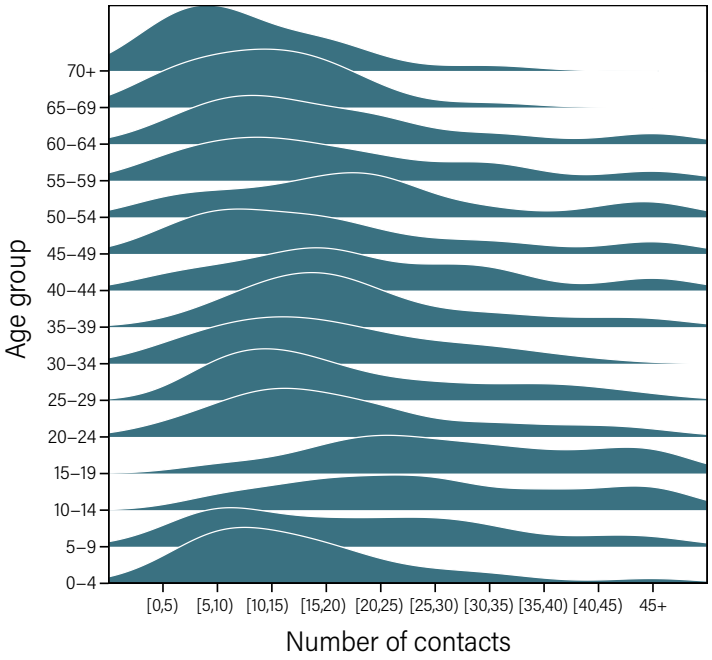

FIGURE 3.4: **Degree distributions for each age bracket with POLYMOD data for Italy.** The maximum number of contacts that could be reported in the survey was 45, as such the empirical distributions are right-censored at that value.

However, the size of the distribution (also known as dispersion parameter) is not, since this parameter depends on the individual variability, but the matrices were obtained using data aggregated by age-group. To properly obtain the distribution, it would be necessary to carry out surveys similar to POLYMOD for each region under consideration, but this type of data is still scarce [386].

In this work, due to the we have parameterized the size of the distributions based on the survey from Italy. This lack of data introduces a limitation for the comparison of different countries, since the different socio-cultural elements of each region might influence the variability of the distribution in some regions. Here, in the construction of networks, we mainly apply the negative binomial distribution.

3.3.2 Network construction

We assign to each node an age group and a number of contacts per unit of time, both extracted from empirical distributions characterizing the demographic structure and the behavioral (contact) pattern of the population. We have

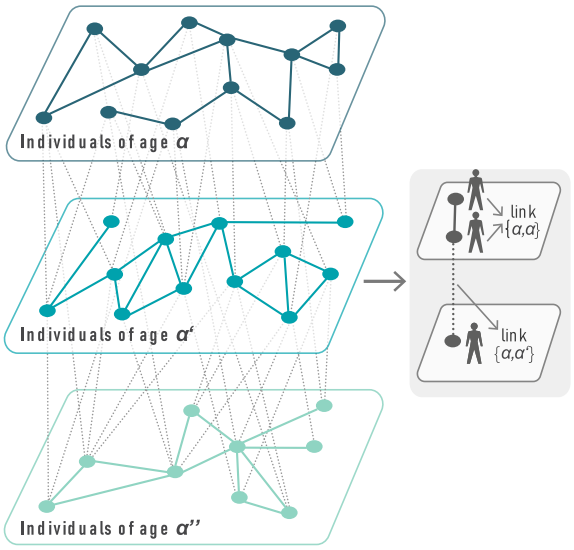

Figure 3.5: **Model of population structure.** The structure of the population is encoded in a multilayer network, and consists of 18 layers, in which connections among nodes on the same layer correspond to mixing between individuals belonging to the same age group (diagonal elements of the contact matrix), whereas interlayer connections account for mixing between different age groups.

considered 18 age-groups, which leads to a multilayer network made up by that same amount of layers, with a number of nodes per layer, N_α, equal to the total number of persons of the age-group of layer α in the synthetic population.

To connect the nodes of the network while satisfying the age mixing patterns, we employ the method introduced in section 3.2.3 to generate adjacent matrix. Note that at each time-step we extract a new network realization from the ensemble generated by $\langle \mathcal{A}_{ij} \rangle$. Fig.3.5 schematically represents the resulting multilayer network for a single time-step [316].

3.3.3 SARS-CoV-2 transmission model

The dynamics of the infection can be described by a SEIR model like the one we introduced in section 2.2.1. But, the compartments in SEIR are too simple to mimic realistic scenarios. In this work, it has been modified to accommodate COVID-19 natural history and the key aspects of SARS-CoV-2 transmission, including asymptomatic infectious individuals and several age-dependencies [387,388] of the model parameters. We use a stochastic, discrete-time compartmental model on top of the multilayer network in which individ-

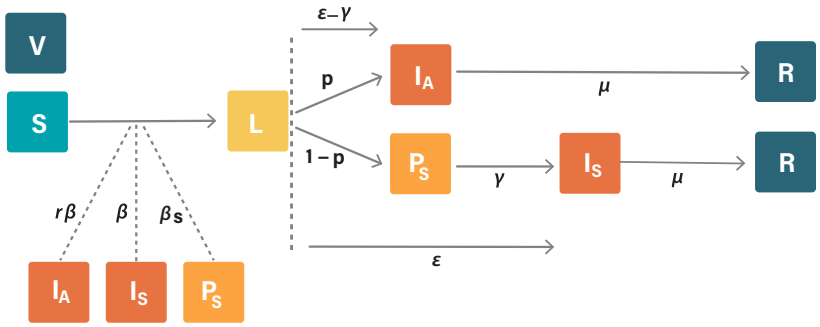

FIGURE 3.6: **Compartmental model description.** The different compartments and transition times from one to another are shown.

uals transition from one state to the other according to the distributions of key time-to-event intervals. The general structure of the model is depicted in Fig. 3.6. A susceptible individual (S) will become infected with probability β_S if she contacts a pre-symptomatic (P_S) individual, β if the contact is with an infectious symptomatic individual (I_S), and $r\beta$ if the contact is in the infectious asymptomatic state (I_A). Once infected, the individual will enter the incubation compartment (L) for a period extracted from a gamma distribution, ϵ, during which she will be infected but not infectious yet. A latent individual will become infectious γ days before the end of the incubation period, to account for pre-symptomatic transmission. Lastly, the individual will be removed (R) from the infectious pool according to an exponential process with rate μ^{-1}, where μ is the average length of the infectious period in days. In order to check on the parameters' assumption we measured in the model the generation time that is in agreement with the epidemiological data. Note that the removed compartment does not imply recovery, only that the individual is no longer infectious. To estimate the number of deaths we later apply the empirical IFR to the set of removed nodes. When vaccination is taken into account a new compartment, V, is created, to distinguish between removed individuals who actually had the disease and those who did not.

3.3.4 Estimate of R_0

In homogeneous populations, the basic reproduction number of this model can be expressed as:

$$R_0 = \frac{\beta r p}{(\gamma+\mu)^{-1}} + \frac{\beta(1-p)}{\mu^{-1}} + \frac{\beta_S(1-p)}{\gamma^{-1}}, \tag{3.7}$$

Parameters	Description	Age group	Value	Ref.
r	relative infectiousness of asymptomatic individuals	-	50%	†
k	proportion of pre-symptomatic transmission	-	50%	[389]
ϵ	incubation period (gamma distributed)	-	shape = 2.08 rate = 0.33	[390]
p	proportion of asymptomatic	-	40%	[389]
γ	pre-symptomatic period	-	2 days	[391]
μ	time to removed	-	2.5 days	$*$
IFR	infection fatality ratio	0-19 20-49 50-59 60-69 70-79 ≥ 80	0% 0% 0.35% 0.88% 5.59% 8.15%	[392]

Table 3.1: Set of parameters of the transmission model. †: assumed ;$*$: calibrated to the generation time T_g.

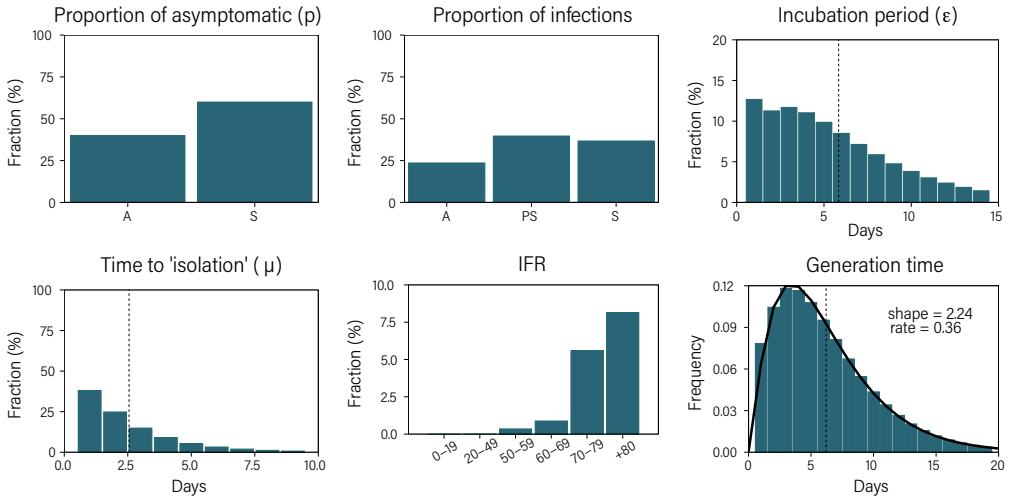

Figure 3.7: **Distributions obtained in the simulation.** Numerical distributions of the model parameters extracted from the simulations performed for Italy with $R_0 = 2.5$. The generation time distribution is well fitted by a gamma distribution with shape = 2.24 and rate = 0.36.

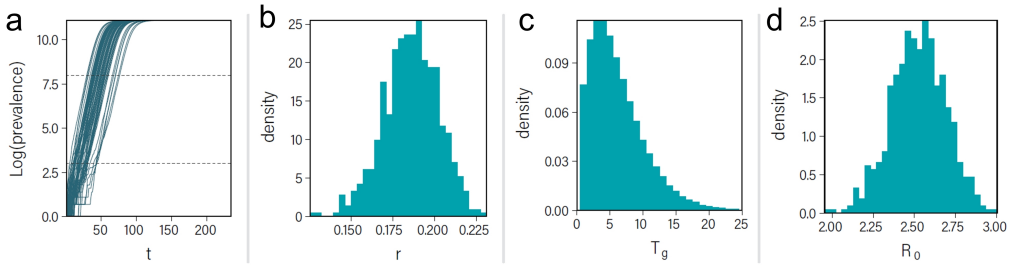

FIGURE 3.8: **Estimation of R_0. a)** Temporal evolution of the logarithm of the prevalence. **b)** Estimated growth rate. **c)** Generation time extracted from the simulation. **d)** R_0 obtained using equation (2.75).

where $\beta_S = \beta\gamma^{-1}k/\mu^{-1}(1-k)$. The description and values of all the parameters is shown in table 3.1. Note that this expression is only valid for homogeneous populations. In structured populations, the particular value of R_0 of each individual will depend on her connectivity. Furthermore, in layers 0 to 3, corresponding to age groups $[0-5), [5-10), [10-15), [15-20)$, individuals have a susceptibility to the disease of 0.56 [388]. As such, in each network, to select the appropriate value of β, we empirically estimate the dependency of R_0 with β. In Fig.3.7 we show some of these distributions directly measured from the output of the model.

Our model does not allow a simple analytical calculation of the R_0 as in the homogeneous assumption. In order to match our simulations with a specific R_0 as measured in a real world setting, we consider the relationship between the reproduction number, epidemic growth rate, and generation time [216]. As we mentioned in section 2.2.4, we follow [216] and estimate the value of the basic reproduction number using the empirical (measured from the simulations) generation time with Eq. 2.75. In Fig. 3.8, we show: (a) the temporal evolution of the prevalence from which the growth rate, r can be estimated (b); (c) the generation time obtained from the simulation; and (d) the corresponding value of R_0.

3.3.5 Estimate of SARS-CoV-2 herd immunity threshold

First, we consider the situation in which the infection circulates unmitigated through the host population (with no mitigation policies in place) and calculate the infection-induced herd immunity threshold (IHIT). This is defined as the proportion of all infected individuals (symptomatic and asymptomatic) at the inflection point (the maximum) in the curve of the incidence of latent individuals. This is the point in time at which the effective reproductive number

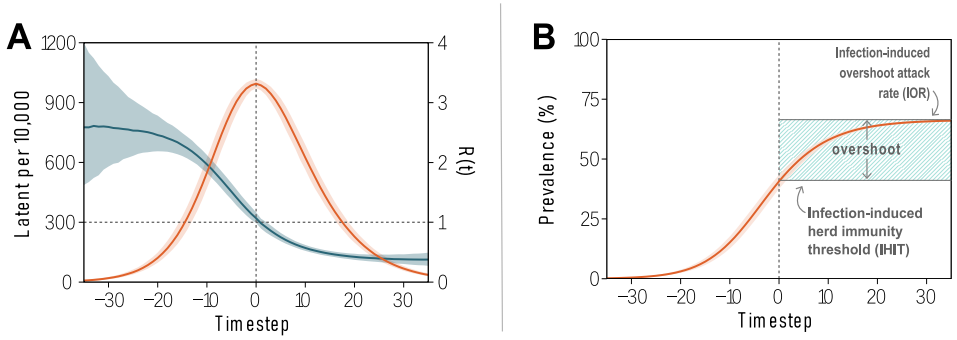

Figure 3.9: **Definition of IHIT and IOR. A)** In orange, individuals in the latent state as a function of time. Simulations are temporally aligned so that the maximum number of latent individuals is reached a time equal to 0. In dark blue evolution of the effective reproduction number computed using the number of newly infectious individuals and a gamma-distributed generation time with shape 2.12 and rate 0.32. **B)** Cumulative fraction of the population that has contracted the disease. We identify the IHIT and the IOR as well as the overshoot fraction of infections.

for the generation of new infections (new latent individuals) decreases below the epidemic threshold of 1 and the epidemic begins to wane, see Fig. 3.9(A). The infection-induced overshoot attack rate (IOR) can then be calculated letting the system evolve until the epidemic dies out naturally because there are no more new infectious individuals circulating in the population, Fig. 3.9(B).

We executed stochastic simulations of the epidemic transmission model and computed numerically the IHIT and IOR values associated with the multilayer network of each country considered. In Fig. 3.10, we report the simulations for the multilayer network built on the Italian data. Our estimate for the infection-induced immunity level for the population of Italy in the case of $R_0 = 2.5$ is 41% [95% CI 38-44]. This value represents the minimal proportion of the population that needs to acquire immunity through infection to thwart circulation of the virus without any NPIs in place. In Fig. 3.10(C), we report the estimated IHIT and IOR values for different R_0 values. It is worth remarking that the values obtained differ considerably from the values obtained for the same R_0 in a homogeneous model, because of the heterogeneous connectivity patterns of individuals.

To simulate the epidemic behavior in a population that has achieved a specific infection-induced immunity level, we performed further numerical simulations in which the system is evolved until a given proportion of the population is infected. Then, we use the infection-induced immune and susceptible population as the initial condition of a new epidemic started with a single infected

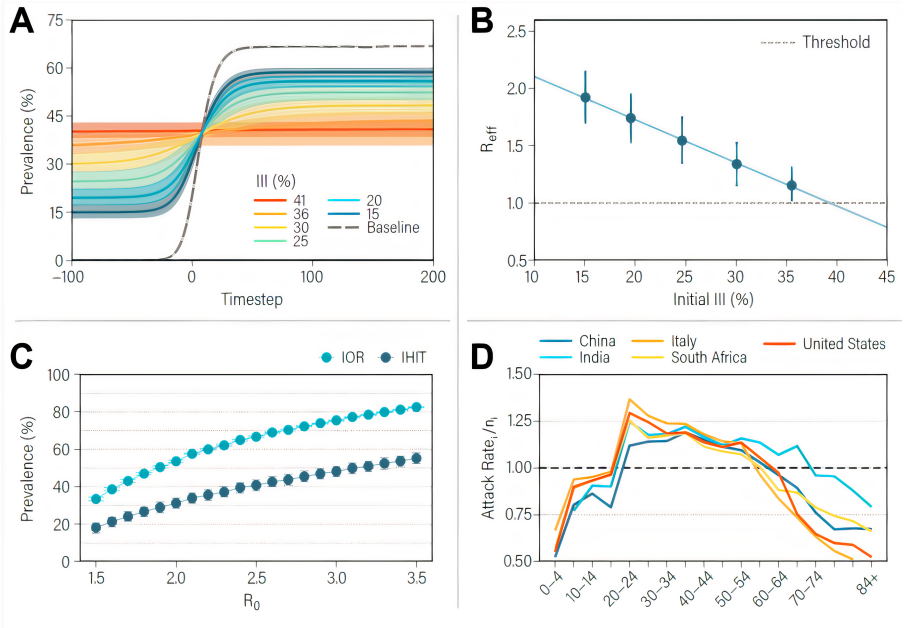

FIGURE 3.10: **Infection-induced immunity threshold (IHIT). A)** Prevalence of the infection in populations with different initial infection-induced immunity (III). In all plots, solid lines represent the median value for 10,000 stochastic realizations and the shaded area the 95% C.I. **B)** The number of secondary infections produced by the seed individual, R_{eff}, is measured in networks with different amounts of initial infection-induced immunity. Results shown in panels A and B correspond to the population of Italy and $R_0 = 2.5$. **C)** Prevalence in the Italian population for different values of R_0 at the peak (IHIT) and at the end of the simulation the infection-induced overshoot attack rate (IOR). **D)** Infection attack rate in each layer over the fraction of nodes that belong to that layer for different countries worldwide versus age-group contained in the layer. Results in panel D correspond to $R_0 = 2.5$.

individual and record the OR reached by letting the epidemic spread unmitigated. This approach mimics a scenario in which the virus is circulating through the population until strict measures cut transmission and reduce incidence to vanishing values, which is followed by the reintroduction of new infectious individuals once such restrictions are lifted. Fig. 3.10(A) shows the results obtained for several values of infection-induced immunity (III) proportion when the pathogen is seeded again. As can be seen, the OR depends on how close the system is to the IHIT. For comparison, we consider as the baseline the curve and IOR corresponding to the situation in which the epidemic spreads unmitigated in a fully susceptible population. The closer the population is to the IHIT, the smaller the overshoot generated by a second

epidemic and the final OR would be.

The previous observation can be further explored using a semi-analytical argument. We may define the number of secondary cases that the seed individual can produce upon reintroduction of the pathogen in the community as R_{eff} (in contrast to R_0, which applies only for the first introduction to the community, i.e., when the whole population is susceptible). In classical heterogeneous populations this value is known to be dependent on both the mean and the variance of the number of contacts per individual [393]. Actually, in the classical SIR model on networks, this value can be expressed as $R_{\text{eff}} = R_0^H \cdot \frac{\langle k^2 \rangle - \langle k \rangle}{\langle k \rangle^2}$, where R_0^H is the reproduction number in the homogeneous model and the second term is a function of the topological properties of the network, its average degree $\langle k \rangle$ and the second moment of the degree distribution, $\langle k^2 \rangle$ [10, 82]. In our model the previous history of infection affects the terms depending on the moments of the degree distribution. Indeed, if some individuals have been removed from the susceptible population after a first wave of infections (either due to recovery or death), the structure of the network changes, modifying the value of R_{eff}. If the network is in a state such that $R_{\text{eff}} < 1$, then reintroduction of the pathogen in the community cannot produce a large outbreak. However, if we remove nodes randomly the values of $\langle k \rangle$ and $\langle k^2 \rangle$ assume a different value thus poising the population not at the IHIT. In Fig. 3.10(B), we explore the value of R_{eff} as a function of the initial III. Note that even though for an III slightly smaller than 41%, the average R_{eff} is close to the threshold, it is possible to have large outbreaks. To provide a better interpretation, we study the size distribution of outbreaks produced in a hypothetical second introduction of the pathogen in populations that completely eliminated it within the III scenario shown in Fig. 3.11. In panel a, we show the fraction of events leading to an outbreak of a given size when the first wave infects 41% of the population (corresponding to the IHIT value). In panels b and c we do the same but with 38% and 36% of initial infection-induced immunity, respectively. Clearly, while outbreaks in the situation close to IHIT are very small, once we move away from that point a second peak in the distribution appears, reflecting the emergence of a giant component in the network created by the infection path.

The preceding expression highlights the role the degree distribution plays in the spreading of infection. Because this distribution is partially determined by the age-mixing patterns of the population, it is expected that the path the infection will follow should vary according to the specific socio-demographic features of each population, which can influence the transmission in our model

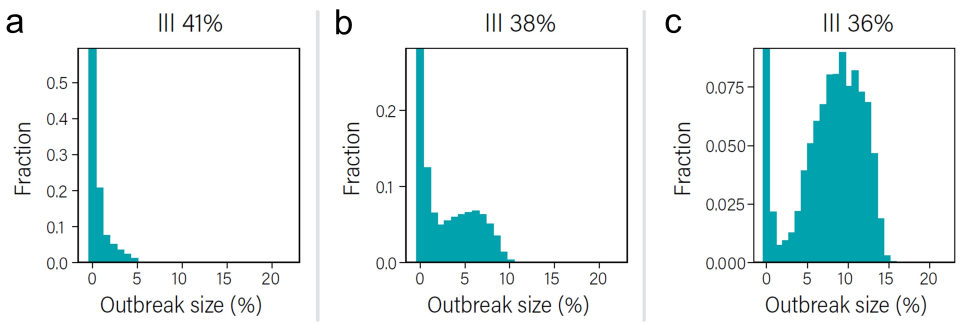

FIGURE 3.11: **Outbreak size in III.** Size of outbreaks produced with different values of initial infection-induced immunity in the population. Panel a shows the results for an initial immunity at the IHIT value, while b and c show examples of situations with slightly smaller initial immunity.

in 3 ways: (i) by changing the degree distribution in each layer; (ii) by modifying the shape of the age mixing patterns; and (iii) through cultural or environmental factors that influence how effective is the transmission of the virus, i.e., the value of β in our model. Unfortunately, we cannot analyze the differences induced by the first factor since that would require precise information on the individual variability of people in each region. The second factor, on the other hand, can be easily studied thanks to the availability of high resolution mixing matrices [361]. In Fig. 3.12(A), we present the value of IHIT obtained in each available region with $R0 = 2.5$ in comparison to the one obtained for Italy.

The previous factors, in essence, only modify the contact matrix. However, there are multiple other elements that can modify the transmissibility of the virus: the way in which individuals of a certain culture greet each other, the distance at which individuals usually interact, the way in which they talk, whether they are used to wear masks, as well as environmental factors that could enhance or diminish the spreading of the virus. In terms of our model, this would imply a different value of β for each region which, once applied to each network (i.e., population structure), could in turn yield a larger or smaller R_0. Note that β and $\langle k \rangle$ are not necessarily correlated, and there could be the case of regions with larger β and lower $\langle k \rangle$ having the same value of R_0 as regions with lower β, as long as their $\langle k \rangle$ were larger. In fact, in the previous comparison we fixed R_0 in all regions, so that the value of β was adapted to the specific contact matrix.

Conversely, in Fig. 3.12(B), we fix the value of β to the one that sets the value of R_0 equal to 2.5 in Italy, and apply it to the rest of the regions. Hence,

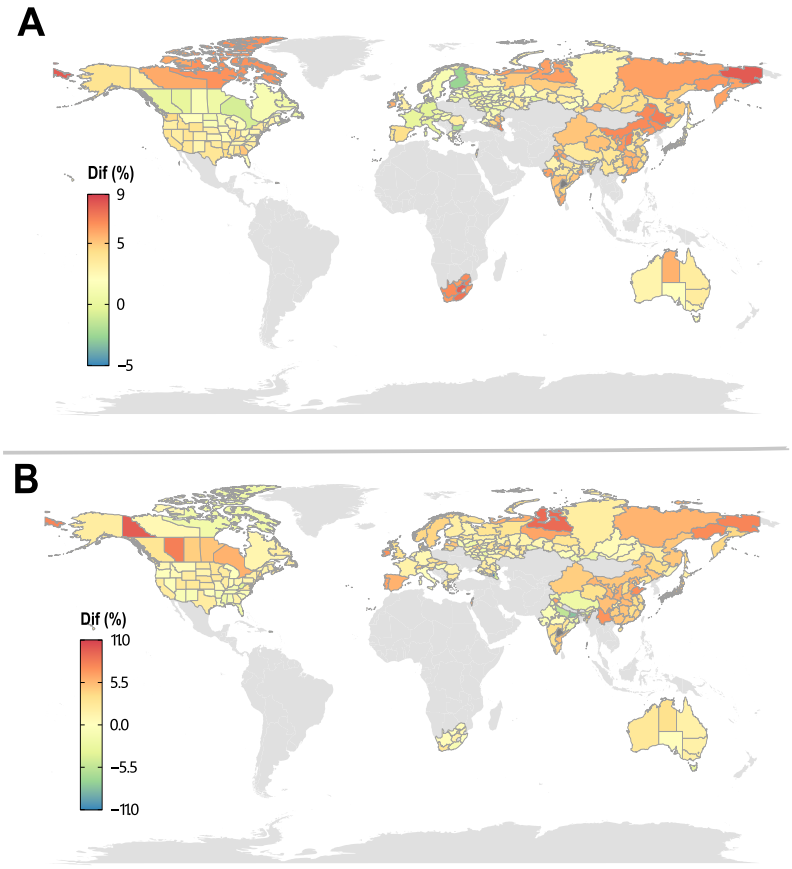

Figure 3.12: **IHIT for several countries from all continents except Antarctica. A)** IHIT in each region with fixed R_0. We set $R0 = 2.5$ and a dispersion parameter for the distributions equal to the one in Italy. **B)** IHIT in each region with fixed β. We set the value of β in all regions to the one that yields $R0 = 2.5$ in Italy. Relative difference of the IHIT value obtained in each region in comparison with the one in Italy.

the value of R_0 will vary, being larger in those areas with larger $\langle k \rangle$, and smaller in those with a smaller $\langle k \rangle$. In this case, we observe larger differences, up to 8%. However, note that in the extraction of the mixing matrices it is assumed that the number of contacts in each setting is the same, regardless of the country (see [361] for details). Thus, if more precise information on the degree distributions in each country were available, the divergences could be much higher. In Fig. 3.10(D), we can see that the path followed by the infection is clearly different from region to region. This is revealed by looking at the attack rate within each age-group (layer) over the fraction of the population that belongs to that group at IHIT, which shows that some age-groups are

more affected by the infection (values larger than 1) than what would be expected if the infections were randomly distributed across the population. In network terms, if there were no correlations between age and connectivity, the normalized attack rate should be 1 for all age-groups. This, in turn, has important implications for defining vaccine prioritization strategies if we aim to reproduce the path the infection would follow in our population.

The above results are relevant to estimate the proportion of the population that needs to be vaccinated for the remaining susceptible individuals to be protected by the group immunity. Moreover, the vaccination coverage depends on how the population is vaccinated. We considered three different scenarios for vaccination: (*i*) the classical random mass vaccination; (*ii*) a behavioral vaccine prioritization scheme in which the first individuals to be vaccinated are those that are more likely to transmit the infection; and (*iii*) a fatality-rate prioritization strategy that targets the eldest first and then vaccinates individuals in decreasing order according to their age. Specifically, at the initial state, a proportion v of the population is immunized. We consider an all-or-nothing vaccine with 95% efficacy in preventing SARS-CoV-2 infection. In scheme (*i*), the fraction v of vaccinated individuals is chosen at random within the whole population. Scheme (*ii*) tried to mimic closely how infection-induced herd immunity is produced. We first simulate the propagation of the disease up to the IHIT to detect those individuals who are more likely to get and transmit the infection in the early stages of the epidemic. Then, we reset all individuals to the susceptible state and extract a random fraction v of those previously identified individuals and vaccinate them. In this way, we mirror how the infection confers natural immunity targeting the individuals that would likely be infected during the natural course of the epidemic. Finally, in scenario (*iii*) the first to be vaccinated are those in the eldest group (85 y.o. or more) and the process continues down in age until the fraction v of immune individuals is reached. In all cases, we start from a completely susceptible population prior to vaccination.

In the light of each of the strategies defined above, we calculate the prevalence of the infection obtained when an initial proportion of the population is first vaccinated and then SARS-CoV-2 spreading is simulated in the population shown in Fig. 3.13. We have considered the same values of Fig. 3.10 for v and a baseline scenario in which no individuals are immunized when the epidemic emerges. As expected, the prevalence of infection in the vaccinated populations decreases when the proportion of immunized individuals in the population increases. However, as not everyone in the population contributes equally to the transmission of infection, protecting the population as a whole

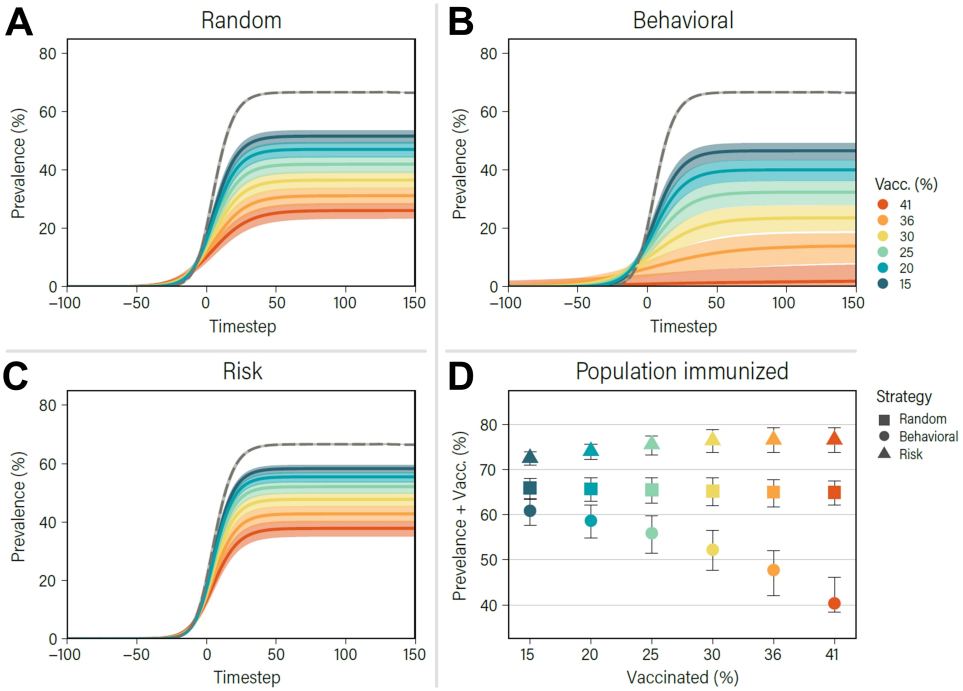

Figure 3.13: **Effect of different vaccine prioritization strategies.** Solid lines represent the median prevalence of the infection as a function of time under the random **(A)**, behavioral-based **(B)** and risk-based **(C)** vaccine prioritization. The dashed lines account for a baseline scenario in which there is no vaccination nor any non pharmaceutical interventions. **D)** Fraction of the population that is removed from the dynamics due to vaccine-induced immunity, infection-induced immunity or death once the disease dies out, for the different vaccination strategies as a function of the vaccine coverage. Results correspond to the population of Italy for $R_0 = 2.5$.

is contingent on the vaccination strategy. Specifically, our results show that the best strategy in terms of reducing the prevalence of the infection is the second scenario, Fig. 3.13(B), as our estimate for this scheme is consistent with the infection-induced threshold computed previously, i.e., a vaccination coverage close to the IHIT would protect the whole population from SARS-CoV-2 infection. Interestingly, random vaccination (Fig. 3.13(A)) also leads to lower prevalence values than the risk vaccination (Fig. 3.13(C)), as immunized individuals are spread through different age groups, which contributes to reducing the circulation of the virus with respect to the risk scenario, that only protects, for most values of v, groups that in general play a secondary role in transmission. Indeed, in Fig. 3.13(D) we also show (full colored dots) the final proportion of removed individuals (i.e., all individuals that are not sus-

Number of averted deaths per 10,000 | $R_0 = 2.5$						
Vaccinated(%)	**Random**		**Behavioral**		**Risk**	
41	33.5	[31.6 - 35.5]	49.5	[46.4 - 50.2]	49.0	[48.9 - 49.1]
36	29.6	[27.3 - 31.8]	41.0	[37.1 - 45.0]	48.4	[47.7 - 48.9]
30	25.3	[22.9 - 27.8]	32.6	[29.0 - 36.0]	47.1	[46.4 - 47.8]
25	20.9	[18.7 - 23.3]	25.5	[22.5 - 29.1]	45.7	[44.5 - 46.5]
20	16.8	[14.7 - 19.0]	19.6	[17.0 - 22.6]	43.3	[42.1 - 44.6]
15	12.9	[11.2 - 15.0]	14.7	[12.7 - 17.2]	41.1	[38.1 - 42.3]

Table 3.2: Median number of averted deaths [95% C.I.] for each strategy per 10,000. In each strategy the population is initially immunized through vaccination under the rules explained in the main text. Results correspond to the population of Italy and an assumed $R_0 = 2.5$.

ceptible at the end of the outbreak) for the different vaccination strategies and percentage of vaccinated population. Random and risk vaccination schemes lead to a final fraction of removed individuals that is greater than the IHIT, yielding comparable or greater levels with respect to the final prevalence in the baseline scenario. This also implies that the vaccine coverage needed to reach the herd immunity threshold with those strategies is generally considerably larger than the IHIT. The final proportion of infections instead depends on v for the behavior-based vaccination that mimics the immunity produced by the infection progression.

Remarkably, although the risk strategy leads to the highest prevalence levels for any proportion of vaccinated individuals, it is the one that averts the most deaths, even when the vaccine is extremely efficacious in blocking forward transmission. We estimate from simulations the total number of averted deaths for each vaccination strategy. Table 3.2 shows the number of averted deaths for each vaccine prioritization strategy with respect to the counterfactual unmitigated scenarios. Risk vaccination greatly reduces the number of deaths due to COVID-19 even for a proportion of vaccinated individuals as low as 15% -almost a factor 3 compared to the second best strategy. These results apply as well to vaccines with lower efficacy 60% see in Fig. 3.14, although they require higher coverage for the behavioral strategy to work. It is important to stress that the results presented here could be relevant in the context of other respiratory diseases. However numerical studies considering vaccine efficacy and infection fatality rate specific to each disease should be carried out.

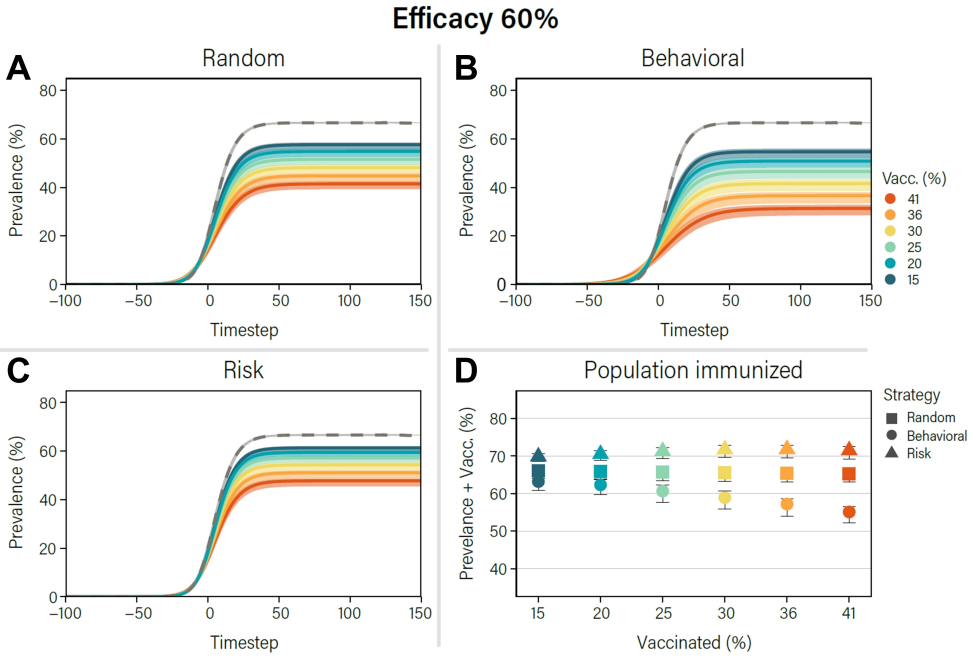

Figure 3.14: **Effect of different vaccination strategies.** Solid lines represent the median prevalence as a function of time under the random **(A)**, behavioral-based **(B)** and risk-based **(C)** vaccine prioritization. The dashed lines account for a baseline scenario in which there is no vaccination nor any non pharmaceutical interventions. **D)** Fraction of the population that is removed from the dynamics due to vaccine-induced immunity, infection-induced immunity or death once the disease dies out, for the different vaccination strategies as a function of the vaccine coverage. The results correspond to the population of Italy for $R_0 = 2.5$ and a vaccine efficacy of 60%.

3.3.6 Conclusions

In this work, we have developed a data-driven multilayer population network that takes into account two factors that play a key role in shaping SARS-CoV-2 transmission and COVID-19 burden, namely, social mixing patterns as given by the number of contacts and age of the individuals of a population. Importantly, our framework needs information only at the population level, from which the network encoding the social mixing is built up. We provide numerical estimates of the IHIT and IOR in realistic populations and show the effects of different vaccination strategies and rates on possible resurgences of the epidemic. The estimates provided in this work refer to the historical SARS-CoV-2 lineage emerged in Wuhan. Although the results hold in general, quantitative estimate may be different for other SARS-CoV-2 variants with

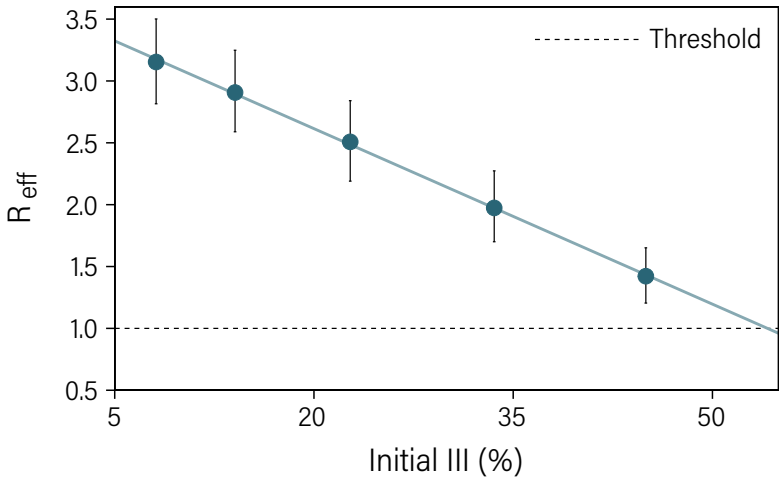

FIGURE 3.15: **Effective reproduction number as a function of initial III.** The immunity induced by the infection modifies the underlying structure of the contact network, diminishing the average number of infections that can be produced by each infectious individual. With $R_0 = 3.5$ the IHIT value is close to 55%.

immune escape. Due to the more robust infectivity of the variants, we assume that the effective number of transmissions reaches to $R_0 = 3.5$ in contrast to the one shown in the previous calculation ($R_0 = 2.5$). In Fig. 3.15, we show the effective reproduction number as a function of the initial III obtained with $R_0 = 3.5$. We observe that the decay is slower and that the value of IHIT is above 50%. This implies that new variants of the virus might modify the fraction of the population that needs to acquire immunity to reach the herd immunity threshold. It is however important to stress that the proposed framework is general enough to be used for the analysis of other infectious diseases such as influenza, which may benefit from age-targeted vaccination programs [394].

Our findings have the following important implications: (i) the variability in social interactions of the population determines the herd immunity threshold; (ii) Risk-based and random vaccination scenarios require higher levels of vaccination coverage to suppress the circulation of SARS-CoV-2 compared to the infection-induced herd immunity; it will thus be of paramount importance to extend vaccination efforts well after reaching the theoretical herd immunity threshold. The previous implications suggest that more research is needed to determine the optimal vaccination strategy considering, and possibly adapting to, the constantly evolving epidemiological situation and tailored to different

populations as there is no one-fits-all solution. For instance, allowing for higher prevalence of acute infection would keep health care systems under pressure longer, which in turn entails the need to keep restrictions and interventions. Additionally, it might have potential important consequences for virus evolution and the emergence of new variants as well as for public health systems given that the long term health consequences of suffering SARS-CoV-2 infection could be severe [395]. Finally, our work also estimates that in many cases the level of coverage needed to achieve the herd immunity threshold in the population may be larger than the fraction of eligible population, especially considering hesitancy and accessibility to vaccines [396, 397]. In several countries this might imply shifting the focus on using vaccines to reduce mortality rather than aiming at reaching the HIT.

3.4 Spatial Spreading of Diseases in Hospitals

Assessing the risk of spatial spreading of diseases in hospitals. (*In preparation*)

D. Lu, A. Aleta, and Y. Moreno

In recent years, the transmission of healthcare-associated infections (HAIs) has led to substantial economic loss, extensive damage and many preventable deaths. A hospital is a setting in which relatively confined spaces create the conditions for constant exposure to infections. The risks related to HAIs are however heterogeneous and spatially distributed, with some categories of spatial units and healthcare workers (HCWs) showing particularly high risks due to their function or mobility through the whole hospital. Despite the fact that previous studies have shown the need to contain HAIs, their dynamics have not attracted much scholarly attention. In this work, we aim at quantitatively assessing the infection risks regarding spatial units and individuals.

To this end, we will make use of data collected with recorded-based methods, i.e., surveys as we mentioned in section 3.2.1. The surveys was designed by three Canadian hospitals especially for recording the information about the behavior of workers. According to the answers that are less granular though, we will try to extract the relationship between individuals and attributes of the study object from datasets so that we can generate a data-driven network that allows us to realistically simulate the spreading of a disease in such a setting. Our purpose is to address the issue "from data to good networks" that we discussed in section 3.1. By exploring in depth the dynamics of HAIs on the generated networks, we will be able to assess the risk of spatial units

as given by the disease hitting time and the number of infections produced in each unit. In addition, We will calculate both the probability of getting infected and effective R_0 and use them as indicators for risk assessment of HCWs categorized by their occupations.

3.4.1 Description of the scenario

Healthcare-associated infections (HAIs), or nosocomial infections, are infections transmitted within healthcare settings. For every one-hundred patients admitted to hospital, between seven to ten will acquire at least one type of HAI [398]. Nosocomial infections also play an important role in the spreading of pandemics, as the recent SARS-CoV-2 pandemic has shown [399, 400]. As such, they have become an important public health concern [401–404]. The prevalence of HAIs not only yields additional waste of financial resources, but also causes substantial morbidity and mortality [405–407]. In the modern healthcare systems, there exist a variety of potential risk factors contributing to the spread of HAIs [408, 409]. In terms of environmental aspects, the relatively restricted spaces in hospitals provide the conditions for the repeated and prolonged exposure to HAIs. Moreover, the various categories of spatial units play different roles in the transmission of HAIs as a consequence of their function.

Given that previous studies have shown that close contact is a major mode of transmission of healthcare-associated infections, the daily activities of healthcare workers potentially increase the risk of infection to patients and themselves [328, 410, 411]. The occupational nature of some healthcare workers also contributes to a certain extent to the transmission of HAIs between hospital units. Therefore, the risks associated to HAIs are heterogeneous and can depend on the characteristics of the categories to which the units belong and the various occupations of healthcare workers.

Over the last decade, effective measures in preventing and containing HAIs have been developed, accounting for the variability of transmission routes [412–414]. Increasing hand hygiene and the regular use of personal protective equipment (PPE) are the most basic infection prevention and control strategies [409]. Although the implementation of disinfection measures has a significant effect on the HAIs spread restraint, understanding the dynamics of HAIs transmitted by respiratory microorganisms can open the path for optimizing current strategies. In this work, our aim is to evaluate the infection risks of certain occupations, and how they spread through the different units of the hospital. To this end, we assess the infection risk of each spatial unit

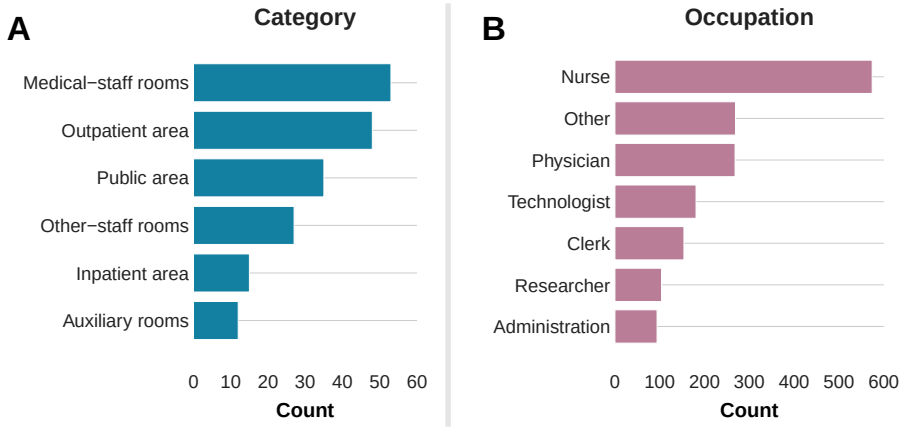

Figure 3.16: **Distribution of the merged classification. A)** The classification of categories based on the function of units. **B)** The classification of occupations based on the self-reported information of HCWs.

by calculating the disease hitting time and the number of infections produced in each location. We also evaluate the risk of different HCWs by analyzing the probability of getting infected and their potential infection capacities.

3.4.2 Network construction

To explore the propagation of respiratory infectious diseases in the hospital settings, we use data collected from surveys carried out in three hospitals on the behavior of workers. The site-specific surveys which use the specific floor plans of each hospital, were created for three urban university-affiliated tertiary care Canadian hospitals as part of the CONNECT I study (henceforth, hospitals A, B and C, in order of size, being A the largest). In the survey, employees were asked to provide information on the amount of time they spent at each location of the hospital during a normal week. The survey identified 19 different HCW occupational categories and over 100 different locations in each hospital (see [328] for a detailed description of the dataset).

In Figs. 3.16 and 3.17, we report some of the results of the survey from hospital B. According to the specific description of areas in the questionnaire, some units can be combined into one unit. Moreover, we group the merged units into different categories based on their function. The distribution of units categories in hospital B is summarized in Fig. 3.16(A). In addition, we have performed the disambiguation based on the similarity between the answers of HCWs' occupation by aggregating them into a representative group. The distribution of occupational classifications in hospital B is shown in Fig. 3.16(B).

FIGURE 3.17: **Interaction patterns of HCW. A)** Floors visited by 4 selected HCW groups in Hospital B during a normal week. **B)** Number of direct contacts with other HCWs reported by members of each category during a typical day. The distributions are fitted to a right-censored negative binomial distribution.

The classification for units and individuals will be applied in the other two hospitals. Furthermore, we explore the interaction patterns of HCWs (see Fig. 3.17). We observe that there is an important heterogeneity in the weekly routines of different HCW groups. For instance, nurses and physicians do not visit the basement, while administrative assistants and those that reported their category as "Other" can be easily found there. Similarly, while nurses and "Other" do not visit the last floor, physicians and administrative assistants do. Regarding their daily number of contacts with other co-workers, nurses are the single-category reporting a larger number, followed by administrative assistants and physicians. The category "Other" is highly heterogeneous and, thus, for the rest of the paper we will ungroup it and then incorporate them into other existing categories, whenever it is possible, by taking into account the information they provided on their occupation.

Using the answers from the survey, we apply a data-driven approach to construct the network of HCW interactions. Due to the lack of precise information, we do not include any patient interactions. Therefore, rather than analyzing the impact of a potential outbreak in the hospital, we focus on understanding how would a disease spread throughout the hospital. To do so, we first assume that two individuals can interact only if they have reported visiting the same unit. The connection relationship is denoted by

$$\mathcal{A}^u_{ij} = \delta_{i,u}\delta_{j,u}, \tag{3.8}$$

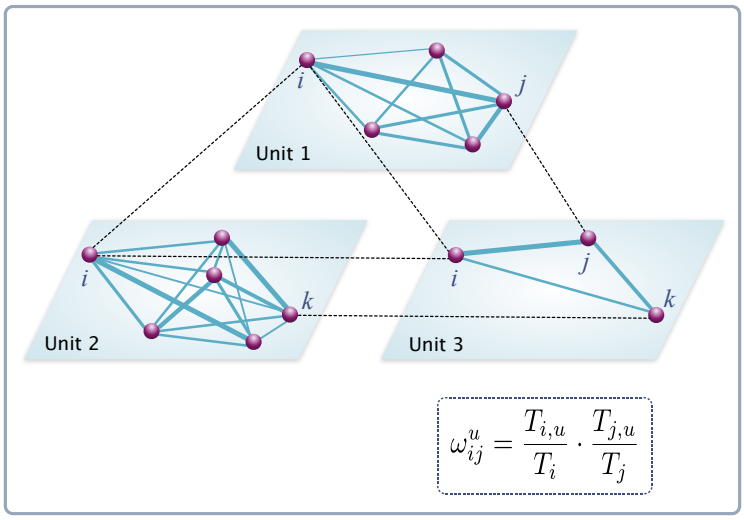

Figure 3.18: **Schematic representation of the network.** The spatial activities of each individual allow us to determine if two individuals could potentially interact. We assume that there is a link between two individuals if they visit the same unit. The weight of each link depends on the time proportion spent by each individual in that unit.

where $\delta_{i,u} = 1$ if the healthcare worker i has visited the unit u and $\delta_{i,u} = 0$ otherwise. To leverage the detailed information contained in the survey, we further take into account the amount of time that each individual spent in said location to weight the interaction. As such, in the generated network, each individual represents one node and the link weight between two nodes i and j in unit u is given by:

$$w_{ij}^{u} = \frac{T_{i,u}}{T_i}\frac{T_{j,u}}{T_j}, \qquad \forall i, j \in u \tag{3.9}$$

where $T_{i,u}$ represents the amount of time that individual i spent in a spatial unit u and T_i represents the total amount of time in the hospital reported by individual i. In Fig. 3.18, we schematically represent the connection relationship among the healthcare workers in our network.

To simulate the spreading of an air-borne infectious disease, we implement an SIR model on top of the network of HCW interactions. In the model, a worker might be in one of three states: *susceptible* (S), *infected* (I), or *recovered* (R). An infected individual, i, will transmit the disease to a susceptible individual j with probability $1 - \exp(-\beta * w_{ij})$, where β is the per-contact transmission probability. This process is run synchronously for all infected individuals at each time step t. Then, those individuals that were already

infected at time t might recover with probability μ. We set $\beta = 0.01$ and $\mu = 0.10$. The average strength (sum of all the weights of each node) in each network is 31, 23 and 18 for hospitals A, B and C, respectively, yielding a value of R_0 in the homogeneous approximation of $3.1, 2.3$ and 1.8 [393].

3.4.3 Risk of units

In this section, we assess the risk of each location in terms of spreading the outbreak. Note that this does not capture where the outbreak originates. Instead, it is assumed that a HCW gets infected, either by a patient in the hospital, or outside, and then the outbreak spreads to the other HCWs.

1. ***Hitting time***

The hitting time is defined as the average amount of time that it takes for the disease to reach a specific location [155]. In the case of hospital units, we define it as the time until one HCW located in unit l gets infected, HT_l. Therefore, the smaller the hitting time, the more at risk a location is. We then gauge the risk of each location in comparison to the rest by dividing each HT_l by the average hitting time in the hospital, $\langle HT \rangle$. In Fig. 3.19(A), we show the risk computed using this procedure for each type of unit. We observe that in the three hospitals the disease will arrive sooner to units under the category "inpatient area". Note also that, even though most locations categorized as "public area" are at an average risk, the riskiest locations belong to this category. These are mainly cafeterias, which are visited by many employees and, thus, it is easy for the disease to reach them.

2. ***Number of infections***

We further explore the risk posed by each unit by computing the average number of infections produced in each unit, NI_l. As in the previous case, we normalize this number by the average number of infections produced in any unit $\langle NI \rangle$ in order to compare different hospitals. The results, Fig. 3.19(B), agree with the previous observation that "inpatient area" is the highest risk category. However, we observe an important contribution of some "medical-staff rooms". A closer inspection reveals that these locations are laboratories and research locations, in which the number of different HCWs is not that large, but the ones that visit those areas are likely to spend an important amount of time there. Thus, even though it takes longer for the disease to arrive, one it does, it can easily spread throughout the workers located in those rooms.

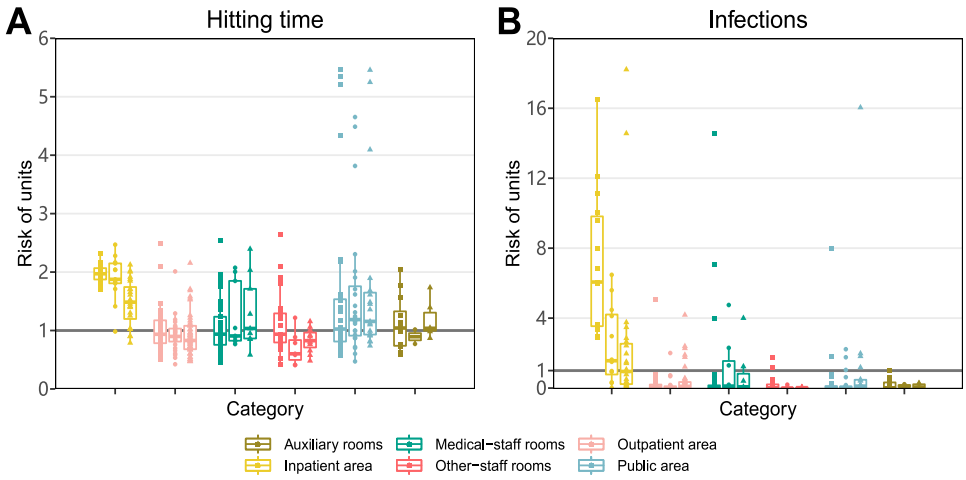

Figure 3.19: **Spatial spreading of a disease across the units in a hospital setting.** In all cases, each boxplot represents the median and the interquartile range of the risk associated to units under each category. Dots indicate the average risk of each individual location within the category, with squares, circles and triangles representing hospitals A, B and C respectively. **A)** The relative risk of is gauged with the hitting time. **B)** The relative risk is measured by taking into account the number of infections produced within each unit. The category of a unit was provided by the management of hospital A, and the same grouping criteria was used for the other hospitals. The two groups on the left represent patient-care areas ("inpatient area" or "outpatient area") while the other four groups are composed by units that are predominantly non-patient-care areas.

To briefly sum up, the results obtained from two methods reveal that the risk of spatial units belonging to "inpatient care" and "public area" categories are relatively higher than others in both methods. The units at lower risk are "other-staff rooms" (accounting, administration, etc.) and "auxiliary rooms" (laundry, housekeeping, etc.).

3.4.4 Risk of individuals

As we saw in Fig. 3.17, there is an important degree of heterogeneity across HCW occupations and their roles on different units. In what follows, we explore the risk associated with each occupation category in order to better understand the dynamics of the spreading. In [328], the 19 self-reported occupations identified in the surveys where grouped in 4 categories, but given the results from the previous section, we extract two groups of HCW from the "other HCW", "Researcher" and "Technologist" (note that in hospital B no one reported anything related to research as their occupation). We also split the "Admin/Support" category into "Administration" and "Clerk" due to the

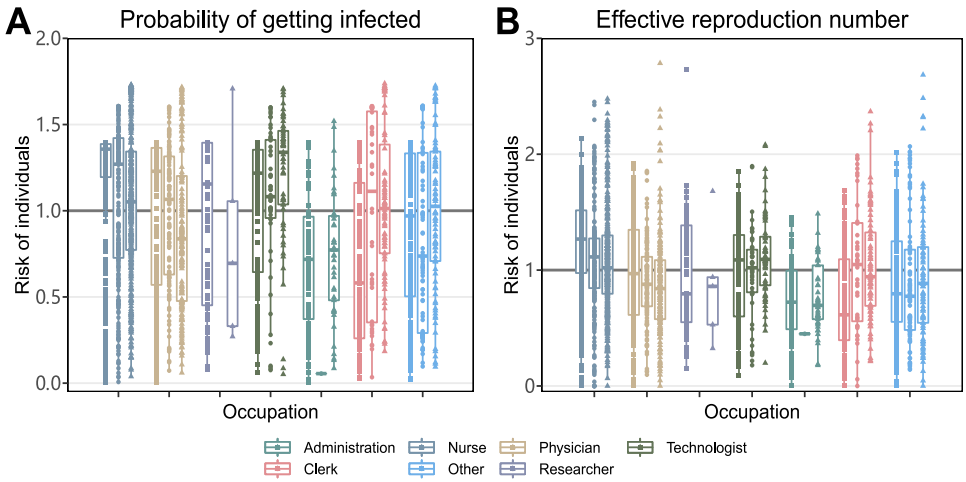

FIGURE 3.20: **Spatial spreading of a disease across HCWs.** In all cases, each boxplot represents the median and interquartile range of the risk associated to each group of HCWs. Dots indicate the average risk of each worker within the category, with squares, circles and triangles representing workers from hospitals A, B and C respectively. **A)** We show the relative risk measured as the probability of getting infected during an outbreak. **B)** Risk is gauged using the average number of infections produced by an individual during an outbreak.

relative large number of individuals in each category.

1. ***The probability of getting infected***

A basic observable of the risk carried by an individual is the probability of getting infected. To obtain it, we run 10,000 stochastic simulations and compute the probability that each individual gets infected, PI_i. Then, we divide it over the average probability of getting infected for all individuals, $\langle PI \rangle$, and group them according to their occupation, Fig.3.20(A). In this case, we observe that nurses and technologists are the HCWs at higher risk. In contrast, people working in administration are at lower risk of getting infected. Note that interactions with patients are not included, and it is expected that nurses will have more contact with patients than other occupations. Yet, the probability of getting infected is greater for them, purely based on their contacts with other HCWs. These observations are largely consistent with the reality in the hospital settings, highlighting the role of occupational heterogeneity play on the risk of spread of HAIs.

2. ***Effective reproduction number***

Lastly, we compute the effective reproduction number of each individual. That is, the average number of secondary infections they produce during an outbreak, R_i. We divide this quantity over the average effective reproduction number, $\langle R \rangle$, to gauge the risk posed by each individual. Then, we group them again according to their occupation, shown in Fig. 3.20(B). Inline with the previous observation, "nurse" is the category with the largest risk in terms of the effective reproduction number. Thus, not only it is more likely for nurses to get infected but also to spread the disease. As such, they should be a priority when implementing new protection measures against HAIs. On the other extreme, working under the "administration" category is relatively less riskier.

3.4.5 Discussion

In the last part of the thesis, we consider the spatial and temporal information self-reported by each healthcare worker in three hospitals in Canada to generate a data-driven network. In hospital settings, the functional characteristics of some categories of units result in a particularly high risk of spreading the healthcare-associated infections. The heterogeneity of the daily activities of healthcare workers is also an important risk factor in the transmission of HAIs. Therefore, the main purpose of our work is to provide quantitative assessment of infection risks for spatial units and individuals, respectively. Accordingly, we delve into the dynamics of HAIs by implementing an SIR model on the generated network to simulate the spread of the disease within the hospital setting.

In the case of assessing the risk of units, we propose two risk indicators given by the disease hitting time and the number of infections generated per unit. We find that the risk levels of units exhibit heterogeneous and spatial distributed characteristics. In particular, the units belonging to "inpatient care" and "public area" show a higher risk in spreading the diseases than others under two assessment methods. Moreover, the "other-staff rooms" and "auxiliary rooms" categories are at relatively lower risk levels to spread the infections in hospitals.

Similarly, we quantitatively assess the risk of groups of HCWs with two methods. We focus on the impact of the diversity of occupations on the risks of HCWs by calculating the probability of getting infected and the effective reproduction number. The results indicate that HCWs belonging to the "Nurse" category are the most susceptible to be infected and, at the same time, "Nurse" is the occupation capable of infecting the largest number of people. In ad-

dition, it is clear to see that most of the HCWs labeled as "Administration" are comparatively difficult to get infected and transmit the disease to others which is largely consistent with their occupational profile.

Lastly, a few remarks are in order. First, we observe that merely the size of the hospital already produces denser and more connected networks, which increases the value of R_0 and thus facilitates the propagation of this type of infectious diseases. Second, the networks were constructed using only the self-reported information on the interaction patterns among co-workers, disregarding the risk that some specific units might pose on the people working there, or the possibility of patients contributing to the spreading. However, we believe this limitation highlights something important. Based solely on the amount of time spent at each location, we have identified which areas and occupations are at highest risk in terms of HAIs. These, in turn, are precisely areas with many patients and in which riskier activities take place, which can only increase their role in spreading HAIs. Thus, special attention should be paid to these interactions, rather than focusing only on patient-worker interactions.

In this work, we finally presented the data-driven model by extracting the nodes relationship from the spatio-temporal information recorded in three surveys. Although data about the attributes of units and individuals are relatively course-grained, we get the results that risk levels are apparently different between categories classified by their specific characteristics. Our model provides insight into the dynamics of healthcare-associated infections in hospital settings. The findings reveal the important influence of diverse categories of units and various occupations of HCWs on the risk of disease spreading. In terms of controlling the transmission of HAIs, we believe that appropriate prevention measures can be developed through quantitatively assessed risks for both units and individuals.

Conclusions 4

"Only two things are infinite: the universe and human stupidity,...and I am not sure about the former."
— Albert Einstein

This dissertation details our research on exploring contagion dynamics in multilevel and structured populations. It is of great significance to understand dynamic processes in networked populations, like the propagation of infectious diseases, the transmission of information and so forth. To this end, we tried to yield a more articulated picture concerning this topic, albeit with incomplete exploration. The concluding remarks of each Chapter are summarized as follows.

By reviewing the development of complex network theory from the beginning to the present, it is worth stressing that the structure plays a key role in characterizing complex systems' dynamics. Since a complex system is composed of a large number of interacting microscopic units that interact nonlinearly, we need the development of a set of mathematical methods to link different scales as well as to explore their statistical characteristics.

In Chapter 2, we first provided a brief overview of the modelling and simulation methods employed in this thesis. In a wide variety of dynamic processes, we focused on exploring the dynamics of contagion processes, especially the problem of epidemics on networks. The heterogeneity of epidemic propagation is unlikely to be portrayed solely by the set of parameters of the differential equations describing the dynamics of homogeneous systems. This needs to be achieved by considering applications on multiple structural types of networks. The basic assumption is that individuals capable of infecting or spreading epidemics are placed at each node of a network. The transmission only proceeds through connections between nodes. We not only investigated the definitions of some important quantities in the field of epidemiology but also compared critical phenomena under different topologies of networks.

We developed a framework to extend the classical SIS epidemic model in multiplex networks with the directionality of edges taken into account. We focused on exploring the effect of directionality on disease contagion. We got the general conclusion that the systems with some directionality have much

greater resistance to epidemics than those mapped as undirected networks. Moreover, we made use of online social platforms to validate our findings for synthetic networks. The framework can be easily implemented on many types of systems, such as transportation systems, as well as on information dissemination to illustrate the generality of our results.

Next, we adopted one of the most commonly used models for analyzing epidemic spreading, the compartmental model, to study a kind of norm-violating behavior. We analyzed the dynamics of a highly stylized model consisting of four flow channels between three compartments, C(*corrupt*), H(*honest*), and O(*ostracism*). We revealed the phase diagram between the HCO model and a modified SIRS model by mean-field predictions, showing that some social interactions, like "warning to wrongdoers", have a crucial impact on the evolution of corruption. Moreover, we applied the HCO model on duplex networks where different flows among three states occur on a specific layer. Then, we investigated the effect of edge overlap and interlayer degree correlations under different underlying population networks on the corruption dynamics. The results demonstrated that various values of edge overlap as a result of rewiring links barely affect the evolution of corruption activities given the same structure of networks regardless of whether they are uncorrelated or correlated. However, high edge overlap due to interlayer correlated coupling can make a difference in the dynamics, allowing for a fast evolution as transition rates increase.

In chapter 3, we overviewed the influence of data science on capturing the dynamics of complex networks. Here, we focused on the infection transmission on contact networks modelled by real data. We developed a data-driven model with age-dependent mixing patterns taken into account. We first made use of this model with age-mixing matrices estimated from 34 countries in which heterogeneous contact patterns between individuals are encoded. Then, we executed simulations of the SARS-CoV-2 transmission with an SEIR-like epidemic model. We estimated quantitatively the infection-induced herd immunity threshold (IHIT) and infection-induced overshoot infection level (IOR) and explored the effects of three vaccine prioritization strategies on suppressing the epidemics. The results show that the transmission-focused vaccination strategy reaches the HIT at a coverage comparable to IHIT, but it has inferior performance on averting deaths than the risk vaccination strategy.

Lastly, we considered the data collected from surveys especially designed in three hospitals in Canada to record behaviors of healthcare workers. We made use of the spatial and temporal information reported by healthcare workers to build a data-driven network. We quantitatively assessed the infection risks

for spatial units and individuals with two methods. The findings indicate that diverse categories of units and various occupations of HCWs play an essential role in the risk assessment of disease spreading in healthcare settings.

All in all, the purpose of this thesis was to explore some contagion processes in networked populations from a multilevel perspective and to analyze their contagion dynamics from the theoretical level to the practical application level when real data is incorporated. Our results on this topic are still limited, and we believe there are still plenty of directions and issues worth exploring in future works.

4.1 Prospects

Regarding the future work for the corruption model, it would be interesting to relax some of the assumptions incorporated in our model. For instance, here we have assumed that (for fixed parameters) the rate of corruption is a one-variable function of the local fraction of corrupt agents and that the rate of delation is also a one-variable function of the local fraction of honest agents. A most promising prospective is to build up general and well-informed functions for the corruption and delation flow rates, so that the model in fact allocates a game-theoretic formulation, i.e., that these flow rates correspond to some game dynamics capable of incorporating fewer stylized ingredients than the ones included here. In this regard, the consideration of flow rates based on utility (benefit) functions not only requires many-variable functions but also enlarges the "information horizon" to second neighbors' shell, likely expanding the scope of model potential applications.

In the case of the project about the spatial spreading of diseases in hospital settings, since there are abundant and informative data collected from the questionnaire in three hospitals, we are considering making use of other information to generate different data-driven networks or develop other theoretical approaches. Hence, we could compare their differences in preventing healthcare-associated infections.

In addition, as an extension of the work about quantitatively estimating the infection-induced herd immunity threshold, we are currently leveraging the collected information on the maximum number of residents at nursing homes in Spain together with the age distribution of the population to estimate contact patterns in such settings. We aim to explore the effect of incorporating this information into SEIR epidemic models.

Although much of the existing work has been conducted considering the structure of populations, both qualitatively and quantitatively, most of it has

focused on static contact structures. In other words, the results are grounded in the assumption that "social contact patterns of individuals do not change over time". However, this assumption is clearly not applicable in the real world, where contact behaviors of individuals are not only influenced by individual-initiated behaviors such as school vacations but also change in response to government control strategies during epidemic outbreaks. The present detection and sensing technologies are not capable of achieving the task of tracking large-scale contact behaviors over time. Therefore, how to model and discover spatio-temporal patterns of mass population exposure could be our next research direction.

Conclusiones 5

Esta disertación detalla nuestra investigación sobre la exploración de dinámicas de contagio en poblaciones estructuradas y multinivel. Resulta de gran importancia entender los procesos dinámicos en poblaciones en red, como la propagación de enfermedades infecciosas, la transmisión de la información, etc. Con este objetivo, hemos intentado mostrar una imagen articulada con respecto a este campo, aunque con una exploración incompleta dado su tamaño. Las conclusiones finales de este capítulo se resumen en lo siguientes puntos.

Al repasar el desarrollo de la teoría de las redes complejas desde su inicio hasta el presente, es importante destacar que la estructura juega un papel fundamental en la caracterización de las dinámicas de los sistemas complejos. Dado que un sistema complejo se compone de un gran número de unidades microscópicas que interactúan de forma no lineal, necesitamos desarrollar técnicas matemáticas que sean capaces de unir diferentes escalas y estudiar sus características estadísticas.

En el capítulo 2, primero dimos un breve repaso a los métodos de modelización y simulación utilizados en esta tesis. En una gran variedad de procesos dinámicos, nos centramos en explorar las dinámicas y los procesos de contagio, especialmente en lo referente a la propagación de epidemias en redes. La heterogeneidad de la propagación de epidemias es difícilmente representable simplemente utilizando un conjunto de parámetros de ecuaciones diferenciales que describan la dinámica homogénea de las redes. La asunción básica es que los individuos capaces de infectar o contagiar las epidemias se sitúan en cada nodo de una red. De esta forma, la transmisión solo se produce a través de las conexiones entre nodos. No solo investigamos la definición de algunas métricas importantes en el campo de la epidemiología, sino que también comparamos fenómenos críticos bajo diferentes topologías de redes.

También desarrollamos un marco teórico capaz de extender el modelo clásico SIS en redes multicapa en la que la direccionalidad de los enlaces se tiene en cuenta. Nos centramos en explorar el efecto de la direccionalidad en la propagación de epidemias. Obtuvimos la conclusión general de que los sistemas en los que hay algo de direccionalidad tienen mucha más resistencia a las epidemias que aquellos que se pueden representar como redes no dirigidas. Además, utilizamos datos de plataformas sociales en línea para validar nue-

stros resultados obtenidos en redes sintéticas. Este marco teórico puede ser extendido a otro tipo de sistemas, como los de transporte, así como a la diseminación de la información, lo que da cuenta de la generalidad de nuestros resultados.

A continuación, adoptamos uno de los modelos más comúnmente utilizados para analizar la propagación de epidemias, el modelo compartimental, para estudiar un tipo de comportamiento que viola las normas. Analizamos la dinámica de un modelo muy estilizado que poseía cuatro canales de transmisión entre tres compartimentos, C(*corrupt*), H(*honest*), y O(*ostracism*). Mostramos el diagrama de fases del modelo HCO y una versión modificada del SIRS utilizando predicciones de campo medio, mostrando que algunas interacciones sociales, como el "castigo a los que lo hacen mal", juegan un papel fundamental en la evolución de la corrupción. Es más, aplicamos le modelo HCO a redes de dos capas de forma que los flujos en cada capa fueran diferentes. Bajo esta premisa, investigamos el efecto que el solapamiento de enlaces y las correlaciones de grado entre capas tienen sobre diferentes redes durante la propagación de la corrupción. Los resultados demuestran que el valor del solapamiento de enlaces obtenido tras reconectar los enlaces apenas afecta a la evolución de las actividades de corrupción dada la misma estructura de redes, independientemente de que sean correlacionadas o no correlacionadas. Sin embargo, un algo solapamiento de enlaces debido a una alta correlación entre las conexiones entre capas puede introducir diferencias en la dinámica, permitiendo una evolución más rápida cuando se incrementan los ritmos de transición.

In el capítulo 3, repasamos la influencia de la ciencia de datos en el estudio de la dinámica de redes complejas. Aquí, nos centramos en la transmisión de infecciones en redes de contacto modelizadas usando datos reales. En particular, desarrollamos un modelo conducido por los datos con patrones de interacción que dependían de la edad. Utilizamos este modelo para crear matrices de interacción por edad sobre 34 países diferentes en las que la heterogeneidad de los contactos entre individuos se tiene en cuenta. Después, ejecutamos simulaciones de transmisión del virus SARS-CoV-2 utilizando un modelo epidemiológico semejante al SEIR. Estimamos cuantitativamente la inmunidad de grupo inducida por la propagación (IHIT) y el exceso en el nivel de infección inducido por la propagación (IOR) y exploramos los efectos que tres estrategias de priorización de vacunación a la hora de suprimir las epidemias. Los resultados muestran que la vacunación centrada en la transmisión es capaz de conseguir una inmunidad de grupo comparable con el IHIT, pero tiene una eficacia menor a al hora de prevenir muertes frente a aun estrategia de

vacunación basada en el riesgo.

Finalmente, consideramos datos obtenidos en encuestas diseñadas específicamente para el estudio de los comportamientos de los trabajadores sanitarios en tres hospitales de Canadá. Utilizamos información espacial y temporal reportada por los propios trabajadores sanitarios para construir las redes. Estimamos cuantitativamente el riesgo de infección en las diferentes unidades espaciales de los hospitales y de los propios trabajadores utilizando dos métodos. Los resultados indican que varias unidades y categorías de trabajadores juegan un papel fundamental en el riesgo de propagación de enfermedades en los entornos sanitarios.

En resumen, el objetivo de esta tesis era explorar algunos procesos de contagio en poblaciones en red desde una perspectiva multinivel para analizar la dinámicas de contagio desde un punto de vista teórico y práctico cuando se dispone de los datos. Nuestros resultados en este área todavía son limitados, por lo que consideramos que todavía existen múltiples direcciones que seguir y problemas por explorar en el futuro.

5.1 Perspectivas

En lo que respecta al modelo de corrupción, sería interesante relajas algunas de las asunciones incorporadas en el modelo. Por ejemplo, aquí hemos asumidos que (para un conjunto de parámetros fijos) la tasa de corrupción es función de una variable local que depende de la fracción de agentes corruptos y que la tasa de delatamiento también es una función de una variable que depende de la fracción local de agentes honestos. Una dirección muy prometedora sería construir funciones más generales y bien informadas para estas tasas, de forma que el modelo se asemeje más a una formulación de teoría de juegos, i.e., que estos flujos se correspondan a dinámicas de juegos capaces de incorporar menos ingredientes estilizados que los utilizados aquí. En este sentido, la consideración de que los flujos se basen en las funciones de utilidad (beneficio) no solo requiere funciones de muchas variables sino también incrementa el horizonte de información a la segunda capa de vecinos, extendiendo la aplicabilidad del modelo.

En el caso del proyecto sobre la propagación de epidemias en hospitales, dado que existe bastante información en los cuestionarios de los tres hospitales, estamos considerando explorar otra información para generar las redes con otras aproximaciones, desarrollando nuevos modelos teóricos. Así, podríamos comparar las diferencias a la hora de prevenir las infecciones asociadas a los centros hospitalarios.

Así mismo, como una extensión del trabajo sobre estimar cuantitativamente la inmunidad de grupo inducida por la infección, estamos actualmente utilizando información obtenida sobre los residentes en centros geriátricos en España para poder estimar la propagación en esos lugares. Nuestro objetivo es explorar el efecto que puede tener incorporar esta información a los modelos epidemiológicos tipo SEIR.

Aunque una gran parte del trabajo se ha realizado teniendo en cuenta la estructura de las poblaciones, tanto cuantitativamente como cualitativamente, la mayor parte se basaba en redes de contacto estáticas. En otras palabras, los resultados se basan en la asunción de que los "patrones sociales de contacto entre individuos no cambian con el tiempo". Sin embargo, esta asunción es claramente no aplicable al mundo real, donde el contacto entre individuos no solo se ve influenciado por eventos como las vacaciones escolares, sino que también pueden cambiar como respuesta a medidas de control que los gobiernos impongan durante la propagación de una epidemia. Las tecnologías de detección y de sensores existentes actualmente no son capaces de seguir los comportamientos sociales a gran escala durante mucho tiempo. Por tanto, cómo modelizar y descubrir estos patrones de interacción espacio-temporales sobre grandes conjuntos de población podría ser una dirección de investigación interesante para el futuro.

Bibliography

[1] R. Gallagher, T. Appenzeller, D. Normile, *et al.*, "Beyond reductionism," *Science*, vol. 284, no. 5411, p. 79, 1999.

[2] J. Louth, "From newton to newtonianism: Reductionism and the development of the social sciences," *Emergence: Complexity and Organization*, vol. 13, no. 4, p. 63, 2011.

[3] J. Earman, "Laplacian determinism, or is this any way to run a universe?," *The Journal of Philosophy*, vol. 68, no. 21, pp. 729–744, 1971.

[4] F. Mazzocchi, "Complexity in biology: exceeding the limits of reductionism and determinism using complexity theory," *EMBO reports*, vol. 9, no. 1, pp. 10–14, 2008.

[5] M. M. Waldrop, *Complexity: The emerging science at the edge of order and chaos*. Simon and Schuster, 1993.

[6] M. Mitchell, *Complexity: A guided tour*. Oxford University Press, 2009.

[7] J. Kwapień and S. Drożdż, "Physical approach to complex systems," *Physics Reports*, vol. 515, no. 3-4, pp. 115–226, 2012.

[8] P. W. Anderson, "More is different," *Science*, vol. 177, no. 4047, pp. 393–396, 1972.

[9] L. da F. Costa, F. A. Rodrigues, G. Travieso, and P. R. V. Boas, "Characterization of complex networks: A survey of measurements," *Advances in Physics*, vol. 56, pp. 167–242, jan 2007.

[10] A. Barrat, M. Barthelemy, and A. Vespignani, *Dynamical processes on complex networks*. Cambridge university press, 2008.

[11] R. Cohen and S. Havlin, *Complex networks: structure, robustness and function*. Cambridge university press, 2010.

[12] L. d. F. Costa, O. N. Oliveira Jr, G. Travieso, F. A. Rodrigues, P. R. Villas Boas, L. Antiqueira, M. P. Viana, and L. E. Correa Rocha, "Analyzing and modeling real-world phenomena with complex networks: a survey of applications," *Advances in Physics*, vol. 60, no. 3, pp. 329–412, 2011.

[13] B. R. Jasny, L. M. Zahn, and E. Marshall, "Special issue on complex systems and networks," *Science*, vol. 325, no. 5939, pp. 405–432, 2009.

[14] M. Newman, *Networks*. Oxford university press, 2018.

[15] L. Euler, "Solutio problematis ad geometriam situs pertinentis," *Commentarii academiae scientiarum Petropolitanae*, pp. 128–140, 1741.

[16] N. Biggs, E. K. Lloyd, and R. J. Wilson, *Graph Theory, 1736-1936*. Oxford University Press, 1986.

[17] A.-L. Barabási, "Network science," *Philosophical Transactions of the Royal Society A: Mathematical, Physical and Engineering Sciences*, vol. 371, no. 1987, p. 20120375, 2013.

[18] F. Menczer, S. Fortunato, and C. A. Davis, *A First Course in Network Science*. Cambridge University Press, jan 2020.

[19] M. E. Newman, "The structure and function of complex networks," *SIAM review*, vol. 45, no. 2, pp. 167–256, 2003.

[20] M. Newman, *Networks: An Introduction*. Oxford University Press, mar 2010.

[21] G. Csardi, T. Nepusz, *et al.*, "The igraph software package for complex network research," *InterJournal, complex systems*, vol. 1695, no. 5, pp. 1–9, 2006.

[22] A. Patrinos and S. L. Hakimi, "Relations between graphs and integer-pair sequences," *Discrete Mathematics*, vol. 15, no. 4, pp. 347–358, 1976.

[23] K.-M. Lee, J. Y. Kim, W.-k. Cho, K.-I. Goh, and I. Kim, "Correlated multiplexity and connectivity of multiplex random networks," *New Journal of Physics*, vol. 14, no. 3, p. 033027, 2012.

[24] S. Boccaletti, G. Bianconi, R. Criado, C. I. Del Genio, J. Gómez-Gardenes, M. Romance, I. Sendina-Nadal, Z. Wang, and M. Zanin, "The structure and dynamics of multilayer networks," *Physics reports*, vol. 544, no. 1, pp. 1–122, 2014.

[25] B. Min, S. D. Yi, K.-M. Lee, and K.-I. Goh, "Network robustness of multiplex networks with interlayer degree correlations," *Physical Review E*, vol. 89, apr 2014.

[26] M. E. J. Newman, "Mixing patterns in networks," *Physical Review E*, vol. 67, feb 2003.

[27] J. Moody, "Race, school integration, and friendship segregation in america," *American journal of Sociology*, vol. 107, no. 3, pp. 679–716, 2001.

[28] P. Erdös and A. Rényi, "On the evolution of random graphs," *Publ. Math. Inst. Hung. Acad. Sci*, vol. 5, no. 1, pp. 17–60, 1960.

[29] P. Erdös and A. Rényi, "On the strength of connectedness of a random graph," *Acta Mathematica Scientia Hungary*, vol. 12, pp. 261–267, 1961.

[30] R. Solomonoff and A. Rapoport, "Connectivity of random nets," *The bulletin of mathematical biophysics*, vol. 13, no. 2, pp. 107–117, 1951.

[31] B. Bollobás and B. Béla, *Random graphs*. No. 73, Cambridge university press, 2001.

[32] R. Albert and A.-L. Barabási, "Statistical mechanics of complex networks," *Reviews of modern physics*, vol. 74, no. 1, p. 47, 2002.

[33] D. J. Watts and S. H. Strogatz, "Collective dynamics of 'small-world' networks," *Nature*, vol. 393, pp. 440–442, jun 1998.

[34] A.-L. Barabási and R. Albert, "Emergence of scaling in random networks," *Science*, vol. 286, pp. 509–512, oct 1999.

[35] M. Faloutsos, P. Faloutsos, and C. Faloutsos, "On power-law relationships of the internet topology," *ACM SIGCOMM Computer Communication Review*, vol. 29, pp. 251–262, oct 1999.

[36] M. Newman, "Power laws, pareto distributions and zipf's law," *Contemporary Physics*, vol. 46, pp. 323–351, sep 2005.

[37] M. Perc, "The matthew effect in empirical data," *Journal of The Royal Society Interface*, vol. 11, no. 98, p. 20140378, 2014.

[38] E. A. Bender and E. R. Canfield, "The asymptotic number of labeled graphs with given degree sequences," *Journal of Combinatorial Theory, Series A*, vol. 24, no. 3, pp. 296–307, 1978.

[39] B. Bollobás, "A probabilistic proof of an asymptotic formula for the number of labelled regular graphs," *European Journal of Combinatorics*, vol. 1, pp. 311–316, dec 1980.

[40] M. Catanzaro, M. Boguñá, and R. Pastor-Satorras, "Generation of uncorrelated random scale-free networks," *Physical Review E*, vol. 71, feb 2005.

[41] R. van der Hofstad, *Random Graphs and Complex Networks*. Cambridge University Press, 2016.

[42] A. Ruciński and N. C. Wormald, "Random graph processes with degree restrictions," *Combinatorics, Probability and Computing*, vol. 1, no. 2, pp. 169–180, 1992.

[43] A. Steger and N. C. Wormald, "Generating random regular graphs quickly," *Combinatorics, Probability and Computing*, vol. 8, no. 04, pp. 377–396, 1999.

[44] J. H. Kim and V. H. Vu, "Generating random regular graphs," in *Proceedings of the thirty-fifth annual ACM symposium on Theory of computing*, pp. 213–222, 2003.

[45] J. H. Conway and N. J. A. Sloane, *Sphere packings, lattices and groups*, vol. 290. Springer Science & Business Media, 2013.

[46] A. Cardillo, J. Gómez-Gardenes, M. Zanin, M. Romance, D. Papo, F. Del Pozo, and S. Boccaletti, "Emergence of network features from multiplexity," *Scientific reports*, vol. 3, no. 1, pp. 1–6, 2013.

[47] M. Kivelä, A. Arenas, M. Barthelemy, J. P. Gleeson, Y. Moreno, and M. A. Porter, "Multilayer networks," *Journal of complex networks*, vol. 2, no. 3, pp. 203–271, 2014.

[48] R. Gallotti and M. Barthelemy, "The multilayer temporal network of public transport in great britain," *Scientific data*, vol. 2, no. 1, pp. 1–8, 2015.

[49] A. Aleta, S. Meloni, and Y. Moreno, "A multilayer perspective for the analysis of urban transportation systems," *Scientific Reports*, vol. 7, mar 2017.

[50] F. Battiston, V. Nicosia, and V. Latora, "Structural measures for multiplex networks," *Physical Review E*, vol. 89, no. 3, p. 032804, 2014.

[51] A. Aleta and Y. Moreno, "Multilayer networks in a nutshell," *Annual Review of Condensed Matter Physics*, vol. 10, pp. 45–62, 2019.

[52] M. De Domenico, A. Solé-Ribalta, E. Cozzo, M. Kivelä, Y. Moreno, M. A. Porter, S. Gómez, and A. Arenas, "Mathematical formulation of multilayer networks," *Physical Review X*, vol. 3, no. 4, p. 041022, 2013.

[53] L. M. Verbrugge, "Multiplexity in adult friendships," *Social Forces*, vol. 57, no. 4, pp. 1286–1309, 1979.

[54] G. F. de Arruda, F. A. Rodrigues, and Y. Moreno, "Fundamentals of spreading processes in single and multilayer complex networks," *Physics Reports*, vol. 756, pp. 1–59, 2018.

[55] M. D. Domenico, A. Sole-Ribalta, S. Gomez, and A. Arenas, "Navigability of interconnected networks under random failures," *Proceedings of the National Academy of Sciences*, vol. 111, pp. 8351–8356, may 2014.

[56] V. Nicosia and V. Latora, "Measuring and modeling correlations in multiplex networks," *Physical Review E*, vol. 92, no. 3, p. 032805, 2015.

[57] A.-M. Kermarrec, L. Massoulié, and A. J. Ganesh, "Probabilistic reliable dissemination in large-scale systems," *IEEE Transactions on Parallel and Distributed systems*, vol. 14, no. 3, pp. 248–258, 2003.

[58] B. Bettencourt, A. Talley, A. J. Benjamin, and J. Valentine, "Personality and aggressive behavior under provoking and neutral conditions: a meta-analytic review.," *Psychological bulletin*, vol. 132, no. 5, p. 751, 2006.

[59] D. J. Daley and D. G. Kendall, "Epidemics and rumours," *Nature*, vol. 204, no. 4963, pp. 1118–1118, 1964.

[60] Y. Moreno, M. Nekovee, and A. F. Pacheco, "Dynamics of rumor spreading in complex networks," *Physical review E*, vol. 69, no. 6, p. 066130, 2004.

[61] D. Trpevski, W. K. Tang, and L. Kocarev, "Model for rumor spreading over networks," *Physical Review E*, vol. 81, no. 5, p. 056102, 2010.

[62] F. Chierichetti, S. Lattanzi, and A. Panconesi, "Rumor spreading in social networks," *Theoretical Computer Science*, vol. 412, no. 24, pp. 2602–2610, 2011.

[63] A. Arenas, A. Díaz-Guilera, and C. J. Pérez-Vicente, "Synchronization reveals topological scales in complex networks," *Physical Review Letters*, vol. 96, mar 2006.

[64] J. Gómez-Gardeñes, Y. Moreno, and A. Arenas, "Paths to synchronization on complex networks," *Physical Review Letters*, vol. 98, jan 2007.

[65] A. Arenas, A. Díaz-Guilera, J. Kurths, Y. Moreno, and C. Zhou, "Synchronization in complex networks," *Physics Reports*, vol. 469, pp. 93–153, dec 2008.

[66] S. H. Strogatz, "Exploring complex networks," *Nature*, vol. 410, pp. 268–276, mar 2001.

[67] R. Albert, I. Albert, and G. L. Nakarado, "Structural vulnerability of the north american power grid," *Physical Review E*, vol. 69, feb 2004.

[68] B. Schäfer, D. Witthaut, M. Timme, and V. Latora, "Dynamically induced cascading failures in power grids," *Nature Communications*, vol. 9, may 2018.

[69] D. Hansel and H. Sompolinsky, "Synchronization and computation in a chaotic neural network," *Physical Review Letters*, vol. 68, no. 5, p. 718, 1992.

[70] G. Dreyfus, *Neural networks: methodology and applications*. Springer Science & Business Media, 2005.

[71] S. Boccaletti, V. Latora, Y. Moreno, M. Chavez, and D. Hwang, "Complex networks: Structure and dynamics," *Physics Reports*, vol. 424, pp. 175–308, feb 2006.

[72] G. Chen, X. Wang, and X. Li, *Fundamentals of complex networks: models, structures and dynamics*. John Wiley & Sons, 2014.

[73] G. Yan, G. Tsekenis, B. Barzel, J.-J. Slotine, Y.-Y. Liu, and A.-L. Barabási, "Spectrum of controlling and observing complex networks," *Nature Physics*, vol. 11, pp. 779–786, aug 2015.

[74] S. Meyn, *Control techniques for complex networks*. Cambridge University Press, 2008.

[75] K. Suchecki, V. M. Eguíluz, and M. S. Miguel, "Conservation laws for the voter model in complex networks," *Europhysics Letters (EPL)*, vol. 69, pp. 228–234, jan 2005.

[76] S. Wasserman, "Analyzing social networks as stochastic processes," *Journal of the American Statistical Association*, vol. 75, pp. 280–294, jun 1980.

[77] M. Boguñá, L. F. Lafuerza, R. Toral, and M. Á. Serrano, "Simulating non-markovian stochastic processes," *Physical Review E*, vol. 90, oct 2014.

[78] I. M. Longini Jr, "A mathematical model for predicting the geographic spread of new infectious agents," *Mathematical Biosciences*, vol. 90, no. 1-2, pp. 367–383, 1988.

[79] S. N. Dorogovtsev, J. F. F. Mendes, and A. N. Samukhin, "Structure of growing networks with preferential linking," *Physical Review Letters*, vol. 85, pp. 4633–4636, nov 2000.

[80] P. L. Krapivsky and S. Redner, "Organization of growing random networks," *Physical Review E*, vol. 63, may 2001.

[81] J. D. Noh and H. Rieger, "Random walks on complex networks," *Physical Review Letters*, vol. 92, mar 2004.

[82] R. Pastor-Satorras, C. Castellano, P. V. Mieghem, and A. Vespignani, "Epidemic processes in complex networks," *Reviews of Modern Physics*, vol. 87, pp. 925–979, aug 2015.

[83] G. St-Onge, V. Thibeault, A. Allard, L. J. Dubé, and L. Hébert-Dufresne, "Master equation analysis of mesoscopic localization in contagion dynamics on higher-order networks," *Physical Review E*, vol. 103, mar 2021.

[84] L. A. Rvachev and I. M. Longini, "A mathematical model for the global spread of influenza," *Mathematical Biosciences*, vol. 75, pp. 3–22, jul 1985.

[85] O. Frank and D. Strauss, "Markov graphs," *Journal of the American Statistical Association*, vol. 81, pp. 832–842, sep 1986.

[86] S. M. Ross, J. J. Kelly, R. J. Sullivan, *et al.*, *Stochastic processes*, vol. 2. Wiley New York, 1996.

[87] P. Van Mieghem, *Performance analysis of complex networks and systems*. Cambridge University Press, 2014.

[88] C. Burke and M. Rosenblatt, "A markovian function of a markov chain," *The Annals of Mathematical Statistics*, vol. 29, no. 4, pp. 1112–1122, 1958.

[89] L. C. Rogers and J. Pitman, "Markov functions," *The Annals of Probability*, pp. 573–582, 1981.

[90] J. M. Yeomans, *Statistical mechanics of phase transitions*. Clarendon Press, 1992.

[91] P. A. Gagniuc, *Markov chains: from theory to implementation and experimentation*. John Wiley & Sons, 2017.

[92] R. C. Tolman, *The principles of statistical mechanics*. Courier Corporation, 1979.

[93] I. Kanter and H. Sompolinsky, "Mean-field theory of spin-glasses with finite coordination number," *Physical Review Letters*, vol. 58, pp. 164–167, jan 1987.

[94] J. P. Gleeson, "High-accuracy approximation of binary-state dynamics on networks," *Physical Review Letters*, vol. 107, aug 2011.

[95] A.-L. Barabási, R. Albert, and H. Jeong, "Mean-field theory for scale-free random networks," *Physica A: Statistical Mechanics and its Applications*, vol. 272, pp. 173–187, oct 1999.

[96] D. J. Daley and J. Gani, *Epidemic modelling: an introduction*. No. 15, Cambridge University Press, 2001.

[97] J. M. Epstein, "Agent-based computational models and generative social science," *Complexity*, vol. 4, no. 5, pp. 41–60, 1999.

[98] J. H. Holland, *Hidden order: How adaptation builds complexity*. Addison Wesley Longman Publishing Co., Inc., 1996.

[99] I. M. Longini, "Containing pandemic influenza with antiviral agents," *American Journal of Epidemiology*, vol. 159, pp. 623–633, apr 2004.

[100] H. Rahmandad and J. Sterman, "Heterogeneity and network structure in the dynamics of diffusion: Comparing agent-based and differential equation models," *Management Science*, vol. 54, pp. 998–1014, may 2008.

[101] G. P. Figueredo, P.-O. Siebers, M. R. Owen, J. Reps, and U. Aickelin, "Comparing stochastic differential equations and agent-based modelling and simulation for early-stage cancer," *PLoS ONE*, vol. 9, p. e95150, apr 2014.

[102] S. Gallagher and J. Baltimore, "Comparing compartment and agent-based models," in *Joint Statistical Meeting, Baltimore*, 2017.

[103] G. V. Bobashev, D. M. Goedecke, F. Yu, and J. M. Epstein, "A hybrid epidemic model: Combining the advantages of agent-based and equation-based approaches," in *2007 Winter Simulation Conference*, IEEE, 2007.

[104] A. Banos, N. Corson, B. Gaudou, V. Laperrière, and S. Coyrehourcq, "The importance of being hybrid for spatial epidemic models:a multi-scale approach," *Systems*, vol. 3, pp. 309–329, nov 2015.

[105] M. E. J. Newman and G. T. Barkema, *Monte Carlo Methods in Statistical Physics*. Oxford University Press, 1999.

[106] W. Krauth, *Statistical mechanics: algorithms and computations*, vol. 13. OUP Oxford, 2006.

[107] B. Schönfisch and A. de Roos, "Synchronous and asynchronous updating in cellular automata," *Biosystems*, vol. 51, pp. 123–143, sep 1999.

[108] Z.-X. Wu and Z. Rong, "Boosting cooperation by involving extortion in spatial prisoner's dilemma games," *Physical Review E*, vol. 90, dec 2014.

[109] P. G. Fennell, S. Melnik, and J. P. Gleeson, "Limitations of discrete-time approaches to continuous-time contagion dynamics," *Physical Review E*, vol. 94, nov 2016.

[110] S. Gómez, A. Arenas, J. Borge-Holthoefer, S. Meloni, and Y. Moreno, "Discrete-time markov chain approach to contact-based disease spreading in complex networks," *EPL (Europhysics Letters)*, vol. 89, no. 3, p. 38009, 2010.

[111] S. Gómez, J. Gómez-Gardenes, Y. Moreno, and A. Arenas, "Nonperturbative heterogeneous mean-field approach to epidemic spreading in complex networks," *Physical Review E*, vol. 84, no. 3, p. 036105, 2011.

[112] E. Cozzo, R. A. Banos, S. Meloni, and Y. Moreno, "Contact-based social contagion in multiplex networks," *Physical Review E*, vol. 88, no. 5, p. 050801, 2013.

[113] M. A. Porter and J. P. Gleeson, "Dynamical systems on networks," *Frontiers in Applied Dynamical Systems: Reviews and Tutorials*, vol. 4, 2016.

[114] D. T. Gillespie, "A general method for numerically simulating the stochastic time evolution of coupled chemical reactions," *Journal of Computational Physics*, vol. 22, pp. 403–434, dec 1976.

[115] D. T. Gillespie, "Exact stochastic simulation of coupled chemical reactions," *The journal of physical chemistry*, vol. 81, no. 25, pp. 2340–2361, 1977.

[116] J. Marro and R. Dickman, *Nonequilibrium phase transitions in lattice models*. Cambridge University Press, 2005.

[117] J. N. Hays, *Epidemics and pandemics: their impacts on human history*. Abc-clio, 2005.

[118] W. H. McNeill, *Plagues and peoples*. Anchor, 1998.

[119] D. Bernoulli, "Essai d'une nouvelle analyse de la mortalité causée par la petite vérole, et des avantages de l'inoculation pour la prévenir," *Histoire de l'Acad., Roy. Sci.(Paris) avec Mem*, pp. 1–45, 1760.

[120] K. Dietz, "The first epidemic model: a historical note on pd en'ko," *Australian Journal of Statistics*, vol. 30, no. 1, pp. 56–65, 1988.

[121] E. B. Wilson and J. Worcester, "The law of mass action in epidemiology," *Proceedings of the National Academy of Sciences*, vol. 31, pp. 24–34, jan 1945.

[122] W. H. Hamer, *Epidemic disease in England: the evidence of variability and of persistency of type*. Bedford Press, 1906.

[123] V. Capasso and G. Serio, "A generalization of the kermack-mckendrick deterministic epidemic model," *Mathematical biosciences*, vol. 42, no. 1-2, pp. 43–61, 1978.

[124] M. E. Newman, "Spread of epidemic disease on networks," *Physical review E*, vol. 66, no. 1, p. 016128, 2002.

[125] M. J. Keeling and P. Rohani, *Modeling Infectious Diseases in Humans and Animals*. Princeton University Press, dec 2008.

[126] F. Brauer, "Mathematical epidemiology: Past, present, and future," *Infectious Disease Modelling*, vol. 2, pp. 113–127, may 2017.

[127] N. T. Bailey, "A simple stochastic epidemic," *Biometrika*, pp. 193–202, 1950.

[128] N. T. Bailey *et al.*, *The mathematical theory of infectious diseases and its applications*. Charles Griffin & Company Ltd, 5a Crendon Street, High Wycombe, Bucks HP13 6LE., 1975.

[129] R. M. Anderson and R. M. May, "Population biology of infectious diseases: Part i," *Nature*, vol. 280, pp. 361–367, aug 1979.

[130] R. M. May and R. M. Anderson, "Population biology of infectious diseases: Part II," *Nature*, vol. 280, pp. 455–461, aug 1979.

[131] N. M. Ferguson, M. J. Keeling, W. J. Edmunds, R. Gani, B. T. Grenfell, R. M. Anderson, and S. Leach, "Planning for smallpox outbreaks," *Nature*, vol. 425, pp. 681–685, oct 2003.

[132] D. A. Cummings, R. A. Irizarry, N. E. Huang, T. P. Endy, A. Nisalak, K. Ungchusak, and D. S. Burke, "Travelling waves in the occurrence of dengue haemorrhagic fever in thailand," *Nature*, vol. 427, pp. 344–347, jan 2004.

[133] L. Stone, R. Olinky, and A. Huppert, "Seasonal dynamics of recurrent epidemics," *Nature*, vol. 446, pp. 533–536, mar 2007.

[134] I. Z. Kiss, J. C. Miller, P. L. Simon, *et al.*, "Mathematics of epidemics on networks," *Cham: Springer*, vol. 598, 2017.

[135] L. Isella, J. Stehlé, A. Barrat, C. Cattuto, J.-F. Pinton, and W. V. den Broeck, "What's in a crowd? analysis of face-to-face behavioral networks," *Journal of Theoretical Biology*, vol. 271, pp. 166–180, feb 2011.

[136] P. S. Dodds, "An experimental study of search in global social networks," *Science*, vol. 301, pp. 827–829, aug 2003.

[137] R. Pastor-Satorras and A. Vespignani, "Epidemic spreading in scale-free networks," *Physical Review Letters*, vol. 86, pp. 3200–3203, apr 2001.

[138] B. Karrer and M. E. J. Newman, "Message passing approach for general epidemic models," *Physical Review E*, vol. 82, jul 2010.

[139] M. Boguñá, C. Castellano, and R. Pastor-Satorras, "Nature of the epidemic threshold for the susceptible-infected-susceptible dynamics in networks," *Physical Review Letters*, vol. 111, aug 2013.

[140] C.-R. Cai, Z.-X. Wu, M. Z. Chen, P. Holme, and J.-Y. Guan, "Solving the dynamic correlation problem of the susceptible-infected-susceptible model on networks," *Physical Review Letters*, vol. 116, jun 2016.

[141] W. Wang, M. Tang, H. E. Stanley, and L. A. Braunstein, "Unification of theoretical approaches for epidemic spreading on complex networks," *Reports on Progress in Physics*, vol. 80, p. 036603, feb 2017.

[142] C. Granell, S. Gómez, and A. Arenas, "Dynamical interplay between awareness and epidemic spreading in multiplex networks," *Physical Review Letters*, vol. 111, sep 2013.

[143] E. Valdano, M. R. Fiorentin, C. Poletto, and V. Colizza, "Epidemic threshold in continuous-time evolving networks," *Physical Review Letters*, vol. 120, feb 2018.

[144] M. Kuperman and G. Abramson, "Small world effect in an epidemiological model," *Physical Review Letters*, vol. 86, pp. 2909–2912, mar 2001.

[145] Z. Liu and B. Hu, "Epidemic spreading in community networks," *Europhysics Letters (EPL)*, vol. 72, pp. 315–321, oct 2005.

[146] M. Á. Serrano and M. Boguñá, "Percolation and epidemic thresholds in clustered networks," *Physical Review Letters*, vol. 97, aug 2006.

[147] Y. Schwarzkopf, A. Rákos, and D. Mukamel, "Epidemic spreading in evolving networks," *Physical Review E*, vol. 82, sep 2010.

[148] V. Colizza, R. Pastor-Satorras, and A. Vespignani, "Reaction–diffusion processes and metapopulation models in heterogeneous networks," *Nature Physics*, vol. 3, pp. 276–282, mar 2007.

[149] S. Meloni, N. Perra, A. Arenas, S. Gómez, Y. Moreno, and A. Vespignani, "Modeling human mobility responses to the large-scale spreading of infectious diseases," *Scientific Reports*, vol. 1, aug 2011.

[150] V. Belik, T. Geisel, and D. Brockmann, "Natural human mobility patterns and spatial spread of infectious diseases," *Physical Review X*, vol. 1, aug 2011.

[151] D. Balcan and A. Vespignani, "Invasion threshold in structured populations with recurrent mobility patterns," *Journal of Theoretical Biology*, vol. 293, pp. 87–100, jan 2012.

[152] J. Gómez-Gardeñes, D. Soriano-Paños, and A. Arenas, "Critical regimes driven by recurrent mobility patterns of reaction–diffusion processes in networks," *Nature Physics*, vol. 14, pp. 391–395, dec 2017.

[153] V. Colizza, A. Barrat, M. Barthélemy, and A. Vespignani, "The role of the airline transportation network in the prediction and predictability of global epidemics," *Proceedings of the National Academy of Sciences*, vol. 103, pp. 2015–2020, feb 2006.

[154] D. Balcan, V. Colizza, B. Goncalves, H. Hu, J. J. Ramasco, and A. Vespignani, "Multiscale mobility networks and the spatial spreading of infectious diseases," *Proceedings of the National Academy of Sciences*, vol. 106, pp. 21484–21489, dec 2009.

[155] D. Brockmann and D. Helbing, "The hidden geometry of complex, network-driven contagion phenomena," *Science*, vol. 342, pp. 1337–1342, dec 2013.

[156] A. Aleta and Y. Moreno, "Evaluation of the potential incidence of COVID-19 and effectiveness of containment measures in spain: a data-driven approach," *BMC Medicine*, vol. 18, may 2020.

[157] A. Aleta, Q. Hu, J. Ye, P. Ji, and Y. Moreno, "A data-driven assessment of early travel restrictions related to the spreading of the novel COVID-19 within mainland china," *Chaos, Solitons & Fractals*, vol. 139, p. 110068, oct 2020.

[158] G. S. Costa, W. Cota, and S. C. Ferreira, "Metapopulation modeling of COVID-19 advancing into the countryside: an analysis of mitigation strategies for brazil," *medRxiv*, may 2020.

[159] D. Calvetti, A. P. Hoover, J. Rose, and E. Somersalo, "Metapopulation network models for understanding, predicting, and managing the coronavirus disease COVID-19," *Frontiers in Physics*, vol. 8, jun 2020.

[160] C. Stegehuis, R. van der Hofstad, and J. S. H. van Leeuwaarden, "Epidemic spreading on complex networks with community structures," *Scientific Reports*, vol. 6, jul 2016.

[161] T. Gross, C. J. D. D'Lima, and B. Blasius, "Epidemic dynamics on an adaptive network," *Physical Review Letters*, vol. 96, may 2006.

[162] Z. Wang, M. A. Andrews, Z.-X. Wu, L. Wang, and C. T. Bauch, "Coupled disease–behavior dynamics on complex networks: A review," *Physics of Life Reviews*, vol. 15, pp. 1–29, dec 2015.

[163] G. Demirel, E. Barter, and T. Gross, "Dynamics of epidemic diseases on a growing adaptive network," *Scientific Reports*, vol. 7, feb 2017.

[164] W. O. Kermack and A. G. McKendrick, "A contribution to the mathematical theory of epidemics," *Proceedings of the Royal Society of London. Series A, Containing Papers of a Mathematical and Physical Character*, vol. 115, pp. 700–721, aug 1927.

[165] W. O. Kermack and A. G. McKendrick, "Contributions to the mathematical theory of epidemics. II. —the problem of endemicity," *Proceedings of the Royal Society of London. Series A, Containing Papers of a Mathematical and Physical Character*, vol. 138, pp. 55–83, oct 1932.

[166] R. M. Anderson and R. M. May, *Infectious diseases of humans: dynamics and control*. Oxford university press, 1992.

[167] V. M. Eguiluz and K. Klemm, "Epidemic threshold in structured scale-free networks," *Physical Review Letters*, vol. 89, no. 10, p. 108701, 2002.

[168] M. Boguñá, R. Pastor-Satorras, and A. Vespignani, "Absence of epidemic threshold in scale-free networks with degree correlations," *Physical Review Letters*, vol. 90, jan 2003.

[169] R. Olinky and L. Stone, "Unexpected epidemic thresholds in heterogeneous networks: The role of disease transmission," *Physical Review E*, vol. 70, sep 2004.

[170] H. McCallum, "How should pathogen transmission be modelled?," *Trends in Ecology & Evolution*, vol. 16, pp. 295–300, jun 2001.

[171] R. C. Dicker, F. Coronado, D. Koo, and R. G. Parrish, "Principles of epidemiology in public health practice; an introduction to applied epidemiology and biostatistics," 2006.

[172] S. Swaroop, "Index of endemicity," *Bulletin of the World Health Organization*, vol. 16, no. 6, p. 1083, 1957.

[173] Y. Moreno, R. Pastor-Satorras, and A. Vespignani, "Epidemic outbreaks in complex heterogeneous networks," *The European Physical Journal B*, vol. 26, pp. 521–529, apr 2002.

[174] Y. Moreno, J. B. Gómez, and A. F. Pacheco, "Epidemic incidence in correlated complex networks," *Physical Review E*, vol. 68, sep 2003.

[175] Y. Moreno, M. Nekovee, and A. Vespignani, "Efficiency and reliability of epidemic data dissemination in complex networks," *Physical Review E*, vol. 69, may 2004.

[176] S. Clémençon, V. C. Tran, and H. de Arazoza, "A stochastic SIR model with contact-tracing: large population limits and statistical inference," *Journal of Biological Dynamics*, vol. 2, pp. 392–414, oct 2008.

[177] J. D. Murray, *Mathematical biology: I. An introduction*, vol. 17. Springer Science & Business Media, 2007.

[178] G. Yan, Z.-Q. Fu, J. Ren, and W.-X. Wang, "Collective synchronization induced by epidemic dynamics on complex networks with communities," *Physical Review E*, vol. 75, jan 2007.

[179] A. Weber, M. Weber, and P. Milligan, "Modeling epidemics caused by respiratory syncytial virus (RSV)," *Mathematical Biosciences*, vol. 172, pp. 95–113, aug 2001.

[180] J. M. Ponciano and M. A. Capistrán, "First principles modeling of nonlinear incidence rates in seasonal epidemics," *PLoS Computational Biology*, vol. 7, p. e1001079, feb 2011.

[181] M. Zheng, M. Zhao, B. Min, and Z. Liu, "Synchronized and mixed outbreaks of coupled recurrent epidemics," *Scientific Reports*, vol. 7, may 2017.

[182] V. Colizza, A. Barrat, M. Barthelemy, and A. Vespignani, "Epidemic predictability in meta-population models with heterogeneous couplings: the impact of disease parameter values," *International Journal of Bifurcation and Chaos*, vol. 17, no. 07, pp. 2491–2500, 2007.

[183] M. Small and C. K. Tse, "Small world and scale free model of transmission of sars," *International Journal of Bifurcation and Chaos*, vol. 15, no. 05, pp. 1745–1755, 2005.

[184] S. He, Y. Peng, and K. Sun, "SEIR modeling of the COVID-19 and its dynamics," *Nonlinear Dynamics*, vol. 101, pp. 1667–1680, jun 2020.

[185] R. Pastor-Satorras and A. Vespignani, "Epidemic dynamics and endemic states in complex networks," *Physical Review E*, vol. 63, may 2001.

[186] R. Pastor-Satorras and A. Vespignani, *Evolution and structure of the Internet: A statistical physics approach*. Cambridge University Press, 2007.

[187] S. N. Dorogovtsev and J. F. Mendes, *Evolution of networks: From biological nets to the Internet and WWW*. OUP Oxford, 2013.

[188] M. Boguá, R. Pastor-Satorras, and A. Vespignani, "Epidemic spreading in complex networks with degree correlations," in *Statistical mechanics of complex networks*, pp. 127–147, Springer, 2003.

[189] M. Boguñá and R. Pastor-Satorras, "Epidemic spreading in correlated complex networks," *Physical Review E*, vol. 66, oct 2002.

[190] P. V. Mieghem, J. Omic, and R. Kooij, "Virus spread in networks," *IEEE/ACM Transactions on Networking*, vol. 17, pp. 1–14, feb 2009.

[191] E. Cator and P. V. Mieghem, "Nodal infection in markovian susceptible-infected-susceptible and susceptible-infected-removed epidemics on networks are non-negatively correlated," *Physical Review E*, vol. 89, may 2014.

[192] K. T. D. Eames and M. J. Keeling, "Modeling dynamic and network heterogeneities in the spread of sexually transmitted diseases," *Proceedings of the National Academy of Sciences*, vol. 99, pp. 13330–13335, sep 2002.

[193] A. S. Mata and S. C. Ferreira, "Pair quenched mean-field theory for the susceptible-infected-susceptible model on complex networks," *EPL (Europhysics Letters)*, vol. 103, p. 48003, aug 2013.

[194] R. Ross, *The prevention of malaria*. John Murray, 1911.

[195] G. Macdonald *et al.*, "The epidemiology and control of malaria.," *The Epidemiology and Control of Malaria.*, 1957.

[196] R. M. Anderson, "Discussion: The kermack-McKendrick epidemic threshold theorem," *Bulletin of Mathematical Biology*, vol. 53, mar 1991.

[197] O. Diekmann, J. Heesterbeek, and J. Metz, "On the definition and the computation of the basic reproduction ratio r 0 in models for infectious diseases in heterogeneous populations," *Journal of Mathematical Biology*, vol. 28, jun 1990.

[198] J. Heffernan, R. Smith, and L. Wahl, "Perspectives on the basic reproductive ratio," *Journal of The Royal Society Interface*, vol. 2, pp. 281–293, jun 2005.

[199] D. Wu, T. Wu, Q. Liu, and Z. Yang, "The SARS-CoV-2 outbreak: What we know," *International Journal of Infectious Diseases*, vol. 94, pp. 44–48, may 2020.

[200] J. M. Hyman and E. Stanley, "Using mathematical models to understand the AIDS epidemic," *Mathematical Biosciences*, vol. 90, pp. 415–473, jul 1988.

[201] K. Dietz, "The estimation of the basic reproduction number for infectious diseases," *Statistical methods in medical research*, vol. 2, no. 1, pp. 23–41, 1993.

[202] J. Heesterbeek and K. Dietz, "The concept of ro in epidemic theory," *Statistica neerlandica*, vol. 50, no. 1, pp. 89–110, 1996.

[203] P. van den Driessche and J. Watmough, "Reproduction numbers and sub-threshold endemic equilibria for compartmental models of disease transmission," *Mathematical Biosciences*, vol. 180, pp. 29–48, nov 2002.

[204] C. Castillo-Chavez and Z. Feng, "To treat or not to treat: the case of tuberculosis," *Journal of mathematical biology*, vol. 35, no. 6, pp. 629–656, 1997.

[205] F. Brauer, C. Castillo-Chavez, and Z. Feng, *Mathematical models in epidemiology*, vol. 32. Springer, 2019.

[206] G. Chowell, N. W. Hengartner, C. Castillo-Chavez, P. W. Fenimore, and J. M. Hyman, "The basic reproductive number of ebola and the effects of public health measures: the cases of congo and uganda," *Journal of theoretical biology*, vol. 229, no. 1, pp. 119–126, 2004.

[207] Y. Caicedo-Ochoa, D. E. Rebellón-Sánchez, M. Peñaloza-Rallón, H. F. Cortés-Motta, and Y. R. Méndez-Fandiño, "Effective reproductive number estimation for initial stage of covid-19 pandemic in latin american countries," *International Journal of Infectious Diseases*, vol. 95, pp. 316–318, 2020.

[208] H. Nishiura and G. Chowell, "The effective reproduction number as a prelude to statistical estimation of time-dependent epidemic trends,"

in *Mathematical and statistical estimation approaches in epidemiology*, pp. 103–121, Springer, 2009.

[209] K. M. Gostic, L. McGough, E. B. Baskerville, *et al.*, "Practical considerations for measuring the effective reproductive number, r t," *PLoS computational biology*, vol. 16, no. 12, p. e1008409, 2020.

[210] C. Fraser, "Estimating individual and household reproduction numbers in an emerging epidemic," *PLoS ONE*, vol. 2, p. e758, aug 2007.

[211] A. Cori, N. M. Ferguson, C. Fraser, and S. Cauchemez, "A new framework and software to estimate time-varying reproduction numbers during epidemics," *American journal of epidemiology*, vol. 178, no. 9, pp. 1505–1512, 2013.

[212] R. Thompson, J. Stockwin, R. van Gaalen, *et al.*, "Improved inference of time-varying reproduction numbers during infectious disease outbreaks," *Epidemics*, vol. 29, p. 100356, dec 2019.

[213] M. Lipsitch, "Transmission dynamics and control of severe acute respiratory syndrome," *Science*, vol. 300, pp. 1966–1970, jun 2003.

[214] J. Wallinga, "Different epidemic curves for severe acute respiratory syndrome reveal similar impacts of control measures," *American Journal of Epidemiology*, vol. 160, pp. 509–516, sep 2004.

[215] O. G. Pybus, "The epidemic behavior of the hepatitis c virus," *Science*, vol. 292, pp. 2323–2325, jun 2001.

[216] J. Wallinga and M. Lipsitch, "How generation intervals shape the relationship between growth rates and reproductive numbers," *Proceedings of the Royal Society B: Biological Sciences*, vol. 274, pp. 599–604, nov 2006.

[217] H. Nishiura, "Time variations in the transmissibility of pandemic influenza in prussia, germany, from 1918–19," *Theoretical Biology and Medical Modelling*, vol. 4, jun 2007.

[218] A. M. Mood, F. A. Graybill, and D. C. Boes, *Introduction to the Theory of Statistics 1974*. McGraw-Hill Kogakusha, 1974.

[219] N. M. Ferguson, D. A. Cummings, S. Cauchemez, *et al.*, "Strategies for containing an emerging influenza pandemic in southeast asia," *Nature*, vol. 437, pp. 209–214, aug 2005.

[220] L. I. Dublin and A. J. Lotka, "On the true rate of natural increase: As exemplified by the population of the united states, 1920," *Journal of the American Statistical Association*, vol. 20, pp. 305–339, sep 1925.

[221] A. Aleta, D. Martín-Corral, A. P. y Piontti, *et al.*, "Modelling the impact of testing, contact tracing and household quarantine on second waves of COVID-19," *Nature Human Behaviour*, vol. 4, pp. 964–971, aug 2020.

[222] R. Cohen, S. Havlin, and D. ben Avraham, "Efficient immunization strategies for computer networks and populations," *Physical Review Letters*, vol. 91, dec 2003.

[223] J. Gómez-Gardeñes, P. Echenique, and Y. Moreno, "Immunization of real complex communication networks," *The European Physical Journal B*, vol. 49, pp. 259–264, jan 2006.

[224] L. K. Gallos, F. Liljeros, P. Argyrakis, A. Bunde, and S. Havlin, "Improving immunization strategies," *Physical Review E*, vol. 75, apr 2007.

[225] N. Madar, T. Kalisky, R. Cohen, D. ben Avraham, and S. Havlin, "Immunization and epidemic dynamics in complex networks," *The European Physical Journal B - Condensed Matter*, vol. 38, pp. 269–276, mar 2004.

[226] J. Goldenberg, Y. Shavitt, E. Shir, and S. Solomon, "Distributive immunization of networks against viruses using the 'honey-pot' architecture," *Nature Physics*, vol. 1, pp. 184–188, dec 2005.

[227] C. M. Schneider, T. Mihaljev, S. Havlin, and H. J. Herrmann, "Suppressing epidemics with a limited amount of immunization units," *Physical Review E*, vol. 84, dec 2011.

[228] L. Hébert-Dufresne, A. Allard, J.-G. Young, and L. J. Dubé, "Global efficiency of local immunization on complex networks," *Scientific Reports*, vol. 3, jul 2013.

[229] R. M. Anderson and R. M. May, "Vaccination and herd immunity to infectious diseases," *Nature*, vol. 318, pp. 323–329, nov 1985.

[230] D. T. Haydon, S. Cleaveland, L. H. Taylor, and M. K. Laurenson, "Identifying reservoirs of infection: A conceptual and practical challenge," *Emerging Infectious Diseases*, vol. 8, pp. 1468–1473, dec 2002.

[231] A. E. W. J. MacNeal, G. Potter, "Contagious abortion of cattle," *Science*, vol. 34, pp. 874–875, dec 1911.

[232] D. Jones and S. Helmreich, "A history of herd immunity," *The Lancet*, vol. 396, pp. 810–811, sep 2020.

[233] P. E. M. Fine, "Herd immunity: History, theory, practice," *Epidemiologic Reviews*, vol. 15, no. 2, pp. 265–302, 1993.

[234] T. J. John and R. Samuel, "Herd immunity and herd effect: new insights and definitions," *European Journal of Epidemiology*, vol. 16, no. 7, pp. 601–606, 2000.

[235] H. E. Randolph and L. B. Barreiro, "Herd immunity: Understanding COVID-19," *Immunity*, vol. 52, pp. 737–741, may 2020.

[236] S. B. Omer, I. Yildirim, and H. P. Forman, "Herd immunity and implications for SARS-CoV-2 control," *JAMA*, vol. 324, p. 2095, nov 2020.

[237] K. O. Kwok, F. Lai, W. I. Wei, S. Y. S. Wong, and J. W. Tang, "Herd immunity – estimating the level required to halt the COVID-19 epidemics in affected countries," *Journal of Infection*, vol. 80, pp. e32–e33, jun 2020.

[238] D. S. Stephens, "Vaccines for the unvaccinated: Protecting the herd," *The Journal of Infectious Diseases*, vol. 197, pp. 643–645, mar 2008.

[239] C. G. Smith, "Prospects for the control of infectious disease," 1970.

[240] K. Dietz, "Transmission and control of arbovirus diseases," *Epidemiology*, vol. 104, pp. 104–121, 1975.

[241] E. Vynnycky and R. White, *An introduction to infectious disease modelling*. OUP oxford, 2010.

[242] P. Fine, K. Eames, and D. L. Heymann, ""herd immunity": A rough guide," *Clinical Infectious Diseases*, vol. 52, pp. 911–916, mar 2011.

[243] C. Metcalf, M. Ferrari, A. Graham, and B. Grenfell, "Understanding herd immunity," *Trends in Immunology*, vol. 36, pp. 753–755, dec 2015.

[244] S. L. Sheridan, K. Frith, T. L. Snelling, K. Grimwood, P. B. McIntyre, and S. B. Lambert, "Waning vaccine immunity in teenagers primed with whole cell and acellular pertussis vaccine: recent epidemiology," *Expert Review of Vaccines*, vol. 13, pp. 1081–1106, aug 2014.

[245] C. Aschwanden, "Five reasons why COVID herd immunity is probably impossible," *Nature*, vol. 591, pp. 520–522, mar 2021.

[246] L. K. Gallos and P. Argyrakis, "Absence of kinetic effects in reaction-diffusion processes in scale-free networks," *Physical Review Letters*, vol. 92, apr 2004.

[247] C. Castellano and R. Pastor-Satorras, "Non-mean-field behavior of the contact process on scale-free networks," *Physical Review Letters*, vol. 96, jan 2006.

[248] G. F. de Arruda, E. Cozzo, T. P. Peixoto, F. A. Rodrigues, and Y. Moreno, "Disease localization in multilayer networks," *Physical Review X*, vol. 7, no. 1, p. 011014, 2017.

[249] A. V. Goltsev, S. N. Dorogovtsev, J. G. Oliveira, and J. F. F. Mendes, "Localization and spreading of diseases in complex networks," *Physical Review Letters*, vol. 109, sep 2012.

[250] R. S. Ferreira and S. C. Ferreira, "Critical behavior of the contact process on small-world networks," *The European Physical Journal B*, vol. 86, nov 2013.

[251] M. M. de Oliveira and R. Dickman, "How to simulate the quasistationary state," *Physical Review E*, vol. 71, jan 2005.

[252] S. C. Ferreira, C. Castellano, and R. Pastor-Satorras, "Epidemic thresholds of the susceptible-infected-susceptible model on networks: A comparison of numerical and theoretical results," *Physical Review E*, vol. 86, oct 2012.

[253] R. Dickman and R. Vidigal, "Quasi-stationary distributions for stochastic processes with an absorbing state," *Journal of Physics A: Mathematical and General*, vol. 35, pp. 1147–1166, jan 2002.

[254] X. Wang, A. Aleta, D. Lu, and Y. Moreno, "Directionality reduces the impact of epidemics in multilayer networks," *New Journal of Physics*, vol. 21, p. 093026, sep 2019.

[255] M. Salehi, R. Sharma, M. Marzolla, M. Magnani, P. Siyari, and D. Montesi, "Spreading processes in multilayer networks," *IEEE Transactions on Network Science and Engineering*, vol. 2, pp. 65–83, apr 2015.

[256] J. A. Drewe, "Who infects whom? Social networks and tuberculosis transmission in wild meerkats," *Proc. Biol. Sci.*, vol. 277, p. 633, Feb 2010.

[257] A. Nicolosi, M. L. C. Leite, M. Musicco, C. Arici, G. Gavazzeni, and A. Lazzarin, "The Efficiency of Male-to-Female and Female-to-Male Sexual Transmission of the Human Immunodeficiency Virus: A Study of 730 Stable Couples," *Epidemiology*, vol. 5, pp. 570–575, Nov 1994.

[258] J. L. Kool and R. A. Weinstein, "Risk of Person-to-Person Transmission of Pneumonic Plague," *Clin. Infect. Dis.*, vol. 40, pp. 1166–1172, Apr 2005.

[259] V. P. Martinez, C. Bellomo, J. S. Juan, D. Pinna, R. Forlenza, M. Elder, and P. J. Padula, "Person-to-Person Transmission of Andes Virus," *Emerg. Infect. Dis.*, vol. 11, p. 1848, Dec 2005.

[260] S. Arregui, A. Aleta, J. Sanz, and Y. Moreno, "Projecting social contact matrices to different demographic structures," *PLoS computational biology*, vol. 14, no. 12, p. e1006638, 2018.

[261] Z. Wang, C. T. Bauch, S. Bhattacharyya, A. d'Onofrio, P. Manfredi, M. Perc, N. Perra, M. Salathé, and D. Zhao, "Statistical physics of vaccination," *Physics Reports*, vol. 664, pp. 1–113, 2016.

[262] S. Arregui, M. J. Iglesias, S. Samper, D. Marinova, C. Martín, J. Sanz, and Y. Moreno, "A data-driven model for the assessment of tuberculosis transmission in evolving demographic structures," *bioRxiv*, p. 112409, 2017.

[263] S. Khajanchi, D. K. Das, and T. K. Kar, "Dynamics of tuberculosis transmission with exogenous reinfections and endogenous reactivation," *Physica A: Statistical Mechanics and its Applications*, vol. 497, pp. 52–71, 2018.

[264] D. S. Callaway, M. E. J. Newman, S. H. Strogatz, and D. J. Watts, "Network robustness and fragility: Percolation on random graphs," *Physical Review Letters*, vol. 85, pp. 5468–5471, dec 2000.

[265] M. E. J. Newman, S. H. Strogatz, and D. J. Watts, "Random graphs with arbitrary degree distributions and their applications," *Physical Review E*, vol. 64, jul 2001.

[266] L. A. Meyers, M. Newman, and B. Pourbohloul, "Predicting epidemics on directed contact networks," *Journal of Theoretical Biology*, vol. 240, pp. 400–418, jun 2006.

[267] A. Tejedor, A. Longjas, E. Foufoula-Georgiou, T. T. Georgiou, and Y. Moreno, "Diffusion dynamics and optimal coupling in multiplex networks with directed layers," *Physical Review X*, vol. 8, sep 2018.

[268] A. Tejedor, A. Longjas, P. Passalacqua, Y. Moreno, and E. Foufoula-Georgiou, "Multiplex networks: A framework for studying multiprocess multiscale connectivity via coupled-network theory with an application to river deltas," *Geophysical Research Letters*, vol. 45, pp. 9681–9689, sep 2018.

[269] Y. Hu, S. Ji, Y. Jin, L. Feng, H. E. Stanley, and S. Havlin, "Local structure can identify and quantify influential global spreaders in large scale social networks," *Proceedings of the National Academy of Sciences*, vol. 115, no. 29, pp. 7468–7472, 2018.

[270] L. Weng, J. Ratkiewicz, N. Perra, *et al.*, "The role of information diffusion in the evolution of social networks," in *Proceedings of the 19th ACM SIGKDD international conference on Knowledge discovery and data mining*, pp. 356–364, 2013.

[271] M. Magnani and L. Rossi, "The ml-model for multi-layer social networks," in *2011 International Conference on Advances in Social Networks Analysis and Mining*, pp. 5–12, IEEE, 2011.

[272] D. Lu, F. Bauza, D. Soriano-Paños, J. Gómez-Gardeñes, and L. M. Floría, "Norm violation versus punishment risk in a social model of corruption," *Physical Review E*, vol. 101, feb 2020.

[273] T. Yamagishi, "The provision of a sanctioning system as a public good.," *Journal of Personality and social Psychology*, vol. 51, no. 1, p. 110, 1986.

[274] e. Hammerstein, Peter, *Genetic and cultural evolution of cooperation*. MIT press, 2003.

[275] E. Fehr and U. Fischbacher, "Third-party punishment and social norms," *Evolution and human behavior*, vol. 25, no. 2, pp. 63–87, 2004.

[276] K. Sigmund, H. De Silva, A. Traulsen, and C. Hauert, "Social learning promotes institutions for governing the commons," *Nature*, vol. 466, no. 7308, pp. 861–863, 2010.

[277] W. Güth and H. Kliemt, "Competition or co-operation: on the evolutionary economics of trust, exploitation and moral attitudes," *Metroeconomica*, vol. 45, no. 2, pp. 155–187, 1994.

[278] C. Bicchieri, *The grammar of society: The nature and dynamics of social norms*. Cambridge University Press, 2005.

[279] H. Gintis, J. Henrich, S. Bowles, R. Boyd, and E. Fehr, "Strong reciprocity and the roots of human morality," *Social Justice Research*, vol. 21, no. 2, pp. 241–253, 2008.

[280] J. M. Weber and J. K. Murnighan, "Suckers or saviors? consistent contributors in social dilemmas.," *Journal of personality and social psychology*, vol. 95, no. 6, p. 1340, 2008.

[281] M. Chudek and J. Henrich, "Culture–gene coevolution, norm-psychology and the emergence of human prosociality," *Trends in cognitive sciences*, vol. 15, no. 5, pp. 218–226, 2011.

[282] J.-H. Lee, Y. Iwasa, U. Dieckmann, and K. Sigmund, "Social evolution leads to persistent corruption," *Proceedings of the National Academy of Sciences*, vol. 116, no. 27, pp. 13276–13281, 2019.

[283] V. N. Kolokoltsov, "Nonlinear markov games on a finite state space (mean-field and binary interactions)," *International Journal of Statistics and Probability*, vol. 1, apr 2012.

[284] V. N. Kolokoltsov and O. A. Malafeyev, "Mean-field-game model of corruption," *Dynamic Games and Applications*, vol. 7, pp. 34–47, nov 2015.

[285] J.-H. Lee, K. Sigmund, U. Dieckmann, and Y. Iwasa, "Games of corruption: How to suppress illegal logging," *Journal of Theoretical Biology*, vol. 367, pp. 1–13, feb 2015.

[286] P. Verma and S. Sengupta, "Bribe and punishment: An evolutionary game-theoretic analysis of bribery," *PLOS ONE*, vol. 10, p. e0133441, jul 2015.

[287] P. Verma, A. K. Nandi, and S. Sengupta, "Bribery games on interdependent regular networks," *Scientific Reports*, vol. 7, feb 2017.

[288] J.-H. Lee, M. Jusup, and Y. Iwasa, "Games of corruption in preventing the overuse of common-pool resources," *Journal of Theoretical Biology*, vol. 428, pp. 76–86, sep 2017.

[289] P. Verma, A. K. Nandi, and S. Sengupta, "Bribery games on interdependent complex networks," *Journal of Theoretical Biology*, vol. 450, pp. 43–52, aug 2018.

[290] C. Castellano, S. Fortunato, and V. Loreto, "Statistical physics of social dynamics," *Reviews of Modern Physics*, vol. 81, pp. 591–646, may 2009.

[291] O. Morgenstern and J. Von Neumann, *Theory of games and economic behavior*. Princeton university press, 1953.

[292] N. Boccara, *Modeling complex systems*. Springer Science & Business Media, 2010.

[293] J. Hofbauer, K. Sigmund, *et al.*, *Evolutionary games and population dynamics*. Cambridge university press, 1998.

[294] H. Gintis, *Game theory evolving: A problem-centered introduction to modeling strategic behavior*. Princeton university press, 2000.

[295] X. Chen, R. Wang, M. Tang, S. Cai, H. E. Stanley, and L. A. Braunstein, "Suppressing epidemic spreading in multiplex networks with social-support," *New Journal of Physics*, vol. 20, p. 013007, jan 2018.

[296] E. Cator and P. V. Mieghem, "Second-order mean-field susceptible-infected-susceptible epidemic threshold," *Physical Review E*, vol. 85, may 2012.

[297] J. P. Gleeson, "Binary-state dynamics on complex networks: Pair approximation and beyond," *Physical Review X*, vol. 3, apr 2013.

[298] S. Chandra, E. Ott, and M. Girvan, "Critical network cascades with re-excitable nodes: Why treelike approximations usually work, when they break down, and how to correct them," *Physical Review E*, vol. 101, no. 6, p. 062304, 2020.

[299] T. Diviák, J. K. Dijkstra, and T. A. B. Snijders, "Structure, multiplexity, and centrality in a corruption network: the czech rath affair," *Trends in Organized Crime*, vol. 22, pp. 274–297, mar 2018.

[300] I. Luna-Pla and J. R. Nicolás-Carlock, "Corruption and complexity: a scientific framework for the analysis of corruption networks," *Applied Network Science*, vol. 5, feb 2020.

[301] V. Nicosia, G. Bianconi, V. Latora, and M. Barthelemy, "Nonlinear growth and condensation in multiplex networks," *Physical Review E*, vol. 90, oct 2014.

[302] S. Milgram, "The small world problem," *Psychology today*, vol. 2, no. 1, pp. 60–67, 1967.

[303] M. Newman, A.-L. Barabási, and D. J. Watts, *The Structure and Dynamics of Networks*. Princeton University Press, dec 2011.

[304] A.-L. Barabási, "The network takeover," *Nature Physics*, vol. 8, pp. 14–16, dec 2011.

[305] P. Naur, *Concise survey of computer methods*. Petrocelli Books, 1974.

[306] V. Marx, "The big challenges of big data," *Nature*, vol. 498, pp. 255–260, jun 2013.

[307] R. Interdonato, M. Atzmueller, S. Gaito, R. Kanawati, C. Largeron, and A. Sala, "Feature-rich networks: going beyond complex network topologies," *Applied Network Science*, vol. 4, jan 2019.

[308] Y.-Y. Liu, J.-J. Slotine, and A.-L. Barabasi, "Observability of complex systems," *Proceedings of the National Academy of Sciences*, vol. 110, pp. 2460–2465, jan 2013.

[309] G. Baggio, D. S. Bassett, and F. Pasqualetti, "Data-driven control of complex networks," *Nature Communications*, vol. 12, mar 2021.

[310] M. C. González and A.-L. Barabási, "From data to models," *Nature Physics*, vol. 3, pp. 224–225, apr 2007.

[311] M. P. H. Stumpf, C. Wiuf, and R. M. May, "Subnets of scale-free networks are not scale-free: Sampling properties of networks," *Proceedings of the National Academy of Sciences*, vol. 102, pp. 4221–4224, mar 2005.

[312] V. Kotu and B. Deshpande, *Data science: concepts and practice*. Morgan Kaufmann, 2018.

[313] W. S. Cleveland, "Data science: an action plan for expanding the technical areas of the field of statistics," *International Statistical Review*, vol. 69, pp. 21–26, apr 2001.

[314] L. Lü, C.-H. Jin, and T. Zhou, "Similarity index based on local paths for link prediction of complex networks," *Physical Review E*, vol. 80, oct 2009.

[315] L. Weng, F. Menczer, and Y.-Y. Ahn, "Virality prediction and community structure in social networks," *Scientific Reports*, vol. 3, aug 2013.

[316] A. Aleta, G. F. de Arruda, and Y. Moreno, "Data-driven contact structures: From homogeneous mixing to multilayer networks," *PLOS Computational Biology*, vol. 16, p. e1008035, jul 2020.

[317] M. E. Dickison, M. Magnani, and L. Rossi, *Multilayer social networks*. Cambridge University Press, 2016.

[318] A. Mahajan, N. A. Sivadas, and R. Solanki, "An epidemic model SIPHERD and its application for prediction of the spread of COVID-19 infection in india," *Chaos, Solitons & Fractals*, vol. 140, p. 110156, nov 2020.

[319] D. Centola, "The spread of behavior in an online social network experiment," *Science*, vol. 329, pp. 1194–1197, sep 2010.

[320] J. Ugander, L. Backstrom, C. Marlow, and J. Kleinberg, "Structural diversity in social contagion," *Proceedings of the National Academy of Sciences*, vol. 109, pp. 5962–5966, apr 2012.

[321] A. Santoro and V. Nicosia, "Optimal percolation in correlated multilayer networks with overlap," *Physical Review Research*, vol. 2, jul 2020.

[322] A. Charnes, E. L. Frome, and P. L. Yu, "The equivalence of generalized least squares and maximum likelihood estimates in the exponential family," *Journal of the American Statistical Association*, vol. 71, pp. 169–171, mar 1976.

[323] W. R. Gilks, S. Richardson, and D. Spiegelhalter, *Markov chain Monte Carlo in practice*. CRC press, 1995.

[324] M. J. Keeling and C. A. Gilligan, "Metapopulation dynamics of bubonic plague," *Nature*, vol. 407, pp. 903–906, oct 2000.

[325] L. F. White, B. Archer, and M. Pagano, "Determining the dynamics of influenza transmission by age," *Emerging Themes in Epidemiology*, vol. 11, mar 2014.

[326] M. Eichner, "Case isolation and contact tracing can prevent the spread of smallpox," *American Journal of Epidemiology*, vol. 158, pp. 118–128, jul 2003.

[327] N. M. Ferguson, D. A. T. Cummings, C. Fraser, J. C. Cajka, P. C. Cooley, and D. S. Burke, "Strategies for mitigating an influenza pandemic," *Nature*, vol. 442, pp. 448–452, apr 2006.

[328] K. M. English, J. M. Langley, A. McGeer, *et al.*, "Contact among healthcare workers in the hospital setting: developing the evidence base for innovative approaches to infection control," *BMC Infectious Diseases*, vol. 18, apr 2018.

[329] N. H. Fefferman and K. L. Ng, "How disease models in static networks can fail to approximate disease in dynamic networks," *Physical Review E*, vol. 76, sep 2007.

[330] S. D. Valle, H. Hethcote, J. Hyman, and C. Castillo-Chavez, "Effects of behavioral changes in a smallpox attack model," *Mathematical Biosciences*, vol. 195, pp. 228–251, jun 2005.

[331] Y. Tonta and H. R. Darvish, "Diffusion of latent semantic analysis as a research tool: A social network analysis approach," *Journal of Informetrics*, vol. 4, pp. 166–174, apr 2010.

[332] J. Mossong, N. Hens, M. Jit, P. Beutels, K. Auranen, R. Mikolajczyk, M. Massari, S. Salmaso, G. S. Tomba, J. Wallinga, J. Heijne, M. Sadkowska-Todys, M. Rosinska, and W. J. Edmunds, "Social contacts and mixing patterns relevant to the spread of infectious diseases," *PLoS Medicine*, vol. 5, p. e74, mar 2008.

[333] A. Schaum and R. B. Jaquez, "Estimating the state probability distribution for epidemic spreading in complex networks," *Applied Mathematics and Computation*, vol. 291, pp. 197–206, dec 2016.

[334] A. R. Moss and P. Bacchetti, "Natural history of hiv infection," *Aids*, vol. 3, no. 2, pp. 55–62, 1989.

[335] P. S. Bearman, J. Moody, and K. Stovel, "Chains of affection: The structure of adolescent romantic and sexual networks," *American journal of sociology*, vol. 110, no. 1, pp. 44–91, 2004.

[336] M. Salathe, M. Kazandjieva, J. W. Lee, P. Levis, M. W. Feldman, and J. H. Jones, "A high-resolution human contact network for infectious disease transmission," *Proceedings of the National Academy of Sciences*, vol. 107, pp. 22020–22025, dec 2010.

[337] L. A. Meyers, B. Pourbohloul, M. Newman, D. M. Skowronski, and R. C. Brunham, "Network theory and SARS: predicting outbreak diversity," *Journal of Theoretical Biology*, vol. 232, pp. 71–81, jan 2005.

[338] Q. Yin, T. Shi, C. Dong, and Z. Yan, "The impact of contact patterns on epidemic dynamics," *PLOS ONE*, vol. 12, p. e0173411, mar 2017.

[339] K. Leung, M. Jit, E. H. Y. Lau, and J. T. Wu, "Social contact patterns relevant to the spread of respiratory infectious diseases in hong kong," *Scientific Reports*, vol. 7, aug 2017.

[340] J. Zhang, M. Litvinova, Y. Liang, Y. Wang, W. Wang, S. Zhao, Q. Wu, S. Merler, C. Viboud, A. Vespignani, M. Ajelli, and H. Yu, "Changes in contact patterns shape the dynamics of the COVID-19 outbreak in china," *Science*, vol. 368, pp. 1481–1486, apr 2020.

[341] P. J. Dodd, C. Looker, I. D. Plumb, *et al.*, "Age- and sex-specific social contact patterns and incidence ofMycobacterium tuberculosisInfection," *American Journal of Epidemiology*, p. kwv160, dec 2015.

[342] D.-L. Luh, Z.-S. You, and S.-C. Chen, "Comparison of the social contact patterns among school-age children in specific seasons, locations, and times," *Epidemics*, vol. 14, pp. 36–44, mar 2016.

[343] L. Danon, J. M. Read, T. A. House, M. C. Vernon, and M. J. Keeling, "Social encounter networks: characterizing great britain," *Proceedings of the Royal Society B: Biological Sciences*, vol. 280, p. 20131037, aug 2013.

[344] K. Eames, S. Bansal, S. Frost, and S. Riley, "Six challenges in measuring contact networks for use in modelling," *Epidemics*, vol. 10, pp. 72–77, mar 2015.

[345] T. Smieszek, E. U. Burri, R. Scherzinger, and R. W. Scholz, "Collecting close-contact social mixing data with contact diaries: reporting errors and biases," *Epidemiology and Infection*, vol. 140, pp. 744–752, jun 2011.

[346] P. Beutels, Z. Shkedy, M. Aerts, and P. V. Damme, "Social mixing patterns for transmission models of close contact infections: exploring self-evaluation and diary-based data collection through a web-based interface," *Epidemiology and Infection*, vol. 134, pp. 1158–1166, may 2006.

[347] N. Eagle, A. Pentland, and D. Lazer, "Inferring friendship network structure by using mobile phone data," *Proceedings of the National Academy of Sciences*, vol. 106, pp. 15274–15278, aug 2009.

[348] A. Stopczynski, V. Sekara, P. Sapiezynski, A. Cuttone, M. M. Madsen, J. E. Larsen, and S. Lehmann, "Measuring large-scale social networks with high resolution," *PLoS ONE*, vol. 9, p. e95978, apr 2014.

[349] A. Barrat, C. Cattuto, A. Tozzi, P. Vanhems, and N. Voirin, "Measuring contact patterns with wearable sensors: methods, data characteristics and applications to data-driven simulations of infectious diseases," *Clinical Microbiology and Infection*, vol. 20, pp. 10–16, jan 2014.

[350] R. M. Christley, G. L. Pinchbeck, R. G. Bowers, *et al.*, "Infection in social networks: Using network analysis to identify high-risk individuals," *American Journal of Epidemiology*, vol. 162, pp. 1024–1031, sep 2005.

[351] R. A. Clark and M. Macdonald, "Identification of effective spreaders in contact networks using dynamical influence," *Applied Network Science*, vol. 6, jan 2021.

[352] J. Dushoff and S. Levin, "The effects of population heterogeneity on disease invasion," *Mathematical Biosciences*, vol. 128, pp. 25–40, jul 1995.

[353] R. Mastrandrea, J. Fournet, and A. Barrat, "Contact patterns in a high school: A comparison between data collected using wearable sensors, contact diaries and friendship surveys," *PLOS ONE*, vol. 10, p. e0136497, sep 2015.

[354] A. Apolloni, C. Poletto, and V. Colizza, "Age-specific contacts and travel patterns in the spatial spread of 2009 h1n1 influenza pandemic," *BMC Infectious Diseases*, vol. 13, apr 2013.

[355] K. Prem, Y. Liu, T. W. Russell, *et al.*, "The effect of control strategies to reduce social mixing on outcomes of the COVID-19 epidemic in wuhan, china: a modelling study," *The Lancet Public Health*, vol. 5, pp. e261–e270, may 2020.

[356] H. Hethcote, "Modeling heterogeneous mixing in infectious disease dynamics," *Models for infectious human diseases: their structure and relation to data*, vol. 6, p. 215, 1996.

[357] J. Wallinga, D. Levy-Bruhl, N. Gay, and C. Wachmann, "Estimation of measles reproduction ratios and prospects for elimination of measles by vaccination in some western european countries," *Epidemiology and Infection*, vol. 127, pp. 281–295, oct 2001.

[358] C. P. Farrington and H. J. Whitaker, "Contact surface models for infectious diseases," *Journal of the American Statistical Association*, vol. 100, pp. 370–379, jun 2005.

[359] S. Blower and M.-H. Go, "The importance of including dynamic social networks when modeling epidemics of airborne infections: does increasing complexity increase accuracy?," *BMC Medicine*, vol. 9, jul 2011.

[360] I. M. Longini, "Containing pandemic influenza at the source," *Science*, vol. 309, pp. 1083–1087, aug 2005.

[361] D. Mistry, M. Litvinova, A. P. y Piontti, *et al.*, "Inferring high-resolution human mixing patterns for disease modeling," *Nature Communications*, vol. 12, jan 2021.

[362] J. Wallinga, P. Teunis, and M. Kretzschmar, "Using data on social contacts to estimate age-specific transmission parameters for respiratory-spread infectious agents," *American Journal of Epidemiology*, vol. 164, pp. 936–944, sep 2006.

[363] P. Rohani, X. Zhong, and A. A. King, "Contact network structure explains the changing epidemiology of pertussis," *Science*, vol. 330, pp. 982–985, nov 2010.

[364] M. Baguelin, S. Flasche, A. Camacho, N. Demiris, E. Miller, and W. J. Edmunds, "Assessing optimal target populations for influenza vaccination programmes: An evidence synthesis and modelling study," *PLoS Medicine*, vol. 10, p. e1001527, oct 2013.

[365] J. Zhang, P. Klepac, J. M. Read, *et al.*, "Patterns of human social contact and contact with animals in shanghai, china," *Scientific Reports*, vol. 9, oct 2019.

[366] R. M. Anderson and R. M. May, "Age-related changes in the rate of disease transmission: implications for the design of vaccination programmes," *Journal of Hygiene*, vol. 94, pp. 365–436, jun 1985.

[367] J. M. Read, J. Lessler, S. Riley, *et al.*, "Social mixing patterns in rural and urban areas of southern china," *Proceedings of the Royal Society B: Biological Sciences*, vol. 281, p. 20140268, jun 2014.

[368] Y. Ibuka, Y. Ohkusa, T. Sugawara, *et al.*, "Social contacts, vaccination decisions and influenza in japan," *Journal of Epidemiology and Community Health*, vol. 70, pp. 162–167, sep 2015.

[369] M. Ajelli and M. Litvinova, "Estimating contact patterns relevant to the spread of infectious diseases in russia," *Journal of Theoretical Biology*, vol. 419, pp. 1–7, apr 2017.

[370] A. Melegaro, M. Jit, N. Gay, E. Zagheni, and W. J. Edmunds, "What types of contacts are important for the spread of infections? using contact survey data to explore european mixing patterns," *Epidemics*, vol. 3, pp. 143–151, sep 2011.

[371] J. M. Hilbe, *Negative binomial regression*. Cambridge University Press, 2011.

[372] D. Lu, A. Aleta, M. Ajelli, R. Pastor-Satorras, A. Vespignani, and Y. Moreno, "Data-driven estimate of SARS-CoV-2 herd immunity threshold in populations with individual contact pattern variations," *medRxiv*, mar 2021.

[373] E. Han, M. M. J. Tan, E. Turk, D. Sridhar, *et al.*, "Lessons learnt from easing COVID-19 restrictions: an analysis of countries and regions in asia pacific and europe," *The Lancet*, vol. 396, pp. 1525–1534, nov 2020.

[374] J. M. Brauner, S. Mindermann, M. Sharma, *et al.*, "Inferring the effectiveness of government interventions against COVID-19," *Science*, vol. 371, p. eabd9338, dec 2020.

[375] J. Dehning, J. Zierenberg, F. P. Spitzner, M. Wibral, J. P. Neto, M. Wilczek, and V. Priesemann, "Inferring change points in the spread of COVID-19 reveals the effectiveness of interventions," *Science*, vol. 369, p. eabb9789, may 2020.

[376] K. Sun, W. Wang, L. Gao, *et al.*, "Transmission heterogeneities, kinetics, and controllability of SARS-CoV-2," *Science*, vol. 371, p. eabe2424, nov 2020.

[377] Y. Li, H. Campbell, D. Kulkarni, *et al.*, "The temporal association of introducing and lifting non-pharmaceutical interventions with the time-varying reproduction number (r) of SARS-CoV-2: a modelling study across 131 countries," *The Lancet Infectious Diseases*, vol. 21, pp. 193–202, feb 2021.

[378] V. Marziano, G. Guzzetta, B. M. Rondinone, *et al.*, "Retrospective analysis of the italian exit strategy from COVID-19 lockdown," *Proceedings of the National Academy of Sciences*, vol. 118, p. e2019617118, jan 2021.

[379] N. Perra, "Non-pharmaceutical interventions during the COVID-19 pandemic: A review," *Physics Reports*, feb 2021.

[380] Y. Dong, T. Dai, Y. Wei, L. Zhang, M. Zheng, and F. Zhou, "A systematic review of SARS-CoV-2 vaccine candidates," *Signal Transduction and Targeted Therapy*, vol. 5, oct 2020.

[381] F. Krammer, "SARS-CoV-2 vaccines in development," *Nature*, vol. 586, pp. 516–527, sep 2020.

[382] T. Britton, F. Ball, and P. Trapman, "A mathematical model reveals the influence of population heterogeneity on herd immunity to SARS-CoV-2," *Science*, vol. 369, pp. 846–849, jun 2020.

[383] A. L. Rasmussen, "Vaccination is the only acceptable path to herd immunity," *Med*, vol. 1, pp. 21–23, dec 2020.

[384] R. Aguas, R. M. Corder, J. G. King, G. Gonçalves, M. U. Ferreira, and M. G. M. Gomes, "Herd immunity thresholds for SARS-CoV-2 estimated from unfolding epidemics," *medRxiv*, jul 2020.

[385] S. J. Fox, P. Potu, M. Lachmann, R. Srinivasan, and L. A. Meyers, "The COVID-19 herd immunity threshold is not low: A re-analysis of european data from spring of 2020," *medRxiv*, dec 2020.

[386] T. Hoang, P. Coletti, A. Melegaro, *et al.*, "A systematic review of social contact surveys to inform transmission models of close-contact infections," *Epidemiology*, vol. 30, pp. 723–736, sep 2019.

[387] N. G. Davies, , P. Klepac, Y. Liu, K. Prem, M. Jit, and R. M. Eggo, "Age-dependent effects in the transmission and control of COVID-19 epidemics," *Nature Medicine*, vol. 26, pp. 1205–1211, jun 2020.

[388] R. M. Viner, O. T. Mytton, C. Bonell, *et al.*, "Susceptibility to SARS-CoV-2 infection among children and adolescents compared with adults," *JAMA Pediatrics*, vol. 175, p. 143, feb 2021.

[389] *Coronavirus Disease 2019 (COVID-19) planning scenarios*, 2020. [Online; accessed 15. Dec. 2020].

[390] S. Hu, W. Wang, Y. Wang, *et al.*, "Infectivity, susceptibility, and risk factors associated with SARS-CoV-2 transmission under intensive contact tracing in hunan, china," *Nature Communications*, vol. 12, mar 2021.

[391] J. A. Backer, D. Klinkenberg, and J. Wallinga, "Incubation period of 2019 novel coronavirus (2019-ncov) infections among travellers from wuhan, china, 20–28 january 2020," *Eurosurveillance*, vol. 25, no. 5, p. 2000062, 2020.

[392] P. Poletti, M. Tirani, D. Cereda, *et al.*, "Age-specific sars-cov-2 infection fatality ratio and associated risk factors, italy, february to april 2020," *Eurosurveillance*, vol. 25, no. 31, p. 2001383, 2020.

[393] R. Anderson, G. Medley, R. May, and A. Johnson, "A preliminary study of the transmission dynamics of the human immunodeficiency virus (HIV), the causative agent of AIDS," *Mathematical Medicine and Biology*, vol. 3, no. 4, pp. 229–263, 1986.

[394] C. Costantino and F. Vitale, "Influenza vaccination in high-risk groups: a revision of existing guidelines and rationale for an evidence-based preventive strategy," *Journal of preventive medicine and hygiene*, vol. 57, no. 1, p. E13, 2016.

[395] C. Huang, L. Huang, Y. Wang, *et al.*, "6-month consequences of COVID-19 in patients discharged from hospital: a cohort study," *The Lancet*, vol. 397, pp. 220–232, jan 2021.

[396] J. V. Lazarus, S. C. Ratzan, A. Palayew, *et al.*, "A global survey of potential acceptance of a COVID-19 vaccine," *Nature Medicine*, vol. 27, pp. 225–228, oct 2020.

[397] W. Wang, Q. Wu, J. Yang, *et al.*, "Global, regional, and national estimates of target population sizes for covid-19 vaccination: descriptive study," *BMJ*, p. m4704, dec 2020.

[398] M. Haque, J. McKimm, M. Sartelli, *et al.*, "Strategies to Prevent Healthcare-Associated Infections: A Narrative Overview," *RMHP*, vol. 13, pp. 1765–1780, Sep 2020.

[399] Y. Li, X. Huang, Y. I. T., W. T. W., and H. Qian, "Role of air distribution in SARS transmission during the largest nosocomial outbreak in Hong Kong.," *Indoor Air*, vol. 15, pp. 83–95, Apr 2005.

[400] M. D. Aaron Richterman, "Hospital-Acquired SARS-CoV-2 Infection: Lessons for Public Health," *JAMA*, vol. 324, pp. 2155–2156, Dec 2020.

[401] P. W. Stone, "Economic burden of healthcare-associated infections: an american perspective," *Expert Review of Pharmacoeconomics & Outcomes Research*, vol. 9, pp. 417–422, oct 2009.

[402] A. Revelas, "Healthcare - associated infections: A public health problem," *Nigerian Medical Journal*, vol. 53, no. 2, p. 59, 2012.

[403] E. Zimlichman, D. Henderson, O. Tamir, C. Franz, P. Song, C. K. Yamin, C. Keohane, C. R. Denham, and D. W. Bates, "Health care–associated infections," *JAMA Internal Medicine*, vol. 173, p. 2039, dec 2013.

[404] P. Datta, H. Rani, R. Chauhan, S. Gombar, and J. Chander, "Healthcare-associated infections: Risk factors and epidemiology from an intensive care unit in northern india," *Indian Journal of Anaesthesia*, vol. 58, no. 1, p. 30, 2014.

[405] G. D. Angelis, A. Murthy, J. Beyersmann, and S. Harbarth, "Estimating the impact of healthcare-associated infections on length of stay and costs," *Clinical Microbiology and Infection*, vol. 16, pp. 1729–1735, dec 2010.

[406] C. A. Umscheid, M. D. Mitchell, J. A. Doshi, *et al.*, "Estimating the proportion of healthcare-associated infections that are reasonably preventable and the related mortality and costs," *Infection Control & Hospital Epidemiology*, vol. 32, pp. 101–114, feb 2011.

[407] D. P. Calfee, "Crisis in hospital-acquired, healthcare-associated infections," *Annual Review of Medicine*, vol. 63, pp. 359–371, feb 2012.

[408] G. Davis, N. Sevdalis, and L. Drumright, "Spatial and temporal analyses to investigate infectious disease transmission within healthcare settings," *Journal of Hospital Infection*, vol. 86, pp. 227–243, apr 2014.

[409] M. Haque, M. Sartelli, J. McKimm, and M. B. A. Bakar, "Health care-associated infections &ndash an overview," *Infection and Drug Resistance*, vol. Volume 11, pp. 2321–2333, nov 2018.

[410] G. Gopalakrishna, P. Choo, Y. S. Leo, *et al.*, "SARS transmission and hospital containment," *Emerging Infectious Diseases*, vol. 10, pp. 395–400, mar 2004.

[411] J.-P. Marcel, M. Alfa, F. Baquero, *et al.*, "Healthcare-associated infections: think globally, act locally," *Clinical Microbiology and Infection*, vol. 14, pp. 895–907, oct 2008.

[412] J. K. Ferguson, "Preventing healthcare-associated infection: risks, healthcare systems and behaviour," *Internal Medicine Journal*, vol. 39, pp. 574–581, sep 2009.

[413] P. M. Polgreen, T. L. Tassier, S. V. Pemmaraju, and A. M. Segre, "Prioritizing healthcare worker vaccinations on the basis of social network analysis," *Infection Control & Hospital Epidemiology*, vol. 31, pp. 893–900, sep 2010.

[414] D. J. Weber, D. Anderson, and W. A. Rutala, "The role of the surface environment in healthcare-associated infections," *Current Opinion in Infectious Diseases*, vol. 26, pp. 338–344, aug 2013.